

---

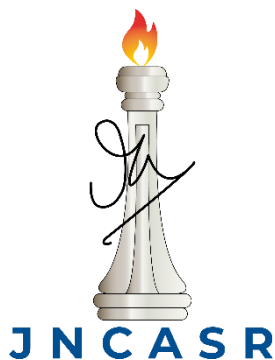
# Design, synthesis and evaluation of peptides and their mimetics to modulate biological and catalytic activity

*A Thesis Submitted for the Degree of*

**Doctor of Philosophy**

*By*

**Debasis Ghosh**



**Bioorganic Chemistry Laboratory, New Chemistry Unit**  
**Jawaharlal Nehru Centre for Advanced Scientific Research**  
*(A Deemed University)*

**Bengaluru-560064, India**

**February 2022**

---

---

*Dedicated to my Parents*

---



---

## **TABLE OF CONTENTS**

Certificate	i
Declaration	iii
Acknowledgements	v
Preface	vii
<b>Chapter 1: Introduction</b>	<b>1</b>
1.1 Peptides and their derivatives as therapeutic agents	3
1.2 Cyclic dipeptides (CDPs)	4
1.3 Alzheimer's disease (AD)	8
1.3.1 A $\beta$ peptides	8
1.3.2 A $\beta$ nucleation process	8
1.3.3 Role of A $\beta$ 14-23 in fibril formation	9
1.4 A $\beta$ aggregation-associated toxicity	9
1.4.1 Oxidative stress	11
1.4.2 Membrane interaction	12
1.5 Current therapeutic strategies of AD	12
1.5.1 Peptides/peptidomimetics inhibitors of A $\beta$ aggregation	13
1.5.2 Small molecule-based modulators	14
1.6 Molecular architectonics	17
1.7 Catalytic peptide	18
1.8 Small molecule and peptide binders of <i>i</i> -motif DNA	21
1.9 Objective	22
1.7 References	24
<b>Chapter 2: Combating the Amyloid-Induced Cellular Toxicity and Stiffness by Designer Peptidomimetics</b>	<b>31</b>
2.1 Design strategy of peptidomimetics	35
2.2 Results and discussion	35

---



---

2.2.1 Thioflavin T assay	35
2.2.2 CD measurements	38
2.2.3 IR study and AFM study	38
2.3 Cytotoxicity assay	41
2.4 Membrane toxicity	44
2.5 Live-dead assay	44
2.6 Inhibition of A $\beta$ induced amyloidogenic stress	46
2.7 PF QNM-AFM imaging for <i>SH-SY5Y</i> cells	46
2.8 Molecular docking study	47
2.9 Experimental section	54
2.9.1 General methods	54
2.9.2 Synthesis of A $\beta$ 14-23 (I) peptide and CDP-peptidomimetics (II-V)	56
2.9.3 Circular Dichroism (CD) studies	57
2.9.4 Fourier-Transform Infrared Spectroscopy (FTIR) studies	57
2.9.5 Transmission electron microscopy (TEM) imaging	57
2.9.6 Aggregation kinetics study using ThT fluorescence	58
2.9.7 PF QNM-AFM imaging	58
2.9.8 Neuronal rescue studies	59
2.9.9 Membrane toxicity	59
2.9.10 Docking studies	60
2.9.11 AFM imaging of A $\beta$ -aggregates using PF QNM-AFM	61
2.9.12 Cytotoxicity assay	61
2.9.13 Live-dead assay	62
2.9.14 Intracellular ROS measurement	62
2.9.15 Enzymatic stability assay	63
2.9.16 Characterizations of kd, A $\beta$ 14-23 (I) and peptidomimetics (II-V)	64
2.10 References	73

---

---

<b>Chapter 3: Differential Copper-Guided Architectures of Amyloid <math>\beta</math> Peptidomimetics Modulate Oxidation States and Catalysis</b>	79
3.1. Design and synthesis	81
3.2 Results and discussions	84
3.3 Conclusion	98
3.4 General methods	98
3.4.1 Synthesis of A $\beta$ 14-23, A $\beta$ 14-23Py, Akd <sup>NMC</sup> , Akd <sup>NMCPy</sup> and HkdPy peptidomimetics	99
3.4.2 Preparation of the peptide stock solution	99
3.4.3 Metal binding study	99
3.4.4 Atomic force microscopy (AFM) characterization	100
3.4.5 Kinetic assay with fluorescein (DCFHDA) derivatives	100
3.4.6 Cyclic voltammetry (CV) experiment	101
3.4.7 Transmission electron microscopy (TEM) characterization	101
3.4.8 Fourier-transform infrared spectroscopy (FTIR)	101
3.4.9 Field emission scanning electron microscopy (FESEM)	102
3.4.10 Circular dichroism (CD) spectroscopy	102
3.4.11 Electron paramagnetic resonance (EPR)	102
3.4.12 Molecular docking	103
3.4.13 DFT calculation	104
3.5 References	113
<b><i>Chapter 4. Dihydrophthalazinediones Accelerate Amyloid <math>\beta</math> Peptide Aggregation to Nontoxic Species</i></b>	117
4.1 Design and synthesis	120
4.2 Results and discussion	121
4.2.1 Synthesis of dihydrophthalazinedione derivatives	121
4.2.2 Inhibition of amyloid $\beta$ aggregation: thioflavin T assay	122
4.2.3 Dot blot assay	123
4.2.4 TEM analysis	125

---

---

4.2.5 Phz induced neuronal cell rescue assay	125
4.3 Conclusion	127
4.4 Materials and methods	128
4.4.1 Syntheses of dihydrophthalazinedione derivatives	128
4.4.2 A $\beta$ 42 monomer and fibrils	129
4.4.3 Thioflavin T (ThT) fluorescence assay	129
4.4.4 Dot blot analysis	129
4.4.5 Transmission electron microscopy (TEM)	130
4.4.6 Cell viability assay	130
4.4.7 Characterization of dihydrophthalazinedione derivatives	131
4.5 References	140
<b>Chapter 5: Tryptophan Rich Peptide Selectively Recognize and Modulates <i>i</i>-motif Structural Dynamics of HIF-1<math>\alpha</math> DNA</b>	145
5.1 Design and synthesis	149
5.2 Results and discussions	151
5.2.1 Trp fluorescence-based screening assay	152
5.2.2 CD study	153
5.2.3 Electrophoretic gel mobility shift assay (EMSA)	153
5.2.4 FRET melting assay	153
5.2.5 Peptide-induced intramolecular folding and unfolding dynamics of HIF-1 $\alpha$	154
5.2.6 Time correlated single photon counting (TCSPC) measurement	156
5.3 Conclusion	157
5.4 Experimental methods	159
5.4.1 Synthesis of W <sub>5</sub> K <sub>5</sub> /F <sub>5</sub> K <sub>5</sub>	159
5.4.2 DNA sequences used in the study	159
5.4.3 DNA sample preparation	160
5.4.4 GEL electrophoresis	160
5.4.5 CD measurement	160

---

---

5.4.6 Fluorescence measurement	161
5.4.7 FRET melting assay	161
5.4.8 FRET theory	162
5.6 References	165
<b><i>List of publications</i></b>	169

---

---

---

## **CERTIFICATE**

I hereby certify that the work described in this thesis entitled “**Design, synthesis and evaluation of peptides and their mimetics to modulate biological and catalytic activity**” has been carried out by **Mr. Debasis Ghosh** under my supervision at the Bioorganic Chemistry Laboratory, New Chemistry Unit, Jawaharlal Nehru Centre for Advanced Scientific Research, Bengaluru, India and that it has not been submitted elsewhere for the award of any degree or diploma.



**Prof. T. Govindaraju**  
(Research Guide)

---

---

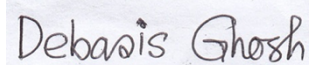
---

---

## **DECLARATION**

I hereby declare that the matter embodied in the thesis entitled “**Design, synthesis and evaluation of peptides and their mimetics to modulate biological and catalytic activity**” is the resultant of the investigations carried out by me at the Bioorganic Chemistry Laboratory, New Chemistry Unit, Jawaharlal Nehru Centre for Advanced Scientific Research, Bengaluru, India under the supervision of **Prof. T. Govindaraju** and that it has not been submitted elsewhere for the award of any degree or diploma.

In keeping with the general practice in reporting the scientific observations, due acknowledgment has been made whenever the work described is based on the findings of other investigators. Any omission that might have occurred due to oversight or error in judgment is regretted.



**Debasis Ghosh**  
(PhD Student)

---

---



---

---

## **ACKNOWLEDGEMENTS**

*First and foremost, I would like to express my sincere gratitude to my research supervisor Prof. T. Govindaraju, Bioorganic Chemistry Laboratory, New Chemistry Unit, JNCASR, for his continuous support, motivation, infinite patience, and guidance throughout my PhD tenure. It has been a great privilege and honor to be associated with him.*

*I would like to thank Prof. C. N. R. Rao, FRS for being the source of inspiration, generous support, and encouragement throughout my stay in JNCASR.*

*I would also like to thank past and present NCU Chairs for providing excellent facilities.*

*I am thankful to my wonderful lab mates Dr. Debabrata, Dr. Avinash, Dr. Pandeewar, Dr. Shivaprasad, Dr. Nangarjun, Dr. Rajasekhar, Dr. Suseela, Dr. Sourav, and present lab members Mr. Sumon, Mr. Biswanath, Dr. Laxmi, Dr. Mouli, Dr. Tanmay, Mr. Madhu, Mr. Ashish, Ms. Dikshaa, Mr. Hari, Dr. Ankita, Dr. Suresh, Dr. Madhu, Dr. Pardasaradhi, Dr. Sadab, Dr. Bappaditya, Dr. Balachandra, Mr. Satyajit, Mr. Harshit, Mr. Sabyasachi, Ms. Krithi, Mr. Mani, Mr. Shiva, Mr. Nabeel for their help and friendly environment in the lab.*

*I would like to thank summer trainees, Ms. Preeti, and Ms. Sangita for helping me in my work.*

*I am thankful to Dr. Jayanta Halder, Dr. Sarit Agasti, Dr. Sridhar Rajaram, Dr. Siddharth Sharma (IISc) for their valuable courses.*

*I would like to thank all my PhD-2016 batch friends and Aritra, Sourav, Ranjan, Swagatam, Manisha, Sunit, Meenakshi, Sumon, Biswanath for extending their help and cooperation throughout my stay in JNCASR.*

*I would like to thank the Academics, Administration, and NCU Office staff and Shivakumar and Deepak for their constant help.*

---

---

*It is indeed a great pleasure to express my sincere thanks to Midnapore College and IIT Guwahati for the most memorable moments of my life.*

*I thank JNCASR Library, Comp Lab, Hostel, and Health Center for providing and maintaining the various facilities that have helped me immensely.*

*Finally, and most importantly, I am grateful to my family, especially my parents (Amal Ghosh and Ruma Ghosh) and my sister's family (Tamasi Ghorai, and Tusar Ghorai) for their love, moral support, and constant encouragement throughout my life. Their love, blessings, and affection made me what I am today. This thesis is dedicated to my parents for their love and support.*

---

---

## PREFACE

This PhD thesis is divided into five chapters. Chapter 1 introduces peptide and peptidomimetics with a brief introduction to cyclic dipeptides (CDPs) and their medicinal and biomaterial applications. Recent developments on multifunctional peptidomimetics-based therapeutic molecules to modulate A $\beta$  toxicity and catalytic activity of A $\beta$ -derived peptidomimetics are discussed, which provide rationale for the research work presented in the thesis.

Chapter 2 presents de novo design, synthesis, and evaluation of a set of protease-resistant peptidomimetics derived from A $\beta$ 14-23 sequence of A $\beta$ 42 by incorporating CDP-based unnatural amino acid units at defined positions in modulating the amyloidogenic stress and adverse cellular stiffness. Our *in vitro* and *in cellulo* study identified Akd<sup>NMC</sup> with CDP units at the middle, N- and C-termini as a potent inhibitor to ameliorate cellular toxicity and maintain healthy cellular mechanics by combating amyloidogenic stress.

Chapter 3 deals with molecular architectonics of A $\beta$ 14-23 peptidomimetics (Akd<sup>NMC</sup>Py) with suitably inserted CDP and pyrene units as molecular assembly modulator and reporter units, respectively, to generate distinct functional architectures. Akd<sup>NMC</sup>Py self-assemble into fibrils, which transform to nanosheets in the presence of Cu<sup>II</sup>. Notably, the serial addition of Cu<sup>II</sup> to Akd<sup>NMC</sup>Py generate micelle-like architectures that were subsequently transformed into nanosheets. While one-off addition of Cu<sup>II</sup> resulted in the formation of nanosheets without forming any intermediate architectures. EPR study showed the micellar-like and nanosheet architectures stabilize Cu<sup>II</sup> and Cu<sup>I</sup>, respectively. The micelle-like and nanosheet architectures were employed to perform Cu<sup>II</sup>-catalyzed oxidative-hydrolysis tandem and Cu<sup>I</sup>-catalyzed alkyne-azide cycloaddition reactions, respectively.

In Chapter 4, we report a set of dihydrophthalazinedione (Phz) based on small molecules (Phz 1-4) to modulate A $\beta$ 42 aggregation and *in cellulo* toxicity. Our study demonstrates that fluorine-containing Phz 4 modulate A $\beta$ 42 aggregation by accelerating the process to form non-toxic aggregation species through hydrophobic and halogen interactions.

---

---

Chapter 5 presents decapeptide with alternative tryptophan and lysine amino acids for targeting of *i*-motif structure corresponding to hypoxia-inducible factor-1 alpha (HIF1 $\alpha$ ) sequence over other DNA conformations. The discussion includes the mode of binding between the peptide and *i*-motif DNA.

In summary, the proposed thesis provides an overview of peptide and peptidomimetics design, synthesis, and evaluation of their biological and catalytic activities. Modulation of A $\beta$  aggregation-induced cellular toxicity and adverse cellular mechanics by the de novo designed A $\beta$ -peptidomimetics with CDP units is discussed in the second chapter. The third chapter presents the distinct architectures of A $\beta$ -peptidomimetics incorporated CDP and pyrene units, and their differential stabilization of copper oxidation states (Cu<sup>II</sup> and Cu<sup>I</sup>) with catalytic activity in tandem and alkyne-azide click reactions, respectively. The fourth chapter describes how fluorine substituted small molecules can alter amyloid aggregation pathways. Our efforts to understand the role of (tryptophan-lysine)<sub>5</sub> decapeptide in binding and altering the *i*-motif DNA conformation is discussed in the fifth chapter.

**Chapter 1**

**Introduction**



Peptides influence many key physiological mechanisms and control vital functions in humans, such as immune defence, metabolism, reproduction, respiration, and pain sensitivity.<sup>1</sup> Peptides exhibit good efficacy and tolerability profile, as well as favourable development stages, which includes the knowledge of a predictable metabolism, and low attrition rates. An increasing number of peptides are entering clinical trials and several of them are being approved as medications because of advancements in structure optimization, formulation, and manufacturing process.<sup>2</sup> However, peptides suffer from several drawbacks such as i) poor proteolytic stability which results in the reduced half-life of in the gastrointestinal tract and serum, ii) relatively high molecular mass, lack of transport systems, poor absorption, and transport qualities often result in early excretion from the body, iii) the N–C $\alpha$  and C $\alpha$ –CO rotational bonds of amino acids provide intrinsic flexibility, resulting in poor selectivity and undesired side effects, and iv) interaction with antibody binding sites generates antigenicity and immunological response in a competent host in an unpredictably variable manner.<sup>3</sup> Peptidomimetics were designed to improve metabolic stability, bioavailability, receptor affinity, and selectivity of peptides (Figure 1). The lead peptide structure is optimized by introducing functional alterations that solve the peptide inherent drawbacks while preserving the structural elements that are responsible for biological activity.<sup>4</sup>

### **1.1 Peptides and their derivatives as therapeutic agents**

Peptides are good candidates for drug discovery because of their selective, effective, reasonably safe, and well-tolerated bioactivity. There are around 7000 natural peptides known to serve vital roles in human physiology.<sup>1,5</sup> These peptides serve as hormones, growth factors, ion channel ligands, and anti-infectives, among others. Normally, peptides

can bind to specific cell surface receptors selectively causing intracellular effects. Thus, peptides have been considered to be effective starting point for the development of novel medicines.

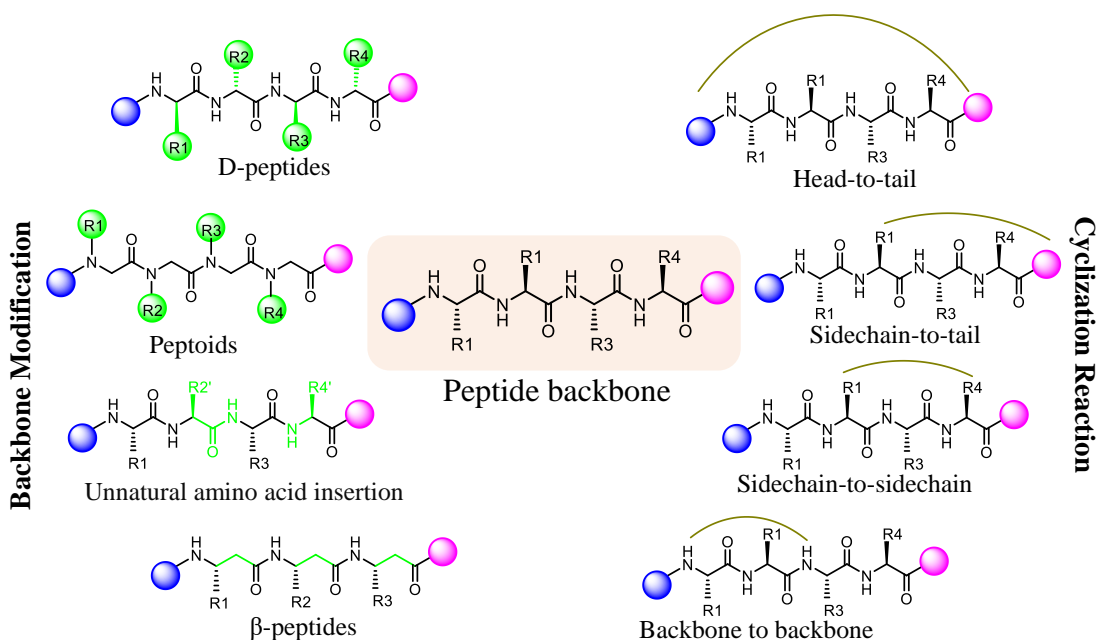


**Figure 1.** Peptidomimetic manipulations of native amino acids.

Peptides have been studied in several fields of medicine and biotechnology for a few decades. Currently, we are witnessing an exponential expansion of peptide-related research due to commercial interest. More than 60 peptide-based medicines have been licensed by the US Food and Drug Administration (FDA), including Lupron™ (Abbott Laboratories), a peptide-based therapy for the treatment of prostate cancer, and many others. In 2011, global sales of peptide medicines accounted for more than \$2.3 billion.<sup>5</sup>

## 1.2 Cyclic dipeptides (CDPs)

CDPs are the simplest form of cyclic peptide scaffold, with a wide range of applications ranging from therapeutics to materials.<sup>6-7</sup> CDPs are made up of a six-membered cyclo-lactam ring with two amide linkages that are conformationally restricted. Unlike linear



dipeptides, structurally rigid CDPs have unique features such as multiple hydrogen bonding donors acceptors, hydrophobic and hydrophilic interactions.<sup>6-9</sup> Several natural compounds containing CDP scaffold have been identified from natural sources, and their biological characteristics and biosynthesis have been documented.<sup>10,11</sup> CDP derivatives exhibit a range of biological activities including antibacterial, antifungal, anticancer, neuroprotective, blood-brain barrier (BBB), and anti-inflammatory activity, among others (Figure 2).<sup>12-15</sup> For instance, cyclo(His-Pro) is found in the human central nervous system (CNS) and exerts neuroprotective and anti-inflammatory function.<sup>15</sup> The neuroprotective property of cyclo(His-Pro) derivatives have been documented, with a promise in Alzheimer's disease (AD) therapeutics.<sup>16,17</sup> The CDP scaffold has been extensively investigated in the construction of structurally varied molecules with potential applications in biology and medicine.<sup>7</sup> Currently, few CDP-based drug candidates are in the market, including Tadalafil (a PDE5 inhibitor), Retsina (an oxytocin inhibitor), and Bicyclomycin (an antibiotic). Clinical trials for phenylahistin and its analogs are underway, with plinabulin (NPI-2358) undergoing a phase-III trial for non-small cell lung cancer (NSCLC) and chemotherapy-induced neutropenia (CIN).<sup>18</sup>

Self-assembling biomolecules like peptides, proteins, nucleic acids (RNA, DNA), phospholipids, and carbohydrates have been used by nature to create a wide range of biological functioning systems and materials. Similarly, synthetic organic and inorganic molecular building blocks have been used to build self-assembled systems and architectures for a variety of material and biological applications.<sup>19-23</sup> Peptides and their derivatives are among the most promising organic molecular building blocks due to their inherent biological relevance with respect to normal physiological and pathological contexts.<sup>21-26,29</sup>

---

---

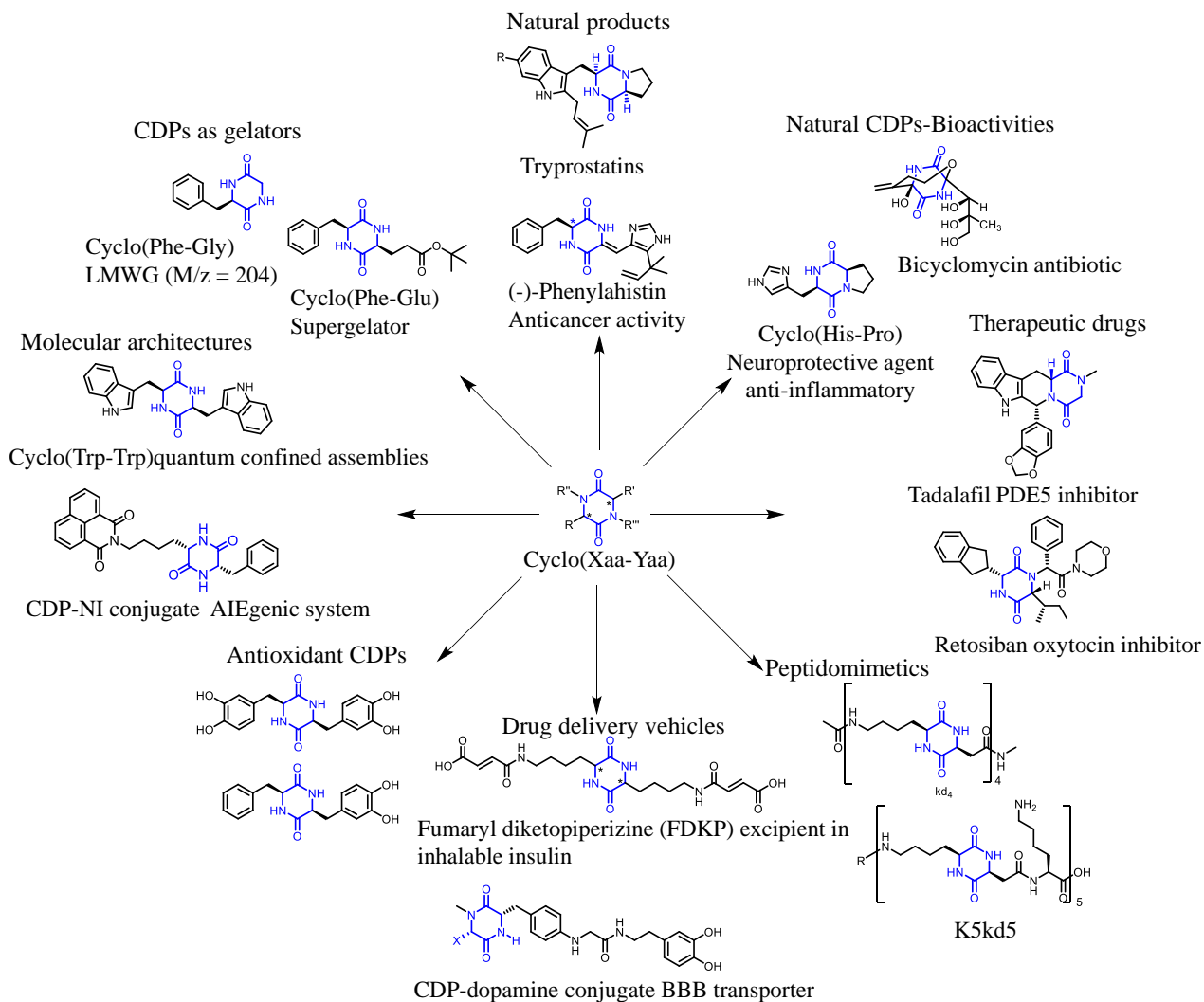


**Figure 2.** CDP serve as privileged scaffold to construct a wide range of structural and functionally useful molecules with variety of applications. X and Y are natural or unnatural amino acids (aa) of the same or different type in cyclo(Xaa-Yaa) (LMWG: low molecular weight gelator). The figure is reproduced with permission from ref 7. Copyright 2021 John Wiley and Sons.

Peptides are attractive scaffolds for molecular assembly and related applications due to their biological relevance and versatility in attaining desired biophysical properties in self-assembled architectures through the choice of amino acids.<sup>27,6</sup> Engineering the molecular assembly of peptide building blocks to into various nano- and microstructures is a promising bottom-up strategy for the construction of functional architectures through the scheme of molecular architectonics (Figure 3). The unique molecular recognition property,

aqueous processability, thermal stability, biocompatibility, and customizable physical characteristics under mild conditions make peptide-based architectures an important class of molecular and material architectures for fundamental applications.<sup>25,26,29</sup>

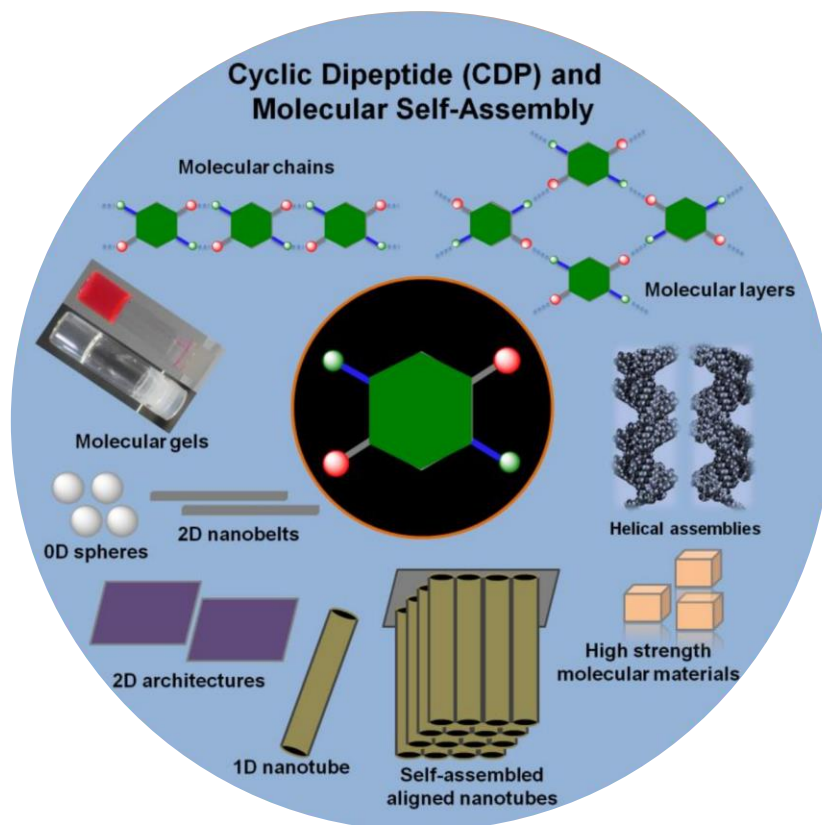


**Figure 3.** Potential uses of molecular and material architectures produced from the molecular assembly of CDPs. Reproduced by permission from ref 6. Copyright 2017 John Wiley and Sons.

CDPs have four hydrogen bonding sites (two donor and two acceptors) from two amide bonds, whereas corresponding linear dipeptides with one amide bond have two hydrogen bonding sites (an acceptor and a donor). Other noncovalent interactions that are useful in driving molecular assembly, such as aromatic interactions, van der Waals forces, and electrostatic and ionic interactions can be introduced by changing the amino acid composition in CDP scaffold. Depending on the type of amino acid and the stereochemistry

at  $\alpha$ -carbons, the CDP molecular platform promotes self-assembly by forming molecular 1D chains or 2D layers.<sup>6, 22-23, 31-32</sup>

### **1.3 Alzheimer's disease (AD)**

Protein misfolding and aggregation-associated toxicity is linked to many neurological disorders, such as AD, Parkinson's' disease (PD), and Huntington's disease (HD). The extracellular deposition of A $\beta$  peptide as senile plaques and intracellular neurofibrillary tangles composed of abnormally hyperphosphorylated tau protein in the brain are the hallmarks of AD, which is the most common form of dementia.<sup>34-35</sup> There is no fully approved treatment for AD that cures or slows the disease progression.

**1.3.1 A $\beta$  peptides.** A $\beta$  peptides and its aggregation species are the key components involved in the progression of AD. The proteolytic enzymes  $\beta$ -secretase ( $\beta$ -site APP-cleaving enzyme 1 - BACE 1, which is an integral membrane protease) and  $\gamma$ -secretase (membrane-bound enzyme) cleave amyloid precursor protein (APP) sequentially in the amyloidogenic pathway to produce A $\beta$ . APP is cleaved first by  $\beta$ -secretase producing APPs $\beta$  and  $\beta$ -CTF (C-terminal fragment) followed by the action of  $\gamma$ -secretase on the transmembrane domain, resulting in the production of A $\beta$  peptides and AICD (amyloid precursor protein intracellular domain).<sup>33-35</sup>

**1.3.2 A $\beta$  nucleation process.** Senile plaques in the AD brain are predominantly made up of insoluble cross  $\beta$ -sheet rich amyloid fibrils formed by the aggregation of A $\beta$  peptide monomer (predominantly random coil) through oligomeric (dimers, trimers, heptamers, etc.) and proto-fibrillar intermediate states. The A $\beta$  aggregation pathway to form insoluble fibrils is the outcome of rate-limiting monomer nucleation (lag phase) that allows for the rapid growth of soluble aggregation species (growth phase) by elongation or association

(Figure 4).<sup>36,37</sup> Intermediates formed during the growth phase of soluble aggregates include oligomers, micelles, amyloid-derived diffusible ligands (ADDLs),  $\beta$ amy balls, amylospheroids (ASPDs), and protofibrils. The intermediate species are commonly classified as low molecular weight species and high molecular weight species.<sup>38-39</sup>

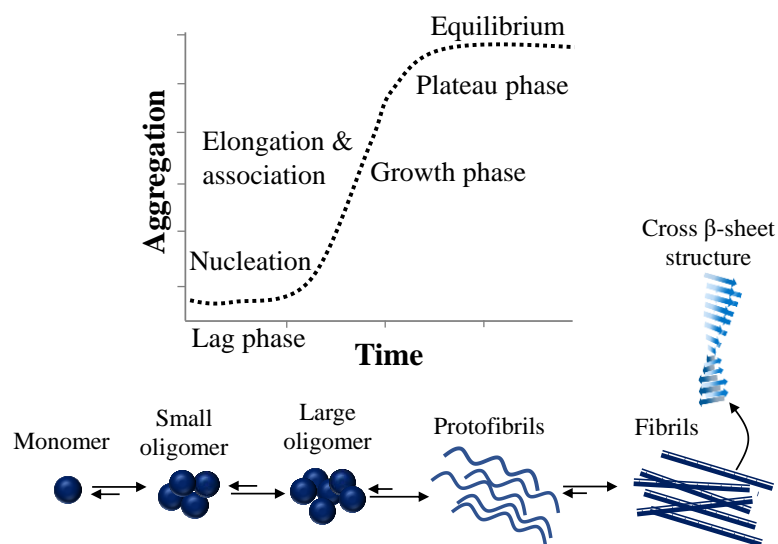


**Figure 4.** The aggregation of A $\beta$  monomer (a random coil structure) into cross  $\beta$ -sheet rich amyloid fibrils via numerous metastable oligomers is schematically depicted (small and large oligomers and protofibrils).

**1.3.3 Role of A $\beta$ 14-23 in fibril formation.** In the amino acid sequence of A $\beta$ 1-42, the region from K16 to A21 (A $\beta$ 16-21) is known to be important for fibrillogenesis. The region from L17 to A21 called the "hydrophobic core," is essential for the fibrillization of full-length A $\beta$  peptides (Figure 5). Pentapeptide A $\beta$ 16-20 has been shown to bind full-length A $\beta$  and preventing its assembly into amyloid fibrils.<sup>40</sup> Interestingly, the pH-dependent aggregation, metal binding, and cytotoxic characteristics of A $\beta$ 14-23 and A $\beta$ 1-42 (the most toxic form of A $\beta$ ) are similar.<sup>41-42</sup>

## 1.4 A $\beta$ aggregation-associated toxicity

A $\beta$ 42 is the most aggregation among A $\beta$  peptides to form toxic soluble and insoluble aggregation species in the brain. Earlier, it was thought that the formation of insoluble fibrils or plaques was the source of disease severity. However, studies have indicated that soluble

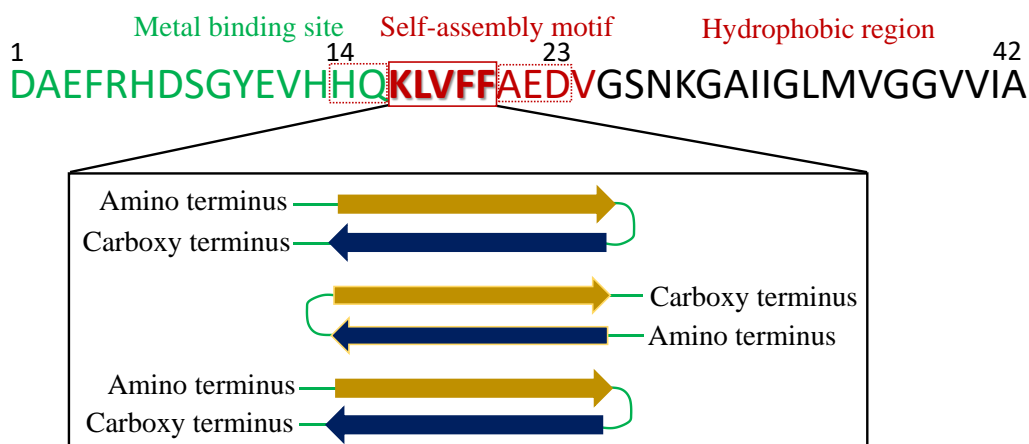


**Figure 5.** The amino acid sequence of A $\beta$ 1-42 peptide. The residues 14-23 of A $\beta$  (HQKLVFFAED) are essential for fibril formation. During aggregation, A $\beta$  forms an anti-parallel  $\beta$ -sheet that results in ordered side-chain stacking of F19 and I32, L34, and V36.

aggregation species of A $\beta$  protein may have a more direct effect on the neurodegeneration compared to insoluble fibrils. In vitro studies have shown that A $\beta$ 42 soluble aggregation species cause cellular malfunction and toxicity in cultivated cells. In AD brain, excess A $\beta$ 42 is produced and predominantly accumulates as amyloid plaques. In comparison to the other A $\beta$  peptides, A $\beta$ 42 shows severe neurotoxicity and has faster aggregation kinetics.<sup>43</sup> The detailed of AD progression and its toxicity mechanisms are poorly understood.<sup>44</sup> A number of studies suggested that A $\beta$  is central to multifaceted amyloid toxicity observed in AD. This has naturally piqued people's interest in learning more about the A $\beta$  toxicity and ways

to ameliorate it. Two important types of A $\beta$ -associated toxicities are explored in the following sections.

**1.4.1 Oxidative stress.** The accumulation of A $\beta$  aggregation species in combination with redox-active metal (Cu, Fe and Zn) ions is thought to cause oxidative damage and inflammation.<sup>45</sup> Accumulation of redox-active Cu ions in amyloid plaques has been observed. The Cu-A $\beta$  complexes catalyse the generation of reactive oxygen species (ROS). A $\beta$  can reduce Cu<sup>II</sup> to Cu<sup>I</sup> or Fe<sup>III</sup> to Fe<sup>II</sup>, and these reduced metal ions react with O<sub>2</sub> to form a superoxide anion, which then take 2H<sup>+</sup> ions to form hydrogen peroxide (H<sub>2</sub>O<sub>2</sub>). Through the Fenton-type reaction, H<sub>2</sub>O<sub>2</sub> reacts with another reduced metal ion to form the deadly hydroxyl (HO<sup>•</sup>) radicals. These radical species are thought to play a role in lipid and protein peroxidation, which eventually leads to neuronal death. Methionine (M35), whose sulfide group may easily oxidize and contribute electrons, is thought to mediate a metal reduction in the Fenton cycle, though recent investigations show that M35 deficiency does not prevent A $\beta$  toxicity.<sup>46,47</sup> Threonine (T10) intermolecular cross-linking is also known to be induced by A $\beta$ , which promotes the development of hazardous oligomeric species.<sup>48</sup> A $\beta$  metal-binding domain exists in the N-terminal region of A $\beta$ , and amino acid residues aspartic acid (D1), Histidine (H6), H13, and H14 are thought to be important in metal chelation. Cu<sup>II</sup> coordinates with D1, H6, H13, and H14, whereas Cu<sup>I</sup> coordinates with H13 and H14. During electron transfer (redox reaction), a large structural rearrangement occurs in the Cu coordination, revealing the presence of an intermediate state implicated in ROS formation. Collin *et al.* recently used mass spectroscopy to demonstrate the existence of an intermediate transition state in which Cu coordinates with alanine (A1), H13, and H14 residues, whereas H6 must break its connection with Cu<sup>II</sup> to trigger the redox process. Such

rearrangement occurring in the Cu-binding site during the redox cycle to generate ROS has been corroborated by  $^{13}\text{C}$  and  $^{15}\text{N}$  NMR investigations.<sup>49</sup> In the lag phase of fibril formation, metal-binding lengthens or stabilizes the oligomeric state.  $\text{Cu}^{\text{II}}$  reacts with  $\text{A}\beta$  to generate poisonous oligomeric species, whereas  $\text{Zn}^{\text{II}}$  reacts with  $\text{A}\beta$  to form amorphous non-fibrillar aggregates that are less hazardous. The effect of  $\text{Zn}^{\text{II}}$  on the  $\text{A}\beta$ -Cu complex on ROS generation is very minimal. Although matured  $\text{A}\beta$  fibrillar aggregates are less hazardous,  $\text{Cu}^{\text{II}}$ -induced  $\text{A}\beta$  fibrillar aggregates retain their redox activity and generate  $\text{HO}^{\bullet}$  from  $\text{H}_2\text{O}_2$ .<sup>50-51</sup>

**1.4.2 Membrane interaction.**  $\text{A}\beta$  aggregation species interact with the cellular membrane and form pores, which cause an influx of excess flow of ions into and out of neuronal cells. These pores allow excess  $\text{Ca}^{\text{II}}$  to enter the cell, causing cellular damage and neuronal death.<sup>52, 53</sup> The mechanism of pore formation by  $\text{A}\beta$  oligomer in the cell membrane is similar to that of how the antibacterial peptides kill bacteria by causing pore formation in the bacterial membrane.<sup>54</sup>

## **1.5 Current therapeutic strategies of AD**

Despite massive efforts and advancements towards the development of diagnosis and treatment options for AD, there are no reliable diagnosis and cure available. The present medications are only good for treating anxiety, sleeplessness, or depression in patients. Some of the strategies followed to develop drug candidates for AD are the following:

(a) Stopping amyloid- $\beta$  production: Inhibiting  $\beta$  and  $\gamma$  secretases to reduces the production of  $\text{A}\beta$  from APP. For instance, Myriad Genetics drug ‘Flurizan<sup>TM</sup>’ has been developed as a  $\gamma$  secretase inhibitor that lowers levels of  $\text{A}\beta_{42}$ .<sup>55-56</sup>



(b) Modulate A $\beta$  aggregation: Inhibition of A $\beta$  fibrillization or dissolution of preformed fibrils by peptide-based molecules is one of the therapeutic approaches (1.5.1 section).

(c) Facilitating excretion of the A $\beta$  peptide: Another treatment option for AD is an antibody-based approach. Antibodies have also been shown to dissolve A $\beta$  aggregates in vitro and in vivo conditions. Holtzman *et al.* reported that antibodies present outside the blood brain barrier (BBB) may help in the removal of soluble peptides such as A $\beta$  from the CNS (Central Nerve System).<sup>57</sup>

**1.5.1 Peptides/peptidomimetics inhibitors of A $\beta$  aggregation.** Inhibition of A $\beta$  fibrillization or dissolution of preformed fibrils by peptide-based molecules is considered a potential therapeutic strategy. The hydrophobic core residues in A $\beta$ 42 from 11 to 25 are critical for fibril formation, and the short peptide sequences from this region have A $\beta$  polypeptide recognition ability (Figure 5, 6). For the past two decades, KLVFF (recognition motif) has been the basis for designing most of the peptide-based modulators of A $\beta$  aggregation. KLVFF (**1**) or LVFFA (**2**) are pentapeptide sequences that can recognize A $\beta$  polypeptides and were employed as recognition units in the development of A $\beta$  fibrillization inhibitors.<sup>58</sup> Xu *et al.* introduced the H102 (HKQLPFFFEED, **3**) recognition unit-based peptide, which prevents A $\beta$  aggregation, decreases expression of p-tau, inflammatory, and apoptotic factors. However, the peptide was rapidly metabolized by proteolytic enzymes. As a result, chemical modifications are necessary to improve its proteolytic stability.<sup>59</sup> The major drawback of peptide-based modulators is their low bioavailability and protease stability. Several modification strategies have been reported in the literature to improve bioavailability, protease stability, and therapeutic value of peptides, including incorporating unnatural amino acids (peptidomimetics), functionalizing

the N- or C-terminus with various organic moieties, and cyclization of modified peptides (Figure 1). Onger *et al.* reported the effect of sugar-based peptidomimetic on A $\beta$ 42 oligomerization and fibrillization by using the capillary electrophoresis technique.<sup>60</sup> Peptidomimetics **4** was found to delay both the early oligomerization and fibrillization of A $\beta$ 42 through hydrophobic, hydrogen bonds, and ionic interactions.<sup>61</sup> Our group has developed recognition unit-based peptidomimetic inhibitors that targeted hydrogen bonding and other noncovalent interactions that are required for A $\beta$  to undergo aggregation. The peptidomimetics of KLVFFA with sarcosine (N-methylglycine) at alternative positions showed both inhibitory and dissolving ability towards A $\beta$  aggregates. **P4** and **P5** were examined in a *Saccharomyces cerevisiae* A $\beta$ 42 model, and they were found to protect yeast cells against A $\beta$ 42 toxicity by dissolving the amyloid aggregates and facilitating their clearance through the autophagy mechanism.<sup>62</sup> A multifunctional peptidomimetic inhibitor (**P6**) of A $\beta$  based on the naturally occurring Cu-chelating tripeptide GHK and a hybrid peptoid-based inhibitor (**P5**) was designed by our research group to tackle multifaceted A $\beta$  toxicity. **P6** effectively prevented the formation of A $\beta$  polymorphic species (oligomers and fibrils). Further, **P6** sequestered Cu<sup>II</sup> from the A $\beta$ 42-Cu<sup>II</sup> complex and kept it in a redox-dormant state, similar to GHK. Thus, **P6** reduced ROS production, oxidative stress, and biomolecules damage to alleviate multifaceted A $\beta$  toxicity.<sup>63, 64</sup> Rahimipour *et al.* reported an anti-amyloidogenic cyclic D, L-peptide architecture. The cyclic peptides (**5**) can suppress the formation of A $\beta$  aggregates and disassemble pre-formed A $\beta$  fibrils.<sup>65</sup> The ability of **5** to bind toxic amyloidogenic oligomers and converts them to more benign species is thought to be the mechanism of inhibition.

### 1.5.2 Small molecule-based modulators.

A number of small molecules have been reported to modulate A $\beta$  aggregation. The majority of small molecules inhibit A $\beta$  fibrillogenesis by interfering with A $\beta$  aggregation-inducing hydrophobic interactions (Figure 7). Curcumin (**8**), resveratrol (**9**), and epigallocatechin-3-gallate (**10**) (EGCG) are natural compounds that reduce A $\beta$  plaques and act as antioxidants.<sup>66</sup> Li *et al.* reported (E)-5-(4-hydroxystyryl) quinoline-8-ol (**11**) based multiple target ligand strategy, which is a combination of clioquinol (a well-known inhibitor for both normal and Cu-induced A $\beta$  fibrillar aggregation) and resveratrol.<sup>67</sup> Compared to its constituents (clioquinol and resveratrol), inhibitor **11** showed greater inhibition and dissolution efficacy for Cu-induced A $\beta$ 42 aggregates, and exhibit antioxidant property, and BBB permeability.

Brazilin (**12**) is a natural product derived from *Caesalpinia sappan*. Brazilin suppressed A $\beta$ 42 aggregation and to prevented A $\beta$  aggregates from serving as secondary nucleation centers for further fibrillogenesis. The molecular docking studies revealed that Brazilin attaches to A $\beta$ 42 via hydrophobic contacts and interferes with the intermolecular salt bridge of D23-K28 via hydrogen bonding, resulting in the formation of non-toxic aggregates.<sup>68</sup>

Our group developed hybrid multifunctional modulators (HMMs) by integrating the metal chelation and antioxidant characteristics of Clq (clioquinol) and EGCG, respectively, to effectively target the multifaceted A $\beta$  toxicity.<sup>69</sup> The lead HMM, **TGR 86** was found to exhibit good cell viability and inhibited metal-independent and dependent A $\beta$  aggregation, and protein damage induced by ROS. Recently, we have reported a berberine-derived (**Ber-D**) molecule that has shown efficient Cu chelation and redox cycle arresting properties. **Ber-D** prevents the formation of ROS and protect biomacromolecules from oxidative

---

damage. In silico simulations confirmed experimentally observed modulation of metal-dependent and independent A $\beta$  aggregation by that **Ber-D**. **Ber-D** treatment prevented mitochondrial dysfunction and apoptosis of the neuronal cell.<sup>70</sup> In an interesting design, we developed a naphthalene monoamide (**TGR 63**) as a potent modulator of A $\beta$  aggregation species (oligomers and fibrils) by disrupting non-covalent interactions such as intermolecular hydrogen bonding and salt bridges among the A $\beta$  peptides.

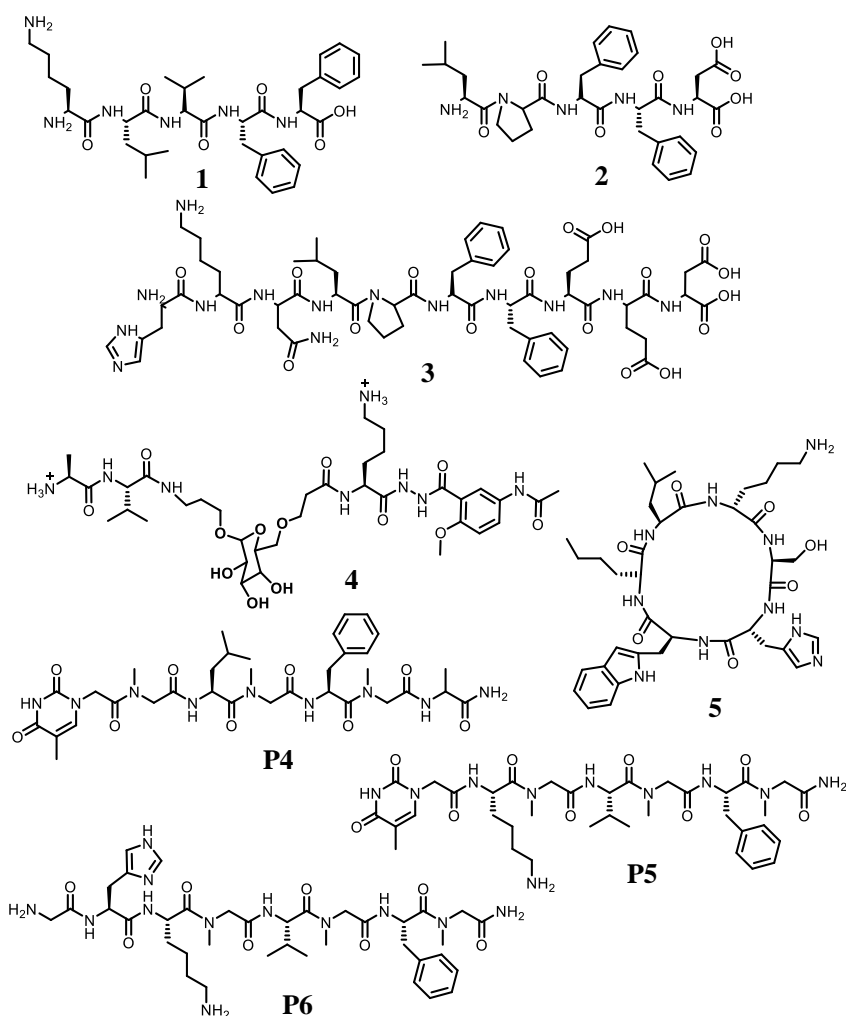


**Figure 6.** Peptide and peptidomimetics-based modulators of A $\beta$  aggregation.

**TGR 63** treatments showed a significant reduction of amyloid burden (cortical and hippocampal) in the progressive stages of APP/PS1 AD mice brain, which resulted in significant improvements in cognitive ability as revealed by behavioral studies.<sup>71</sup> Orcein, a natural product **13**, is reported to enhance the formation of A $\beta$ 42 fibrillar aggregates from

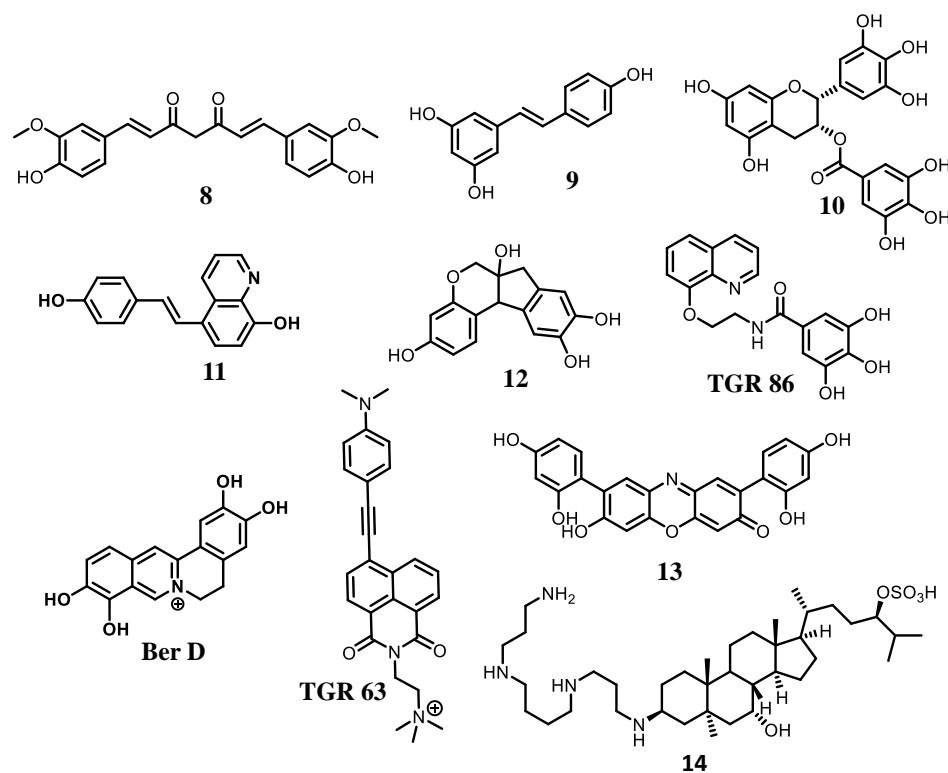


**Figure 7.** Small molecule-based modulators of A $\beta$  aggregation.

highly toxic A $\beta$ 42 oligomeric species. Orcein has been found to bind parallel to the long axis of A $\beta$ 42 aggregates, indicating that it is targeting the hydrophobic portion of spherical oligomeric A $\beta$ 42 species. It nucleated the production of less hazardous higher-order A $\beta$ 42 fibrillar aggregates.<sup>72</sup> Dobson and co-workers reported an aminosterol (trodosquemine, **14**) that ramps up aggregation by facilitating monomer-dependent secondary nucleation, but it also minimizes the toxicity of the produced oligomers to neuroblastoma cells by preventing them from attaching to cell membranes.<sup>73</sup>

## 1.6 Molecular architectonics

The essence of molecular architectonics is the custom design and engineering of molecular assemblies using non-covalent forces to construct molecular and nano architectures with novel properties and functionalities.<sup>27-29</sup> The art of mastering pre-programmed molecular organization is a challenge due to many complex factors at the molecular level. Biomolecules with built-in information for molecular recognition can serve as auxiliaries to guide the assembly of custom designed molecular building blocks to produce nano, micro, and macro-architectures with functional properties and applications, which is the essence of molecular architectonics (Figure 8). Amino acids and peptides are sought-after auxiliaries in the scheme of molecular architectonics for guiding the directed molecular self-assembly and co-assembly to construct of functional molecular and material architectures.<sup>74-76</sup>

## 1.7 Catalytic peptide

Proteins with characteristic three-dimensional structures and catalytic abilities serve as enzymes. These enzymes typically are gigantic protein (>10,000 Da), which is possibly required to adapt a stable 3D catalytic architecture. The shorter peptides can adapt well-defined conformations through molecular assembly, viz., forming amyloid fibrils (Figure 9). Several peptide ensembles have been designed to exhibit catalytic activity with efficiency comparable to enzymes, as demonstrated in model reactions.

Escuder *et al.* reported a proline-based self-assembled catalytic peptide system which is capable of percolating water in the pH range of 6 to 8, and the reaction exhibited Michaelis–

Menten type kinetics. The replacement of imidazole with proline in Pro-Val (**15**) resulted in modest hydrolytic activity towards p-NPA and non-activated aminoacyl esters (**16**) (Figure 10).<sup>77</sup> Qi and co-workers reported a comparable supramolecular co-assembled peptide artificial hydrolase by combining catalytic triads (Fmoc-FFH, Fmoc-FFS, and Fmoc-FFD) with Fmoc-FF. A new molecular imprinting approach was also used to improve the hydrolysis activity and selectivity. The catalytic triad residues were pre-organized into appropriate orientation

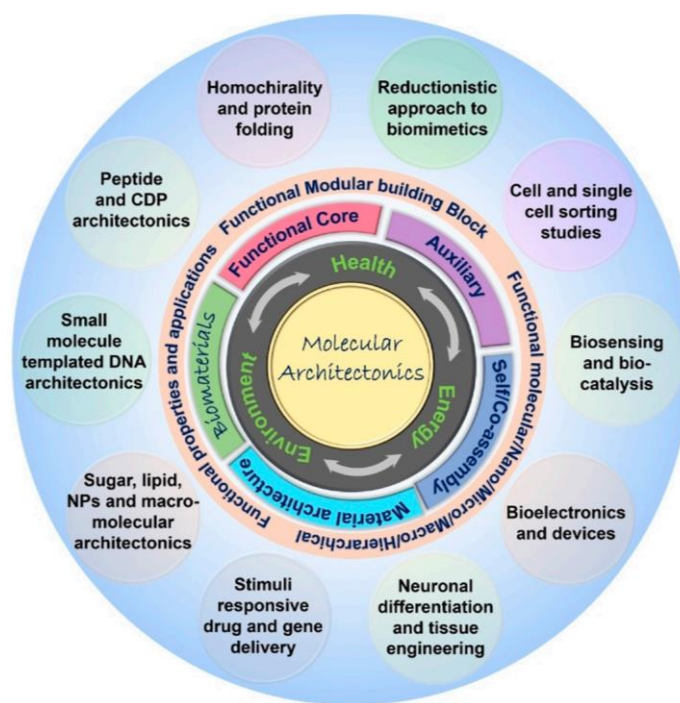


**Figure 8.** Design of functional molecular and material architectures and their biomaterial applications through the scheme of molecular architectonics. Functional molecular building blocks or modules are designed by combining a functional core with assembly-directing auxiliary units, which is then subjected to molecular assembly to produce defined molecular and material architectures with diverse functional properties and applications in the inter-related domains of health, energy, and environment. Reproduced by permission from ref 27. Copyright 2021 John Wiley and Sons.

using the p-NPA as a molecular template, which was then fixed by supramolecular nanostructure formation. The removing of the template increased the exposure of the

catalytic triad residues at the catalytic centre, boosting the artificial co-assembled enzyme's efficiency (7.86 times higher than non-imprinted co-assembled triads and 13.48 times higher than self-assembled Fmoc-FFH, **16**), as well as its selectivity for the imprinted substrate (p-NPA).<sup>78</sup> Our group reported a gluconamide amphiphile design with a hydrophilic-hydrophobic balance and amide as a metal ion coordination centre which enhanced the catalytic activity of  $\text{Pb}^{\text{II}}$  in glucose hydrolysis.<sup>79</sup>

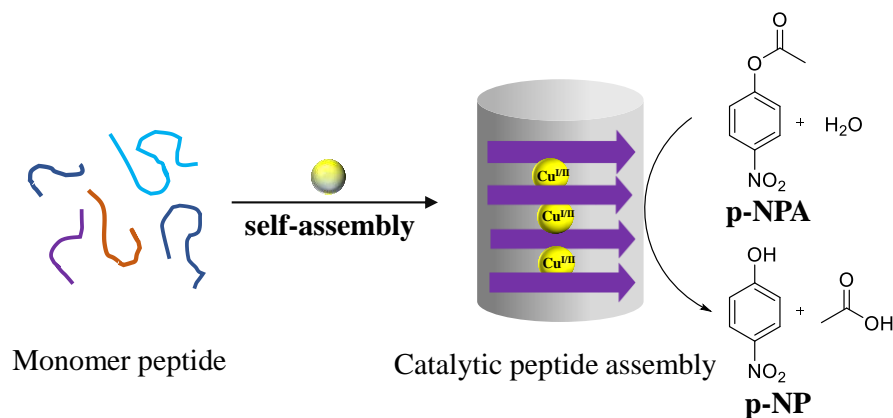


**Figure 9.** Hydrolysis of para-nitrophenyl acetate (p-NPA) to para-nitrophenol (p-NP) by metal (copper)-peptide assembly architecture.<sup>26</sup>

The assembly architecture and dispersed state of the gluconamide- $\text{Pb}^{\text{II}}$  complexes exhibit distinct kinetics towards glucose hydrolysis. Under ambient conditions, the metal gluconamide ( $\text{Pb}^{\text{II}}$ -NC) self-assembles to form an efficient secondary coordination sphere, which displayed improved catalytic activity for alkaline glucose hydrolysis. The catalytic activity of functional amphiphile ligands and derived architectures was found to differ depending on the type of hydrophobic moiety (aromatic/alkyl).

Gazit and co-workers reported a cyclo-dipeptidyl supramolecular nano-superstructure to mimic the active site of CAII (carbonic anhydrase II). The self-assembly of cyclo-HH (**22**) was modulated using zinc ions to form zero-dimensional, homogenous nanostructures that



can be subsequently employed as basic units to form a higher-order nanoarchitecture. The nano-superstructure has a large number of catalytic active sites and accessible to reactant through diffusion. As a result, effective hydrolytic activity of  $93.21 \text{ M}^{-1}\text{s}^{-1}$  ( $k_{\text{cat}}/K_{\text{a}}$ , calculated catalytic efficiency, where  $k_{\text{cat}}$  is the turnover number and  $K_{\text{a}}$  is adsorption equilibrium constant) was achieved.<sup>80</sup> The copper-binding amyloids of peptide **19** has been reported to accelerate phosphoester hydrolysis of paraoxon, a widely used and highly

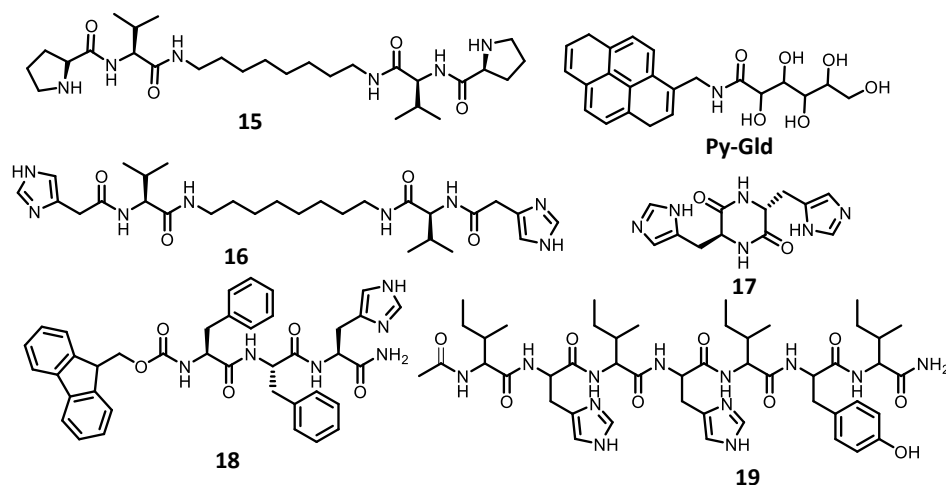


**Figure 10.** Structure of catalytic peptide and peptidomimetics.

toxic organophosphate insecticide.<sup>81</sup> These findings have implications for the development of self-assembled nanoarchitectures of peptide incorporated with biological and non-biological metal ions, as catalysts.

### 1.8 Small molecule and peptide binders of *i*-motif DNA

In addition to the well-known double-helical structure, DNA can adopt a variety of non-canonical structural conformations. G-quadruplexes (G4s) and *i*-motif (C4s) have emerged as the common non-canonical DNA structures. The *i*-motifs are four-stranded DNA structures formed by the hemi-protonated and intercalated cytosine base pairs (C:C<sup>+</sup>).<sup>82-83</sup>

All elements of preserving and accessing genetic information rely on interactions between proteins and nucleic acids (DNA and RNA). The majority of nucleic acid-binding proteins have at least one DNA or RNA-binding domain, which interacts with amino acids in a specific or generic manner. Waller and Shchekotikhin *et al.* reported heliomycin derivative 7-deoxy-7-(2-aminoethyl) amino-10-O-methylheliomycin (**20**), which displays a promising affinity and selectivity toward *i*-motif-forming DNA sequences over duplex and G4, implying that heliomycin derivatives could be used to target *i*-motif DNA structures (Figure 11).<sup>84</sup> A peptidomimetics **21** has been reported to bind BCL-2-C *i*-motif preferentially over G4 DNA.<sup>85</sup> Cellular studies have revealed that **21** upregulates BCL-2 gene expression. Chatterjee et al. reported peptide candidate **22**, which preferentially stabilize the 5-propeller loop of c-MYC G4 through arginine-driven electrostatic interactions with the sugar-phosphate backbone.<sup>86</sup>

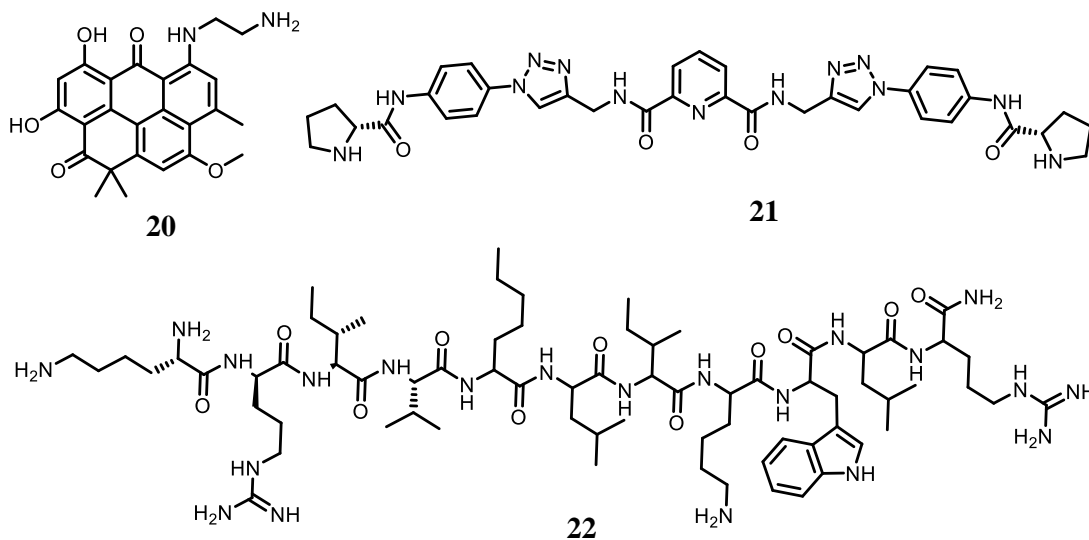


**Figure 11.** The *i*-motif binding small molecule (**20** and **21**) and c-MYC quadruplex binding peptide (**22**).

## 1.9 Objective

The thesis begins with a brief overview of peptides and peptidomimetics, followed by a discussion on cyclic dipeptides (CDPs) and their medicinal and biomaterial applications (Chapter 1). Development of small molecule and peptidomimetics-based therapeutic candidates to modulate A $\beta$  toxicity, catalytic activity of A $\beta$ -derived peptidomimetics, and *i*-motif binding peptides are presented in chapters 2-5 (Figure 12).

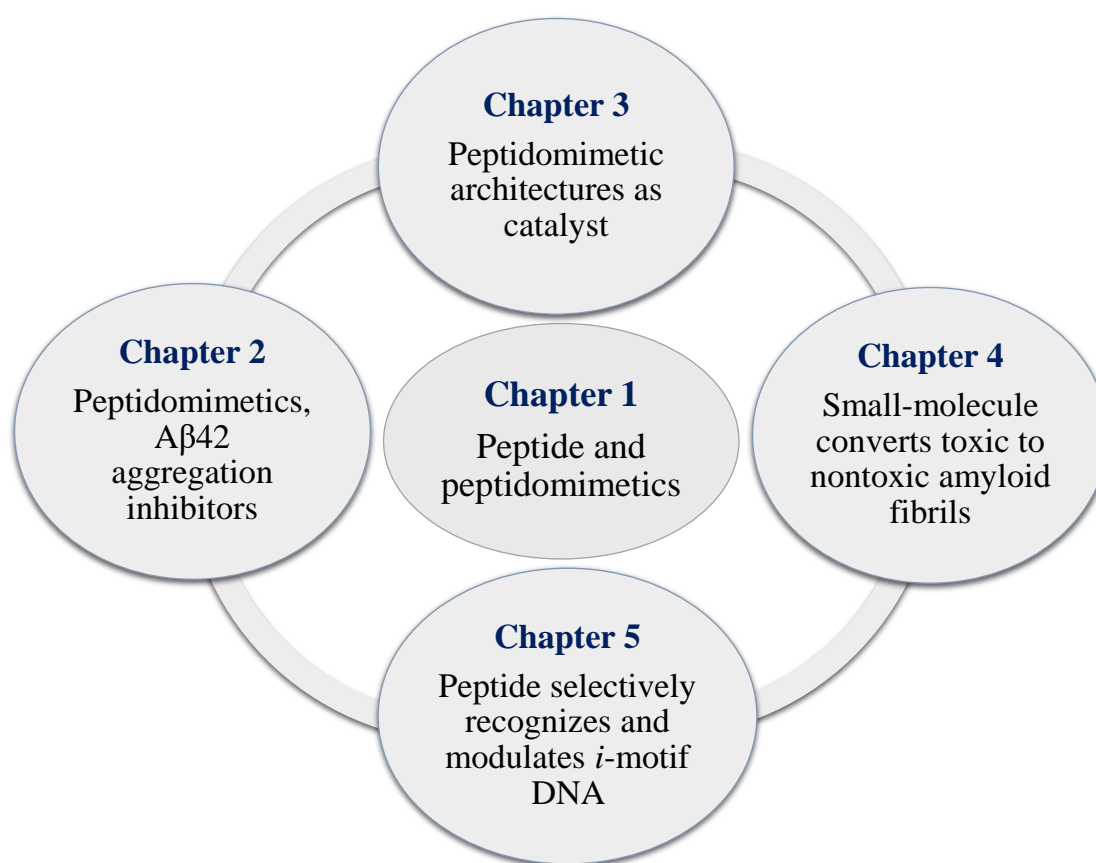


**Figure 12.** Thesis outline

### 1.10 References

- [1] Fosgerau, K.; Hoffmann, T., Peptide therapeutics: current status and future directions. *Drug Discov.* **2015**, *20*, 122-128.
- [2] Qvit, N.; Rubin, S. J.; Urban, T. J.; Mochly-Rosen, D.; Gross, E. R., Peptidomimetic therapeutics: scientific approaches and opportunities. *Drug Discov.* **2017**, *22*, 454-462.
- [3] Van Regenmortel, M., Antigenicity and immunogenicity of synthetic peptides. *Biologicals* **2001**, *29*, 209-213.
- [4] Guarna, A.; Trabocchi, A., Peptidomimetics in Organic and Medicinal Chemistry: the art of transforming peptides in drugs. *John Wiley & Sons*: **2014**.
- [5] Muttenthaler, M.; King, G. F.; Adams, D. J.; Alewood, P. F., Trends in peptide drug discovery. *Nat. Rev. Drug Discov.* **2021**, *20*, 309-325.
- [6] Manchineella, S.; Govindaraju, T., Molecular self-assembly of cyclic dipeptide derivatives and their applications. *ChemPlusChem* **2017**, *82*, 88-106.
- [7] Balachandra, C.; Padhi, D.; Govindaraju, T. Cyclic dipeptide: A privileged molecular scaffold to derive structural diversity and functional utility. *ChemMedChem* **2021**, *16*, 2558-2587.
- [8] Prasad, C., Bioactive cyclic dipeptides. *Peptides* **1995**, *16*, 151-164.
- [9] Borthwick, A. D., 2, 5-Diketopiperazines: synthesis, reactions, medicinal chemistry, and bioactive natural products. *Chem. Rev.* **2012**, *112*, 3641-3716.
- [10] Borgman, P.; Lopez, R. D.; Lane, A. L. The expanding spectrum of diketopiperazine natural product biosynthetic pathways containing cyclodipeptide synthases. *Org. Biomol. Chem.* **2019**, *17*, 2305-2314.
- [11] Godfrey, R. C.; Green, N. J.; Nichol, G. S.; Lawrence, A. L. Total synthesis of brevianamide A. *Nat. Chem.* **2020**, *12*, 615-619.
- [12] Huang, R.-M.; Yi, X.-X.; Zhou, Y.; Su, X.; Peng, Y.; Gao, C.-H., An update on 2, 5-diketopiperazines from marine organisms. *Mar. Drugs* **2014**, *12*, 6213-6235.
- [13] Cui, C.-B.; Kakeya, H.; Osada, H., Novel mammalian cell cycle inhibitors, spirotryprostatins A and B, produced by *Aspergillus fumigatus*, which inhibit mammalian cell cycle at G2/M phase. *Tetrahedron* **1996**, *52*, 12651-12666.

- [14] Teixidó, M.; Zurita, E.; Malakoutikhah, M.; Tarragó, T.; Giralt, E., Diketopiperazines as a tool for the study of transport across the blood– brain barrier (BBB) and their potential use as BBB-shuttles. *J. Am. Chem. Soc.* **2007**, *129*, 11802-11813.
- [15] Minelli, A.; Grottelli, S.; Mierla, A.; Pinnen, F.; Cacciatore, I.; Bellezza, I., Cyclo (His-Pro) exerts anti-inflammatory effects by modulating NF-κB and Nrf2 signalling. *Int. J. Biochem.* **2012**, *44*, 525-535.
- [16] Bellezza, I.; Peirce, M. J.; Minelli, A., Cyclic peptides in neurological disorders: the case of Cyclo (His-Pro). *Quorum Sensing* **2019**, 257-286
- [17] Turkez, H.; Cacciatore, I.; Arslan, M. E.; Fornasari, E.; Marinelli, L.; Di Stefano, A.; Mardinoglu, A., Histidyl-proline diketopiperazine isomers as multipotent anti-alzheimer drug candidates. *Biomolecules* **2020**, *10*, 737.
- [18] Mita, M. M.; Spear, M. A.; Yee, L. K.; Mita, A. C.; Heath, E. I.; Papadopoulos, K. P.; Federico, K. C.; Reich, S. D.; Romero, O.; Malburg, L., Phase 1 first-in-human trial of the vascular disrupting agent plinabulin (NPI-2358) in patients with solid tumors or lymphomas. *Clin. Cancer Res.* **2010**, *16*, 5892-5899.
- [19] Yang, L.; Tan, X.; Wang, Z.; Zhang, X., Supramolecular polymers: historical development, preparation, characterization, and functions. *Chem. Rev.* **2015**, *115*, 7196-7239.
- [20] Krieg, E.; Bastings, M. M.; Besenius, P.; Rybtchinski, B., Supramolecular polymers in aqueous media. *Chem. Rev.* **2016**, *116*, 2414-2477.
- [21] Avinash, M.; Govindaraju, T., Amino acid derivatized arylenediimides: A versatile modular approach for functional molecular materials *Adv.Mater.* **2012**, *24*, 3905–3922.
- [22] Avinash, M.; Govindaraju, T., Two-dimensional nanoarchitectonics: organic and hybrid materials. *Nanoscale*, **2012**, *4*, 6102–6117
- [23] Avinash, M.; Govindaraju, T., Nanoarchitectonics of biomolecular assemblies for functional applications. *Nanoscale*, **2014**, *6*, 13348–13369
- [24] Schneider, J. P.; Pochan, D. J.; Ozbas, B.; Rajagopal, K.; Pakstis, L.; Kretsinger, J., Responsive hydrogels from the intramolecular folding and self-assembly of a designed peptide. *J. Am. Chem. Soc.* **2002**, *124*, 15030-15037.
- [25] Zhao, X.; Pan, F.; Xu, H.; Yaseen, M.; Shan, H.; Hauser, C. A.; Zhang, S.; Lu, J. R., Molecular self-assembly and applications of designer peptide amphiphiles. *Chem. Soc. Rev.* **2010**, *39*, 3480-3498.
- [26] Rufo, C. M.; Moroz, Y. S.; Moroz, O. V.; Stöhr, J.; Smith, T. A.; Hu, X.; DeGrado, W. F.; Korendovych, I. V., Short peptides self-assemble to produce catalytic amyloids. *Nat. Chem.* **2014**, *6*, 303-309.

- [27] Moorthy, H.; Datta, L. P.; Govindaraju, T., Molecular architectonics-guided design of biomaterials. *Chem. Asian J* **2021**, *16*, 423-442.
- [28] Avinash, M.; Govindaraju, T., Architectonics: design of molecular architecture for functional applications. *Acc. Chem. Res.* **2018**, *51*, 414-426.
- [29] Roy, B; Govindaraju, Amino acids and peptides as functional components in arylenediimide-based molecular architectonics. *Bull. Chem. Soc. Jpn.* **2019**, *92*, 1883–1901.
- [30] Corey, R. B., The crystal structure of diketopiperazine. *J. Am. Chem. Soc.* **1938**, *60*, 1598-1604.
- [31] Govindaraju, T.; Pandeewar, M.; Jayaramulu, K.; Jaipuria, G.; Atreya, H. S., Spontaneous self-assembly of designed cyclic dipeptide (Phg-Phg) into two-dimensional nano-and mesosheets. *Supramol Chem* **2011**, *23*, 487-492.
- [32] Govindaraju, T., Spontaneous self-assembly of aromatic cyclic dipeptide into fibre bundles with high thermal stability and propensity for gelation. *Supramol Chem* **2011**, *23*, 759-767.
- [33] Rajasekhar, K.; Govindaraju, T., Current progress, challenges and future prospects of diagnostic and therapeutic interventions in Alzheimer's disease. *RSC Adv.* **2018**, *8*, 23780-23804.
- [34] Rajasekhar, K.; Chakrabarti, M.; Govindaraju, T., Function and toxicity of amyloid beta and recent therapeutic interventions targeting amyloid beta in Alzheimer's disease. *Chem. Commun.*, **2015**, *51*, 13434-13450.
- [35] Govindaraju, T. Alzheimer's Disease: recent findings in pathophysiology, diagnostic and therapeutic modalities. RSC: London, **2021**
- [36] Ahmed, M.; Davis, J.; Aucoin, D.; Sato, T.; Ahuja, S.; Aimoto, S.; Elliott, J. I.; Van Nostrand, W. E.; Smith, S. O., Structural conversion of neurotoxic amyloid- $\beta$  1–42 oligomers to fibrils. *Nat. Struct. Mol. Biol.* **2010**, *17*, 561-567.
- [37] Roychaudhuri, R.; Yang, M.; Hoshi, M. M.; Teplow, D. B., Amyloid  $\beta$ -protein assembly and Alzheimer disease. *J. Biol. Chem.* **2009**, *284*, 4749-4753.
- [38] Ward, R. V.; Jennings, K. H.; Jepras, R.; Neville, W.; Owen, D. E.; Hawkins, J.; Christie, G.; Davis, J. B.; George, A.; Karran, E. H., Fractionation and characterization of oligomeric, protofibrillar and fibrillar forms of  $\beta$ -amyloid peptide. *Biochem. J.* **2000**, *348*, 137-144.
- [39] Wu, W.-h.; Liu, Q.; Sun, X.; Yu, J.-s.; Zhao, D. s.; Yu, Y.-p.; Luo, J.-j.; Hu, J.; Yu, Z.-w.; Zhao, Y.-f., Fibrillar seeds alleviate amyloid- $\beta$  cytotoxicity by omitting formation of higher-molecular-weight oligomers. *Biochem. Biophys. Res. Commun.* **2013**, *439*, 321-326.
- [40] Esler, W. P.; Stimson, E. R.; Ghilardi, J. R.; Lu, Y.-A.; Felix, A. M.; Vinters, H. V.; Mantyh, P. W.; Lee, J. P.; Maggio, J. E., Point substitution in the central hydrophobic cluster of a human  $\beta$ -

amyloid congener disrupts peptide folding and abolishes plaque competence. *Biochemistry* **1996**, *35*, 13914-13921.

[41] Pallitto, M. M.; Ghanta, J.; Heinzelman, P.; Kiessling, L. L.; Murphy, R. M., Recognition sequence design for peptidyl modulators of  $\beta$ -amyloid aggregation and toxicity. *Biochemistry* **1999**, *38*, 3570-3578;

[42] Tjernberg, L. O.; Näslund, J.; Lindqvist, F.; Johansson, J.; Karlström, A. R.; Thyberg, J.; Terenius, L.; Nordstedt, C., Arrest of amyloid fibril formation by a pentapeptide ligand (\*). *J. Biol. Chem.* **1996**, *271*, 8545-8548.

[43] Conicella, A. E.; Fawzi, N. L., The C-terminal threonine of A $\beta$ 43 nucleates toxic aggregation via structural and dynamical changes in monomers and protofibrils. *Biochemistry* **2014**, *53*, 3095-3105.

[44] Hayden, E. Y.; Teplow, D. B., Amyloid  $\beta$ -protein oligomers and Alzheimer's disease. *Alzheimer's Res. Ther.* **2013**, *5*, 1-11.

[45] Carrillo-Mora, P.; Luna, R.; Colín-Barenque, L., Amyloid beta: multiple mechanisms of toxicity and only some protective effects? *Oxid. Med. Cell. Longev* **2014**, *2014*, 795375.

[46] Butterfield, D. A.; Sultana, R., Methionine-35 of A $\beta$  (1-42): importance for oxidative stress in Alzheimer disease. *J. Amino Acids* **2011**, *2011*, 198430-40.

[47] Maiti, P.; Lomakin, A.; Benedek, G. B.; Bitan, G., Despite its role in assembly, methionine 35 is not necessary for amyloid  $\beta$ -protein toxicity. *J. Neurochem.* **2010**, *113*, 1252-1262.

[48] Al-Hilaly, Y. K.; Williams, T. L.; Stewart-Parker, M.; Ford, L.; Skaria, E.; Cole, M.; Bucher, W. G.; Morris, K. L.; Sada, A. A.; Thorpe, J. R., A central role for dityrosine crosslinking of Amyloid- $\beta$  in Alzheimer's disease. *Acta Neuropathol. Commun.* **2013**, *1*, 1-17.

[49] Parthasarathy, S.; Yoo, B.; McElheny, D.; Tay, W.; Ishii, Y., Capturing a reactive state of amyloid aggregates. *J. Biol. Chem.* **2014**, *289*, 9998-10010.

[50] Cheignon, C. M.; Tomas, M.; Bonnefont-Rousselot, D.; Faller, P.; Hureau, C.; Collin, F.; Oxidative stress and the amyloid beta peptide in Alzheimer's disease. *Redox Biol.* **2018**, *14*, 450-64.

[51] Faller, P.; Hureau, C.; La Penna, G.; Metal ions and intrinsically disordered proteins and peptides: from Cu/Zn amyloid- $\beta$  to general principles. *Acc. Chem. Res.* **2014**, *47*, 2252-9.

[52] Kawahara, M.; Kuroda, Y., Molecular mechanism of neurodegeneration induced by Alzheimer's  $\beta$ -amyloid protein: channel formation and disruption of calcium homeostasis. *Brain Res. Bull.* **2000**, *53*, 389-397.

[53] Zhao, L. N.; Long, H. W.; Mu, Y.; Chew, L. Y., The toxicity of amyloid  $\beta$  oligomers. *Int. J. Mol. Sci.* **2012**, *13*, 7303-7327.

---

---

- [54] Tofoleanu, F.; Buchete, N. V., Alzheimer A $\beta$  peptide interactions with lipid membranes: fibrils, oligomers and polymorphic amyloid channels. *Prion* **2012**, *6*, 339-345.
- [55] Best, J. D. et al. In vivo characterization of A $\beta$  (40) changes in brain and cerebrospinal fluid using the novel gamma-secretase inhibitor N-[cis-4-[(4-chlorophenyl) sulfonyl]-4-(2,5-difluorophenyl) cyclohexyl]-1,1 trifluoro methane sulphonamide (MRK-560) in the rat. *J. Pharmacol. Exp. Ther.* **2006**, *317*, 786-790.
- [56] Peretto, I. et al. Synthesis and biological activity of flurbiprofen analogues as selective inhibitors of  $\beta$ -amyloid (1-42) secretion. *J. Med.Chem.* **2005**, *48*, 5705-5720.
- [57] DeMattos, R. B., Bales, K. R., Cummins, D. J., Dodart, J. C., Paul, S. M., & Holtzman, D. M. Peripheral anti-A $\beta$  antibody alters CNS and plasma A $\beta$  clearance and decreases brain A $\beta$  burden in a mouse model of Alzheimer's disease. *Proc. Natl Acad. Sci. USA*, **2001**, *98*, 8850-8855.
- [58] Tjernberg, L. O.; Naslund, J.; Lindqvist, F.; Johansson, J.; Karlstrom, A. R.; Thyberg, J.; Terenius, L.; Nordstedt, C., Arrest of  $\beta$ -amyloid fibril formation by a pentapeptide ligand. *J. Biol. Chem.* **1996**, *271*, 8545-8548.
- [59] Soto, C.; Sigurdsson, E. M.; Morelli, L.; Asok Kumar, R.; Castano, E. M.; Frangione, B.,  $\beta$ -sheet breaker peptides inhibit fibrillogenesis in a rat brain model of amyloidosis: Implications for Alzheimer's therapy. *Nat. Med.* **1998**, *4*, 822-826.
- [60] Brinet, D.; Kaffy, J.; Oukacine, F.; Glumm, S.; Ongeri, S.; Taverna, M. An improved capillary electrophoresis method for in vitro monitoring of the challenging early steps of A $\beta$ 1–42 peptide oligomerization: Application to anti-Alzheimer's drug discovery. *Electrophoresis* **2014**, *35*, 3302–3309.
- [61] Kaffy, J.; Brinet, D.; Soulier, J-L.; Correia, I.; Tonali, N.; Fera, KF.; *et al.* Designed glycopeptidomimetics disrupt protein–Protein interactions mediating amyloid  $\beta$ -peptide aggregation and restore neuroblastoma cell viability. *J. Med. Chem.* **2016**, *59*, 2025-40.
- [62] Rajasekhar, K.; Suresh, S.; Manjithaya, R.; Govindaraju, T., Rationally designed peptidomimetic modulators of A $\beta$  toxicity in Alzheimer's disease. *Sci. Rep.* **2015**, *5*, 1-9.
- [63] Rajasekhar, K.; Madhu, C.; Govindaraju, T., Natural tripeptide-based inhibitor of multifaceted amyloid  $\beta$  toxicity. *ACS Chem. Neurosci.* **2016**, *7*, 1300-1310
- [64] Samanta, S.; Rajasekhar, K.; Babagond, V.; Govindaraju, T., Small molecule inhibits metal-dependent and-independent multifaceted toxicity of Alzheimer's disease. *ACS Chem. Neurosci* **2019**, *10*, 3611-3621.
- [65] Richman, M.; Wilk, S.; Chemerovski, M.; Wärmländer, S. K.; Wahlström, A.; Gräslund, A.; Rahimipour, S., In vitro and mechanistic studies of an anti-amyloidogenic self-assembled cyclic d, 1- $\alpha$ -peptide architecture. *J. Am. Chem. Soc.* **2013**, *135*, 3474-3484.



- [66] Ji, H. f.; Zhang, H. y., Multipotent natural agents to combat Alzheimer's disease. Functional spectrum and structural features 1. *Acta Pharmacol. Sin.* **2008**, *29*, 143-151.
- [67] Mao, F.; Yan, J.; Li, J.; Jia, X.; Miao, H.; Sun, Y.; Huang, L.; Li, X., New multi-target-directed small molecules against Alzheimer's disease: a combination of resveratrol and clioquinol. *Org. Biomol. Chem.* **2014**, *12*, 5936-5944.
- [68] Du, W.-J.; Guo, J.-J.; Gao, M.-T.; Hu, S.-Q.; Dong, X.-Y.; Han, Y.-F.; Liu, F.-F.; Jiang, S.; Sun, Y., Brazilin inhibits amyloid  $\beta$ -protein fibrillogenesis, remodels amyloid fibrils and reduces amyloid cytotoxicity. *Sci. Rep.* **2015**, *5*, 1-10.
- [69] Rajasekhar, K.; Mehta, K.; Govindaraju, T., Hybrid multifunctional modulators inhibit multifaceted A $\beta$  toxicity and prevent mitochondrial damage. *ACS Chem. Neurosci.* **2018**, *9*, 1432-1440.
- [70] Rajasekhar, K.; Samanta, S.; Bagoband, V.; Murugan, N. A.; Govindaraju, T., Antioxidant berberine-derivative inhibits multifaceted amyloid toxicity. *iScience* **2020**, *23*, 101005.
- [71] Samanta, S.; Rajasekhar, K.; Ramesh, M.; Murugan, N. A.; Alam, S.; Shah, D.; Clement, J. P.; Govindaraju, T., Naphthalene monoimide derivative ameliorates amyloid burden and cognitive decline in a transgenic mouse model of Alzheimer's Disease. *Adv. Ther.* **2021**, *4*, 2000225.
- [72] Bieschke, J.; Herbst, M.; Wiglenda, T.; Friedrich, R. P.; Boeddrich, A.; Schiele, F.; Kleckers, D.; del Amo, J. M. L.; Grüning, B. A.; Wang, Q., Small-molecule conversion of toxic oligomers to nontoxic  $\beta$ -sheet-rich amyloid fibrils. *Nat. Chem. Biol.* **2012**, *8*, 93-101.
- [73] Limbocker, R.; Chia, S.; Ruggeri, F. S.; Perni, M.; Cascella, R.; Heller, G. T.; Meisl, G.; Mannini, B.; Habchi, J.; Michaels, T. C., Trodusquemine enhances A $\beta$  42 aggregation but suppresses its toxicity by displacing oligomers from cell membranes. *Nat. Commun.* **2019**, *10*, 1-13.
- [74] Govindaraju, T., Ariga, K. (Eds.), Molecular architectonics and nanoarchitectonics, in the Series of Nanostructure Science and Technology. David J. Lockwood (Ed.), Singapore, Springer Nature, **2021**.
- [75] Datta, L. P.; Ghosh, D.; Govindaraju, T., Functional molecule-templated DNA molecular architectonics: Molecular architectonics and nanoarchitectonics. *Springer*: **2022**; pp 281-305.
- [76] Ghosh, D.; Datta, L. P.; Govindaraju, T., Molecular architectonics of DNA for functional nanoarchitectures. *Beilstein J. Nanotechnol.* **2020**, *11*, 124-140.
- [77] Singh, N; Conte, M. P.; Ulijn, R. V.; Miravet, J. F.; Escuder, B. Insight into the esterase like activity demonstrated by an imidazole appended self-assembling hydrogelator. *Chem. Commun.* **2015**, *51*, 13213–13216.

- [78] Wang, M.; Lv, Y.; Liu, X.; Qi, W.; Su, R.; He, Z., Enhancing the activity of peptide-based artificial hydrolase with catalytic Ser/His/Asp triad and molecular imprinting. *ACS Appl. Mater. Interfaces* **2016**, *8*, 14133-14141.
- [79] Roy, B.; Pal, S.; Govindaraju, T., Intrinsic role of molecular architectonics in enhancing the catalytic activity of lead in glucose hydrolysis. *ACS Appl. Mater. Interfaces* **2020**, *12*, 14057-14063.
- [80] Gazit, E.; Chen, Y.; Yang, Y.; Orr, A. A.; Makam, P.; Redko, B.; Haimov, E.; Wang, Y.; Shimon, L. J.; Rencus-Lazar, S., Self-assembled peptide nano-superstructure towards enzyme mimicking hydrolysis. *Angew. Chem. Int. Ed.* **2021**, *60*, 17164–17170.
- [81] Lengyel, Z.; Rufo, C. M.; Moroz, Y. S.; Makhlynets, O. V.; Korendovych, I. V., Copper-containing catalytic amyloids promote phosphoester hydrolysis and tandem reactions. *ACS Catal.* **2018**, *8*, 59-62.
- [82] Suseela, Y.; Narayanaswamy, N.; Pratihar, S.; Govindaraju, T.; Far-red fluorescent probes for canonical and non-canonical nucleic acid structures: current progress and future implications. *Chem. Soc. Rev.* **2018**, *47*, 1098-131.
- [83] Mattath, M. N.; Ghosh, D; Pratihar, S.; Shi, S; Govindaraju, T.; Nucleic acid architectonics for pH-responsive DNA systems and devices. *ACS Omega* **2022**, DOI: 10.1021/acsomega.1c06464
- [84] Tikhomirov, A. S.; Abdelhamid, M. A.; Nadysev, G. Y.; Zatonky, G. V, Bykov E. E, Chueh P. J, *et al.* Water-soluble heliomycin derivatives to target *i*-motif DNA. *J. Nat. Prod.* **2021**, *84*, 5, 1617-1625.
- [85] Debnath, M.; Ghosh, S.; Chauhan, A.; Paul, R.; Bhattacharyya, K.; Dash, J. Preferential targeting of *i*-motifs and G-quadruplexes by small molecules. *Chem. Sci.* **2017**, *8*, 7448-56.
- [86] Sengupta, P.; Banerjee, N.; Roychowdhury, T.; Dutta, A.; Chattopadhyay, S.; Chatterjee, S. Site-specific amino acid substitution in dodecameric peptides determines the stability and unfolding of c-MYC quadruplex promoting apoptosis in cancer cells. *Nucleic Acids Res.* **2018**, *46*, 9932-50.

## **Chapter 2**

### **Combating the Amyloid-Induced Cellular Toxicity and Stiffness by Designer Peptidomimetics**



Aberrant aggregation of A $\beta$  peptides and their extracellular deposition in the human brain are the major hallmarks of AD.<sup>1-3</sup> The compelling evidence suggests that the accumulation of amyloid aggregation species in the brain tissues induces significant stress on neurons through cell membrane interaction.<sup>4-7</sup> This causes redox imbalance and reorganization of the cytoskeletal system of neuronal cells.<sup>4</sup> A $\beta$  aggregation species elicit endoplasmic reticulum (ER) stress and oxidative stress through the production of excessive reactive oxygen species (ROS).<sup>6,7</sup> Although there are cellular pathways to reverse the stress, the adverse outcome of this pathogenic situation is cell apoptosis. Under the amyloid-induced stress conditions, the cells become rough and rigid due to the polymerization and stiffening of cytosolic actin filaments leading to the formation of stress fibres.<sup>8-11</sup> Atomic force microscopy (AFM)-based advanced imaging technique is one of the best methods to assess such amyloid-induced physio-mechanical changes of the cells.<sup>12-15</sup> PeakForce Quantitative NanoMechanics-AFM (PF QNM-AFM) offers high-resolution imaging of cells with real-time spatial resolution mapping of nanoindentation parameters Derjaguin-Muller-Toporov (DMT) modulus (measure of stiffness).<sup>16,17</sup> In this study, special emphasis is given to understand the neuronal cells under amyloid-induced cellular stress conditions and their rescue by de novo designed peptidomimetics inhibitors employing confocal and PF QNM-AFM techniques. Natural peptide-based amyloid inhibitors offer numerous advantages over the small molecule inhibitors<sup>18-21</sup> owing to their biological origin, biocompatibility, target-specific binding, sequence variability, and ease of synthesis.<sup>22-29</sup> Short peptides with <sup>16</sup>KLVFF<sup>20</sup> derived from A $\beta$ 42 have been shown to inhibit A $\beta$  aggregation.<sup>30-33</sup> The propensity of natural peptides for proteolytic cleavage and self-aggregation lead to the development of peptidomimetics-based inhibitors such as peptoids and cyclic peptides.<sup>34-37</sup>

We hypothesized that the incorporation of rigid, proteolytically stable CDP units into A $\beta$ 14-23 at defined positions would overcome the limitations of linear peptides, and cytotoxicity and flexibility issues often associated with large cyclic peptides based amyloid modulators.

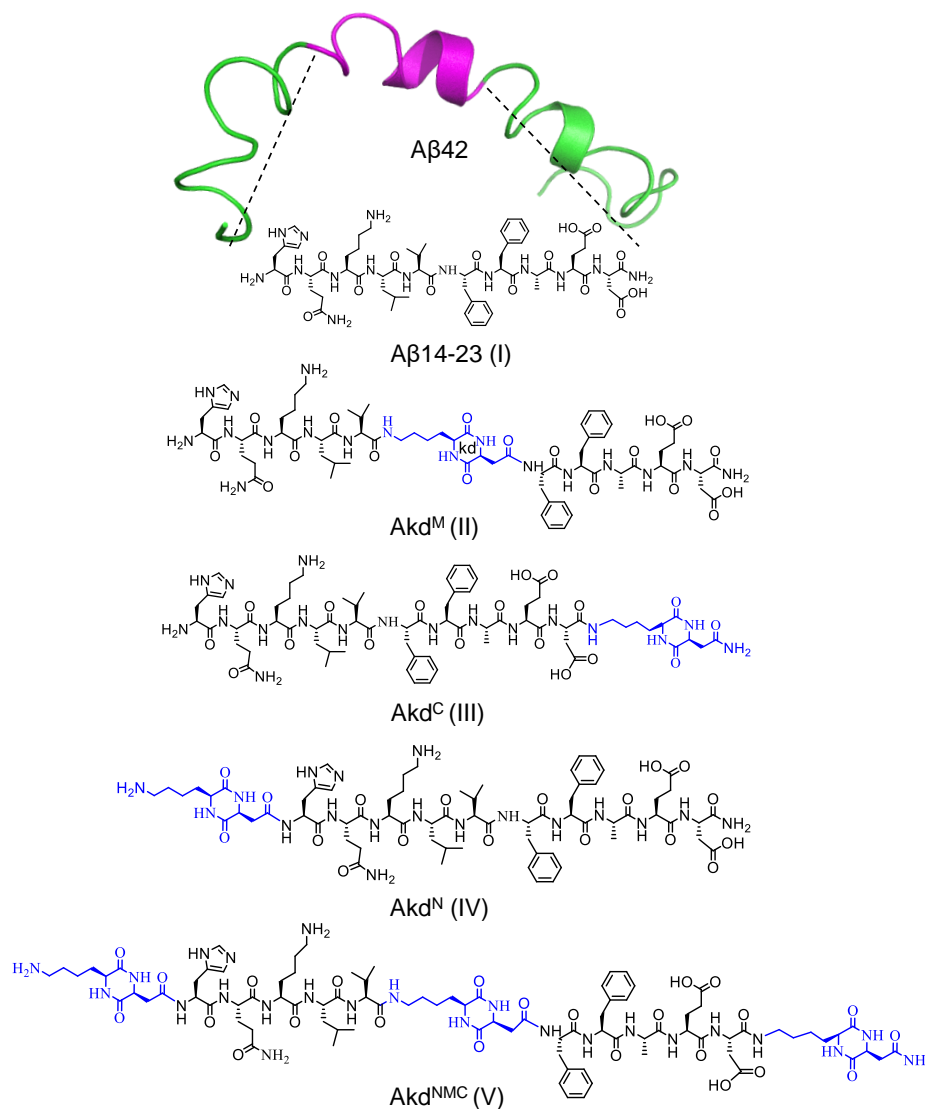


**Figure 1.** Structures of A $\beta$ 14-23 (I) derived from A $\beta$ 42 (PDB: 1Z0Q) and CDP (kd) inserted peptidomimetics (II-V).

The exceptional intermolecular hydrogen bonding ability and biological activities of CDPs are anticipated to control A $\beta$  aggregation and associated stress-induced cellular mechanical changes through the interactions with A $\beta$  monomers or aggregation species.<sup>38-40</sup>

## 2.1 Design strategy of peptidomimetics

We designed and synthesized a set of A $\beta$ 14-23 (I) peptidomimetics by incorporating cyclo (Lys-Asp)-based CDP-unnatural amino acid (kd) at middle (Akd<sup>M</sup>, II), C-terminal (Akd<sup>C</sup>, III), N-terminal (Akd<sup>N</sup>, IV), and at all three positions (Akd<sup>NMC</sup>, V) (Figure 1, detailed characterizations in Table 3 and 4). The resemblance between A $\beta$ 14-23 (I) and A $\beta$ 42 (the most toxic form of A $\beta$ ) in their pH-dependent aggregation, metal binding, and cytotoxic properties<sup>32, 41-43</sup> prompted us to investigate the aggregation behavior of I in the presence of II-V in pH 2.0 (glycine-HCl buffer, 10 mM) and pH 7.4 (PBS: phosphate buffer saline, 10 mM) conditions. First, we sought to identify a competitive in vitro inhibitor of A $\beta$ 14-23 aggregation from II-V. Thereafter, we envisioned to evaluate the efficiency of the lead inhibitor to ameliorate cellular toxicity and adverse cell mechanics caused by A $\beta$ 42 amyloid-induced cellular stress.

## 2.2 Results and discussion

### 2.2.1 Thioflavin T assay

A time-dependent thioflavin T (ThT) fluorescence assay was performed to assess the aggregation kinetics of A $\beta$ 14-23 and determine the aggregation rate constant ( $\kappa$ ) and lag time ( $T_{Lag}$ ) upon treatment with II-V for 20 days at two pH conditions (Figure 2a-c). The aggregation of A $\beta$ 14-23 was plateaued after 6 and 15 days under pH 2.0 and 7.4 conditions, respectively. A $\beta$ 14-23 showed faster aggregation with  $\kappa = 1.1$  day<sup>-1</sup> at pH 2.0 as compared to pH 7.4 ( $\kappa = 0.5$  day<sup>-1</sup>). The co-incubation with II-V distinctly influenced the A $\beta$ 14-23 aggregation propensity. A $\beta$ 14-23 treatment with V resulted in the longest  $T_{Lag}$  (199.2 and 316.8 h for pH 2.0 and 7.4, respectively) with low  $\kappa$  values ( $\sim 0.4$  day<sup>-1</sup>). This data suggests effective interaction of V with A $\beta$ 14-23 at lag phase and stabilization of monomeric state. The  $T_{Lag}$  values for II (100.8 and 216.0 h in pH 2.0 and 7.4,

respectively) and III (120.0 and 124.8 h in pH 2.0 and 7.4, respectively) treated A $\beta$ 14-23 samples suggest monomer stabilization albeit to a lesser extent as compared to V.

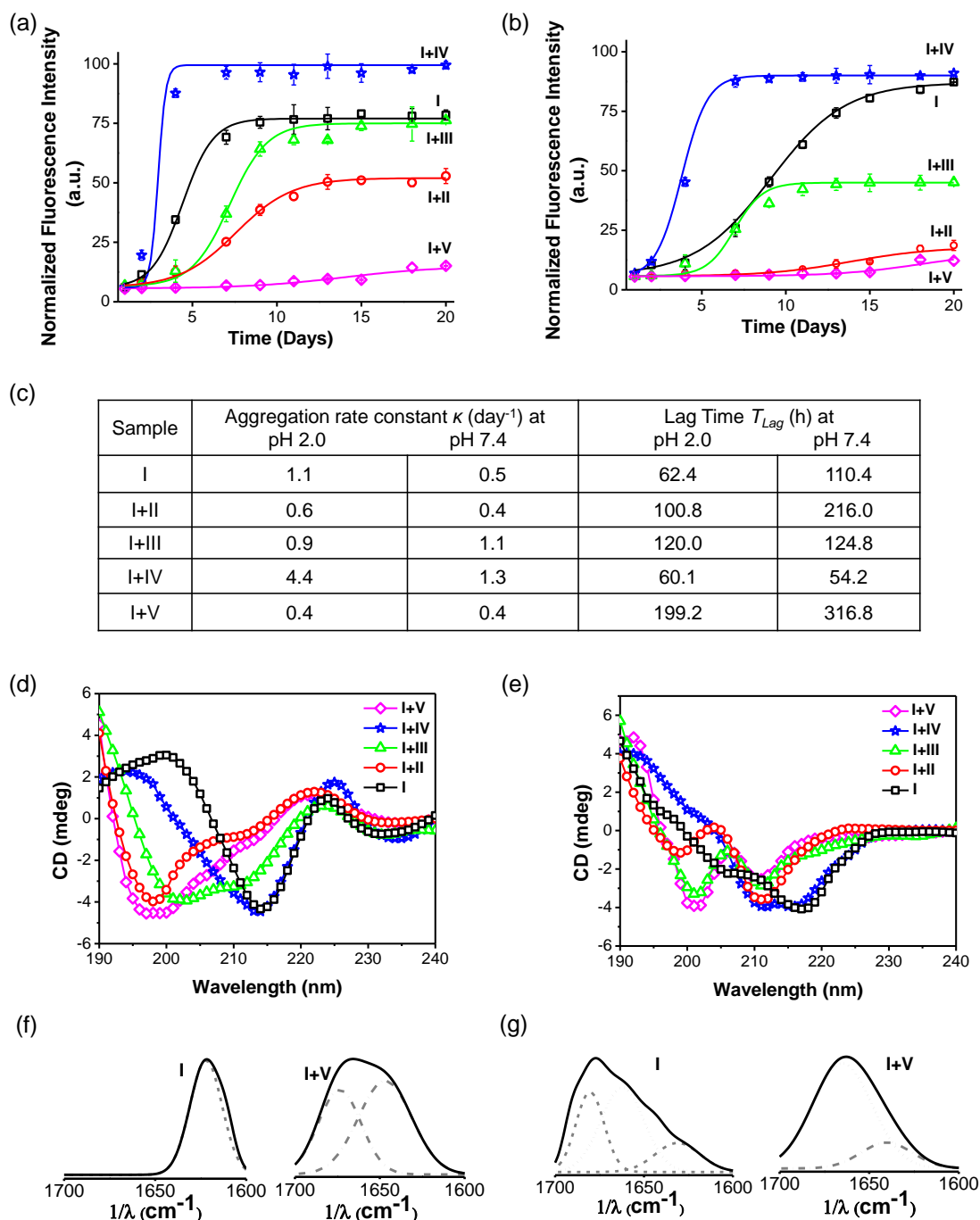


**Figure 2.** A $\beta$ 14-23 (I) aggregation in the absence and presence of the II, III, IV and V at pH 2.0 (left panel) and 7.4 (right panel) for 20 days. (a,b) Time-dependent ThT fluorescence ( $\lambda_{em} = 482$  nm) assay data, I Aggregation parameters,  $\kappa$  and  $T_{Lag}$ . (d,e) CD spectra, and (f, g) Deconvoluted FTIR spectra (amide I region: 1600-1700  $\text{cm}^{-1}$ , solid line) at pH 2.0 and 7.4, respectively. Dotted-line:  $\alpha$ -helix, dotted-dashed line: random coil and dashed-line:  $\beta$ -sheet.



Relatively better inhibitory efficiency was observed for II compared to III. While, IV was found to enhance the aggregation rate of A $\beta$ 14-23 by shortening  $T_{Lag}$  (60.1 and 54.2 h in pH 2.0 and 7.4, respectively). The higher  $\kappa$  for IV-treated A $\beta$ 14-23 is attributed to rapid aggregation of monomers into growth-directing critical nuclei at the lag phase.

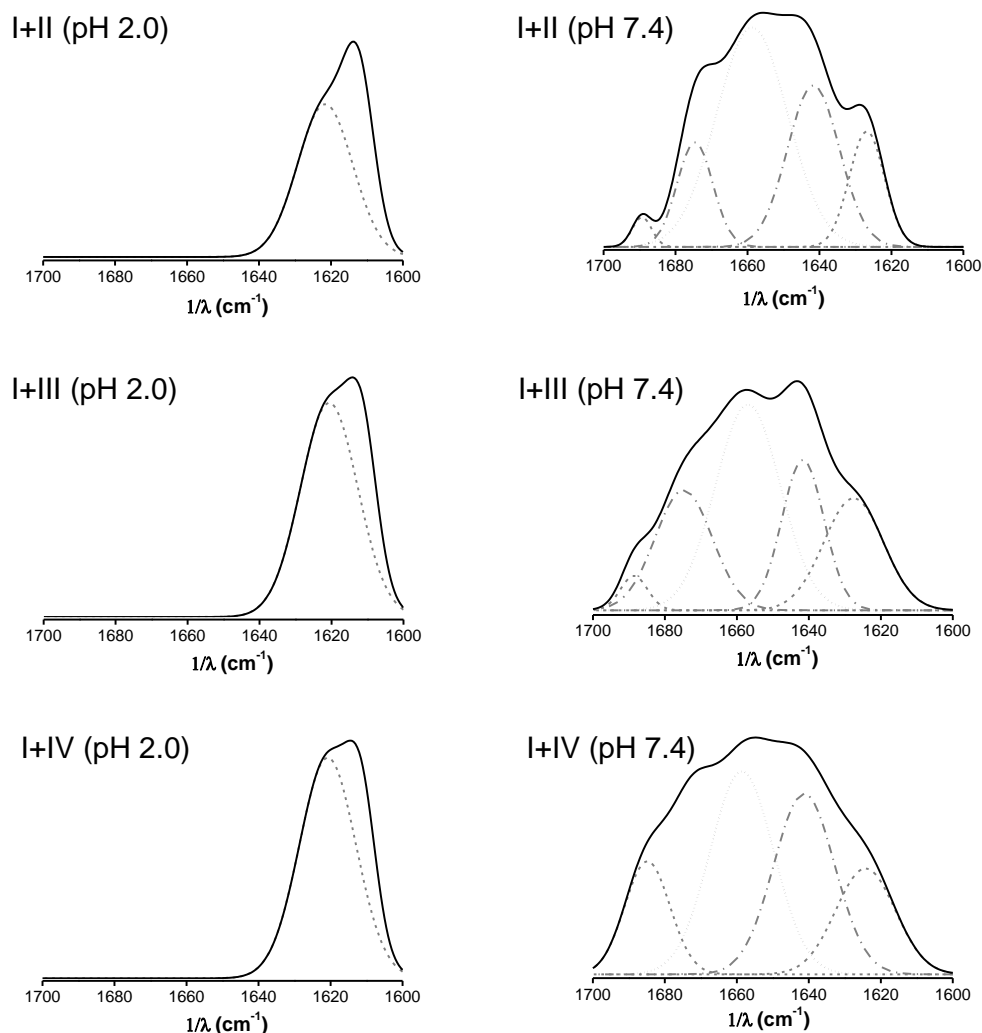


**Figure 3.** FTIR spectra of pre-incubated I (25  $\mu$ M) in the absence and presence of peptidomimetics II-IV (25  $\mu$ M) at pH 2.0 and 7.4. (Dotted line:  $\alpha$ -helix, dotted-dashed line: Random coil; dashed line:  $\beta$ -Sheet).

The kinetic analysis thus inferred that II, III, and V inhibited A $\beta$ 14-23 aggregation under both acidic and physiological conditions. The position of kd in peptidomimetics plays a crucial role in the modulation of A $\beta$ 14-23 aggregation. Peptidomimetics with single kd at middle (II) or C-

terminal (III) and three kd units at middle, N- and C-termini (V) are effective modulators of A $\beta$ 14-23 aggregation with overall inhibitory efficiency in the order of V > II > III. In contrast, IV with kd at the N-terminal exhibited propensity for enhancing the amyloid aggregation.

### **2.2.2 CD measurements**

A $\beta$  undergoes aggregation through conformational changes from random coil to  $\alpha$ -helix to  $\beta$ -sheet.<sup>41</sup> We performed circular dichroism (CD) and Fourier transform infrared (FTIR) studies to understand the effect of II-V on A $\beta$ 14-23 aggregation-induced secondary conformations. The negative ellipticity around 218-220 nm ( $\sim$ -4.2 mdeg) in the CD spectra of A $\beta$ 14-23 at both pH conditions confirmed its aggregation through  $\beta$ -sheet structure (Figure 2d, e). Upon incubation with II, III and V at pH 2.0, the CD band at 218 nm (-4.2 mdeg) was shifted to 200 nm (-3.4, -3.6, and -4.5 mdeg) suggesting stabilization of A $\beta$ 14-23 monomers with random coil conformation (Figure 2d). The random coil and  $\beta$ -sheet features observed upon treatment with III indicated its moderate effect in stabilizing A $\beta$ 14-23 monomers. Further, the negative bands around 200 and 210 nm (around -4 and -3 mdeg, respectively) at pH 7.4 suggested the monomer stabilization of A $\beta$ 14-23 through random coil and  $\alpha$ -helix conformations, respectively, in the presence of II, III and V (Figure 2e). While, the CD spectra of IV-treated A $\beta$ 14-23 showed broad negative bands around 216-218 nm (-3.9 mdeg), which confirmed  $\beta$ -sheet-driven aggregation at both pH conditions. The weak positive CD signal ( $\sim$ 0.8 mdeg) observed for I at pH 2.0 is possibly attributed to the twisted nature of aggregates as revealed by the transmission electron microscopy (TEM) study (Figure 5).<sup>44</sup>

### **2.2.3 IR study and AFM study**

The amide I region (1600-1700 cm<sup>-1</sup>) of FTIR spectra confirmed the aggregation propensity of A $\beta$ 14-23 with characteristic features of parallel (1620 cm<sup>-1</sup>) and antiparallel (1620 and 1680 cm<sup>-1</sup>)

---

---

$\beta$ -sheet conformations at pH 2.0 and 7.4, respectively (Figure 2f, g).<sup>45</sup> A $\beta$ 14-23 samples incubated with II-IV showed significant  $\beta$ -sheet characteristics at both pH (Figure 3). Under similar conditions, treatment with V induced either random coil (1640 and 1670  $\text{cm}^{-1}$ ) or  $\alpha$ -helix (1660  $\text{cm}^{-1}$ ) features confirming its potential to stabilize A $\beta$ 14-23 monomers.  $^1\text{H}$  NMR study has validated the stabilization of monomeric state of I by V (Figure 6).

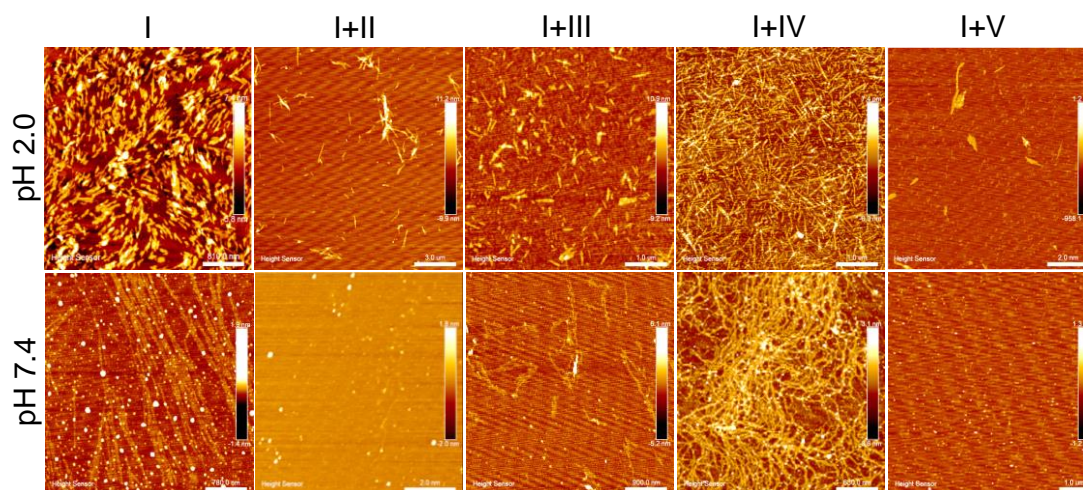


**Figure 4.** AFM images of pre-incubated A $\beta$ 14-23 (I) in the absence and presence of II-V.

AFM data showed the formation of topographically and morphologically distinct aggregates by A $\beta$ 14-23 at two pH (2.0 and 7.4) conditions (Figure 4). The short fibril-like compact aggregates

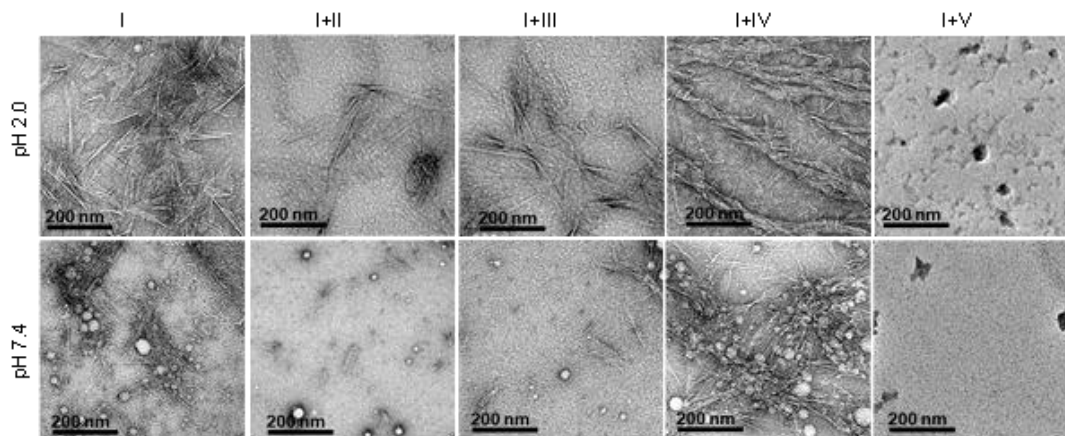


**Figure 5.** TEM images of pre-incubated I in the absence and presence of II-V at pH 2.0 and 7.4.

(average height ~3-5 nm) and typical oligomer-associated elongated fibrils (average height ~1-2 nm) were observed at pH 2.0 and 7.4, respectively. The TEM images also observed that A $\beta$ 14-23 formed short, twisted fibrils at pH 2.0 and elongated fibrils with oligomers at pH 7.4 (Figure 5). The formation of short fibril-like aggregates at lower pH is anticipated to follow the non-cooperative elongation mechanism.<sup>46</sup>

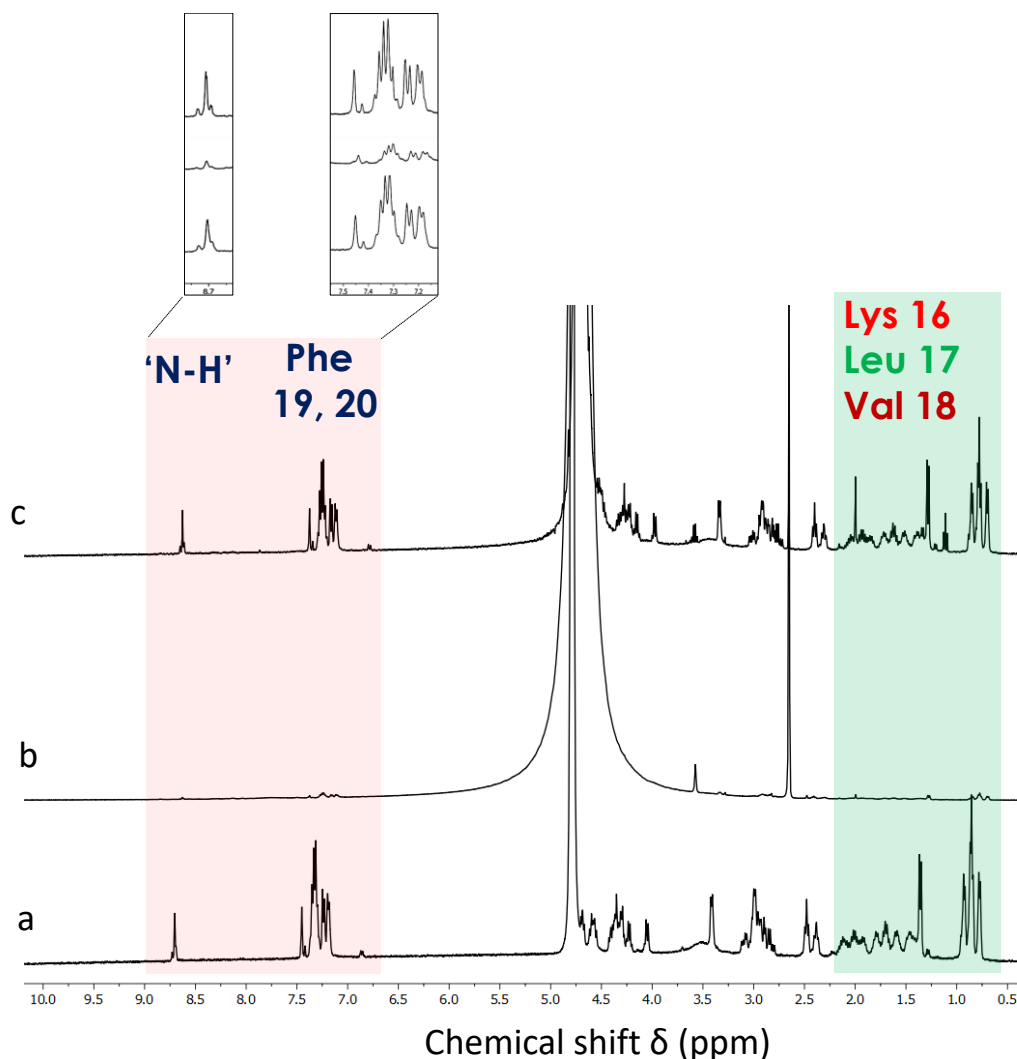


**Figure 6.** (a)  $^1\text{H}$  NMR spectrum of A $\beta$ 14-23 (I) at room temperature show a broad range of chemical shifts confirming its native monomer conformation. (b) The spectral features of fibrillar A $\beta$ 14-23 show the disappearance of most of the amide and aromatic (Phe 19, 20) proton signals, which suggest the fibril formation. (c)  $^1\text{H}$  NMR spectrum of solution containing an equimolar ratio of Akd<sup>NMC</sup> (V) and I, which show well-distributed protons with a broad range of chemical shifts comparable to that of control sample (monomer) of I (a). The observed proton signals of I similar to monomer conformation in the presence of V confirmed the stabilization of monomeric state of A $\beta$ 14-23 (I) by V.

The inhibition of A $\beta$ 14-23 aggregation by II, III, and V was confirmed by both AFM and TEM studies with inhibition efficacy in the order of V > II > III (Figure 4, Figure 5). The abundant fibrillar aggregates of IV-treated A $\beta$ 14-23 sample (I+IV) reiterated the fibrillation promoting nature of IV.

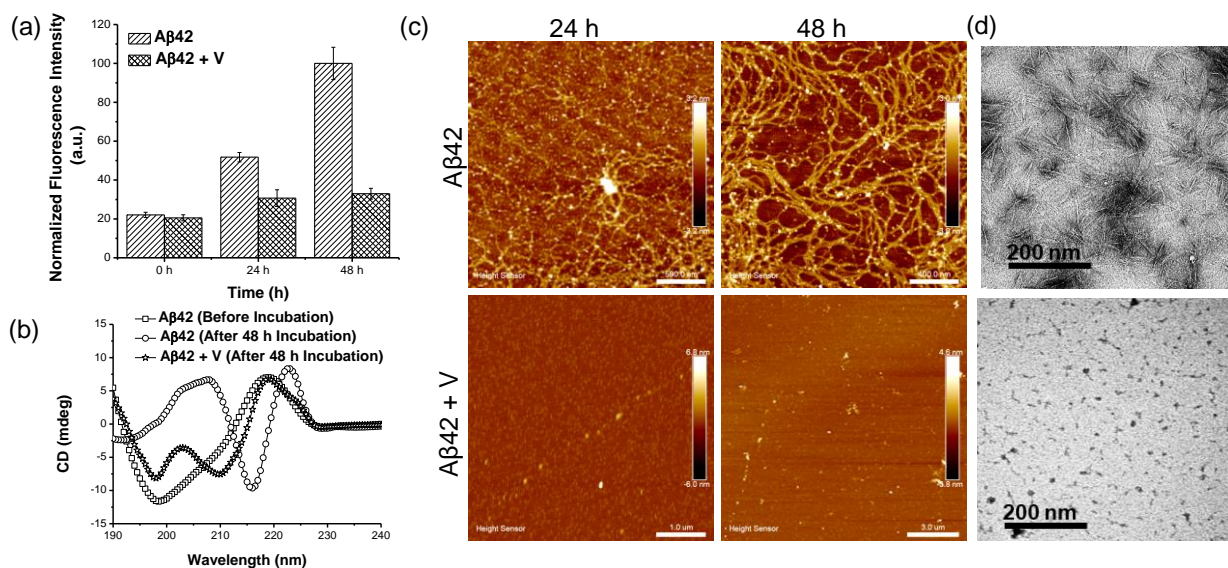


**Figure 7.** A $\beta$ 42 aggregation in the presence and absence of Akd<sup>NMC</sup> (V) in phosphate buffer saline (PBS) conditions (pH 7.4) at 37 °C over a period of 2 days. (a) Time-dependent ThT fluorescence assay data ( $\lambda_{em}$  = 482 nm) showed inhibition of A $\beta$ 42 aggregation in the presence of V. (b) CD spectra of A $\beta$ 42 in the absence and presence of V show A $\beta$ 42 aggregation with  $\beta$ -sheet conformation in the absence of V after 48 h incubation, while inhibitor V induced stabilization of A $\beta$ 42 through  $\alpha$ -helical (content) conformation. (c,d) AFM and TEM images of pre-incubated A $\beta$ 42 and A $\beta$ 42+V in PBS (pH 7.4) that confirmed the inhibition of A $\beta$  aggregation by V.

### 2.3 Cytotoxicity assay

Next, we assessed cytotoxicity of II-V in cultured neuronal cells (SH-SY5Y). The treatment of cells with II-V (10  $\mu$ M) for 24 h showed cell viability of ~93, 99, 99, and 99%, respectively, compared to PBS (10 mM, pH 7.4) treated control (100%) (Figure 8a, b). This result suggests the excellent viability and biocompatibility of II-V to neuronal cells. To evaluate the efficacy of the peptidomimetics to rescue the cells from A $\beta$ 14-23-aggregation induced cytotoxicity, the cells were treated with A $\beta$ 14-23 (10  $\mu$ M) in the absence and presence of II-V at 1:1 stoichiometric ratio. As



expected, A $\beta$ 14-23 treatment showed reduced cell viability of ~66%, which confirmed its neurotoxic nature. The cells treated with A $\beta$ 14-23 in the presence of II-V showed ~90, 83, 69 and 97% cell viability, respectively, which corresponds to ~24, 17, 3, and 31% improved viability over A $\beta$ 14-23 treated cells (Figure 8c). From these results, we identified II and V as the potential inhibitors of A $\beta$ 14-23-induced in cellulo toxicity.

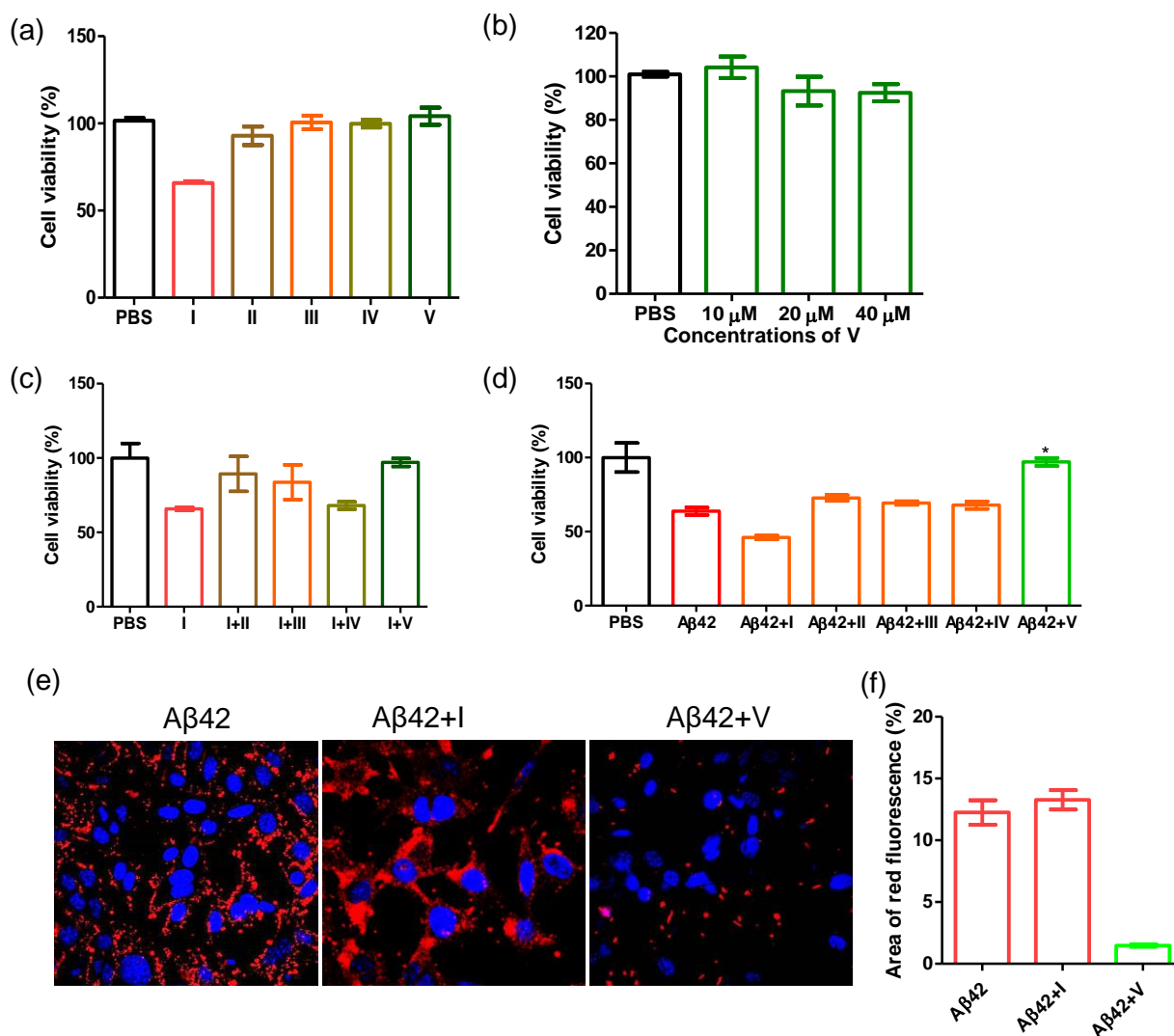


**Figure 8.** Cytotoxicity of peptidomimetics and their neuronal rescue ability from amyloid-induced cellular stress. (a) The cell viability of the SH-SY5Y after treating (24 h) with PBS buffer (10 mM), I (10  $\mu$ M) and peptidomimetics II-V (10  $\mu$ M) at pH 7.4. The result confirmed that peptidomimetics are nontoxic to neuronal cells, while A $\beta$ 14-23 (I) exhibited significant amyloidogenic toxicity. (b) The cell viability of the SH-SY5Y after treating (24 h) with PBS buffer (10 mM) and different concentrations of V (10-40  $\mu$ M), which indicate relatively non-toxic nature of V in that concentration range. (c) The cell viability of SH-

SH-SY5Y after treating (24 h) with PBS, pre-incubated (48 h) I (10  $\mu$ M) alone and with peptidomimetics (II-V) at pH 7.4. The result confirmed the potential of peptidomimetic II and V to rescue the neuronal cells. (d) The cell viability of the SH-SY5Y after treating (24 h) with PBS, pre-incubated (48 h) A $\beta$ 42 (10  $\mu$ M) in the absence and presence of peptidomimetic I-V (10  $\mu$ M) at pH 7.4. The result confirmed that peptidomimetic V is the most potent to rescue the neuronal cells from amyloid-induced cytotoxicity. (e) Confocal images of immunostained SH-SY5Y cells with OC and secondary antibody (red). Blue: nuclear staining with DAPI in the presence of A $\beta$ 42, A $\beta$ 42+I, A $\beta$ 42+V samples. Scale bar: 20  $\mu$ m. (f) Representative bar plot indicating total cytotoxic area (% area of red fluorescence) for the samples A $\beta$ 42, A $\beta$ 42+I, and A $\beta$ 42+V in (e), which proved that I induced membrane-localized amyloid aggregates formation and V act as a potent inhibitor of amyloid aggregation.

The effects of I-V on the A $\beta$ 42-induced toxicity was further assessed by treating the cells with A $\beta$ 42 (10  $\mu$ M) with I-V at 1:1 ratio for 24 h (Figure 8d). A $\beta$ 42 alone showed cell viability of  $\sim$ 64% indicating its highly toxic nature towards SH-SY5Y cells. The cells incubated with A $\beta$ 42 in the presence of I-V showed viabilities of  $\sim$ 47, 72, 68, 67, and 97%, respectively.

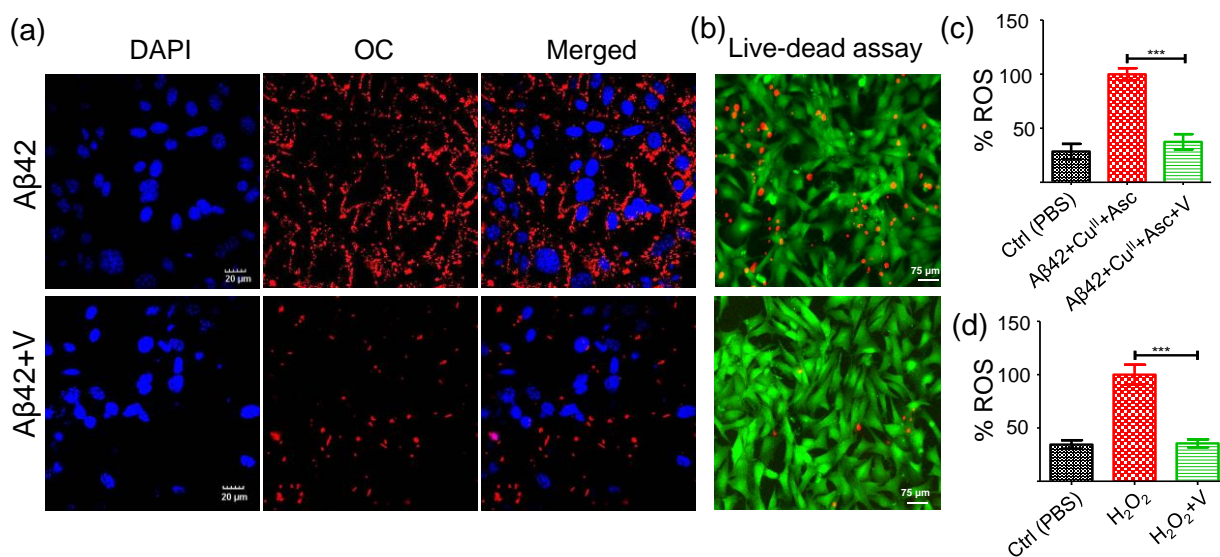


**Figure 9.** (a) Confocal images of A $\beta$ 42 (10  $\mu$ M) and A $\beta$ 42+V (10  $\mu$ M, 1:1) treated SH-SY5Y cells in PBS (pH 7.4) immunostained with OC and secondary antibody (red). Blue: nuclear staining with DAPI. Scale bar: 20  $\mu$ m. (b) Fluorescence microscopy images of SH-SY5Y cells upon treatment with A $\beta$ 42 (10  $\mu$ M) and A $\beta$ 42+V (1:1) for 24 h. Green: staining with calcein AM, red: staining with propidium iodide. (c) Intracellular ROS generation in SH-SY5Y cells incubated with A $\beta$ 42 (10  $\mu$ M), Cu<sup>2+</sup> (10  $\mu$ M), ascorbate (300  $\mu$ M), in the absence and presence of V (10  $\mu$ M). (d) ROS levels measured in SH-SY5Y cells upon incubating (4h) with H<sub>2</sub>O<sub>2</sub> in the absence and presence of V. ROS produced is quantified by measuring DCF fluorescence emission at 529 nm for a given time point. Each experiment was repeated three times (n= 3), and error bars represent the standard deviation (SD) (\*p< 0.0001).

Notably, A $\beta$ 42+I showed severe cytotoxicity to cells due to high aggregation propensity of both I and A $\beta$ 42. Remarkably, V showed a strong neuronal rescue with  $\sim$ 33% improved viability

compared to A $\beta$ 42-treated cells. These results motivated us to perform a detailed evaluation of the inhibitory potential of V against amyloid-induced alterations at cellular levels using confocal imaging-based immunocytochemistry, fluorescence imaging-based live/dead assay and modulation of ROS generation. The ThT, CD, AFM and TEM-based biophysical data of A $\beta$ 42 and A $\beta$ 42+V are in good agreement with in cellulo studies and support V as a potential inhibitor of A $\beta$  aggregation at pH 7.4 (Figure 7).

#### **2.4 Membrane toxicity**

Immunocytochemistry assay unambiguously evaluates the efficiency of an inhibitor to prevent the membrane-localization of A $\beta$ 42 aggregates by stabilizing the nontoxic monomers.<sup>47</sup> For this study, the SH-SY5Y cells were incubated independently with A $\beta$ 42, A $\beta$ 42+I, and A $\beta$ 42+V at pH 7.4 for 3 h followed by successive staining with fibril specific primary antibody (OC), fluorescently-labelled secondary antibody ( $\lambda_{ex}$ = 633 nm and  $\lambda_{em}$ = 650 nm) and DAPI (nuclear staining dye). The confocal microscopy images showed localization of A $\beta$  aggregates in abundance on the cell membrane both in A $\beta$ 42 (12.3%) and A $\beta$ 42+I (13.3%) treated cells, while A $\beta$ 42+V displayed significant reduction of membrane-localized aggregates (1.5%) indicating the amyloid inhibitory potential of V under cellular conditions (Figure 9a, Figure 8 e, f).

#### **2.5 Live-dead assay**

We also performed a live/dead assay to confirm the cytotoxicity of A $\beta$ 42 and neuronal rescue from amyloid-induced stress upon treatment with V. The SH-SY5Y cells were cultured in 35 mm confocal dish and treated with calcein-AM (2  $\mu$ M) and propidium iodide (4.5  $\mu$ M) to stain the live (green) and dead (red) cells, respectively. The fluorescence images displayed a significant extent of dead cells present in A $\beta$ 42 (10  $\mu$ M) treated samples (Figure 9b and Figure 10). While the samples treated with A $\beta$ 42+V (10  $\mu$ M, 1:1) showed an appreciable reduction in the number of



dead cells. Quantitatively, the ImageJ analysis revealed that A $\beta$ 42 treated samples contained ~36% dead cells, which reduced to ~4% in the presence of V compared to PBS treated controls. These findings have proved that V successfully attenuates A $\beta$ 42 aggregation-induced toxicity under in cellulo conditions. We have demonstrated the role of A $\beta$ 42 in excessive ROS production and oxidative stress in previous studies.<sup>18,24</sup>

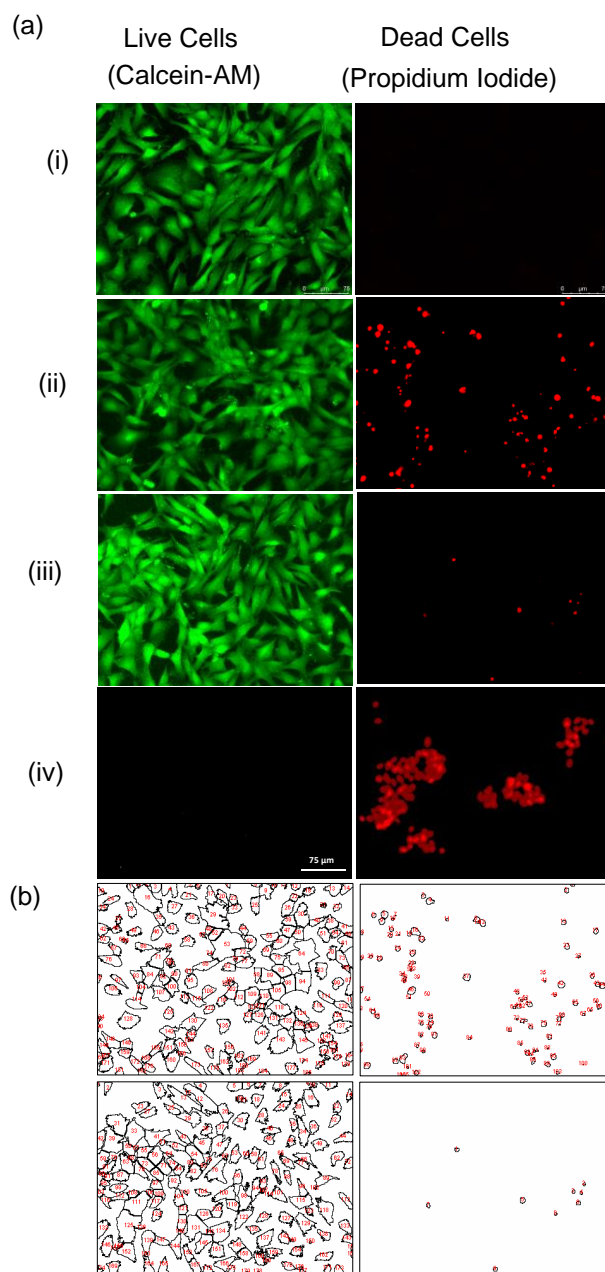


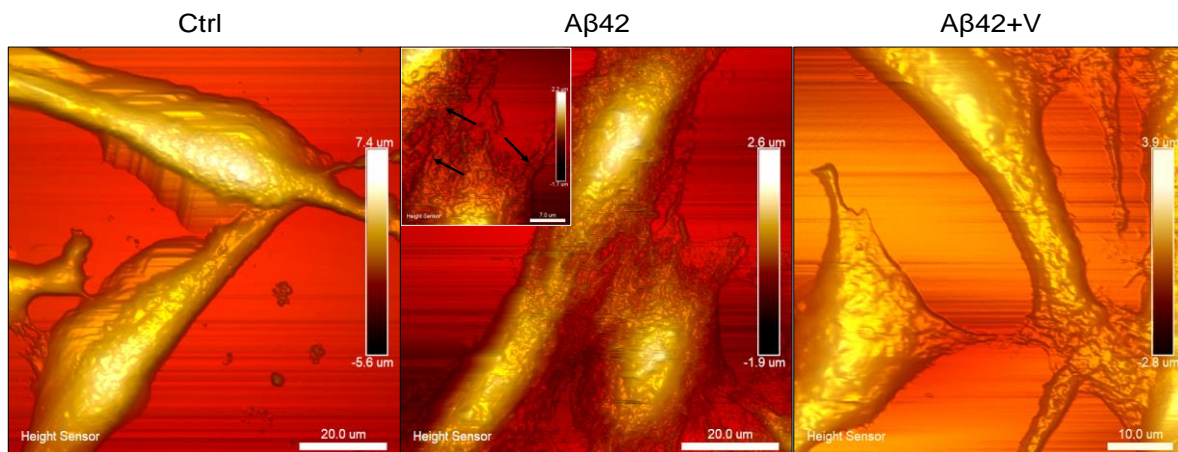
**Figure 10.** (a) Fluorescence microscopy images of SH-SY5Y cells in Live/Dead staining assay upon treatment with A $\beta$ 42 and A $\beta$ 42+V for 24 h, Panel (i): untreated cells (negative control); panel (ii) cells treated with A $\beta$ 42 (10  $\mu$ M); panel (iii): cells treated with A $\beta$ 42+V (1:1); panel (iv): cells treated with 0.1% Triton X (positive control); Scale bar is 75  $\mu$ m. (b) The number of dead cells for A $\beta$ 42, A $\beta$ 42+V-treated samples are 36% and 4 %, respectively. Images are quantified using ImageJ software.

## 2.6 Inhibition of A $\beta$ induced amyloidogenic stress

Here, we attempted to evaluate the role of V in reducing ROS levels in A $\beta$ 42-induced amyloidogenic conditions. Intracellular ROS levels in SH-SY5Y cells (in the form of hydroxyl and peroxy radicals) was investigated using DCFDA (2,7-dichlorofluorescein diacetate) fluorescence dye. In this study, A $\beta$ 42-Cu<sup>II</sup> (10  $\mu$ M), ascorbate (300  $\mu$ M), and A $\beta$ 42-Cu<sup>II</sup>+V (10  $\mu$ M) were added to DCFDA-treated SH-SY5Y cells and the DCF fluorescence was monitored at 529 nm. Our data revealed that V significantly reduced the ROS level produced by A $\beta$ 42-Cu<sup>II</sup>+Asc system in cells to ~38% (Figure 9c). The cellular study also demonstrated that V effectively reduces the exogenously added H<sub>2</sub>O<sub>2</sub> to ~35% (Figure 9d). Overall, V acts as an effective amyloid inhibitor and modulator of amyloid-induced excessive ROS generation and related cellular stress.

## 2.7 PF QNM-AFM imaging for SH-SY5Y cells

PF QNM-AFM was employed to gain insights into the changes in physio-mechanical properties of the cell membrane due to A $\beta$ 42-induced cellular stress and the rescuing effect of V. From the PF QNM-AFM data, we evaluated parameters such as the height, peak force error (a measure of exact tip-surface interactions) and cell stiffness (DMT modulus) with spatial resolution for both single (Figure 12a-c) and colony of SH-SY5Y cells (Figure 11) treated with A $\beta$ 42 and A $\beta$ 42+V for 24 h.



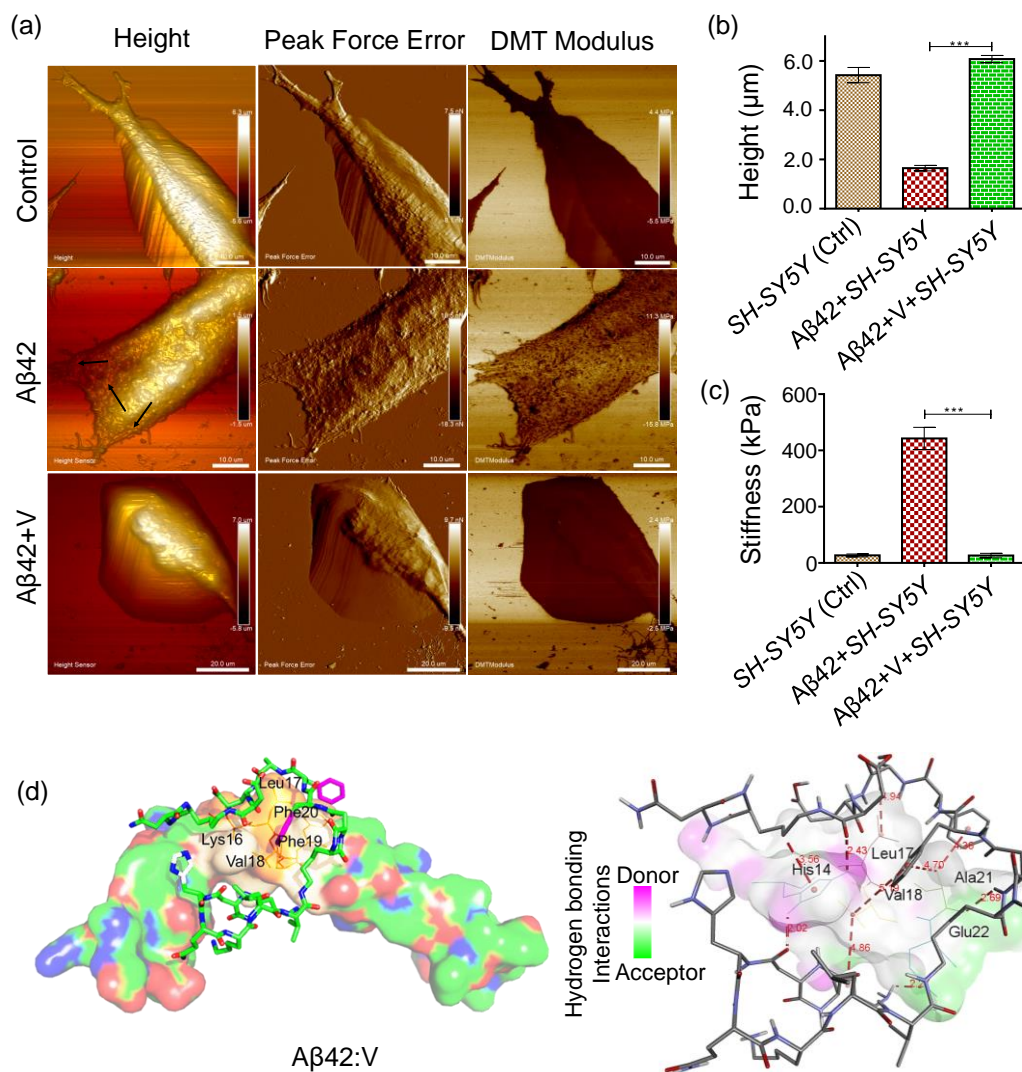
**Figure 11.** PF QNM-AFM images of SH-SY5Y cells (colony) treated with PBS (Ctrl, 10 mM), A $\beta$ 42 (10  $\mu$ M), A $\beta$ 42+V (10  $\mu$ M, 1:1) for 24 h at pH 7.4. These AFM images confirmed the amyloid stress induced membrane damage in neuronal cells, which can be reduced in the presence of peptidomimetic V (Akd<sup>NMC</sup>). Inset in A $\beta$ -treated cells clearly show stress fiber formation due to the emergence of amyloid-induced cellular stress upon A $\beta$ -membrane interactions. The treatment of the peptidomimetics V on the A $\beta$ -treated cells rescues the neuronal cells from the amyloid-induced cellular stress.

Figure 12a shows smooth topography (height  $5.4 \pm 0.6 \mu\text{m}$ ) with low mechanical stiffness ( $30 \pm 5$  kPa) for control cells, where no sign of stress fiber formation was observed. The smooth topography and mechanical stiffness of  $30 \pm 5$  kPa indicate healthy cellular characteristics of control cells.<sup>11</sup> Upon A $\beta$ 42 treatment, the cells were deformed (height  $1.6 \pm 0.2 \mu\text{m}$ ) with increased cell stiffness ( $417 \pm 39$  kPa), and formation of networks of stress-fibers was observed (indicated by the arrows). The stress-fiber-containing deformed cellular features with rigid mechanics (high stiffness) indicate the emergence of stress due to A $\beta$ -membrane interactions.<sup>9-11</sup> Remarkably, A $\beta$ 42+V treated cells showed cell morphology (height  $6.4 \pm 0.4 \mu\text{m}$ ), stiffness ( $21 \pm 9$  kPa) and cytoskeletal organization comparable to the control cells. This affirmatively validated V as a potential candidate to combat amyloid-induced cellular stress and to maintain the healthy cellular mechanics.

## 2.8 Molecular Docking Study

We performed molecular docking to investigate the binding interactions between A $\beta$ 42 and V. The docking results showed that V binds to A $\beta$ 42 with a binding energy of -5.2 kcal/mole (Table

1). Data in Table 1 also indicates that KLVFF recognition plays an important role in the binding of V around 14-23 region of A $\beta$ 42. Multiple hydrogen bonding and hydrophobic interactions via His14, Leu17, Val18, Ala21 and Glu 22 residues of A $\beta$ 42 and kd residues of V are found to stabilize the hydrophobic 14-23 region (Figure 12d). V-mediated spatial interactions with A $\beta$ 42 can segregate the A $\beta$ 42 monomers and thus inhibit amyloid aggregation inhibition, as revealed by



**Figure 12.** PF QNM-AFM images of SH-SY5Y cells under healthy and amyloid-induced stress conditions in height, peak force error and DMT modulus modes. The cells treated with (a) PBS, pH 7.4 (control), A $\beta$ 42 and A $\beta$ 42+V. Arrows in A $\beta$ 42 treated cells indicate stress fibers. (b, c) Height and mechanical stiffness calculated from PF QNM-AFM data. Number of experiments = 3, Mean  $\pm$  SD, \*P < 0.001. (d) Representative docked conformation between A $\beta$ 42 (surface representation) and V (stick representation)

(Left) and their possible interactions based on the hydrogen bonding donor-acceptor sites in 14-23 region of A $\beta$ 42 (surface, Right).

the spectroscopy data. Further, the docking analyzes revealed V as the most effective amyloid inhibitor, stabilized A $\beta$ 14-23 monomers through KLVFF recognition (Figure 13, Table 2).

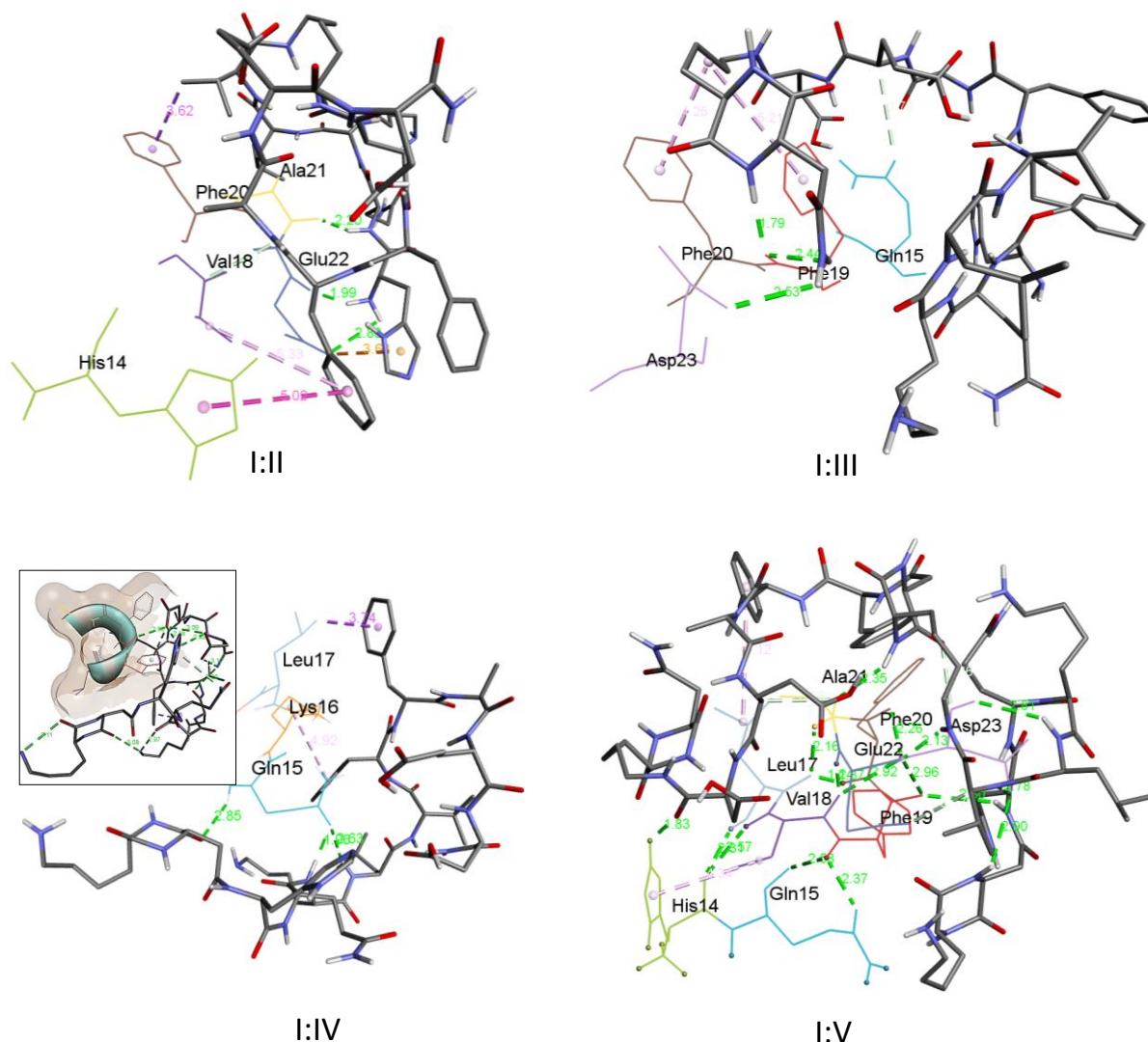


**Figure 13.** Representative docked structures with the residue-specific intermolecular interactions for I:II, I:III, I:IV (inset shows intensive intramolecular interactions within IV that makes it too inflexible to stabilize the hydrophobic region (surface presentation) of I leading to induced aggregation), and I:V (I : line representation), II-V : stick representation, grid dimension: 48Å x 46Å x 34Å). The docking results indicate that II, III, IV, and V bind to I with binding energies of -4.1, -4.1, -3.1, and -4.9 kcal/mol, respectively. Considering the binding energies and the number of hydrogen bonding interactions, V was found to be the best interacting and stabilizing inhibitor of I. Detailed binding interaction are shown in Table 2.



**Table 1** List of the docking parameters: Binding energies and hydrogen bond distances between different atoms of the A $\beta$ 42 peptide and the ligand Akd<sup>NMC</sup> (V).

Interacting Sites	Bond distance (Å)	Category of Bond	Type of Bond
Intermolecular Interactions (A $\beta$ 42: V, Binding Energy: -5.2 kcal/mole)			
His14:H* <sup>S</sup> - N-kd:O	2.02	Hydrogen Bond	Conventional Hydrogen Bond
His14:H* <sup>S</sup> - Asp:O	2.43	Hydrogen Bond	Conventional Hydrogen Bond
Ala21:O - M-kd:H	2.69	Hydrogen Bond	Conventional Hydrogen Bond
Glu22:O* <sup>S</sup> - N-kd:H	2.27	Hydrogen Bond	Conventional Hydrogen Bond
His14 - C-kd:H	3.56	Hydrophobic	$\pi$ - $\sigma$
Val18 - N-kd	4.86	Hydrophobic	Alkyl
Leu17 - Ala:C	4.94	Hydrophobic	Alkyl
Ala21 - Phe2	4.36	Hydrophobic	$\pi$ -Alkyl
Val18 - Phe1	5.19	Hydrophobic	$\pi$ -Alkyl
Ala21 - Phe1	4.70	Hydrophobic	$\pi$ -Alkyl

**Table 2** List of the docking parameters and binding interactions for the docked structures of I:II, I:III, I:IV, and I:V.

Interacting Sites	Bond distance (Å)	Category of Bond	Type of Bond
Intermolecular Interactions (I:II, Binding Energy: -4.1 kcal/mole)			
Glu22:O* <sup>S</sup> - His:H	2.83	Hydrogen Bond	Conventional Hydrogen Bond
Glu22:O - His:H	1.99	Hydrogen Bond	Conventional Hydrogen Bond
Ala21:O - Gln:H	2.20	Hydrogen Bond	Conventional Hydrogen Bond
Val18:C* <sup>S</sup> - Phe:O	3.07	Hydrogen Bond	Carbon Hydrogen Bond
Glu22:O* <sup>S</sup> - His	3.63	Electrostatic	$\pi$ -Anion
Phe20 - Val:C	3.62	Hydrophobic	$\pi$ - $\sigma$
His14 - Phe2	5.02	Hydrophobic	$\pi$ - $\pi$ T-shaped
Val18 - Phe2	5.33	Hydrophobic	$\pi$ -Alkyl
Intermolecular Interactions (I:III, Binding Energy: -4.1 kcal/mole)			
Phe19:O - C-kd:H	1.79	Hydrogen Bond	Conventional Hydrogen Bond
Asp23:O* <sup>S</sup> - C-kd:H	2.53	Hydrogen Bond	Conventional Hydrogen Bond
Phe19:O - C-kd:H	2.44	Hydrogen Bond	Conventional Hydrogen Bond
Gln15:O* <sup>S</sup> -Glu :C	3.79	Hydrogen Bond	Carbon Hydrogen Bond
Phe19 - C-kd	5.21	Hydrophobic	$\pi$ -Alkyl
Phe20 - C-kd	4.25	Hydrophobic	$\pi$ -Alkyl
Intermolecular Interactions (I:IV, Binding Energy: -3.1 kcal/mole)			
Gln15:HN - N-kd:O	2.85	Hydrogen Bond	Conventional Hydrogen Bond
Gln15:O* <sup>S</sup> -Lys:H	1.99	Hydrogen Bond	Conventional Hydrogen Bond
Gln15:O* <sup>S</sup> -Leu:H	2.63	Hydrogen Bond	Conventional Hydrogen Bond
Leu17:C* <sup>S</sup> - Phe2	3.74	Hydrophobic	$\pi$ - $\sigma$
Lys16 - Phe1	4.92	Hydrophobic	$\pi$ -Alkyl
Intramolecular Interactions within IV			
Leu:N - Asp:O	3.20	Hydrogen Bond	Conventional Hydrogen Bond
Asp:N - Asp:O	3.17	Hydrogen Bond	Conventional Hydrogen Bond
Asp:OH- Glu:O	3.09	Hydrogen Bond	Conventional Hydrogen Bond

Asp:O - Lys:N	2.99	Hydrogen Bond	Conventional Hydrogen Bond
Glu:O - His:N	2.88	Hydrogen Bond	Conventional Hydrogen Bond
Lys:N - Lys:O	2.97	Hydrogen Bond	Conventional Hydrogen Bond
kd:O - Lys:N	3.08	Hydrogen Bond	Conventional Hydrogen Bond
kd:N - kd:O	3.11	Hydrogen Bond	Conventional Hydrogen Bond
His:N - Gln	3.91	Hydrogen Bond	$\pi$ -Donor Hydrogen Bond
Leu:C - Phe1	3.65	Hydrophobic	$\pi$ - $\sigma$
Intermolecular Interactions (I:V, Binding Energy: -4.9 kcal/mole)			
His14:H* <sup>S</sup> - Asp:O	1.83	Hydrogen Bond	Conventional Hydrogen Bond
Phe19:O - His:H	2.80	Hydrogen Bond	Conventional Hydrogen Bond
Asp23:O - Leu:H	2.81	Hydrogen Bond	Conventional Hydrogen Bond
Asp23:O* <sup>S</sup> - Val:H	2.78	Hydrogen Bond	Conventional Hydrogen Bond
Glu22:O - M-kd:H	2.13	Hydrogen Bond	Conventional Hydrogen Bond
Ala21:OH - M-kd:H	2.35	Hydrogen Bond	Conventional Hydrogen Bond
Asp23:O* <sup>S</sup> - N-kd:H	2.90	Hydrogen Bond	Conventional Hydrogen Bond
Asp23:C - M-kd:O	2.66	Hydrogen Bond	Carbon Hydrogen Bond
Glu22:O* <sup>S</sup> - Val:C	3.17	Hydrogen Bond	Carbon Hydrogen Bond
Ala21:O - Glu:C	3.08	Hydrogen Bond	Carbon Hydrogen Bond
Leu17 - Phe2	5.12	Hydrophobic	$\pi$ -Alkyl

Sidechain atoms (\*s) of I (left-side residues: I and right-side residues: II/III/IV/V)  
Phe1 = <sup>19</sup>Phe of the ligand (II-V), Phe2 = <sup>20</sup>Phe of the ligand (II-V)

The innocuous inhibitor V was found to exhibit significant stability against the enzymatic (trypsin) degradation and non-self-aggregation property as confirmed by time-dependent AFM studies (Figure 14 and Figure 15). It should be noted that IV exhibited self-aggregation property (ThT fluorescence studies, Figure 16a, b) which explain its aggregation-enhancing behavior towards I. Analyses of the experimental and theoretical results reveal that a single kd unit at the N-terminal (IV) is far away from the aggregation inducer region with FF, which explains the inability of IV to stop the self-aggregation of I, instead it serves as A $\beta$  aggregation enhancer through  $\beta$ -sheet structure (Figure 13). Interestingly, incorporation of kd units nearby FF (II, III and V) of I was found to effectively stabilize the A $\beta$  monomers through multiple hydrogen bonding and other noncovalent interactions (Figure 12d). The highest A $\beta$  aggregation-inhibition of V is not only

attributed to the presence of multiple kd units, but also their positions, especially at the middle and C-terminus (Table 1 and 2). The docked structures of A $\beta$ 42:V and I:V suggest that the binding sites of middle and C-terminal kd units are suitably positioned to provide maximum interaction around KLVFF to stabilize A $\beta$  monomer, while kd unit at N-terminal offer supporting interaction.

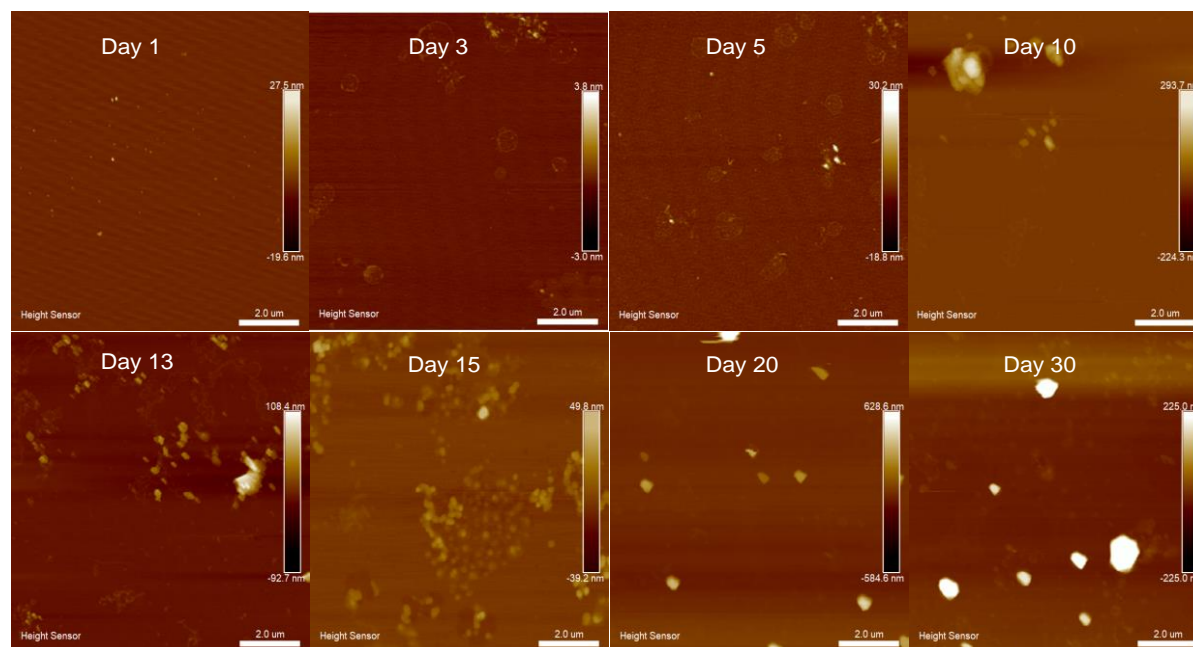


**Figure 14.** Time-dependent AFM images of V (5  $\mu$ M) incubated independently in PBS (10 mM) at pH 7.4 and 37  $^{\circ}$ C for 30 days. The prolonged time incubation of the peptidomimetics V with no aggregation species confirms its non-self-aggregating nature.

In summary, A $\beta$ 14-23 peptidomimetics incorporated with CDP units (kd) effectively combat amyloid-induced membrane toxicity, excessive ROS production and adverse cellular mechanics under stress conditions. Our study demonstrated that A $\beta$ 14-23 peptidomimetics with three kd units at N- and C-termini and middle (V) is a potent inhibitor of amyloid aggregation of both A $\beta$ 14-23 and A $\beta$ 42. In A $\beta$ 14-23, incorporation of kd units at the middle and C-terminal (II and III, respectively) proximal to FF region was found to impart effective aggregation-inhibition ability. While a single kd unit at N-terminal (IV) away from FF region turns out to be aggregation enhancer due to its self-aggregation behavior. The PF QNM-AFM study proved that the neuronal cells were



grown with healthy cell-stiffness and other features in the presence of V under amyloid-induced stress conditions.

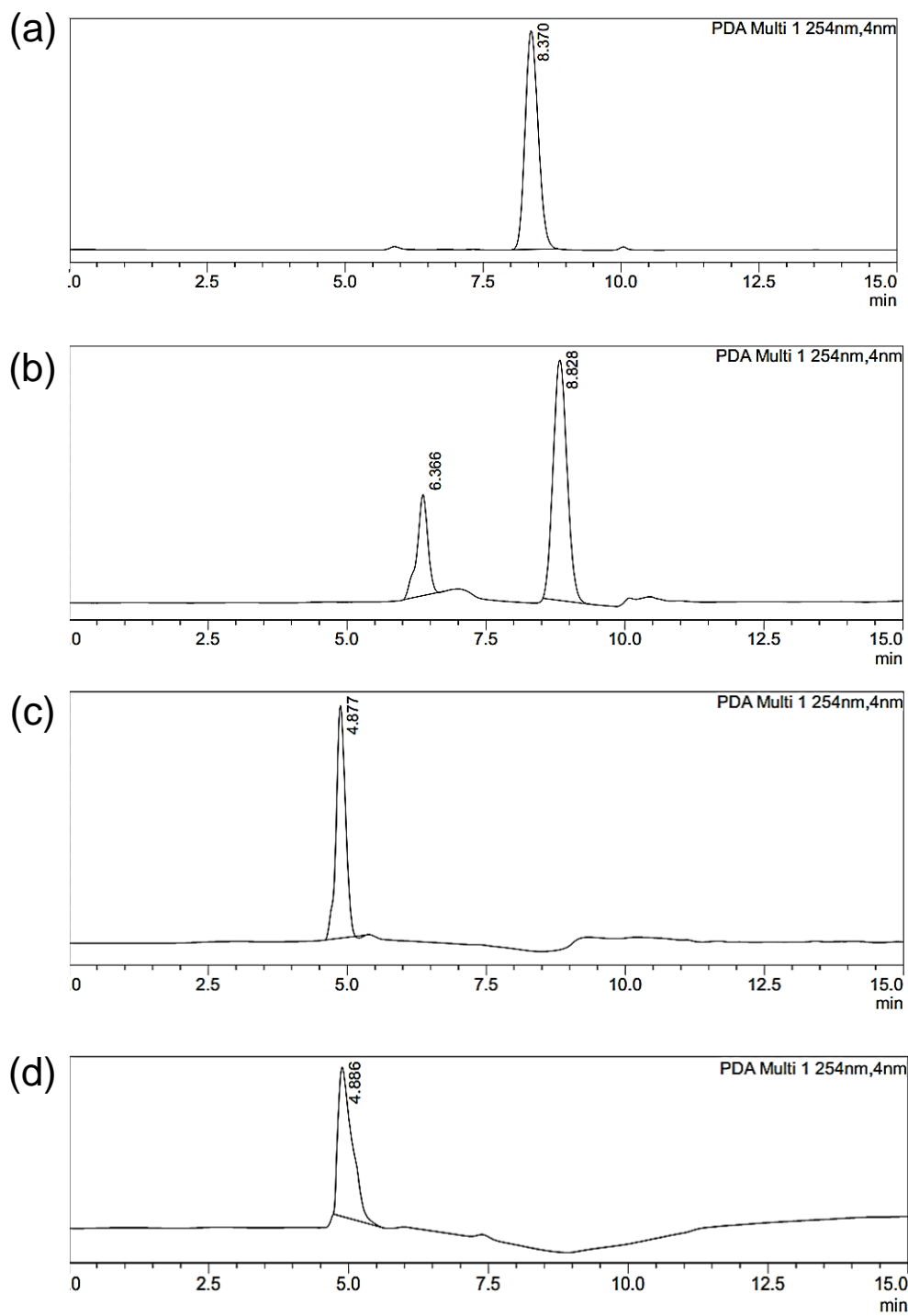


**Figure 15.** Stability of A $\beta$ 14-23 (100  $\mu$ M) and Akd<sup>NMC</sup> (100  $\mu$ M) against the enzymatic degradation (trypsin, 5  $\mu$ M). (a) and (b) Analytical HPLC data of A $\beta$ 14-23 before and after the incubation (24 h) with trypsin, respectively. (c) and (d) Analytical HPLC data of Akd<sup>NMC</sup> before and after the incubation (24 h) with trypsin, respectively. The chromatogram confirms that Akd<sup>NMC</sup> is stable against enzymatic degradation, which satisfies the design strategy.

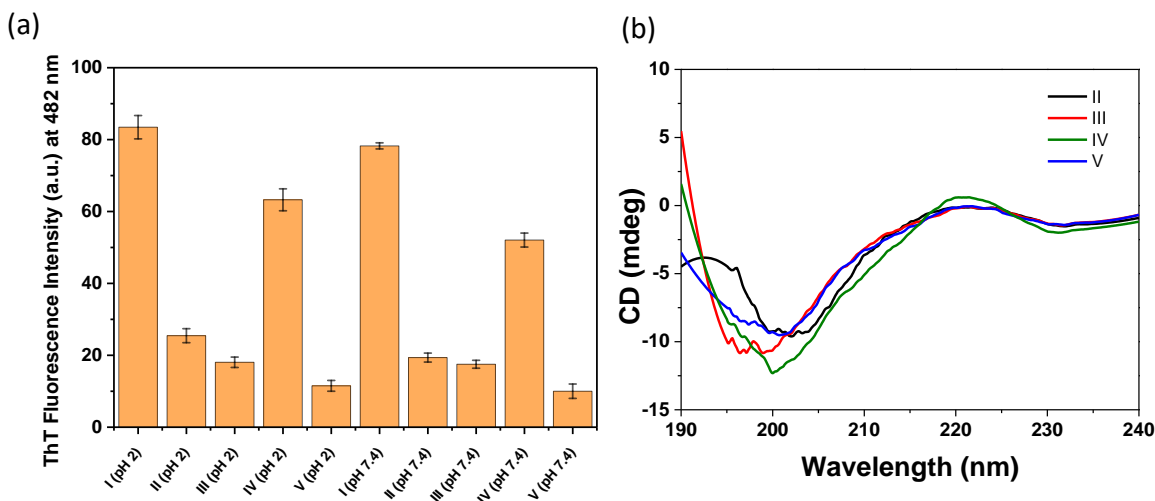


**Figure 16.** (a) ThT fluorescence assay of the individual peptide (I) and CDP-peptidomimetics (II-V) at pH 2.0 and 7.4 upon incubating the samples for 20 days and 37  $^{\circ}$ C temperature. ThT assay indicates self-aggregation potential of I and IV at both pH conditions, whereas the peptidomimetics II, III, V possess negligible self-aggregation properties as compared to I and IV. The higher self-aggregation propensity of IV could be the reason for the enhanced fibrillation of I in the presence of IV. (b) CD spectra of II-V peptidomimetics alone shows that II, III, V does not form any secondary conformation.

The biocompatibility, enzymatic stability and non-self-aggregating properties combined with effective modulation of A $\beta$  aggregation and ROS generation thus demonstrated V as the potential candidate to ameliorate amyloid induced toxicity and adverse cellular mechanics.

## 2.9 Experimental section

### 2.9.1 General methods

All solvents and reagents were obtained from Spectrochem or Merck and used without further purification unless mentioned. Dulbecco's Modified Eagle Medium/Nutrient Mixture F12 (DMEM F12), Roswell Park Memorial Institute (RPMI), fetal bovine serum (FBS) and Alamar blue was obtained from Invitrogen. Amyloid beta (A $\beta$ 42) peptide (PP69-

0.05 MG), anti-amyloid fibrils (OC) and fluorescently labelled secondary antibody were obtained from Merck. Thioflavin T (ThT) was obtained from Sigma-Aldrich (T3516) and DAPI (4',6-diamidino-2-phenylindole) from Vector Laboratories, CA, USA (H-1200). Agilent Cary eclipse fluorescence spectrophotometer and microplate reader (SpectraMax i3x) were used for fluorescence assays. A Bruker IFS 66/V spectrometer and JASCO-815 spectropolarimeter were employed to perform Fourier Transform Infrared (FTIR) and circular dichroism (CD) spectroscopy studies, respectively.  $^1\text{H}$  and  $^{13}\text{C}$  NMR spectra were recorded in Bruker AV-400 and JEOL-600 MHz spectrometers using tetramethylsilane (TMS) as internal standard. MALDI-TOF, HRMS, LCMS and HPLC spectra were acquired from Bruker Autoflex Speed MALDI-TOF spectrometer, Agilent 6538 UHD HRMS/Q-TOF high-resolution spectrometer, Shimadzu LCMS-2020 and SHIMADZU reverse phase HPLC (using C18 column), respectively. A mixture of acetonitrile and water was used as mobile phase in HPLC and the peptide or peptidomimetics were collected using PDA detector (absorbance at 254 nm). Confocal images were captured using confocal fluorescence microscope (Olympus FV3000). Calculated amount of A $\beta$ 14-23 (I), Akd<sup>M</sup> (II), Akd<sup>C</sup> (III), Akd<sup>N</sup> (IV), and Akd<sup>NMC</sup> (V) were dissolved in hexafluoroisopropanol (HFIP, 200  $\mu\text{L}$ ), followed by the removal of HFIP under nitrogen atmosphere, and dried under vacuum to obtain monomeric peptide/peptidomimetics samples. Glycine-HCl buffer (10 mM) and phosphate buffer saline (10 mM) prepared in water (passed through 0.22-micron filter, conductivity at 25  $^{\circ}\text{C}$  < 100  $\mu\text{S}/\text{cm}$ , Milli Q) were used for maintaining the solution pH at 2.0 and 7.4, respectively. The experimental raw data were processed using Origin 8.5, Prism 6 or ChemDraw professional 15.

### 2.9.2 Synthesis of A $\beta$ 14-23 (I) peptide and CDP-peptidomimetics (II-V)

The cyclic dipeptide (CDP) [cyclo(Lys-Asp)]-based unnatural amino acid (kd) was synthesized by 9-fluorenylmethoxycarbonyl (Fmoc)-deprotection of dipeptide Fmoc-Lys(Boc)-Asp(O $t$ Bu)-OMe followed by the cyclization and deprotection of Boc-protecting groups. A $\beta$ 14-23 (I) and kd-incorporated A $\beta$ 14-23 peptidomimetics Akd<sup>M</sup> (II), Akd<sup>C</sup> (III), Akd<sup>N</sup> (IV), Akd<sup>NMC</sup> (V) were synthesized following standard Fmoc solid phase peptide synthesis (SPPS) protocol. Fmoc-amino acids (H: Histidine, Q: Glutamine, K: Lysine, L: Leucine, V: Valine, F: Phenyl alanine, A: Alanine, E: Glutamic acid, and D: Aspartic acid) with  $t$ Boc and  $t$ But protection on the side chains of the respective -NH<sub>2</sub> and -COOH functionalities were used to synthesize the peptide or peptidomimetics. Rink amide resin (loading 0.76 mmol/gm) was employed as the solid support in SPPS. For the coupling of Fmoc-amino acids (2.5 eq.) and Fmoc-kd (2.5 eq.) in the desired peptide sequence, HBTU (2.5 eq.)-HOBt (2.5 eq.), DIPEA (4 eq.) and DMF were used as activating agent, base, and solvent, respectively. The completion of the coupling and Fmoc-deprotection of amino acids were confirmed by Kaiser test. After every coupling and deprotection step, resin was thoroughly washed with DMF and DCM. The synthesized peptide or peptidomimetics were cleaved from the resin using a cleavage-cocktail solution of TFA: TIPS: DCM (95:2.5:2.5) at room temperature and the product was collected through precipitation from cold diethyl ether. All the synthesized peptide or peptidomimetics were finally purified by reverse phase HPLC (C18 column) using acetonitrile: water system and the product purity and integrity were ascertained by analytical HPLC and HRMS. <sup>1</sup>H NMR (400 MHz, DMSO- $d_6$ )  $\delta$  (ppm): 1.30 (4H, m); 1.68 (2H, m); 2.61-2.63 (2H, m); 2.95-2.97 (2H, d,  $J = 8$  Hz); 3.88 (1H, s); 4.18-4.20 (2H, d,  $J = 8$  Hz); 4.22 (2H, s); 7.23-7.43 (9H, m); 8.0 (1H, s); 8.19 (1H, s). <sup>13</sup>C

NMR (100 MHz, DMSO-d<sub>6</sub>):  $\delta$  (ppm): 21.4, 29.2, 31.3, 36.5, 38.8, 40.1, 46.7, 50.9, 53.8, 65.2, 120.1, 125.1, 127.0, 127.5, 140.7, 143.9, 156.9, 167.5, 168.1, 171.3. HRMS (ESI-TOF) m/z: [M + H]<sup>+</sup> calculated for C<sub>25</sub>H<sub>28</sub>N<sub>3</sub>O<sub>6</sub>, 466.1978; observed 466.1970.

### 2.9.3 Circular Dichroism (CD) studies

The changes in secondary structural conformations of peptide I upon aggregation in the absence and presence of peptidomimetics (II-V) were monitored by CD spectroscopy. To record the CD spectra, peptide I (25  $\mu$ M) was incubated in the presence and absence of peptidomimetics (25  $\mu$ M) at 37 °C for 20 days at pH 2.0 (10 mM) and 7.4 (10 mM). A quartz cuvette of path length 0.1 cm was used, and the spectra were recorded in the wavelength range of 190 - 240 nm at 50 nm/min scan rate. For CD analyzes, the background correction was performed using the CD spectrum recorded in only PBS buffer.

### 2.9.4 Fourier-Transform Infrared Spectroscopy (FTIR) studies

For FTIR spectroscopy studies, aliquots (10  $\mu$ L) of peptide I (25  $\mu$ M) incubated with and without peptidomimetics (25  $\mu$ M) at 37 °C for 20 days at pH 2.0 (10 mM) and 7.4 (10 mM) were independently placed on clean dry coverslips to form thin film. The FTIR spectra of the dried thin film samples were recorded at room temperature in the spectral range of 4000 - 400 cm<sup>-1</sup> using FT-IR Spectrometer (Model: Bruker IFS 66/V spectrometer, Mode: ATR). A Dimond ATR was used for the acquisition of 100 spectra. A spectrum against air was used for the background correction of FTIR spectra.

### 2.9.5 Transmission electron microscopy (TEM) imaging

For TEM imaging, the pre-incubated A $\beta$ 14-23 samples (25  $\mu$ M) in the absence and presence of II-V (25  $\mu$ M) were diluted to 5  $\mu$ M and placed on a carbon-coated copper grid of 200 mesh size and negatively stained with 0.2 % uranyl acetate. Prior to imaging, the

sample-containing grids were washed twice with purified water (MiliQ) and dried in a desiccator under nitrogen atmosphere. Finally, the imaging was performed in JEOL JEM 3010 TEM.

### 2.9.6 Aggregation kinetics study using ThT fluorescence

The aggregation kinetics of peptide I (A $\beta$ 14-23) was studied in the presence and absence of peptidomimetics (II-V) using Thioflavin T (ThT) fluorescent dye ( $\lambda_{ex}$ = 442 nm and  $\lambda_{em}$ = 482 nm). The peptide I (25  $\mu$ M) alone and with peptidomimetics (25  $\mu$ M) was incubated with ThT (20  $\mu$ M) for 20 days at 37 °C in pH 2.0 (Glycine-HCl buffer, 10 mM) and pH 7.4 (PBS, 10 mM) under shaking conditions. ThT fluorescence was monitored in a time-dependent manner using microplate reader (SpectraMax i3x). The data were fitted to the following sigmoidal equation.<sup>48</sup>

$$y = y_0 + \frac{y_{max} - y_0}{1 + e^{-(t-t_{1/2})\kappa}}$$

Where,  $y$  denotes the fluorescence intensity at time  $t$ ,  $y_0$  and  $y_{max}$  indicate the initial and maximum fluorescence intensities, respectively,  $t_{1/2}$  is the time required for half maximum of the fluorescence intensity (halfway from nuclei to fibrils), and  $\kappa$  is the apparent first-order rate constant of aggregation. The lag time ( $T_{Lag}$ ) was determined by  $t_{1/2} - 2\kappa$ .

### 2.9.7 PF QNM-AFM imaging

The SH-SY5Y cells were cultured in glass bottom petri dishes (14026-20, TED PELLA, Inc.) using Dulbecco's modified eagle medium/nutrient mixture (DMEM/F-12) media supplemented with 10% fetal bovine serum (FBS) and 1% Penicillin-streptomycin (PS) in a humidified CO<sub>2</sub> (5%) incubator at 37 °C. The cells were treated with pre-incubated (48 h) A $\beta$ 42 (20  $\mu$ M) alone and with Akd<sup>NMC</sup> (20  $\mu$ M) for 24 h under cell growing conditions. Then the cells were washed with PBS (10 mM, pH 7.4) and fixed with 4%

---

---

paraformaldehyde (PFA) solution. The PeakForce Quantitative NanoMechanics-AFM (PF QNM-AFM) was used to acquire the AFM images of neuronal cells along with the nanoindentation parameter DMT modulus using Bruker BIOSCOPE Resolve AFM Instrument with PeakForce Tapping Technique. For fluid imaging, a non-conductive, backside reflective Au-coated silicon nitride (MCLT-BIO, force constant: 0.01 Nm<sup>-1</sup>) tip of length 0.55  $\mu$ m and resonance frequency 7 kHz was used. Finally, the images were processed using NanoScope analysis software 1.8 (Bruker, Inc.).

### **2.9.8 Neuronal rescue studies**

The ability of peptidomimetics (II-V) to rescue neuronal cells from amyloid-induced stress induced by A $\beta$ 14-23 (I) and A $\beta$ 42 was studied using Alamar blue assay in SH-SY5Y cell line. At first, the cells were cultured in 96-well plate (15,000 cells/well) using DMEM/F-12 medium (Gibco, Invitrogen) containing FBS (10%) and PS (1%). Then the cell media was replaced with low serum (2% FBS) containing DMEM/F-12 media. Next, the cells were treated (24 h) with the peptide I (10  $\mu$ M) and A $\beta$ 42 (10  $\mu$ M), which were preincubated (48 h) at pH 7.4 in the absence and presence of peptidomimetics (10  $\mu$ M). Finally, experimental cells were treated with Alamar blue solution for 2 h at 37 °C and the absorbance was measured at 570 nm using microplate reader. The data were plotted and analyzed using GraphPad prism software (one-way ANOVA).

### **2.9.9 Membrane toxicity**

To determine the modulation of A $\beta$ 42-induced plasma membrane toxicity by peptidomimetics, we performed immunocytochemistry in SH-SY5Y cell line. The cells were cultured in 35 mm confocal dish using DMEM/F-12 medium (Gibco, Invitrogen) containing FBS (10%) and PS (1%) and treated (3 h) with 10  $\mu$ M A $\beta$ 42 (fibrils) alone and

preincubated with Akd<sup>NMC</sup> (10  $\mu$ M). The cells were washed with PBS (10 mM, pH 7.4) and fixed with 4% PFA solution and the cells were again washed with PBS (3 time) and blocked using 5% bovine serum albumin (BSA). Next, the cells were treated with A $\beta$ 42 fibril-specific primary antibody OC (1:250) for 16 h at 4  $^{\circ}$ C followed by treatment of red fluorescent-labelled ( $\lambda_{\text{ex}}= 633$  nm and  $\lambda_{\text{em}}= 650$  nm) anti-mouse IgG secondary antibody (1:200). The excess antibody was washed using PBS and the cell nuclei were stained with DAPI for the confocal imaging. The images were acquired using OLYMPUS FLUOVIEW FV3000 confocal microscope and analyze using cellSens software.

### 2.9.10 Docking studies

Molecular docking studies were performed using AutoDock Vina software (Version: 1.1.2).<sup>49</sup> The crystal structure of A $\beta$ 42 peptide (PDB ID: 1Z0Q, protein) was retrieved from RCSB Protein Data Bank and a full chain of A $\beta$ peptide (1-42) was selected for the docking. The PDB structure of A $\beta$ 14-23 (I, protein) was created from A $\beta$ 42 using AutoDock tools. The PDB structure of Akd<sup>NMC</sup> (V, ligand) was created and optimized through energy minimization in Avogadro software applying the MMFF94 force field. Gasteiger partial charges and polar hydrogen were added using AutoDock tools. For the I:V and A $\beta$ 42:V docking experiments, the entire protein domains (I and A $\beta$ 42) were covered with the grid box of dimensions 48 $\text{\AA}$  X 46 $\text{\AA}$  X 34  $\text{\AA}$  and 126 $\text{\AA}$  X 62 $\text{\AA}$  X 58 $\text{\AA}$ , respectively. The total number of run involved in the docking experiment was determined by the exhaustiveness parameter which was set to a maximum value of 8 on the scale of 1–8, while keeping all other parameters as default.<sup>50</sup> After the completion of docking runs (I:V and A $\beta$ 42:V), the energy minimized docked poses were viewed and analyzed using *PyMOL* software.



### 2.9.11 AFM imaging of A $\beta$ -aggregates using PF QNM-AFM

The PF QNM-AFM study was performed to visualize the aggregation species of A $\beta$ 14-23 (I) or A $\beta$ 42 in the absence and presence of peptidomimetics. For the experiment, we have diluted the pre-incubated stock solutions of peptides (25  $\mu$ M, I, I+II, I+III, I+IV, I+V, A $\beta$ 42, A $\beta$ 42+V) to a concentration of 5  $\mu$ M and placed on freshly cleaved mica foils to dry them at room temperature. The AFM images were acquired in Bruker BIOSCOPE Resolve with PeakForce Tapping AFM instrument. A silicon nitride tip (SCANASYST-ATR, force constant: 21-98  $\text{Nm}^{-1}$ ) of length 115  $\mu$ m and resonance frequency 146-236 kHz was used. The AFM images were processed and analyzed using NanoScope 1.8 analysis software (Bruker, Inc.).

### 2.9.12 Cytotoxicity assay

The cytotoxicity of peptidomimetics was determined using Alamar blue assay in *SH-SY5Y* cell line. At first, the cells were cultured in 96-well plate (15,000 cells/well) using DMEM/F-12 medium (Gibco, Invitrogen) containing FBS (10%) and PS (1%). Then the cell media was replaced with low serum (2% FBS) containing DMEM/F-12 media. Next, the cells were exposed to the peptidomimetics (10  $\mu$ M), which were preincubated (24 h, 37  $^{\circ}$ C) at pH 7.4 for 24 h in the cell growing conditions. Finally, experimental cells were treated with Alamar blue solution for 2 h at 37  $^{\circ}$ C and the absorbance was measured at 570 nm using microplate reader. The data were plotted and analyzed using GraphPad prism software (One way ANOVA).

### 2.9.13 Live-dead assay

The well plates were seeded with the *SH-SY5Y* cells. The seeded cells were independently treated with A $\beta$ 42 (10  $\mu$ M) and A $\beta$ 42+V (1:1) solutions. Cells treated with 0.1% Triton-X

and untreated cells were considered as positive and negative controls, respectively. After a single wash with 1X PBS, the untreated and treated cells were stained with of calcein-AM (2 $\mu$ M) and propidium iodide (4.5  $\mu$ M) in a 5 percent CO<sub>2</sub> environment for 15 min at 37 °C. The excess dyes were removed by washing the cells in 1X PBS, and images were acquired using a Leica DM2500 fluorescence microscope using 20X objective. A band-pass filter for calcein-AM (at 500-550 nm) and a long-pass filter for propidium iodide (at 590-800 nm) were used for imaging.

#### **2.9.14 Intracellular ROS Measurement**

The *SH-SY5Y* cells were seeded at a density of 12,000 cells/well in a 96-well plate in DMEM/F-12 medium (Gibco, Invitrogen) with foetal bovine serum (FBS; 10%), horse serum (HS; 5%), and pen-strep (1 percent; Genetix) at 37°C in a CO<sub>2</sub> atmosphere of 5% to assess the effects of peptidomimetics (V) on ROS generated by A $\beta$ 42-Cu<sup>II</sup> using 2,7-dichlorodihydrofluorescein diacetate (DCFDA; Invitrogen). The cells were grown for 18 h, the media was changed to low serum DMEM, followed by further incubation of 6 h. The cells were then rinsed in PBS and treated with DCFDA dissolved in DMEM medium for 30 min. The cells were washed and treated with A $\beta$ 42 peptide (10  $\mu$ M), Cu<sup>2+</sup> (10  $\mu$ M), and ascorbate (300  $\mu$ M) in absence and presence of 10  $\mu$ M of peptidomimetics V for 6 h at 37°C. For metal independent assay, cells were independently treated with exogenous H<sub>2</sub>O<sub>2</sub> (100  $\mu$ M) and H<sub>2</sub>O<sub>2</sub>+V (1:1). The cells were rinsed in PBS, and the DCF fluorescence intensity was assessed using excitation and emission wavelengths of 495 and 529 nm, respectively (significance was determined using GraphPad prism's one-way ANOVA).

### **2.9.15 Enzymatic stability assay**

The enzymatic stability of A $\beta$ 14-23 and Akd<sup>NMC</sup> was preformed against trypsin. A $\beta$ 14-23 (100  $\mu$ M) and Akd<sup>NMC</sup> (100  $\mu$ M) were independently incubated with 5  $\mu$ M trypsin in tris-HCl (10 mM, pH 8) buffer at 37 °C under shaking conditions. After 24 h, the reaction was halted with 0.05% formic acid. The amount of intact peptide/peptidomimetics was analyzed using analytical HPLC (SHIMADZU LCMS-2020).

### **2.9.16 NMR spectroscopy protocol for A $\beta$ 14-23**

NMR experiments for determination of aggregate characteristics of A $\beta$ 14-23 fibrill, were performed in JEOL 600 MHz NMR spectrometer (12,000 scan). Samples containing 100  $\mu$ M of A $\beta$ 14-23 was prepared in PBS (10 mM, pH 7.4) containing 5% DMSO d6. The possibility of rapid proton exchange at low pH prompted us to consider DMSO d6 over D<sub>2</sub>O. For the inhibition study by Akd<sup>NMC</sup> we incubated sample A $\beta$ 14-23 with Akd<sup>NMC</sup> (1:1) for 48 h.

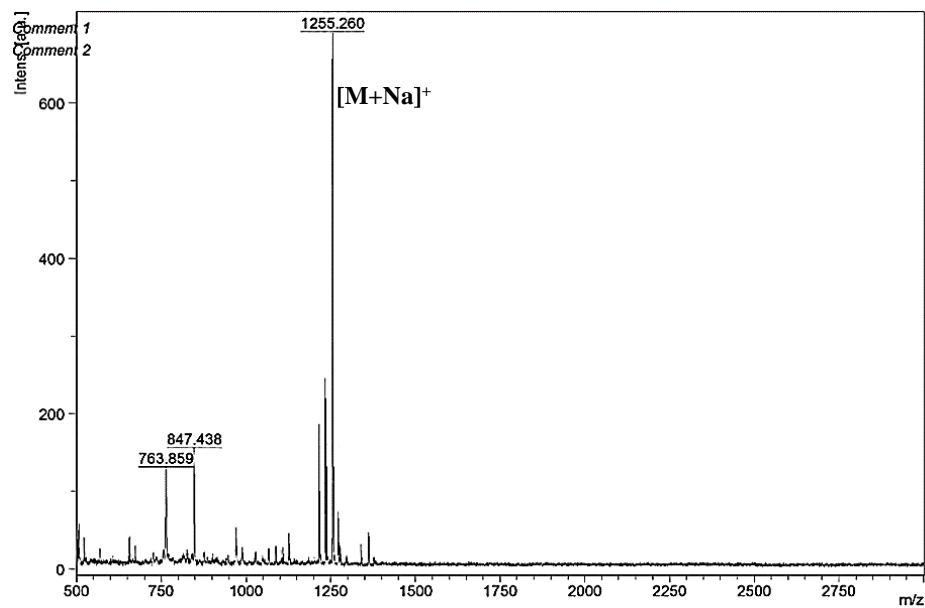
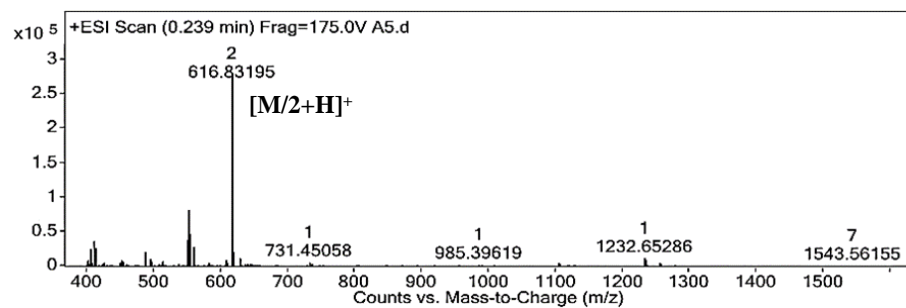
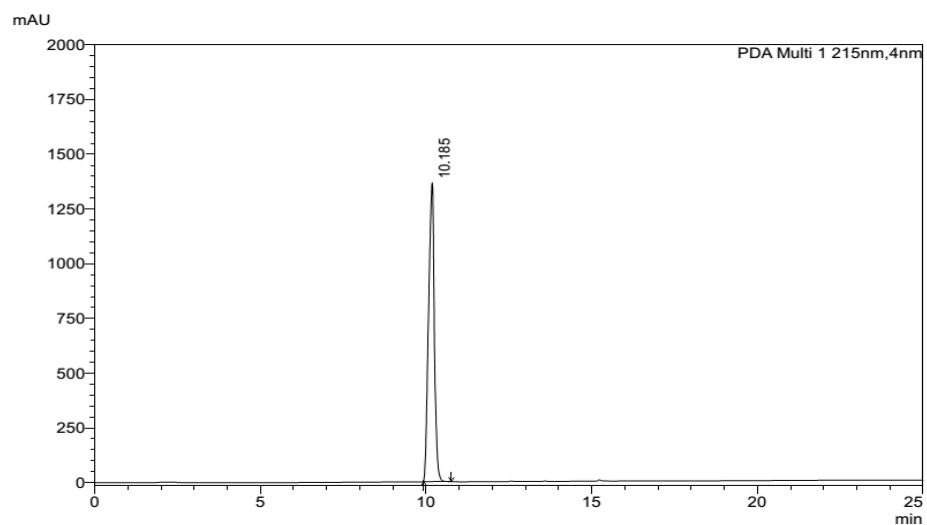
2.9.16 Characterizations of kd, A $\beta$ 14-23 (I) and peptidomimetics (II-V)

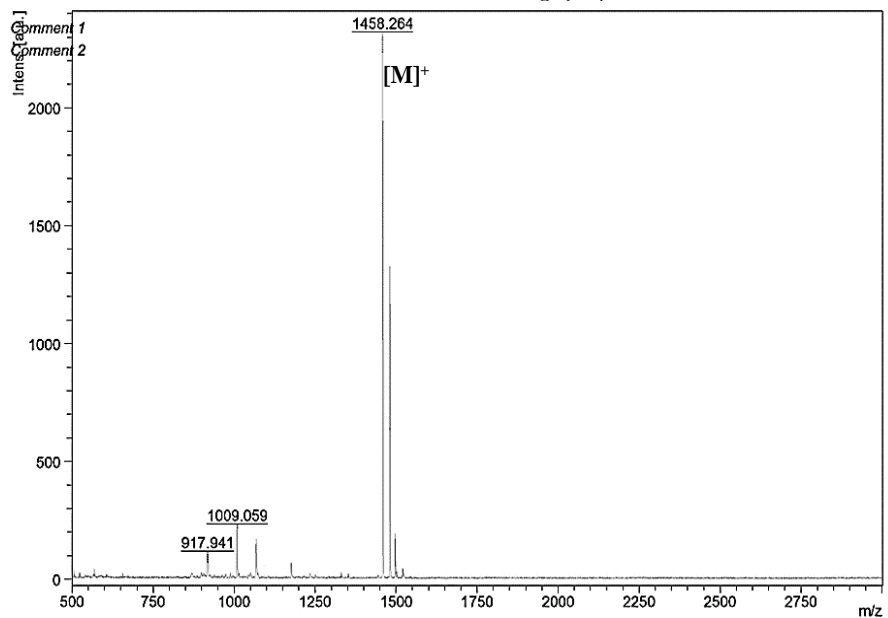
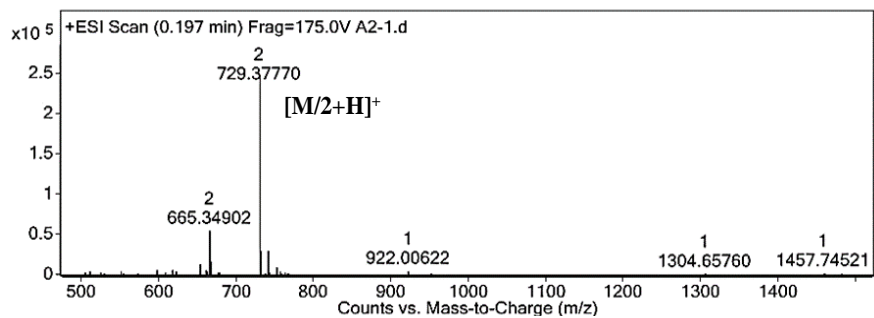
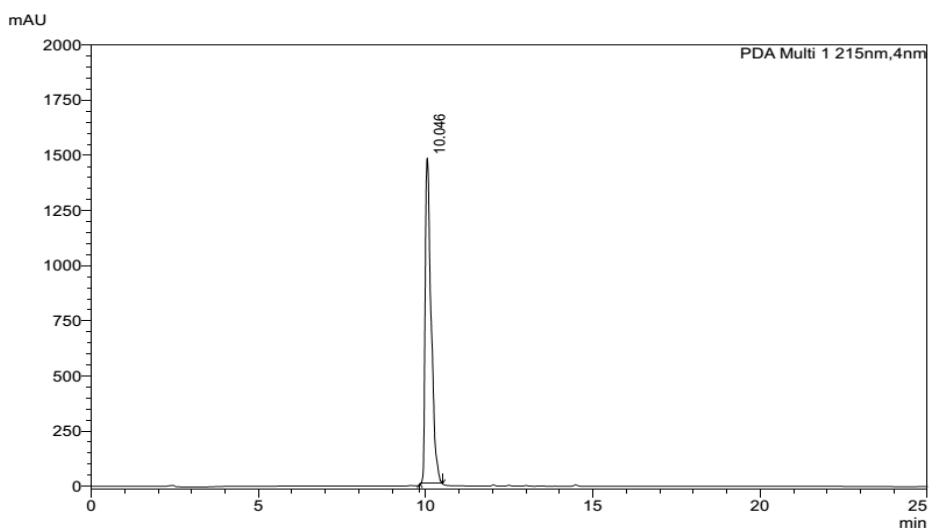
Table 3. HRMS and MALDI mass analysis.

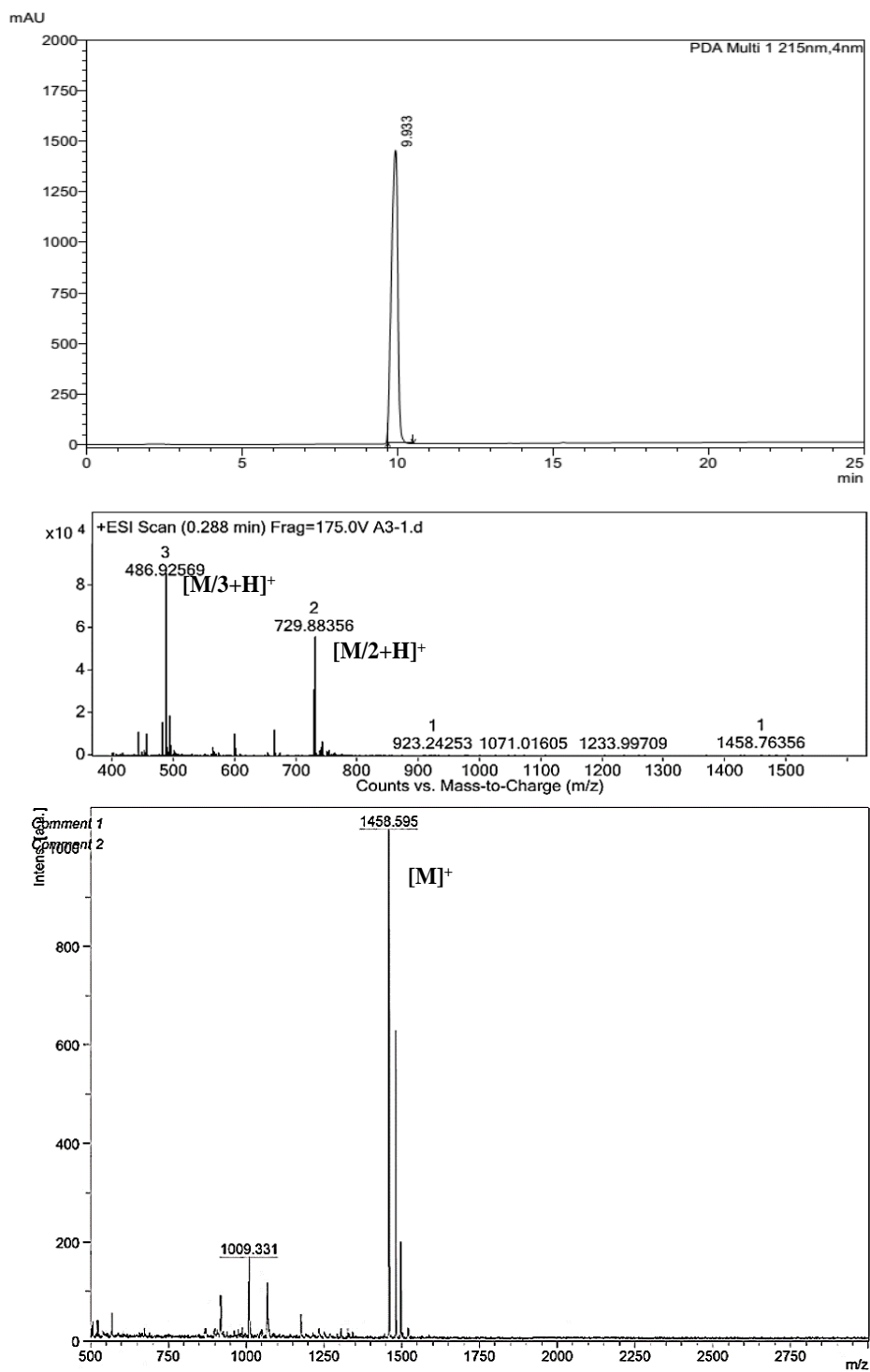
Name	Sequence	Calculated exact mass	Observed mass	
			HRMS	MALDI
Fmoc-kd	Fmoc-cyclo(Asp-Lys)	465.1900	466.1790 [M+H] <sup>+</sup>	-
I	His-Gln-Lys-Leu-Val-Phe-Phe-Ala-Glu-Asp	1231.6350	616.8319 [M/2+H] <sup>+</sup>	1255.26 [M+Na] <sup>+</sup>
II	His-Gln-Lys-Leu-Val- <u>kd</u> -Phe-Phe-Ala-Glu-Asp	1456.7463	729.3777 [M/2+H] <sup>+</sup>	1458.26 [M] <sup>+</sup>
III	His-Gln-Lys-Leu-Val-Phe-Phe-Ala-Glu-Asp- <u>kd</u>	1456.7463	729.8835 [M/2+H] <sup>+</sup> 486.9256 [M/3+H] <sup>+</sup>	1458.59 [M] <sup>+</sup>
IV	<u>kd</u> -His-Gln-Lys-Leu-Val-Phe-Phe-Ala-Glu-Asp	1456.7463	729.3808 [M/2+H] <sup>+</sup> 486.5907 [M/3+H] <sup>+</sup>	1457.86 [M] <sup>+</sup>
V	<u>kd</u> - His-Gln-Lys-Leu-Val- <u>kd</u> -Phe-Phe-Ala-Glu-Asp- <u>kd</u>	1906.9690	954.9907 [M/2+H] <sup>+</sup>	1909.09 [M+H] <sup>+</sup>

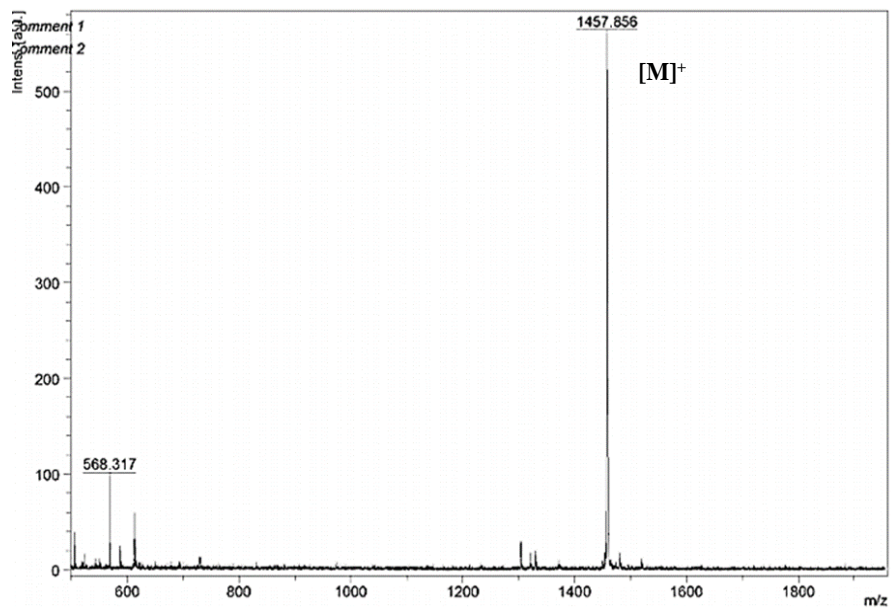
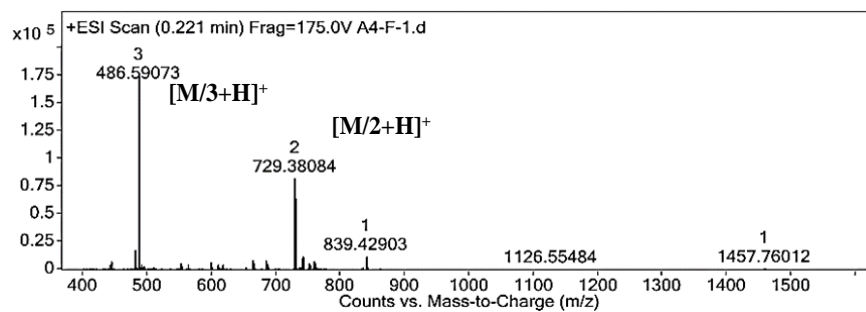
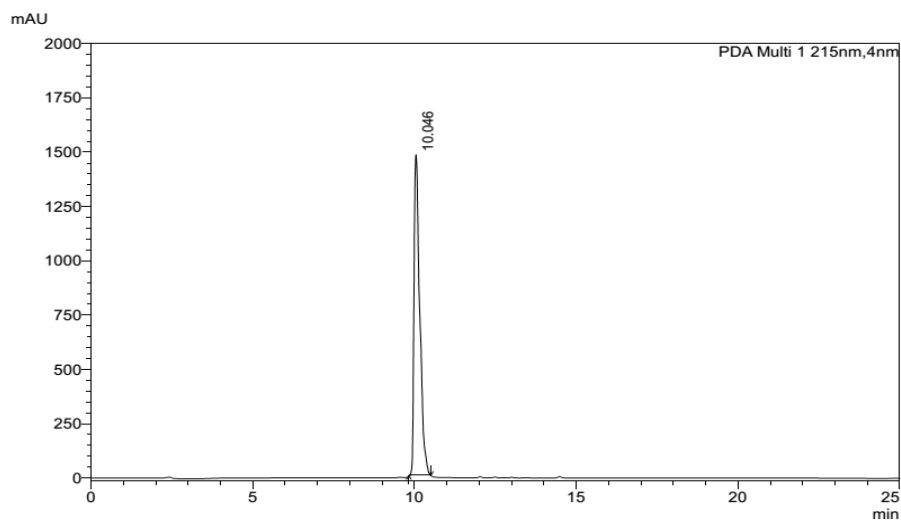
Table 4 Purification (HPLC) of A $\beta$ 14-23 (I) and peptidomimetics (II-V)

Samples	Gradient of the mobile phase	Flow rate (ml/min)	Retention time (min)	Purity (%)
I	5-95% MeCN (0.1% TFA) in H <sub>2</sub> O (0.1% TFA) for 25 min	8	10.18	>99
II	5-95% MeCN (0.1% TFA) in H <sub>2</sub> O (0.1% TFA) for 25 min	8	10.04	>99
III	5-95% MeCN (0.1% TFA) in H <sub>2</sub> O (0.1% TFA) for 25 min	8	9.93	>99
IV	5-95% MeCN (0.1% TFA) in H <sub>2</sub> O (0.1% TFA) for 25 min	8	10.04	>99
V	5-95% MeCN (0.1% TFA) in H <sub>2</sub> O (0.1% TFA) for 25 min	8	10.27	>99

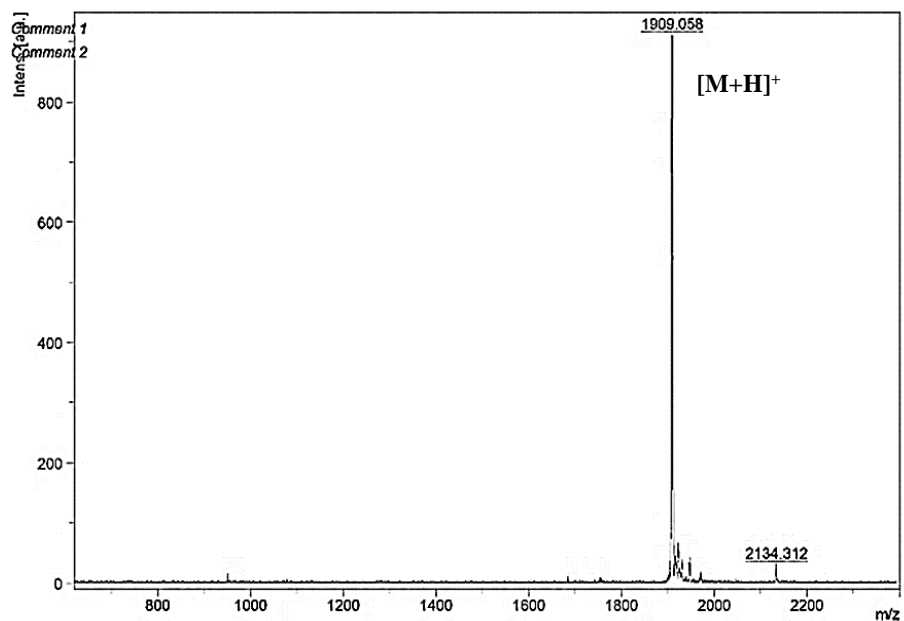
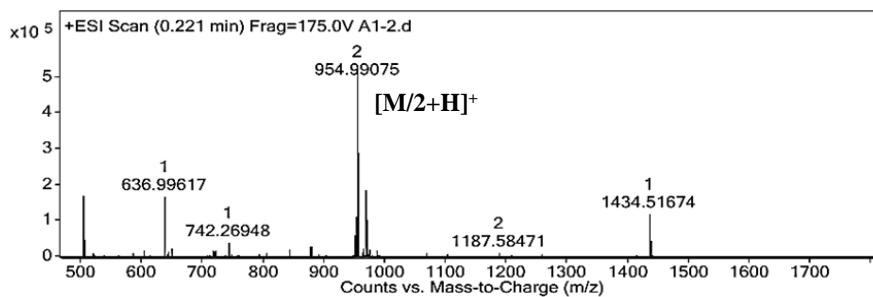
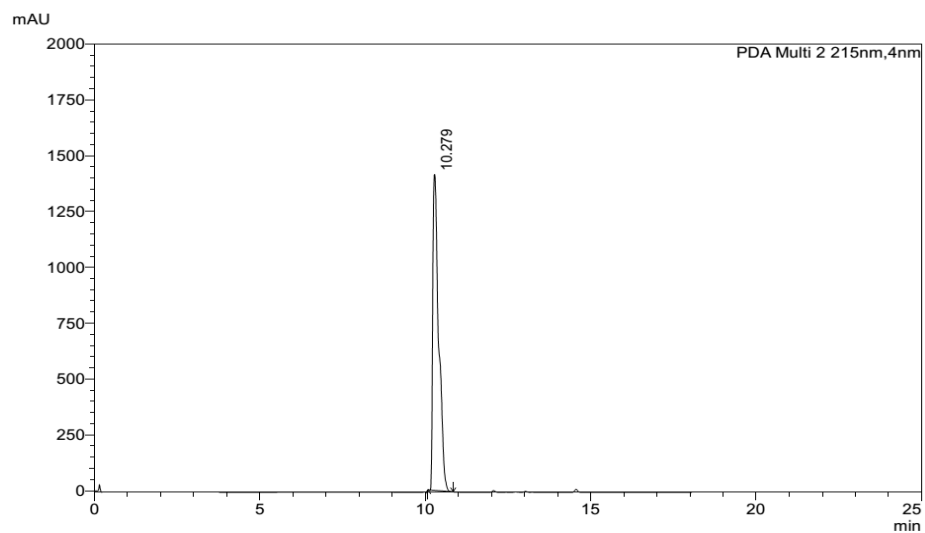
HPLC chromatogram, HRMS and MALDI mass of A $\beta$ 14-23 (I)

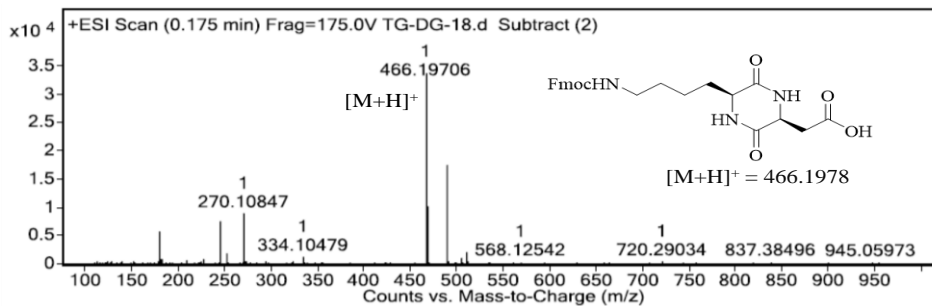
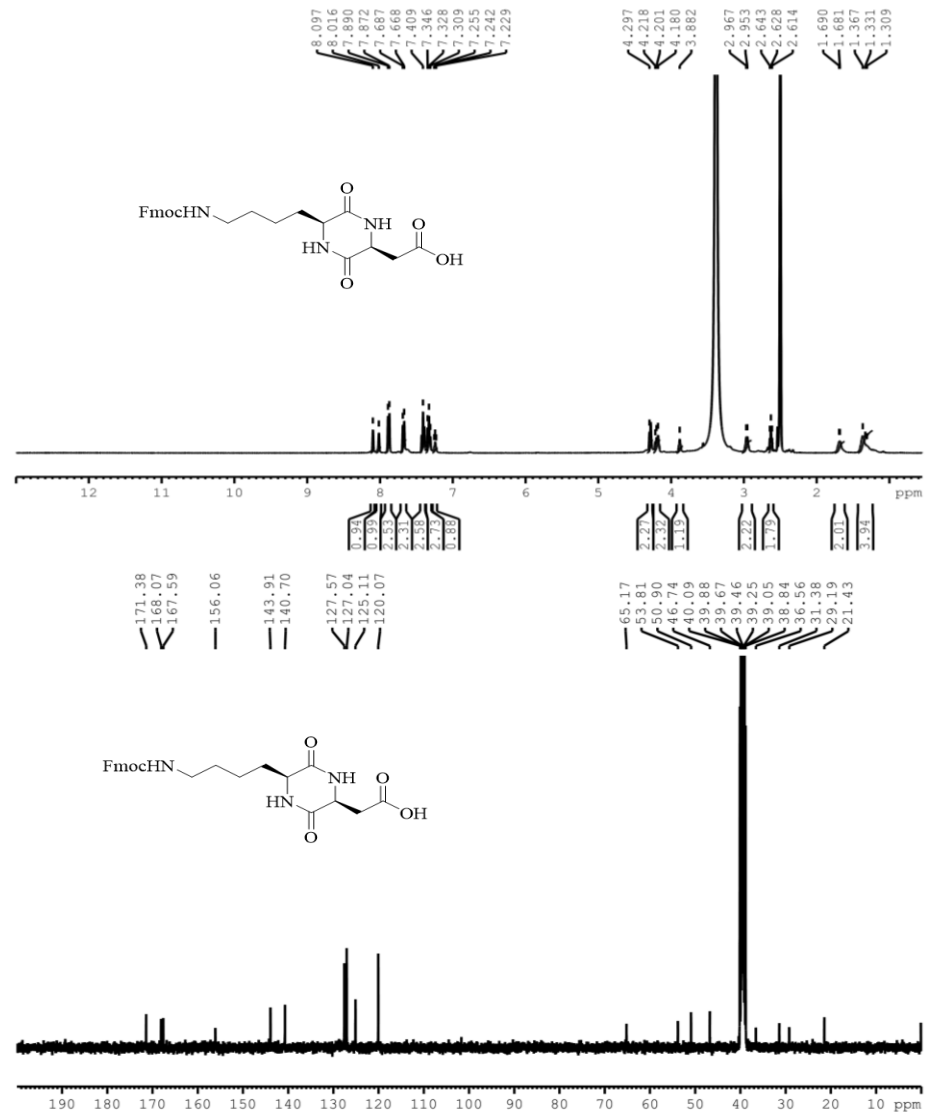
HPLC chromatogram, HRMS, and MALDI mass of Akd<sup>M</sup> (II)

HPLC chromatogram, HRMS and MALDI mass of Akd<sup>C</sup> (III)

HPLC chromatogram, HRMS and MALDI mass of Akd<sup>N</sup> (IV)



HPLC chromatogram, HRMS and MALDI mass of Akd<sup>NMC</sup> (V)

**<sup>1</sup>H and <sup>13</sup>C NMR and HRMS data of Fmoc-kd**

## Statistical analysis of Figure 12b

1way ANOVA						
1	Table Analyzed	Data 2				
2						
3	One-way analysis of variance					
4	P value	P<0.0001				
5	P value summary	***				
6	Are means signif. different? (P < 0.05)	Yes				
7	Number of groups	3				
8	F	120.4				
9	R squared	0.9678				
10						
11	ANOVA Table	SS	df	MS		
12	Treatment (between columns)	42.67	2	21.34		
13	Residual (within columns)	1.417	8	0.1772		
14	Total	44.09	10			
15						
16	Tukey's Multiple Comparison Test	Mean Diff.	q	Significant? P < 0.05?	Summary	95% CI of diff
17	Ctrl SH-SY5Y vs A $\beta$ 42 + SH-SY5Y	3.780	17.96	Yes	***	2.930 to 4.630
18	Ctrl SH-SY5Y vs A $\beta$ 42 + SH-SY5Y + V	-0.6517	2.867	No	ns	-1.570 to 0.2670
19	A $\beta$ 42 + SH-SY5Y vs A $\beta$ 42 + SH-SY5Y + V	-4.432	19.49	Yes	***	-5.350 to -3.513

## Statistical analysis of Figure 12c

1way ANOVA						
1	Table Analyzed	Data 3				
2						
3	One-way analysis of variance					
4	P value	P<0.0001				
5	P value summary	***				
6	Are means signif. different? (P < 0.05)	Yes				
7	Number of groups	3				
8	F	106.0				
9	R squared	0.9593				
10						
11	ANOVA Table	SS	df	MS		
12	Treatment (between columns)	0.4617	2	0.2309		
13	Residual (within columns)	0.01960	9	0.002178		
14	Total	0.4813	11			
15						
16	Tukey's Multiple Comparison Test	Mean Diff.	q	Significant? P < 0.05?	Summary	95% CI of diff
17	Ctrl SH-SY5Y vs A $\beta$ 42 + SH-SY5Y	-0.4158	17.82	Yes	***	-0.5079 to -0.3236
18	Ctrl SH-SY5Y vs A $\beta$ 42 + SH-SY5Y + V	0.0007250	0.03107	No	ns	-0.09141 to 0.09286
19	A $\beta$ 42 + SH-SY5Y vs A $\beta$ 42 + SH-SY5Y + V	0.4165	17.85	Yes	***	0.3243 to 0.5086

Statistical analysis of Figure 9c, d

1 way ANOVA						
2						
3	One-way analysis of variance					
4	P value	P<0.0001				
5	P value summary	***				
6	Are means signif. different? (P < 0.05)	Yes				
7	Number of groups	6				
8	F	31.90				
9	R squared	0.9410				
10						
11	ANOVA Table	SS	df	MS		
12	Treatment (between columns)	17530	5	3505		
13	Residual (within columns)	1099	10	109.9		
14	Total	18630	15			
15						
16	Tukey's Multiple Comparison Test	Mean Diff.	q	Significant? P < 0.05?	Summary	95% CI of diff
17	ctrl (PBS) vs Aβ42+Cu <sup>II</sup> +Asc	-78.52	11.60	Yes	***	-111.8 to -45.28
18	ctrl (PBS) vs Aβ42+Cu <sup>II</sup> +Asc+V	-16.02	2.367	No	ns	-49.25 to 17.22
19	ctrl (PBS) vs ctrl (PBS)	-9.074	1.224	No	ns	-45.48 to 27.33
20	ctrl (PBS) vs H <sub>2</sub> O <sub>2</sub>	-78.52	11.60	Yes	***	-111.8 to -45.28
21	ctrl (PBS) vs H <sub>2</sub> O <sub>2</sub> +V	-14.10	2.083	No	ns	-47.33 to 19.14
22	Aβ42+Cu <sup>II</sup> +Asc vs Aβ42+Cu <sup>II</sup> +Asc+V	62.50	10.33	Yes	***	32.78 to 92.23
23	Aβ42+Cu <sup>II</sup> +Asc vs ctrl (PBS)	69.45	10.26	Yes	***	38.21 to 102.7
24	Aβ42+Cu <sup>II</sup> +Asc vs H <sub>2</sub> O <sub>2</sub>	-0.00002289	0.000003782	No	ns	-29.73 to 29.73
25	Aβ42+Cu <sup>II</sup> +Asc vs H <sub>2</sub> O <sub>2</sub> +V	64.42	10.65	Yes	***	34.70 to 94.15
26	Aβ42+Cu <sup>II</sup> +Asc+V vs ctrl (PBS)	6.942	1.026	No	ns	-26.29 to 40.18
27	Aβ42+Cu <sup>II</sup> +Asc+V vs H <sub>2</sub> O <sub>2</sub>	-62.50	10.33	Yes	***	-92.23 to -32.78
28	Aβ42+Cu <sup>II</sup> +Asc+V vs H <sub>2</sub> O <sub>2</sub> +V	1.920	0.3173	No	ns	-27.81 to 31.65
29	ctrl (PBS) vs H <sub>2</sub> O <sub>2</sub>	-89.45	10.26	Yes	***	-102.7 to -36.21
30	ctrl (PBS) vs H <sub>2</sub> O <sub>2</sub> +V	-5.021	0.7421	No	ns	-38.26 to 28.21
31	H <sub>2</sub> O <sub>2</sub> vs H <sub>2</sub> O <sub>2</sub> +V	64.42	10.65	Yes	***	34.70 to 94.15

## 2.10 References

1. 2021 Alzheimer's disease facts and figures. *Alzheimer's Dement.* **2021**, *17*, 327-406.
2. Selkoe, D. J.; Hardy, J., The amyloid hypothesis of Alzheimer's Disease at 25 years. *EMBO Mol. Med.* **2016**, *8*, 595-608.
3. Knowles, T. P. J.; Vendruscolo, M.; Dobson, C. M., The amyloid state and its association with protein misfolding diseases. *Nat. Rev. Mol. Cell Biol.* **2014**, *15*, 384-396.
4. Rajasekhar, K.; Chakrabarti, M.; Govindaraju, T., Function and toxicity of amyloid  $\beta$  and recent therapeutic interventions targeting amyloid  $\beta$  in Alzheimer's disease. *Chem. Commun.* **2015**, *51*, 13434-13450.
5. Kreuzer, A. G.; Nowick, J. S., Elucidating the structures of amyloid oligomers with macrocyclic  $\beta$ -hairpin peptides: insights into Alzheimer's disease and other amyloid diseases. *Acc. Chem. Res.* **2018**, *51*, 706-718.
6. Nguyen, P. H., et al., Amyloid oligomers: a joint experimental/computational perspective on Alzheimer's disease, parkinson's disease, Type II diabetes, and amyotrophic lateral sclerosis. *Chem. Rev.* **2021**, *121*, 2545-2647.
7. Cheignon, C.; Tomas, M.; Bonnefont-Rousselot, D.; Faller, P.; Hureau, C.; Collin, F., Oxidative stress and the amyloid beta peptide in Alzheimer's disease. *Redox Biol.* **2018**, *14*, 450-464.
8. Fletcher, D. A.; Mullins, R. D., Cell mechanics and the cytoskeleton. *Nature* **2010**, *463*, 485-92
9. Lulevich, V.; Zimmer, C. C.; Hong, H. s.; Jin, L. w.; Liu, G. y., Single-cell mechanics provides a sensitive and quantitative means for probing A $\beta$  peptide and neuronal cell interactions. *Proc. Natl. Acad. Sci.* **2010**, *107*, 13872-13877.
10. Gao, Q.; Fang, Y.; Zhang, S.; Wong, H. S. H.; Chan, Y. E.; Wong, S. S. M.; Yung, K. K. L.; Lai, K. W. C., Dynamic effect of  $\beta$ -amyloid 42 on cell Mechanics. *J. Biomech.* **2019**, *86*, 79-88.

11. Fang, Y.; Iu, C. Y. Y.; Lui, C. N. P.; Zou, Y.; Fung, C. K. M.; Li, H. W.; Xi, N.; Yung, K. K. L.; Lai, K. W. C., Investigating dynamic structural and mechanical changes of neuroblastoma cells associated with glutamate-mediated neurodegeneration. *Sci Rep* **2014**, *4*, 7074.
12. Luo, Q.; Kuang, D.; Zhang, B.; Song, G., Cell stiffness determined by atomic force microscopy and its correlation with cell motility. *Biochim. Biophys. Acta, Gen. Subj.* **2016**, *1860*, 1953-1960.
13. Kruger, T. M.; Bell, K. J.; Lansakara, T. I.; Tivanski, A. V.; Doorn, J. A.; Stevens, L. L., Reduced extracellular matrix stiffness prompts Sh-Sy5y cell softening and actin turnover to selectively increase A $\beta$  (1–42) Endocytosis. *ACS Chem. Neurosci.* **2019**, *10*, 1284-1293.
14. Wang, X.; Bleher, R.; Brown, M. E.; Garcia, J. G. N.; Dudek, S. M.; Shekhawat, G. S.; Dravid, V. P., Nano-biomechanical study of spatio-temporal cytoskeleton rearrangements that determine subcellular mechanical properties and endothelial permeability. *Sci Rep* **2015**, *5*, 11097.
15. Corvaglia, S.; Sanavio, B.; Hong Enriquez, R. P.; Sorce, B.; Bosco, A.; Scaini, D.; Sabella, S.; Pompa, P. P.; Scoles, G.; Casalis, L., Atomic force microscopy based nanoassay: a new method to study  $\alpha$ -synuclein-dopamine bioaffinity interactions. *Sci Rep* **2014**, *4*, 5366.
16. Viji Babu, P. K.; Rianna, C.; Mirastschijski, U.; Radmacher, M., Nano-mechanical mapping of interdependent cell and ecm Mechanics by afm force spectroscopy. *Sci Rep* **2019**, *9*, 12317.
17. Hu, J.; Chen, S.; Huang, D.; Zhang, Y.; Lü, S.; Long, M., Global mapping of live cell mechanical features using peakforce Qnm Afm. *Biophys. Rep.* **2020**, *6*, 9-18.
18. Rajasekhar, K.; Samanta, S.; Bagoband, V.; Murugan, N. A.; Govindaraju, T., Antioxidant berberine-derivative inhibits multifaceted amyloid toxicity. *iScience* **2020**, *23*, 101005.
19. Samanta, S.; Rajasekhar, K.; Ramesh, M.; Murugan, N. A.; Alam, S.; Shah, D.; Clement, J. P.; Govindaraju, T., Naphthalene monoimide derivative ameliorates amyloid burden and cognitive decline in a transgenic mouse model of Alzheimer's disease. *Adv. Ther.* **2021**, *4*, 2000225
20. Yao, J.; Gao, X.; Sun, W.; Yao, T.; Shi, S.; Ji, L., Molecular hairpin: a possible model for inhibition of tau aggregation by tannic acid. *Biochemistry* **2013**, *52*, 1893-1902.

21. Doig, A. J.; del Castillo-Frias, M. P.; Berthoumieu, O.; Tarus, B.; Nasica-Labouze, J.; Sterpone, F.; Nguyen, P. H.; Hooper, N. M.; Faller, P.; Derreumaux, P., Why is research on amyloid- $\beta$  failing to give new drugs for Alzheimer's disease? *ACS Chem. Neurosci.* **2017**, *8*, 1435
22. Soto, C.; Sigurdsson, E. M.; Morelli, L.; Asok Kumar, R.; Castaño, E. M.; Frangione, B.,  $\beta$ -sheet breaker peptides inhibit fibrillogenesis in a rat brain model of amyloidosis: implications for Alzheimer's therapy. *Nat. Med.* **1998**, *4*, 822-826.
23. Maity, D.; Howarth, M.; Vogel, M. C.; Magzoub, M.; Hamilton, A. D., Peptidomimetic-based vesicles inhibit amyloid- $\beta$  fibrillation and attenuate cytotoxicity. *J. Am. Chem. Soc.* **2021**, *143*, 3086-3093.
24. Samanta, S.; Rajasekhar, K.; Babagond, V.; Govindaraju, T., Small molecule inhibits metal-dependent and -independent multifaceted toxicity of Alzheimer's disease. *ACS Chem. Neurosci.* **2019**, *10*, 3611-3621.
25. Dai, B., et al., Tunable assembly of amyloid-forming peptides into nanosheets as a retrovirus carrier. *Proc. Natl. Acad. Sci.* **2015**, *112*, 2996-3001.
26. Frydman-Marom, A.; Shaltiel-Karyo, R.; Moshe, S.; Gazit, E., The generic amyloid formation inhibition effect of a designed small aromatic  $\beta$ -breaking peptide. *Amyloid* **2011**, *18*, 119-127.
27. Ikenoue, T.; Aprile, F. A.; Sormanni, P.; Vendruscolo, M., Rationally Designed bicyclic peptides prevent the conversion of A $\beta$ 42 assemblies into fibrillar structures. *Front Neurosci* **2021**, *15*, 623097-623097.
28. Abbott, A.; Dolgin, E., Leading Alzheimer's theory survives drug failure. *Nature* **2016**, *540*, 15-16.
29. Kokkoni, N.; Stott, K.; Amijee, H.; Mason, J. M.; Doig, A. J., N-Methylated peptide inhibitors of  $\beta$ -Amyloid aggregation and toxicity. optimization of the inhibitor structure. *Biochemistry* **2006**, *45*, 9906-9918.
30. Frydman-Marom, A.; Convertino, M.; Pellarin, R.; Lampel, A.; Shaltiel-Karyo, R.; Segal, D.; Caflish, A.; Shalev, D. E.; Gazit, E., Structural basis for inhibiting  $\beta$ -amyloid oligomerization by a non-coded  $\beta$ -breaker-substituted endomorphin analogue. *ACS Chem. Biol.* **2011**, *6*, 1265-1276.
- 
-

31. Bernstein, S. L., et al., Amyloid- $\beta$  protein oligomerization and the importance of tetramers and dodecamers in the aetiology of Alzheimer's disease. *Nat. Chem.* **2009**, *1*, 326-331.
32. Tjernberg, L. O.; Näslund, J.; Lindqvist, F.; Johansson, J.; Karlström, A. R.; Thyberg, J.; Terenius, L.; Nordstedt, C., Arrest of  $\beta$ -amyloid fibril formation by a pentapeptide ligand (\*). *J. Biol. Chem.* **1996**, *271*, 8545-8548.
33. Senguen, F. T.; Lee, N. R.; Gu, X.; Ryan, D. M.; Doran, T. M.; Anderson, E. A.; Nilsson, B. L., Probing aromatic, hydrophobic, and steric effects on the self-assembly of an amyloid- $\beta$  fragment peptide. *Mol. BioSyst.* **2011**, *7*, 486-496.
34. Henning-Knechtel, A., et al., Designed cell-penetrating peptide inhibitors of amyloid- $\beta$  aggregation and cytotoxicity. *Cell Rep. Phys. Sci.* **2020**, *1*, 100014.
35. Richman, M.; Wilk, S.; Chemerovski, M.; Wärmländer, S. K. T. S.; Wahlström, A.; Gräslund, A.; Rahimipour, S., In vitro and mechanistic studies of an anti-amyloidogenic self-assembled cyclic D, L- $\alpha$ -peptide architecture. *J. Am. Chem. Soc.* **2013**, *135*, 3474-3484.
36. Luo, J.; Abrahams, J. P., Cyclic peptides as inhibitors of amyloid fibrillation. *Chemistry* **2014**, *20*, 2410-9.
37. Kaffy, J., et al., Designed glycopeptidomimetics disrupt protein-protein interactions mediating amyloid  $\beta$ -peptide aggregation and restore neuroblastoma cell viability. *J. Med. Chem.* **2016**, *59*, 2025-2040.
38. Balachandra, C.; Govindaraju, T., Cyclic dipeptide-guided aggregation-induced emission of naphthalimide and its application for the detection of phenolic drugs. *J. Org. Chem.* **2020**, *85*, 1525-1536.
39. Govindaraju, T.; Balachandra, C.; Padhi, D., Cyclic Dipeptide: A privileged molecular scaffold to derive structural diversity and functional utility. *ChemMedChem*, **2021**, *16*, 2558-2587
40. Borthwick, A. D., 2,5-Diketopiperazines: Synthesis, reactions, medicinal chemistry, and bioactive natural products. *Chem. Rev.* **2012**, *112*, 3641-3716.



41. Li, M.; Howson, S. E.; Dong, K.; Gao, N.; Ren, J.; Scott, P.; Qu, X., Chiral metallo helical complexes enantioselectivity target amyloid  $\beta$  for treating Alzheimer's disease. *J. Am. Chem. Soc.* **2014**, *136*, 11655-11663.
42. Hsieh, M.-C.; Liang, C.; Mehta, A. K.; Lynn, D. G.; Grover, M. A., Multistep conformation selection in amyloid assembly. *J. Am. Chem. Soc.* **2017**, *139*, 17007-17010.
43. Abe, H.; Kawasaki, K.; Nakanishi, H., pH-dependent aggregate forms and conformation of Alzheimer amyloid  $\beta$ -peptide (12-24). *J. Biochem.* **2002**, *132*, 863-74.
44. A. Micsonai, F. Wien, L. Kernya, Y. H. Lee, Y. Goto, M. Refregiers and J. Kardos, Accurate secondary structure prediction and fold recognition for circular dichroism spectroscopy, *Proc. Natl. Acad. Sci. U. S. A.*, **2015**, *112*, E3095–103
45. Zandomenighi, G.; Krebs, M. R. H.; McCammon, M. G.; Fändrich, M., Ftir Reveals structural differences between native  $\beta$ -sheet proteins and amyloid fibrils. *Protein science: a publication of the Protein Society* **2004**, *13*, 3314-3321.
46. Carrota, R.; Manno, M.; Bulone, D.; Martorana, V.; San Biagio, P. L., Protofibril formation of amyloid  $\beta$ -protein at low pH via a non-cooperative elongation mechanism. *J. Biol. Chem.* **2005**, *280*, 30001-8.
47. Jin, S.; Kedia, N.; Illes-Toth, E.; Haralampiev, I.; Prisner, S.; Herrmann, A.; Wanker, E. E.; Bieschke, J., A $\beta$  (1-42) Aggregation initiates its cellular uptake and cytotoxicity. *J. Biol. Chem.* **2016**, *291*, 19590-19606.
48. Bag, S.; Sett, A.; DasGupta S.; and Dasgupta, S., Hydrophathy: the controlling factor behind the inhibition of A $\beta$  fibrillation by graphene oxide *RSC Adv.* **2016**, *6*, 103242–103252.
49. Trott, O.; and Olson, A. J.; AutoDock Vina: improving the speed and accuracy of docking with a new scoring function, efficient optimization and multithreading *J. Comput. Chem.* **2010**, *31*, 455-461.
50. Morris, G. M.; Huey, R.; Lindstrom, W.; Sanner, M. F.; Belew, R. K.; Goodsell, D. S.; and Olson, D. S.; AutoDock4 and AutoDockTools4: Automated docking with selective receptor flexibility *J. Comput. Chem.* **2009**, *30*, 2785-2791.
- 
-



## **Chapter 3**

### **Differential Copper-Guided Architectures of Amyloid $\beta$ Peptidomimetics Modulate Oxidation States and Catalysis**



The controlled organization of designer molecular building blocks to generate well-defined material architectures with unique functional properties and applications is the guiding principle of molecular architectonics.<sup>1-3</sup> Molecular recognition driven self-assembly and co-assembly through controlled noncovalent interactions are indispensable in the construction of diverse architectures. In the scheme of molecular architectonics, biomolecules play a key role as functional auxiliaries.<sup>4</sup> The self-assembly of peptides and proteins has been shown to produce structurally and functionally diverse multifunctional architectures with potential applications in the fields of optoelectronics, sensing, bioimaging, and biomaterials.<sup>5,6</sup> The linear and cyclic peptides are attractive molecular building blocks to construct biomaterial scaffolds owing to their functional tolerability, ease of synthesis, biocompatibility, and enzyme mimetic ability.<sup>7,8</sup> The self-assembly of amyloid-forming short and oligopeptides and peptidomimetics produce catalytic amyloids in the presence of metal ions with catalytic activity in various hydrolytic and redox chemical transformations.<sup>9-12</sup> Ventura et al. recently demonstrated a pH-dependent assembly of the short peptide with two divergent catalytic activities.<sup>13</sup> Recently, CDPs are being used as versatile building blocks and auxiliaries to construct functional architectures.<sup>14,15</sup> Gazit et al. reported CDP-based nano-superstructure with efficient catalysis in the hydrolysis of para-nitrophenol acetate.<sup>16</sup> The potential of CDP-driven assembly architectures as catalytic systems in multiple chemical reactions is largely unexplored. In the present work, we judiciously designed A $\beta$  peptide-based CDP peptidomimetics and their metal-mediated assembly to produce differential architectures with distinct catalytic activities.

### **3.1 Design and synthesis**

We designed and synthesized peptidomimetics (Akd<sup>NMC</sup> and Akd<sup>NMC</sup>Py) of A $\beta$ 14-23 incorporated with unnatural CDP amino acid cyclo(L-Lys - L-Asp) (kd) and pyrene (Py) units at specific

positions as shown in Figure 1 and Figure 2. A $\beta$ 14-23 (<sup>14</sup>HQKLVFFAE<sup>23</sup>D) has a self-recognition motif 'KLVFF' for amyloid assembly and metal-binding affinity.<sup>17</sup>

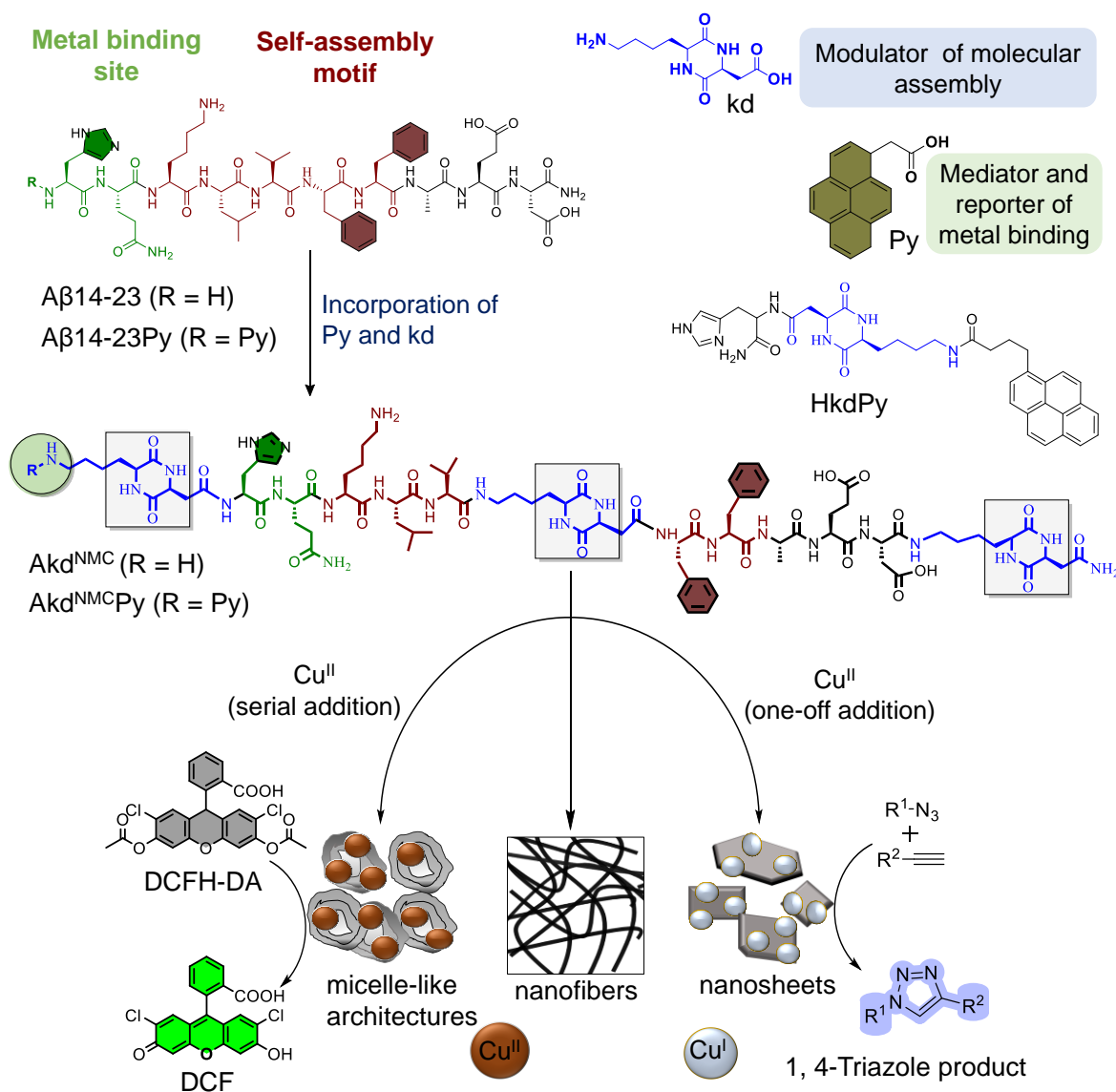


**Figure 1.** Design of A $\beta$ 14-23 peptidomimetics (Akd<sup>NMC</sup> and Akd<sup>NMCPy</sup>) incorporated with kd and Py units. HkdPy is a model peptidomimetics. Molecular assembly of Akd<sup>NMCPy</sup> in the absence and presence of one-off and serial additions of Cu<sup>II</sup> to generate distinct architectures that stabilize Cu<sup>II</sup> and Cu<sup>I</sup> states with catalytic activity in tandem oxidative-hydrolysis of DCFDA and alkyne-azide click reaction, respectively.

Metal chelation of A $\beta$ 14-23 through N-terminal histidine (14H) prompted us to orchestrate its metal-directed assembly into differential functional architectures. To strengthen metal chelation,

and assembly, A $\beta$ 14-23 was incorporated with Py at N-terminal and three kd units at the middle, N, and C-termini to obtain Akd<sup>NMC</sup>Py (Figure 1).<sup>18</sup>

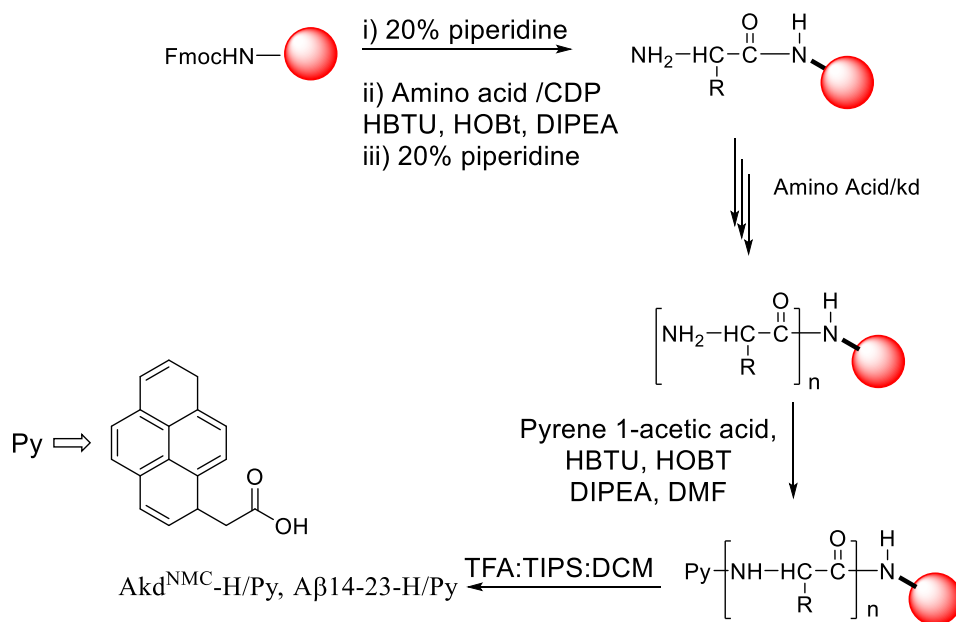


**Figure 2.** A general SPPS scheme for the synthesis of peptides and peptidomimetics.

The kd with rigid ring-core, multiple hydrogen bonding, and metal coordinating sites (amide linkages) was anticipated to influence metal binding and self-assembly of Akd<sup>NMC</sup>Py. The fluorescent Py assists the monitoring of metal binding-mediated assembly of Akd<sup>NMC</sup>Py through its characteristic spectral properties. We investigated the molecular architectonics of Akd<sup>NMC</sup>Py upon binding to Cu<sup>II</sup> in phosphate buffer saline (PBS, 10 mM, pH 7.4) (Figure 4). Cu as an important biocatalytic metal is capable of orchestrating distinct architectures with different oxidation states (Cu<sup>II</sup> or Cu<sup>I</sup>) and catalytic activity.<sup>19</sup>

We thus studied the assembly of Akd<sup>NMC</sup>Py (15  $\mu$ M) by adding Cu<sup>II</sup> in two distinct ways, (i) one-off addition: Cu<sup>II</sup> (100  $\mu$ M) was added in one-shot, and (ii) serial addition: Cu<sup>II</sup> (100  $\mu$ M) was added as 20 aliquots of 5  $\mu$ M each with an interval of 3.6 min (Figure 5 and 6). In the former case,

Akd<sup>NMC</sup>Py assembly was progressed upon immediate complexation with Cu<sup>II</sup> to produce stable 2D sheet architectures.<sup>20, 21</sup> While controlled complexation of Akd<sup>NMC</sup>Py to Cu<sup>II</sup> in later case resulted in stepwise assembly to form sheets via metastable micelle-like core-shell architectures. Interestingly, Cu<sup>II</sup> reduced to Cu<sup>I</sup> during the sheet formation, while micelle-like architectures retained Cu<sup>II</sup> state. The distinct architectures prompted us to exploit their functional utility in Cu<sup>II</sup> and Cu<sup>I</sup> catalyzed tandem oxidative-hydrolysis, and alkyne-azide click reactions, respectively. To the best of our knowledge, this is the first report of metal-induced differential architectures of A $\beta$ -peptidomimetics that stabilize Cu<sup>II</sup> and Cu<sup>I</sup> states to accomplish distinctive catalytic activities.

### **3.2 Results and discussions**

We probed the complexation of Akd<sup>NMC</sup>Py with Cu<sup>II</sup> by UV-vis absorption, fluorescence, and circular dichroism (CD) in PBS (10 mM, 7.4 pH) (Figure 3A-C). Akd<sup>NMC</sup>Py emission intensity in the 350-400 nm region (pyrene) was gradually quenched as a function of Cu<sup>II</sup> concentration with corresponding enhancement in the absorption intensity around 280-290 nm. This is attributed to change in the microenvironment of Phe (F) residues because of Cu<sup>II</sup> complexation-induced assembly of Akd<sup>NMC</sup>Py. The absence of Py excimer band ruled out the possible Py-Py interactions. The decrease in fluorescence lifetime (dynamic quenching) of Py (Akd<sup>NMC</sup>Py) from 140.8 to 113.9 ns in the presence of Cu<sup>II</sup> supported Py-Cu<sup>II</sup> interaction (Figure 3D and Table 2). This assumption was further supported by docking studies where Akd<sup>NMC</sup>Py was blindly docked with Akd<sup>NMC</sup>Py+Cu<sup>II</sup>. The energy minimized docked pose showed a short F-Py distance (3.5 Å) as compared to Py-Py distance (3.8 Å) (Figure 3F, Figure 8).<sup>22,23</sup> We speculate that Akd<sup>NMC</sup>Py adopted a spatial orientation to accommodate Cu<sup>II</sup> that prevented Py-Py interaction while promoting F-Py interactions, as supported by UV-vis absorption, fluorescence, and docking studies.



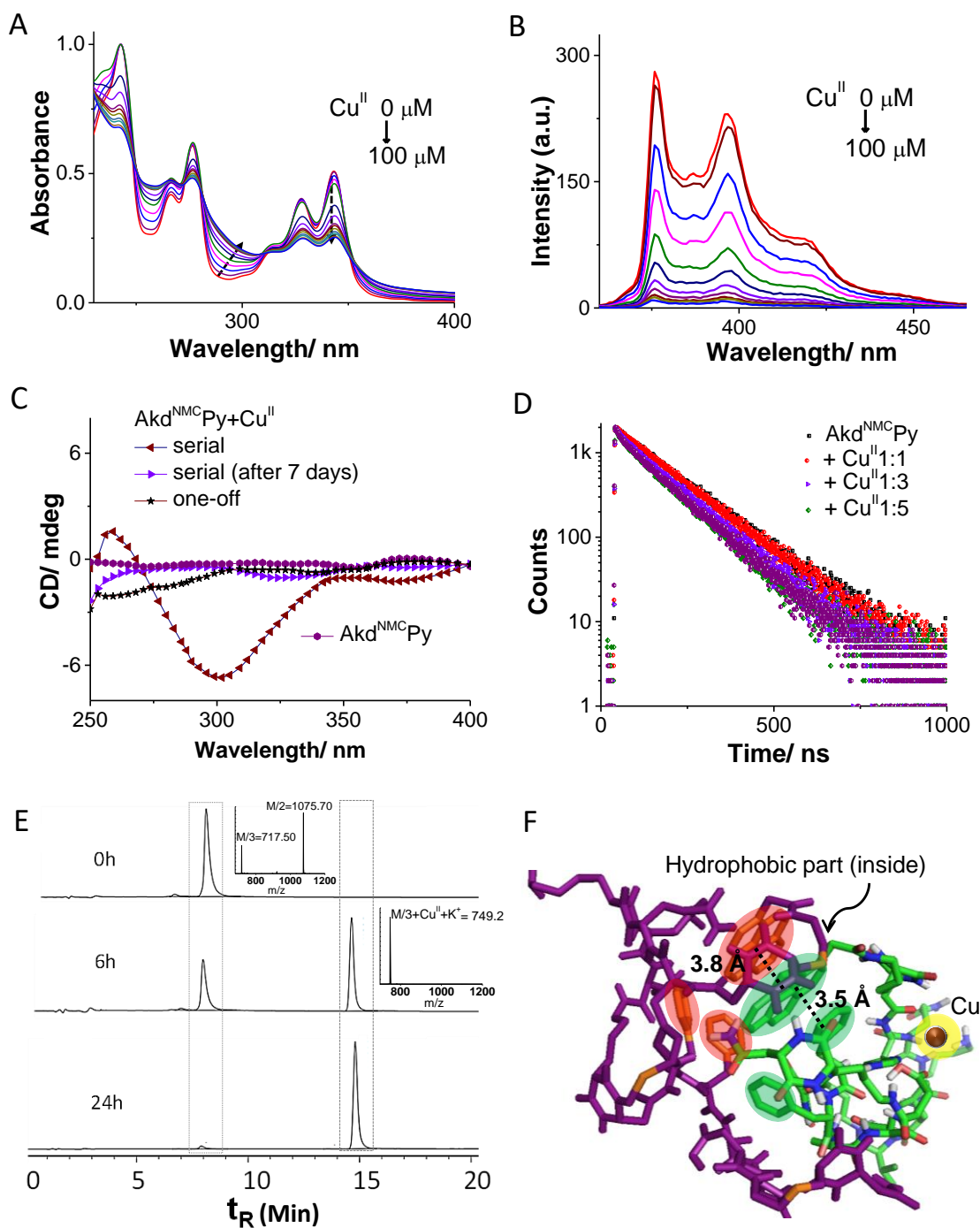


**Figure 3.** A) Absorbance, and B) fluorescence spectra of Akd<sup>NMCpy</sup> (15 μM) upon gradual addition of Cu<sup>II</sup> (0 μM to 100 μM). C) CD spectra of Akd<sup>NMCpy</sup> and upon addition of Cu<sup>II</sup> (one-off and serial additions). D) Fluorescence lifetime measurements of Akd<sup>NMCpy</sup> ( $\lambda_{\text{ex}}$  343 nm) with Cu<sup>II</sup>. E) Time-dependent LC of Akd<sup>NMCpy</sup>+Cu<sup>II</sup> (inset MS data). F) Molecular docking image of Akd<sup>NMCpy</sup>+Cu<sup>II</sup> and Akd<sup>NMCpy</sup> with Py-Py and Py-Phe distances shown (dotted lines).

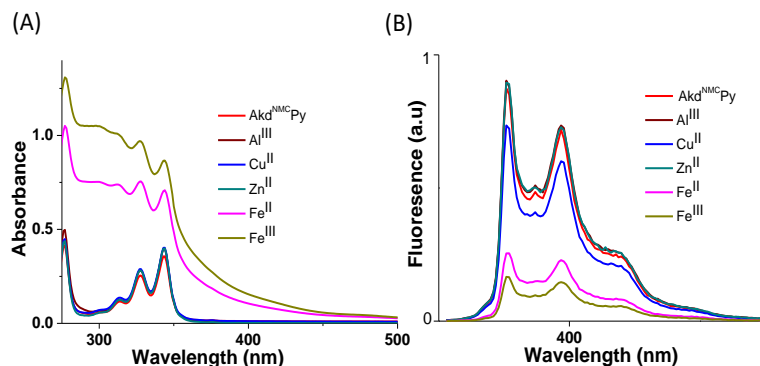


**Figure 4.** Akd<sup>NMC</sup>Py to various metal ions. (A) Absorbance spectra of Akd<sup>NMC</sup>Py (15  $\mu$ M) and in the presence of metal ions 25  $^{\circ}$ C in PBS buffer (10 mM, pH 7.4). (B) Fluorescence spectra of Akd<sup>NMC</sup>Py and in the presence of metal ions at 25  $^{\circ}$ C in PBS buffer (10 mM, pH 7.4) at the excitation wavelength  $\lambda_{ex}$  = 343 nm. [Metal ion] = 100  $\mu$ M, [Akd<sup>NMC</sup>Py] = 15  $\mu$ M.

CD spectra revealed Cu<sup>II</sup>-complexation-induced conformational change of Akd<sup>NMC</sup>Py. A distinct negative CD band observed around 298 nm indicated the generation of chiral environment due to Cu<sup>II</sup> complexation-induced assembly of Akd<sup>NMC</sup>Py.

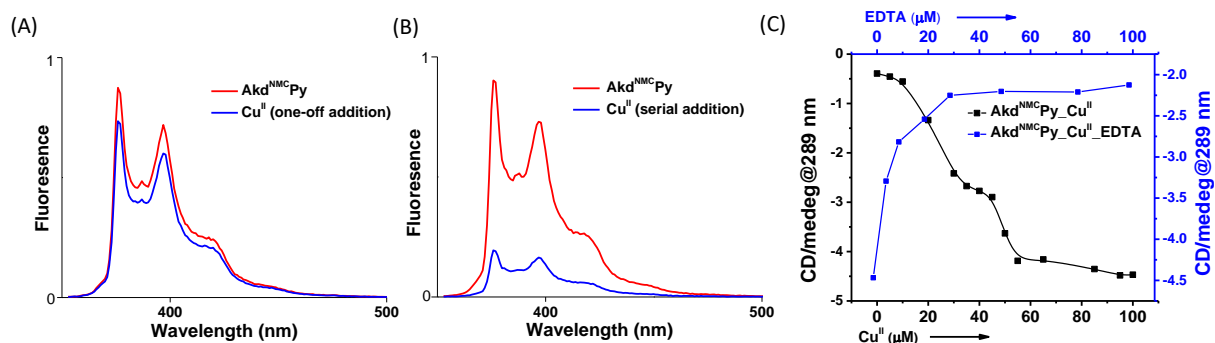


**Figure 5.** Spectral changes during the one-off and serial addition of Cu<sup>II</sup> into the Akd<sup>NMC</sup>Py solution. (A) Fluorescence spectra after one-off addition of Cu<sup>II</sup> (100  $\mu$ M) in Akd<sup>NMC</sup>Py (15  $\mu$ M). (B) Fluorescence quenching after serial addition of Cu<sup>II</sup> (100  $\mu$ M) (Cu<sup>II</sup> concentration increment is 5  $\mu$ M each time of addition). (C) The CD spectra (gradual diminishment of the negative cotton band at 289 nm) showed the effects of Cu<sup>II</sup> were reversible by adding a strong chelator (EDTA).

The spatial alignment of hydrophobic (F and Py) and hydrophilic moieties (-C=O of Asp, Glu and kd) of Akd<sup>NMC</sup>Py in the energy minimized docked structure of Akd<sup>NMC</sup>Py+Cu<sup>II</sup> also suggested chirality induction upon complexation. Interestingly, the negative CD band at 298 nm was disappeared over a period of 7 days suggesting two distinct assembly architectures for

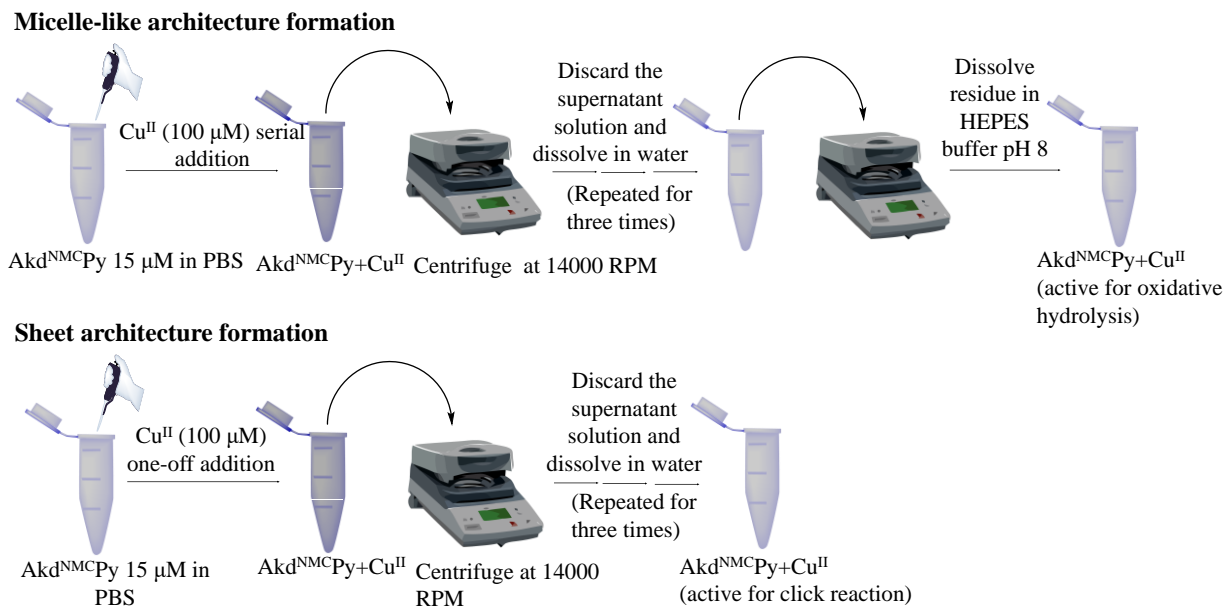


**Figure 6.** Detailed experimental procedure for the micelle-like and sheet architectures formation.

$\text{Akd}^{\text{NMC}}\text{Py}+\text{Cu}^{\text{II}}$  complex with initial chirally-active and final chirally-inactive states (Figure 3C).<sup>24</sup> Fourier-transform infrared (FTIR) studies of  $\text{Akd}^{\text{NMC}}\text{Py}$  and NMR spectrum of a model peptidomimetic  $\text{HkdPy}$  with  $\text{Cu}^{\text{II}}$  confirmed  $\text{Cu}^{\text{II}}-^{14}\text{H}$  ( $\text{Akd}^{\text{NMC}}\text{Py}$ ) binding interactions (Figure 9, 11).

	Time (h)	Retention time (min)	Mass found (m/z)
i	0	7.8	$\text{Akd}^{\text{NMC}}\text{Py}+3\text{H}^+$ (M/3= 717) $\text{Akd}^{\text{NMC}}\text{Py}+2\text{H}^+$ (M/2= 1076)
ii	6	7.8 14.8	$\text{Akd}^{\text{NMC}}\text{Py}+3\text{H}^+$ (M/3= 717) $\text{Akd}^{\text{NMC}}\text{Py}+2\text{H}^+$ (M/2= 1076) $\text{Akd}^{\text{NMC}}\text{Py}+\text{Cu}^{\text{II}}+\text{K}^+$ (M/3= 749)
iii	24	14.8	$\text{Akd}^{\text{NMC}}\text{Py}+\text{Cu}^{\text{II}}+\text{K}^+$ (M/3= 749)

**Table 1:** The time-dependent LC-MS of  $\text{Akd}^{\text{NMC}}\text{Py}+\text{Cu}^{\text{I/II}}$  complex.

The morphological outcomes of  $\text{Akd}^{\text{NMC}}\text{Py}+\text{Cu}^{\text{II}}$  assemblies was investigated by time-dependent transmission electron microscopy (TEM) imaging over a period of 1 to 14 days.  $\text{Akd}^{\text{NMC}}\text{Py}$  (15  $\mu\text{m}$ ) self-assembled to form fibrillar aggregates in PBS (Figure 12). One-off addition of  $\text{Cu}^{\text{II}}$  (100

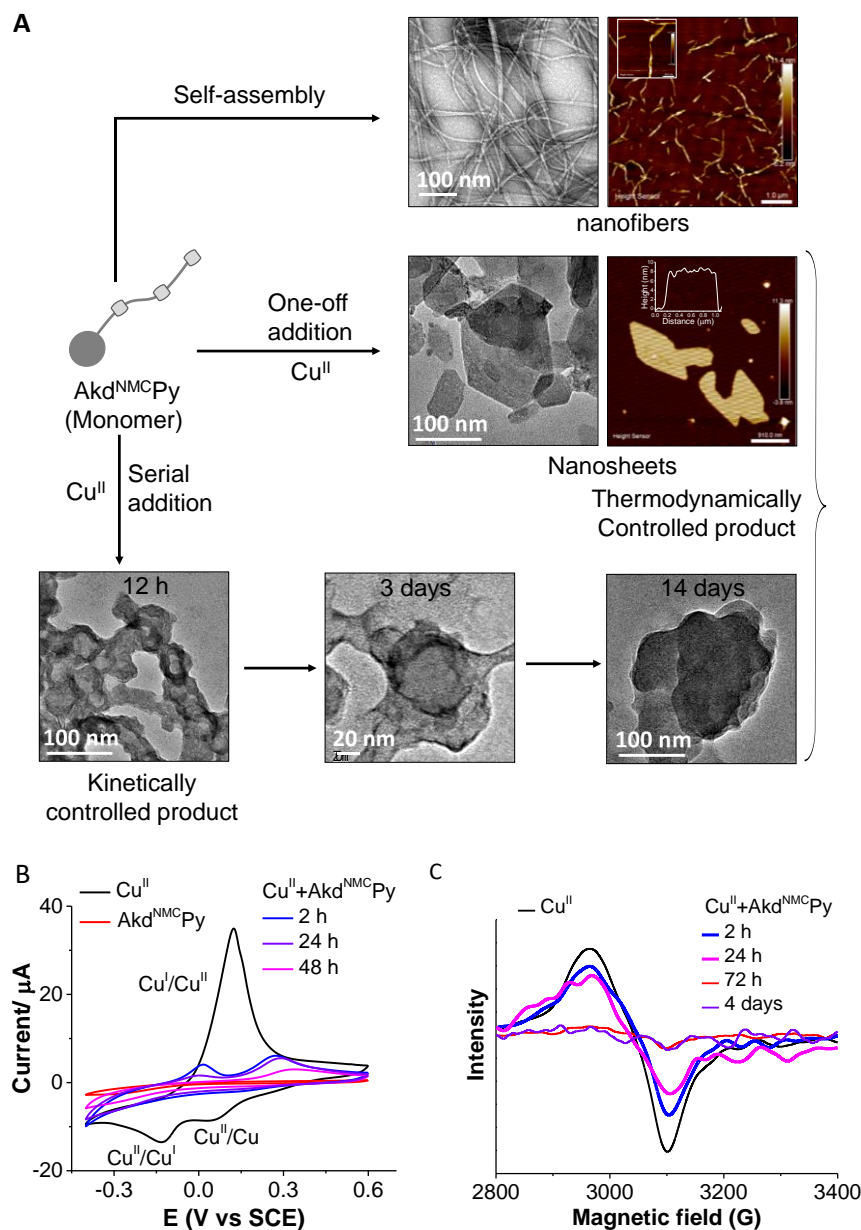


**Figure 7.** A) Differential morphologies of Akd<sup>NMC</sup>Py in the absence and presence of Cu<sup>II</sup>. Akd<sup>NMC</sup>Py self-assemble to form nanofibers. One-off addition of Cu<sup>II</sup> produces 2D nanosheets, while serial addition formed sheets through intermediate micelle-like core-shell architectures. B and C) CV and EPR spectra of Akd<sup>NMC</sup>Py and Cu<sup>II</sup>, and their complex at various time intervals.

$\mu\text{m}$ ) into Akd<sup>NMC</sup>Py (15  $\mu\text{m}$ ) resulted in the formation of stable nanosheets. Atomic force microscopy (AFM) has confirmed the formation of nanosheets with  $\sim 7$  nm thickness and 92.4 MPa DMT (Derjaguin-Muller-Toporov) modulus (Figure 7A, Figure 10, Figure 13).<sup>25</sup>

Serial addition of Cu<sup>II</sup> (20 aliquots of 5 μM each) to Akd<sup>NMC</sup>Py formed micelle-like core-shell architectures. The docking results have shown that the core pocket constitutes hydrophobic region (<sup>19</sup>F<sup>20</sup>F and Py), which is surrounded by the backbone and nucleophilic residues of Akd<sup>NMC</sup>Py to form Cu<sup>II</sup>-induced micelle-like architectures. After 14 days of incubation, Akd<sup>NMC</sup>Py with serially added Cu<sup>II</sup> (5 μM x 20 times) transformed from micelle-like architectures to 2D nanosheets (Figure 7A). Field emission scanning electron microscopy (FESEM) images and corresponding elemental mapping showed higher Cu-content in micelle-like architecture compared to nanosheets (Figure 14).

Akd <sup>NMC</sup> Py with Cu <sup>II</sup>	Excited state lifetime (λ <sub>345 nm</sub> )
Akd <sup>NMC</sup> Py	140.8 ns
Akd <sup>NMC</sup> Py+Cu <sup>II</sup> (1:1)	136.8 ns
Akd <sup>NMC</sup> Py+Cu <sup>II</sup> (1:3)	121.5 ns
Akd <sup>NMC</sup> Py+Cu <sup>II</sup> (1:5)	113.9 ns

**Table 2.** Excited-state lifetime experiment data of Akd<sup>NMC</sup>Py with Cu<sup>II</sup> with varying concentration ratios.

We postulated that the micelle-like architectures formed initially is a kinetically trapped metastable state, which restructured and transformed into thermodynamically stable 2D nanosheet architectures over time. After 7 days of incubation under similar conditions, Aβ14-23, Aβ14-23Py, Akd<sup>NMC</sup>, and HkdPy did not form sheet or micellar-like architectures (Figure 15).

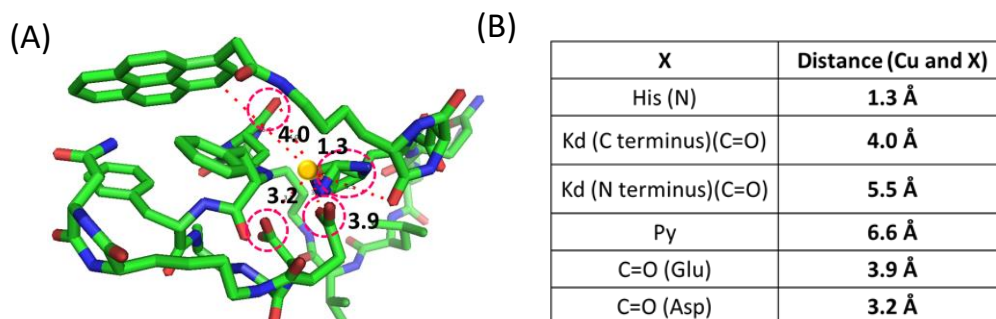


**Figure 8.** (A) Most stable conformation of Akd<sup>NMC</sup>Py+Cu<sup>II</sup>. (B) Distance between Cu and different closer atoms (X) in Akd<sup>NMC</sup>Py.

The collective experimental evidence confirmed the binding of Akd<sup>NMC</sup>Py with Cu<sup>II</sup> followed by distinct assembly pathways to form nanosheets or micelle-like core-shell architectures which subsequently transformed into thermodynamically stable nanosheets. Next, the binding stoichiometry between Akd<sup>NMC</sup>Py and Cu<sup>II</sup>, and the redox behavior of bound Cu ions were studied by liquid chromatography-mass spectrometry (LCMS), cyclic voltammetry (CV), and electron paramagnetic resonance (EPR) experiments. Upon addition of Cu<sup>II</sup>, LCMS spectra showed gradual disappearance of Akd<sup>NMC</sup>Py peak at retention time ( $t_R$ ) = 7.9 min and concomitant appearance of a new peak at  $t_R$  = 14.8 min (Figure 3E, Table 1), which confirmed equimolar stoichiometric complexation between Akd<sup>NMC</sup>Py and Cu<sup>II</sup>. The CV measurements of Cu<sup>II</sup> solutions after mixing with Akd<sup>NMC</sup>Py showed a sharp decrease in cathodic (-15  $\mu$ A at -0.18 V) and anodic (38  $\mu$ A at 0.13 V) peak current intensities with time. At 48 h incubation with Akd<sup>NMC</sup>Py, the cathodic and anodic peaks of Cu<sup>II</sup> were completely disappeared inferring the complexation-induced decrease of free Cu<sup>II</sup> in the presence of Akd<sup>NMC</sup>Py (Figure 7B).

We performed low-temperature EPR spectroscopy measurements to investigate Cu<sup>II</sup> coordination environment and oxidation state in the presence of Akd<sup>NMC</sup>Py.<sup>26</sup> EPR data showed diminishing of Cu<sup>II</sup> signal at 3100 gauss (G) in the presence of Akd<sup>NMC</sup>Py which is attributed to the reduction of

$\text{Cu}^{\text{II}}$  to diamagnetic  $\text{Cu}^{\text{I}}$  (Figure 7C). Thus, we postulate that the complexation of  $\text{Cu}^{\text{II}}$  by  $\text{Akd}^{\text{NMC}}\text{Py}$  initially forms micelle-like architectures, which gradually reorganize to nanosheets guided by the in-situ reduction of  $\text{Cu}^{\text{II}}$  to  $\text{Cu}^{\text{I}}$ .

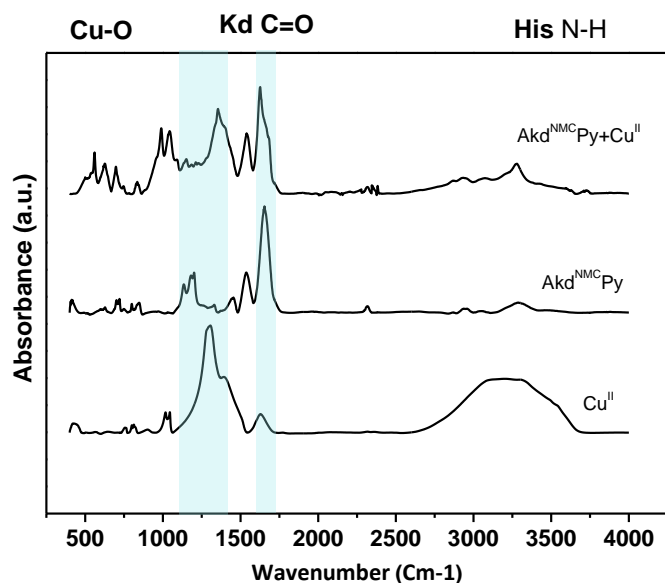


**Figure 9.** FTIR spectra of (A) sheet structure of  $\text{Akd}^{\text{NMC}}\text{Py}$  with  $\text{Cu}^{\text{II}}$  (B)  $\text{Akd}^{\text{NMC}}\text{Py}$ , and (C)  $\text{Cu}^{\text{II}}$ . The data showed shifting of stretching frequencies of N-H (14H) and  $-\text{C}=\text{O}$  (kd) in  $\text{Akd}^{\text{NMC}}\text{Py}$  from 3300 to 3275  $\text{cm}^{-1}$  and 1654 to 1623  $\text{cm}^{-1}$ , respectively, in the presence of  $\text{Cu}^{\text{II}}$  which suggest 14H as the major binding site for  $\text{Cu}^{\text{II}}$ .

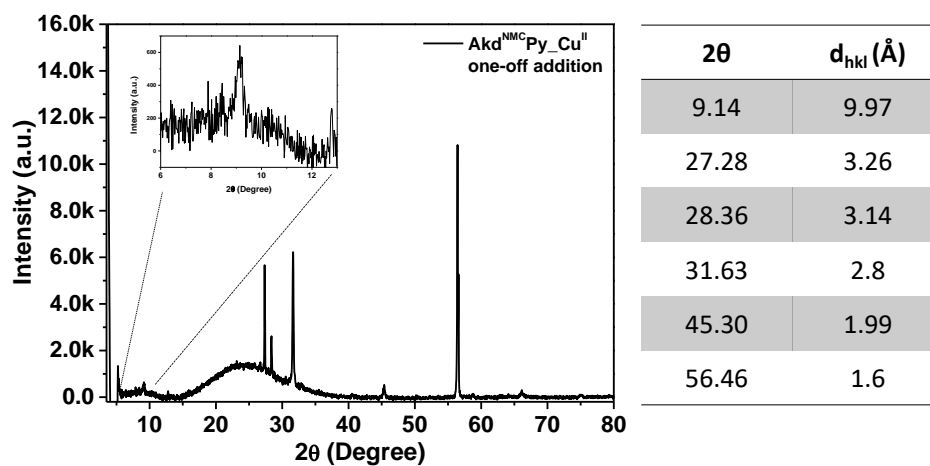


**Figure 10.** Powder XRD pattern of  $\text{Akd}^{\text{NMC}}\text{Py} + \text{Cu}^{\text{I}}$  sheet structure. X-ray diffraction (PXRD) data suggested crystalline nature of the nanosheets with a d-spacing of 3.26 Å.



Next, we demonstrated the use of distinct architectures of Akd<sup>NMCPy</sup> as catalytic systems in performing chemical transformations specific to Cu<sup>II</sup> and Cu<sup>I</sup>. The catalytic utility of micelle-like architectures of Akd<sup>NMCPy</sup>+Cu<sup>II</sup> was investigated in a tandem reaction involving oxidative-hydrolysis of 2',7'-dichlorofluorescein diacetate (DCFH-DA) (Figure 16A).<sup>9,27</sup>

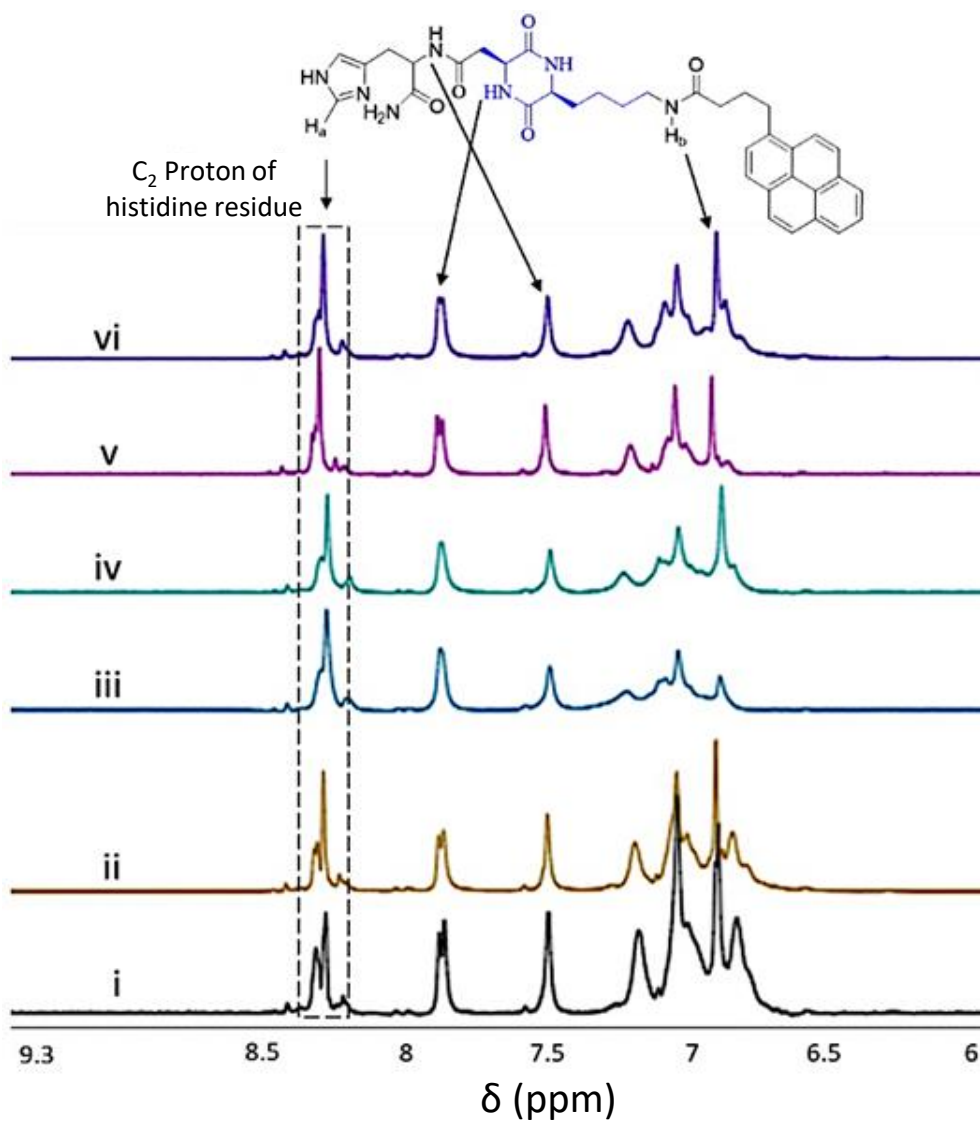


**Figure 11.** <sup>1</sup>H NMR titration of HkdPy with Cu<sup>II</sup> in D<sub>2</sub>O solution at 25 °C and at a pH of 7.4. Spectrum (i) HkdPy (30 μM) dissolved in phosphate-buffered D<sub>2</sub>O (pH 7.45); spectra ii to vi are for same solution with Cu<sup>II</sup> (50 μM), incubation time point are as follows: ii, 2 h; iii, 18 h; iv, 28 h; v, 40 h; vi, 2 days. The downfield shift of C<sub>2</sub> proton of <sup>14</sup>H confirms the Cu<sup>II</sup>-H (Akd<sup>NMCPy</sup>) binding interactions.



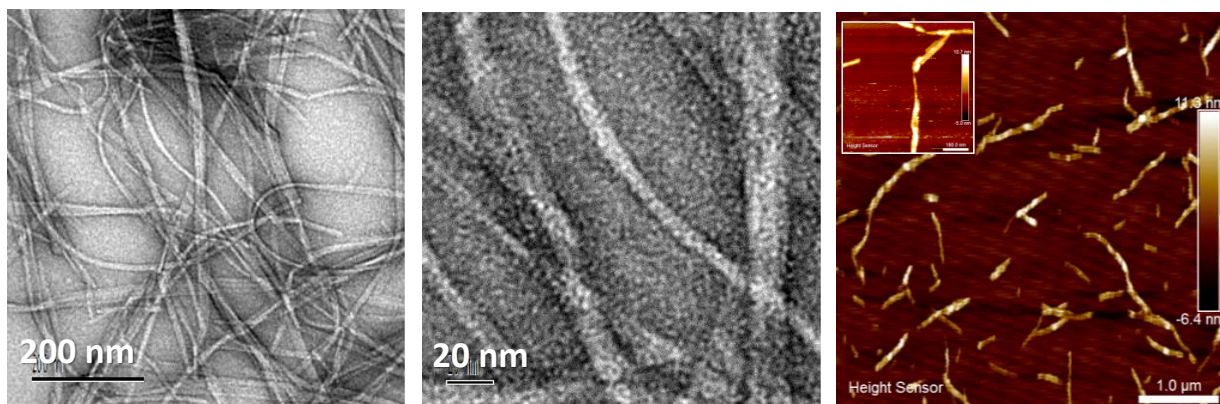


**Figure 12.** TEM images of Akd<sup>NMC</sup>Py in PBS (pH 7.4) after 24 h of incubation, form matured fibrillar architecture.

The micelle-like architectures were prepared by the serial addition of Cu<sup>II</sup> to Akd<sup>NMC</sup>Py, centrifugation, water washing, and finally dispersed in HEPES buffer (25 mM, pH 8). The oxidative-hydrolysis of DCFH-DA by Akd<sup>NMC</sup>Py+Cu<sup>II</sup> was monitored by recording the absorbance of 2',7'-dichlorofluorescein (DCF) at  $\lambda_{\max} = 504$  nm (Figure 17).

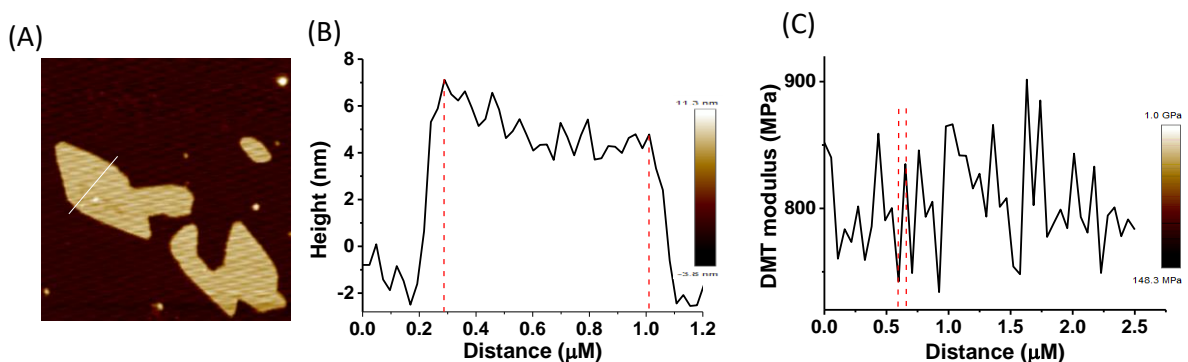


**Figure 13.** (A) AFM images of Akd<sup>NMC</sup>Py+Cu<sup>I</sup> (Sheet) in PBS (10 mM, pH 7.4) (B) Height plot (C) DMT modulus plot of sheet architecture.

The conversion of DCFH-DA into DCF was observed with an initial rate of 8.7 nM min<sup>-1</sup> (Figure 16B, 17). The calculated  $K_M$  and catalytic efficiency ( $k_{\text{cat}}/K_M$ ) were 0.5 mM and 120 M<sup>-1</sup>min<sup>-1</sup>, respectively, which are in agreement with reported peptide-based cascade reactions (Table 3).<sup>9,27,28</sup>

The control reactions revealed that Cu<sup>II</sup>, His, Akd<sup>NMC</sup>Py, Akd<sup>NMC</sup>, A $\beta$ 14-23, A $\beta$ 14-23Py, and HkdPy were catalytically inefficient under similar assay conditions (Figure 16B). Finally, we

evaluated the activity of nanosheets of  $\text{Akd}^{\text{NMC}}\text{Py}$  in  $\text{Cu}^{\text{I}}$ -catalyzed alkyne-azide cycloaddition (CuAAC) reaction to form triazole products.<sup>29</sup> The nanosheets were found to

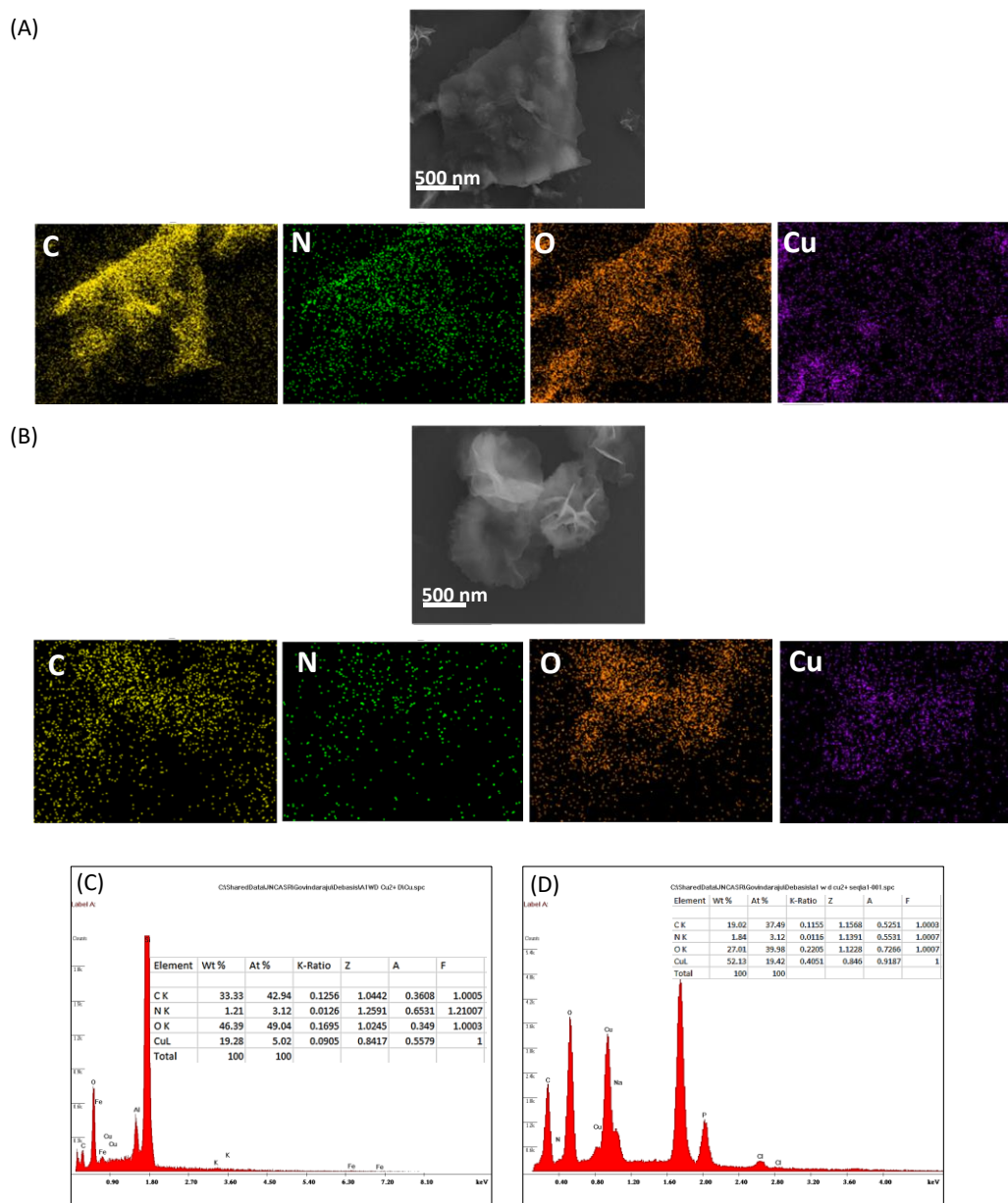


**Figure 14.** FESEM images of  $\text{Akd}^{\text{NMC}}\text{Py} + \text{Cu}^{\text{II}}$ . (A) sheet (B) micelle-like architectures and corresponding elemental mapping images. EDAX ZAF quantification (Element Normalized) of (C) sheet (D) micelle-like architectures. The micelle-like architecture contains higher Cu content (wt% 52.13) compared to nanosheets (wt% 19.28).

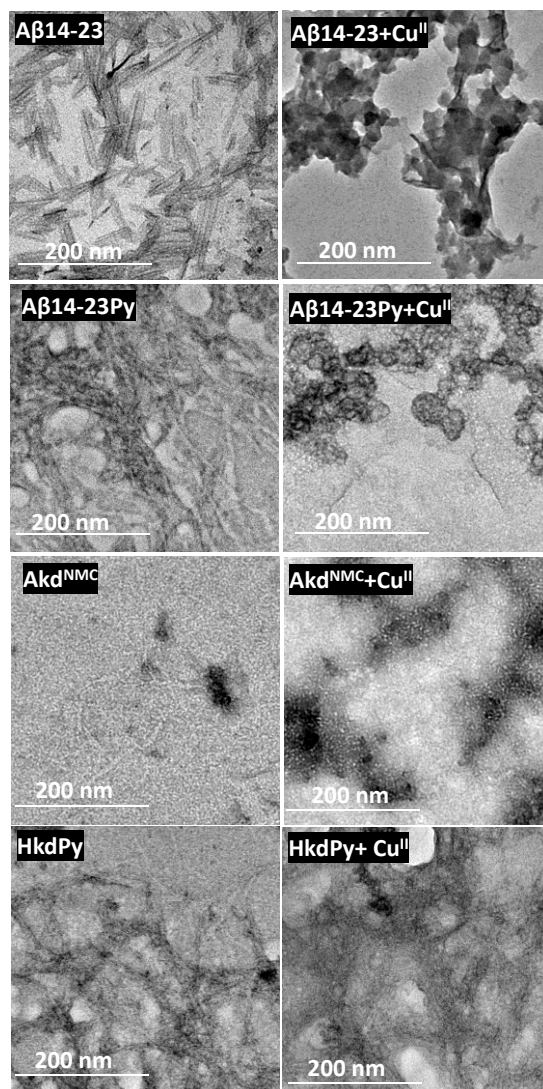


**Figure 15.** TEM images of A $\beta$ 14-23, A $\beta$ 14-23Py, Akd<sup>NMC</sup>, HkdPy and in the presence of Cu<sup>II</sup> in PBS (pH 7.4). The data did not show sheet or micelle-like architectures upon prolonged incubation time.

efficiently catalyze the reaction with varied combinations of azide and alkyne to yield 1,4-cycloaddition products as shown in Figure 16D. The triazole adducts were quantitatively analyzed and characterized by LCMS (Table S4). . The product started forming within 10 min and reached completion by 60 min, as was monitored by NMR spectroscopy (Figure 18). Our study further revealed that nanosheet architectures of AkdNMC<sup>Py</sup> + Cu<sup>I</sup> catalyze CuAAC reactions with a considerably faster rate and excellent yields compared to a standard CuSO<sub>4</sub> + sodium ascorbate

catalyst system (Figures 19, 20). The detailed results from various spectroscopy techniques, oxidative-hydrolysis of DCFH-DA and CuAAC reactions

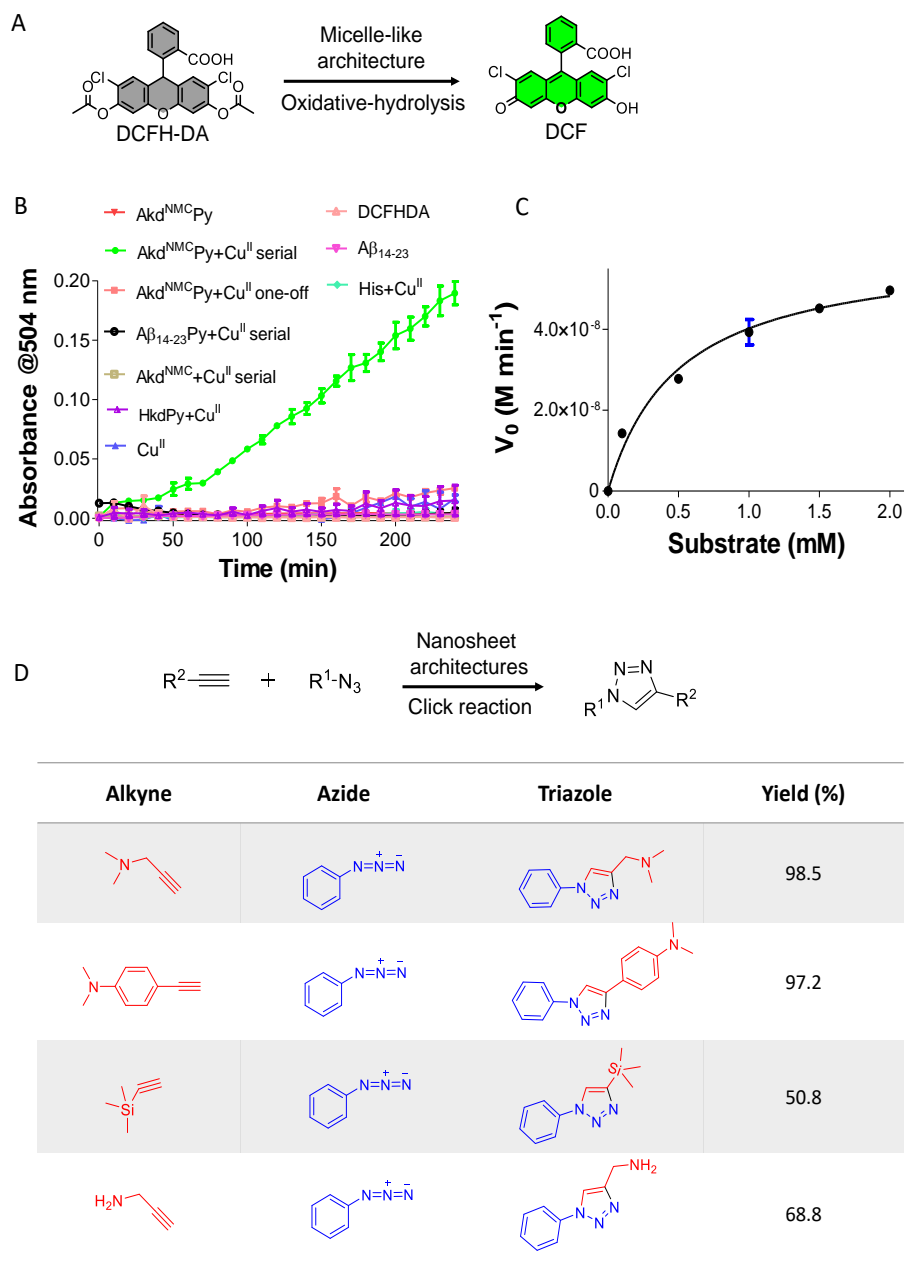


**Figure 16.** A) Micelle-like architectures of catalyzed conversion of DCFH-DA to DCF in HEPES (25 mM, pH 8). B) Absorbance vs reaction time plots for oxidative-hydrolysis of DCFH-DA catalyzed by micelle-like architectures and other control systems. C) The plot of initial rate ( $V_0$ ) vs different substrate (DCFH-DA) concentrations. D) Alkyne-azide click reaction catalyzed by nanosheets. Substrates with variable substituents and product yields calculated from LC-MS.

confirmed the stabilization of  $\text{Cu}^{\text{II}}$  state in micelle-like architectures and in-situ reductions of  $\text{Cu}^{\text{II}}$  to  $\text{Cu}^{\text{I}}$  in nanosheets of  $\text{Akd}^{\text{NMC}}\text{Py}$ .

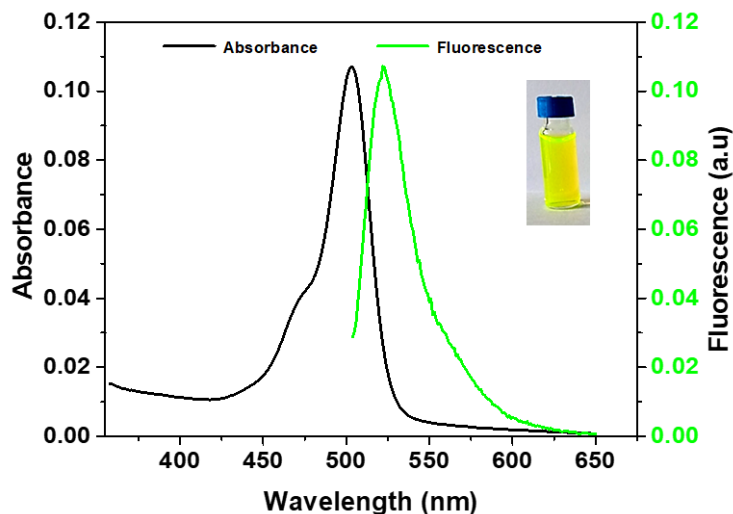


**Figure 17.** Absorbance ( $\lambda_{\text{max}} = 504 \text{ nm}$ ) of DCFHDA and fluorescence ( $\lambda_{\text{em}} = 520 \text{ nm}$ ) spectra of DCF in the presence of micelle-like architectures of  $\text{Akd}^{\text{NMC}}\text{Py} + \text{Cu}^{\text{II}}$ .

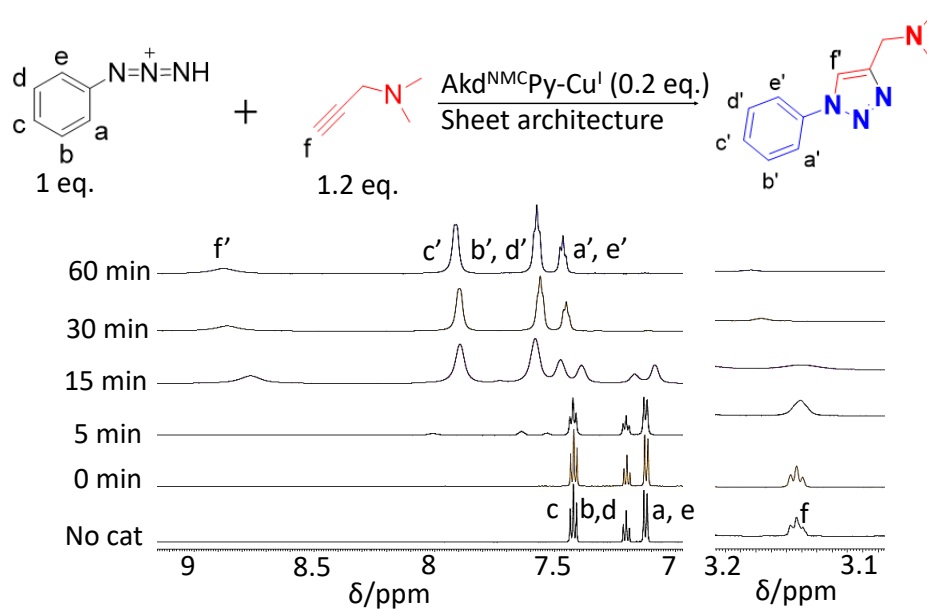


**Figure 18.**  $^1\text{H}$ -NMR spectra to follow the reaction between phenyl azide (1 eq) and N, N-dimethylprop-2-yn-1-amine (1.2 eq) in the presence of  $\text{Akd}^{\text{NMC}}\text{Py} + \text{Cu}^{\text{I}}$  (0.2 eq).  $\text{Akd}^{\text{NMC}}\text{Py} + \text{Cu}^{\text{I}}$  added at 0 min and product formation was observed within 10 min and reaction was completed in 30 min.

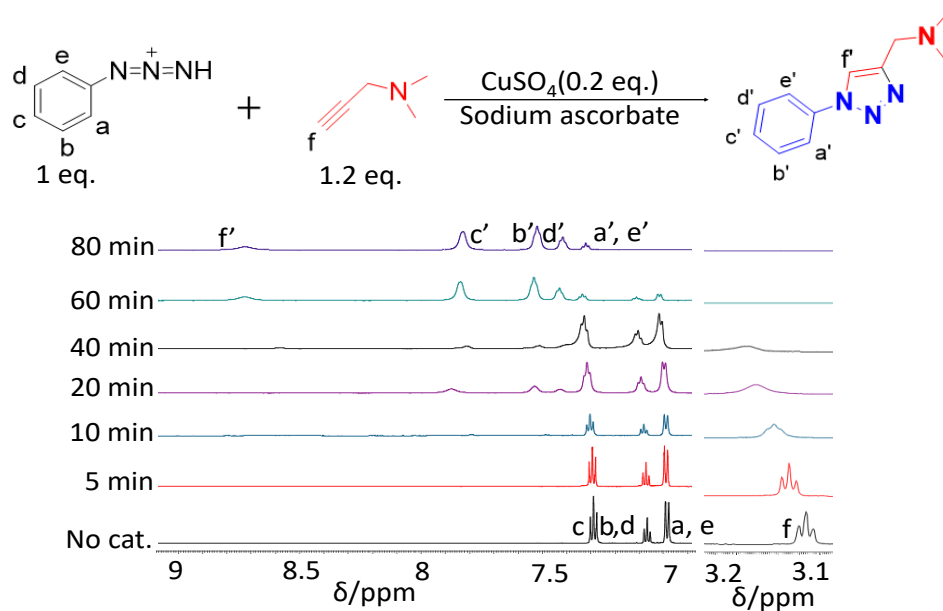
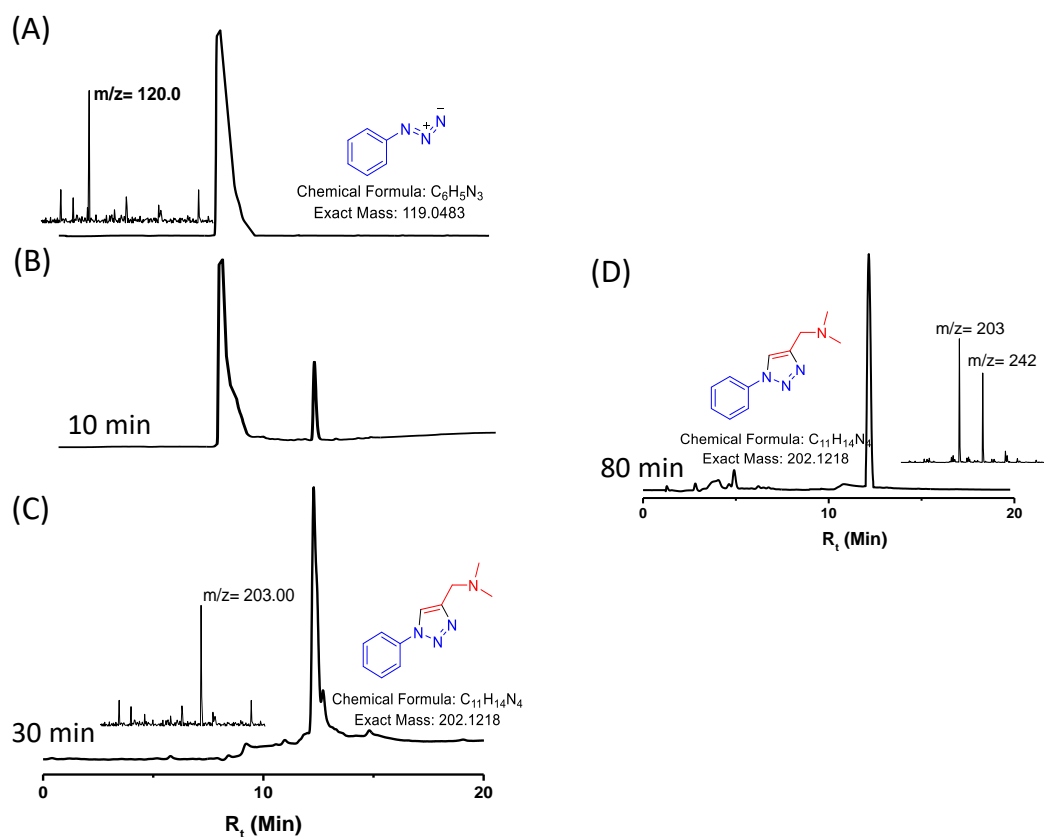


**Figure S19.** Time-dependent  $^1\text{H-NMR}$  spectra of reaction between phenyl azide (1 eq.) and N, N-dimethylprop-2-yn-1-amine (1.2 eq.) in the presence of  $\text{CuSO}_4$ +sodium ascorbate (0.2 eq.) added at 0 min and the product formation was assessed.  $\text{CuSO}_4$ +sodium ascorbate was added at 0 min and product formation was observed within 20 min and reaction was completed 80 min.



---

**Figure 20.** The triazole product conversion was monitored using LC-MS. (A) LCMS of only phenyl azide (Rt=8.2 min). (B) Akd<sup>NMC</sup>Py-CuI catalyzed alkyne-azide reaction (10% product triazole product, Rt= 13.0 min, m/z=203) after 10 min, (C) 97% triazole product was observed at 30 min, (D) LCMS profile of CuSO<sub>4</sub>+sodium ascorbate catalyzed alkyne-azide reaction after 80 min showed 95 % triazole product.

### 3.3 Conclusion

In summary, we demonstrated CDP and Cu-directed molecular architectonics of Akd<sup>NMC</sup>Py to form functional material architectures that differentially modulate Cu-oxidation states and catalytic activities. The fibrillar assembly of Akd<sup>NMC</sup>Py was engineered into thermodynamically stable nanosheets or kinetically controlled micelle-like architectures by one-off or serial additions of Cu<sup>II</sup> to Akd<sup>NMC</sup>Py. The experimental studies showed that micelle-like architectures and nanosheets of Akd<sup>NMC</sup>Py differentially stabilized Cu<sup>II</sup> and Cu<sup>I</sup> states, which were efficient catalytic systems in tandem oxidation-hydrolysis and click reactions, respectively. This work is anticipated to inspire the design of artificial biocatalytic architectures capable of performing multiple chemical transformations. Further, the metal-complexation-guided distinct functional architectures that stabilize different oxidation states could help in understanding the complex redox activities of metalloproteins.

### 3.4 General methods

All the peptides and peptidomimetics are synthesized by standard solid phase peptide synthesis (SPPS) protocols. Fmoc-rink amide resin (Novabiochem) was used as solid support. Amino acids and unnatural CDP-amino acid (kd) were coupled using HBTU/HOBt as the activating reagent, DIPEA as the base in DMF. For deprotection of the Fmoc protecting group, 20% piperidine in DMF was used. All peptides were purified using reverse-phase (RP) semi-preparative HPLC using a C18 column at 40 °C. The product purity was >99%, as ascertained by the analytical HPLC. The molecular mass of peptides was verified by HRMS (Q-TOF) analysis. The sequence and structural information of synthesized kd-incorporated peptidomimetics are given in Table S5.

### 3.4.1 Synthesis of A $\beta$ 14-23, A $\beta$ 14-23Py, Akd<sup>NMC</sup>, Akd<sup>NMC</sup>Py and HkdPy peptidomimetics

The unnatural CDP amino acid (kd) was synthesized by cyclizing Fmoc-Asp (OtBu)-OH and H-Lys (Boc)-OMe.<sup>29-30</sup> We used standard 9-fluorenylmethoxycarbonyl (Fmoc) SPPS protocols to synthesize kd-incorporated peptidomimetics. Fmoc-amino acids (H: Histidine, Q: Glutamine, K: Lysine, L: Leucine, V: Valine, F: Phenylalanine, A: Alanine, E: Glutamic acid, D: Aspartic acid, and Py: Pyrene acetic acid) with the Boc and t<sub>Bu</sub> protected side chains of the corresponding -NH<sub>2</sub> and -COOH functions were employed. The rink amide resin (loading 0.76 mmol/gm) was used as solid support. HBTU/HOBt (2.5 eq. each), DIPEA (4 eq.), and DMF were employed as activating reagent, base, and solvent, respectively, for coupling the Fmoc-amino acids (2.5 eq.) and the Fmoc-kd (2.5 eq.) in the desired sequence. In the final step, 2.5 eq of 1-pyrene acetic acid (Py) was conjugated to the N-terminus. Kaiser test was used to ensure that the amino acid's coupling and Fmoc-deprotection processes were completed. The resin was properly washed with DMF and DCM after each coupling and deprotection procedure. Using a cocktail solution of TFA: TIPS: DCM (95:2.5:2.5) at room temperature, the entire sequence of the peptidomimetics was cleaved from the resin and the product was collected as solid precipitate from the cold diethyl-ether. Reverse-phase HPLC was used to purify the synthesized peptidomimetics (C18 column).

### 3.4.2 Preparation of the peptide stock solution

Purified lyophilized peptides were dissolved in water (Mili-Q) to make a 1 mM stock solution.

### 3.4.3 Metal-binding study

The binding and selectivity of Akd<sup>NMC</sup>Py (15  $\mu$ M) peptide toward various metal ions, e.g. Al<sup>III</sup>, Cu<sup>II</sup>, Zn<sup>II</sup>, Fe<sup>II</sup> and Fe<sup>III</sup> were evaluated by absorbance and fluorescence studies. A 6.5-fold higher concentration of metal ions (100  $\mu$ M) was used during the sample preparation, Cu<sup>II</sup>, Fe<sup>II</sup> and Fe<sup>III</sup>



were found to bind efficiently to Akd<sup>NMC</sup>Py, as confirmed by the significant change in fluorescence of Akd<sup>NMC</sup>Py.

#### **3.4.4 Atomic force microscopy (AFM) characterization**

The AFM imaging was performed for Akd<sup>NMC</sup>Py, and one-off addition Akd<sup>NMC</sup>Py+Cu<sup>II</sup> samples. 10  $\mu$ L of 5  $\mu$ M aliquot was drop-casted onto freshly cleaved mica and incubated for 5 min, followed by rinsing with water (Milli-Q) and dried by the flow of air. The AFM images were acquired using Bruker BIOSCOPE Resolve with PeakForce Tapping mode. The silicon Tip on the Nitride Lever (SCANASYST-ATR) was used. The length and resonance frequency of the tip is 115  $\mu$ m and 146–236 kHz, respectively; and the force constant is 21–98 Nm<sup>-1</sup>. All the images were processed using NanoScope analysis software.

#### **3.4.5 Kinetic assay with fluorescein (DCFHDA) derivatives**

Kinetics measurements were carried out in 96-well plates using SpectraMax i3x microplate reader (Molecular Devices), by monitoring the absorbance of the product generated (DCF, 2',7'-dichlorofluorescein) at 504 nm at 37 °C. DCFH-DA (Sigma Aldrich) was dissolved in DMSO to obtain a stock solution (10 mM). Varying concentrations of substrate (DCFH-DA) including 100  $\mu$ M, 500  $\mu$ M, 1 mM, 2 mM, and 2.5 mM were used in the assays. The concentration of metal-peptide utilized in the studies was 2  $\mu$ M. The absorbance of DCF generated was measured after mixing with Akd<sup>NMC</sup>Py+Cu<sup>II</sup> complex. The studies were carried out in HEPES buffer (25 mM, pH 8). For the kinetics investigation, the control sample (negative control) was considered during the experiment, e. g. only Cu<sup>II</sup>, Akd<sup>NMC</sup>Py, Akd<sup>NMC</sup>, A $\beta$ 14-23, A $\beta$ 14-23Py, and HkdPy. The linear portion of the absorbance vs. time plot was fitted to a linear equation and the initial rate of the reaction was calculated using the slope/extinction coefficient of the product at pH 8 (90,750 M<sup>-1</sup>cm<sup>-1</sup>). Kinetic parameters were obtained by fitting the data to the Michaelis–Menten equation  $V_0$

=  $k_{\text{cat}}[E]_0[S]_0/(K_M+[S]_0)$ ,  $K_{\text{cat}}$  calculated from  $V_{\text{max}}/(E)$ , and catalytic efficiency was calculated from  $k_{\text{cat}}/K_M$  (Turnover number).

### **3.4.6 Cyclic voltammetry (CV) experiment**

The electrochemical experiments were performed using CHI 832 electrochemical workstation (CH Instruments, Austin, Texas). Cyclic voltammograms were obtained at room temperature, nitrogen gas was purged into the electrolyte solution. The saturated calomel electrode was used as a reference electrode, platinum coil as a counter electrode, and platinum disk as a working electrode. The redox behavior of the  $\text{Cu}^{\text{II}}$  (copper nitrate) was carried out in 0.2 M KCl. It had been observed that electroactive  $\text{Cu}^{\text{II}}$  solution gives two cathodic peaks and an anodic peak. The first cathodic peak current was at  $-8.6 \mu\text{A}$  and potential 0.034 V, and the second peak was at  $-1.35 \mu\text{A}$  and potential  $-0.128$  V. The anodic peak current was  $33.5 \mu\text{A}$  and the potential 0.124 V. This implied the two-electron reversible system. In the presence of  $\text{Akd}^{\text{NMC}}\text{Py}$  the current density decreased due to binding  $\text{Akd}^{\text{NMC}}\text{Py}$  with  $\text{Cu}^{\text{II}}$ . In the presence of  $\text{Akd}^{\text{NMC}}\text{Py}$ , only an anodic positive peak at 0.015 V and another at 0.27 V were observed. More importantly, the reduction peak becomes less significant, which provided information about the redox state of copper in the presence  $\text{Akd}^{\text{NMC}}\text{Py}$ .

### **3.4.7 Transmission electron microscopy (TEM) characterization**

$5 \mu\text{L}$  of the sample was placed onto a carbon-coated copper grid and dried completely. Then  $2 \mu\text{L}$  of 2 % (w/v) uranyl acetate solution was added for 45 sec and excess solution was wicked off by filter paper. Sample concentrations were typically 10-15  $\mu\text{M}$  in 10 mM PBS. The specimen was observed using JEOL-JEM 2010 instrument operating at 120 kV and the image was recorded with SC 1000 CCD camera (Gatan). The data were analyzed using Digital Micrograph software.

#### **3.4.8 Fourier-transform infrared spectroscopy (FTIR)**

FTIR spectra were recorded on Frontier (model: Sr No. 96466) spectrometer and in ATR mode. The aqueous solution of each sample (20  $\mu\text{L}$ ) was drop-casted on the thin coverslip, and then the sample was dried at room temperature under high vacuum. During the experiment, the scan rate was kept around 60  $\text{min s}^{-1}$ . The baseline correction for each recorded sample was performed by the instrument inbuilt software. The final data were plotted using the Origin software.

#### **3.4.9 Field emission scanning electron microscopy (FESEM)**

FESEM images were acquired using FEI Nove-nano SEM-600 equipped with a gun operating with the voltage 10.00 kV. The sample was prepared by drop-casting on a Si-wafer (111) substrate. The  $\text{Akd}^{\text{NMC}}\text{Py-Cu}^{\text{II}}$  complexes showed two distinct nanoarchitectures formations depending on the modes of addition of  $\text{Cu}^{\text{II}}$  (one-off or serial addition). In the serial addition mode, we found micelle-like core-shell architectures, and in one-off addition resulted in the formation of 2D nanosheets.

#### **3.4.10 Circular dichroism (CD) spectroscopy**

CD measurements were carried out on Jasco J-815 spectrometer under a nitrogen atmosphere to avoid water condensation. Scans were performed with the sample in 1 cm quartz cell over the range of 195–600 nm with a scan speed of 100 nm/min, and the spectra represent an average of three scans. A blank sample containing PBS buffer (10 mM, pH = 7.4) was treated in the same manner and subtracted from the collected data. Interestingly, in the case of serial addition, we observed a negative Cotton effect at 298 nm. With increasing concentration of  $\text{Cu}^{\text{II}}$  the band at 298 nm showed an enhanced negative cotton effect.

### **3.4.11 Electron paramagnetic resonance (EPR)**

Aqueous solution of Cu<sup>II</sup> (1 mM, 75  $\mu$ L) and peptide stock solution (1 mM) were mixed. The mixture was diluted in PBS (10 mM, pH 7.4). The mixture was incubated at room temperature for 2 h. The sample was transferred into an EPR tube and flash-frozen in liquid nitrogen. The EPR spectra were recorded in a time-dependent manner in Wilmad tube using a JEOL, JES-X320 EPR spectrometer by considering  $g^{\text{II}}$  and  $A^{\text{II}}$  values for Cu<sup>II</sup>. Thank you for the question. The parameters we have used for the experiments are Mod width (1 $\times$ 100), amplitude (7 $\times$ 100), Time constant (0.03 sec), Magnetic field (300 mT), power (1.5 mW), Frequency (9225.4 MHz).

### **3.4.12 Molecular docking**

Akd<sup>NMC</sup>Py peptidomimetic was docked with Akd<sup>NMC</sup>Py-Cu by using AutoDock Vina (version 1.1.2) software. The PDB format of Akd<sup>NMC</sup>Py was generated by OpenBabel software (version 2.4.1) after minimizing energy. AutoDock 4.2 MGL Tools (version 1.5.6) was applied for the preparation of Akd<sup>NMC</sup>Py-Cu (here as a receptor), where to predict binding mode more accurately, water molecules were eliminated, polar hydrogen atoms were added to it to find plausible polar contacts with any atom, gasteiger charges of the peptidomimetics were included and saved as pdbqt format. Also, the pdbqt format of Akd<sup>NMC</sup>Py was created to coordinate files, which consist of atomic partial charges and atom types. Torsion angles were determined to consign the fixable and non-bonded rotation of molecules. The grid file, modified to calculate the grid parameters, is an imaginary box of customized volume so that Akd<sup>NMC</sup>Py can bind to the best reasonable binding site with the lowest binding energy and with higher binding affinity. We performed a blind docking experiment of Akd<sup>NMC</sup>Py with grid volume of 84 x 84 x 84 points, grid spacing of 0.503 Å and centered (-0.671 for x-axis, -6.274 for y-axis, and -16.394 for z-axis) on the receptor Akd<sup>NMC</sup>Py-Cu. At the end of the experiment, the output file was produced as ligand\_out.pdbqt which includes

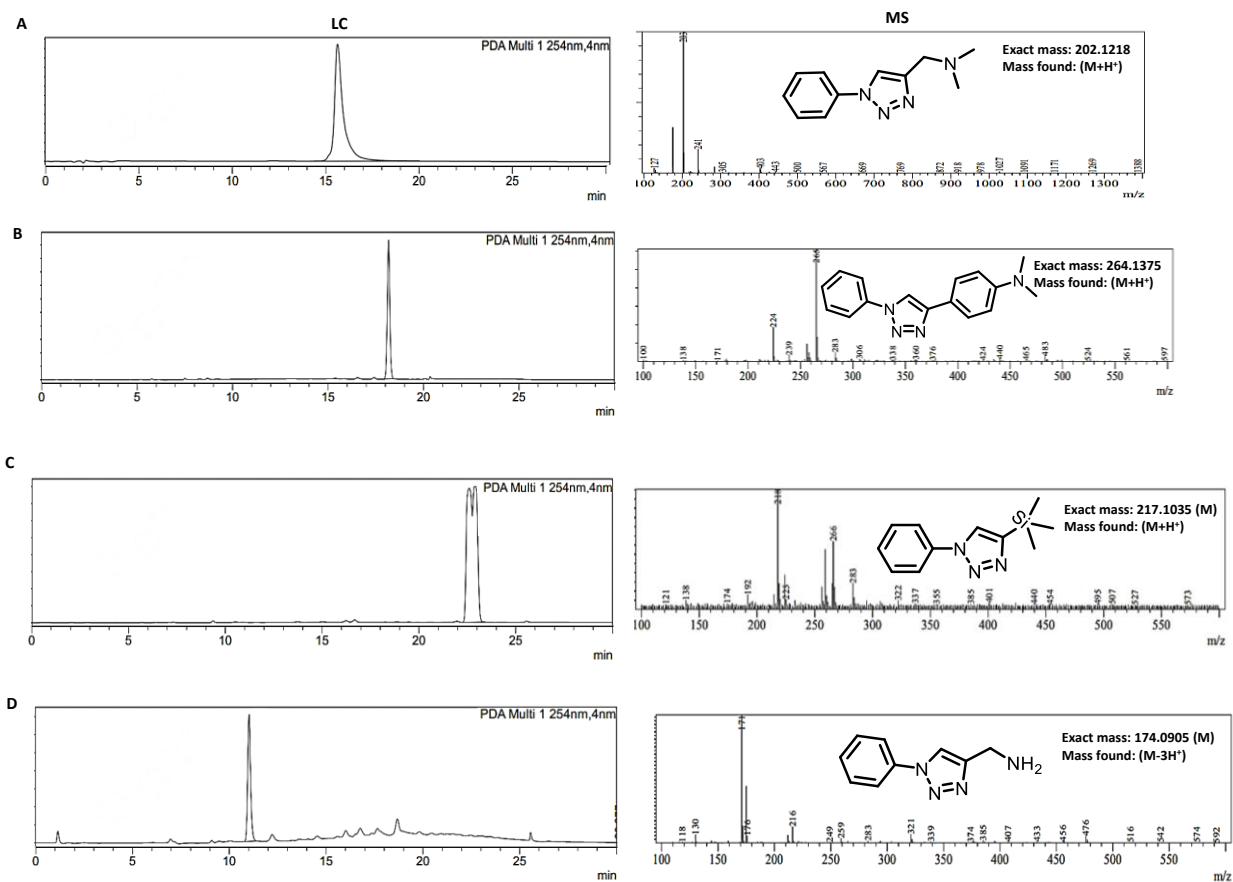
binding affinity (-5.4 in kcal/mol), RMSD lb, and RMSD ub. PyMOL software (version 1.7.4.5) was used to analyze the results of molecular docking. The hydrophobic residues were selected and labeled as required.

### 3.4.13 DFT calculation

From the most stable conformation of Akd<sup>NMC</sup>Py-Cu<sup>II</sup> (Figure 8), calculated by DFT (B3LYP, 6-31G), it was evident that Cu<sup>II</sup> was coordinated by 14His (1.3 Å), 22Glu (3.9 Å), 23Asp (3.2 Å), and C-terminus kd (4.0 Å, N-terminus kd 5.5 Å); and aromatic interactions play a crucial role to form the zipper structure where pyrene was 6.6 Å apart from Cu<sup>II</sup>. Based on the statistical analysis on the PDB, the RING server classified various interaction types, among which the strict and relaxed distance for the pi-cation interaction were reported as 5 Å and 7 Å respectively. Besides parallel, lateral and normal orientations, a peak around 6.2 Å was found for the orthogonal (N) conformation, corresponding to a situation where the charged group is placed opposite to the interacting ring.<sup>31</sup> Further,  $\pi$ - $\pi$  aromatic interactions support in favour of thermodynamically stable sheet architecture. The density functional theory (DFT) was calculated by Gaussian 5.0.9 program to get the most stable conformation of copper bound Akd<sup>NMC</sup>Py. Herein, B3LYP was used as an energy functional and 6-31G as a basis set.

**Table 3.** Comparison of the artificial hydrolase (oxidative-hydrolysis)

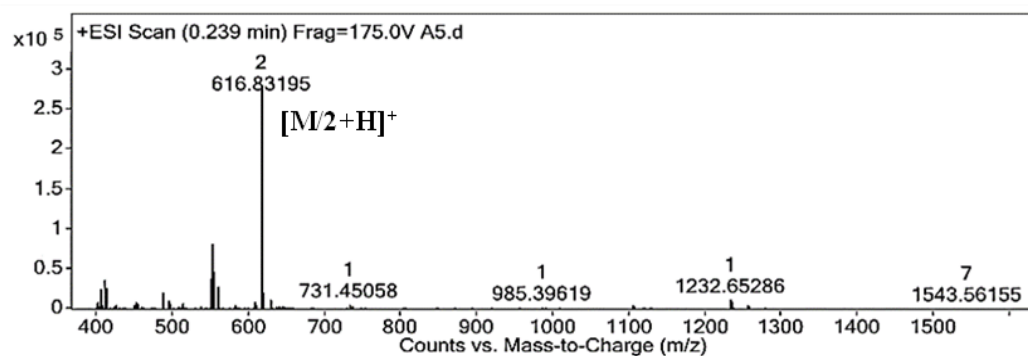
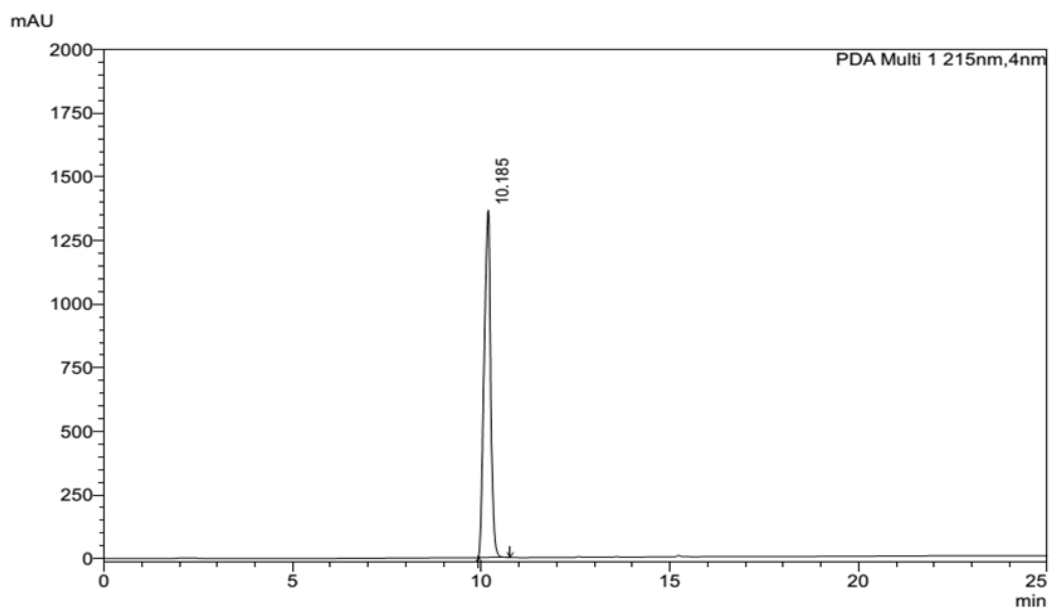
References	Artificial Hydrolase	Substrate	$k_{cat}/K_m$	Condition
Korendovych <sup>32</sup>	Ac-IHIHIYI-NH <sub>2</sub> +Cu <sup>II</sup>	DCFH-DA	61.2 (k <sub>2</sub> M <sup>-1</sup> min <sup>-1</sup> )	HEPES (pH 8)
<b>Our work</b>	<b>Akd<sup>NMC</sup>Py+Cu<sup>II</sup></b>	<b>DCFH-DA</b>	<b>120.96 (M<sup>-1</sup>min<sup>-1</sup>)</b>	<b>HEPES (pH 8)</b>

**Table S4.** Liquid chromatogram (LC) and mass (MS) profiles of different triazole products.**Table S5.** Characterizations of the peptidomimetics by HRMS and HPLC

Name	Sequence	Exact mass	Observed mass HRMS
<b>Aβ14-23</b>	His-Gln-Lys-Leu-Val-Phe-Phe -Ala-Glu-Asp	1231.6350	616.8319 [M/2+H] <sup>+</sup>
<b>Aβ14-23Py</b>	Py-His-Gln-Lys-Leu-Val-Phe-Phe-Ala-Glu-Asp	1473.7081	737.8486 [M/2+H] <sup>+</sup>
<b>Akd<sup>NMC</sup></b>	kd- His-Gln-Lys-Leu-Val-kd-Phe-Phe-Ala-Glu-Asp-kd	1906.9690	954.9907 [M/2+H] <sup>+</sup>
<b>Akd<sup>NMC</sup>Py</b>	Py-kd- His-Gln-Lys-Leu-Val-kd-Phe-Phe-Ala-Glu-Asp-kd	2149.0421	1076.0255 [M/2+H] <sup>+</sup> 717.687 [M/3+H] <sup>+</sup>
<b>HkdPy</b>	Py-kd-His	649.3012	650.3004 [M+H] <sup>+</sup>

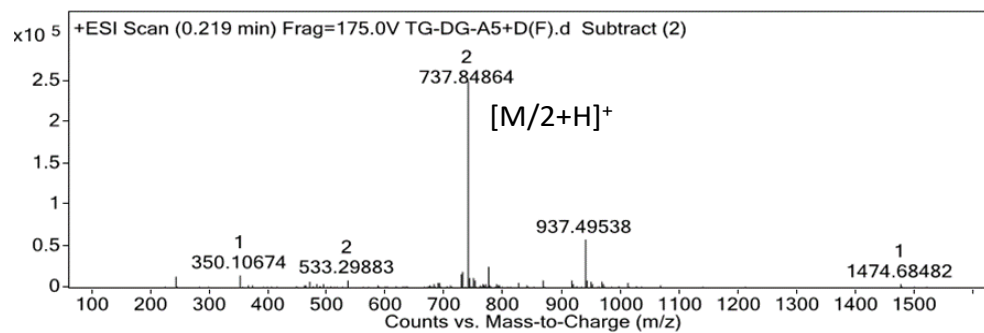
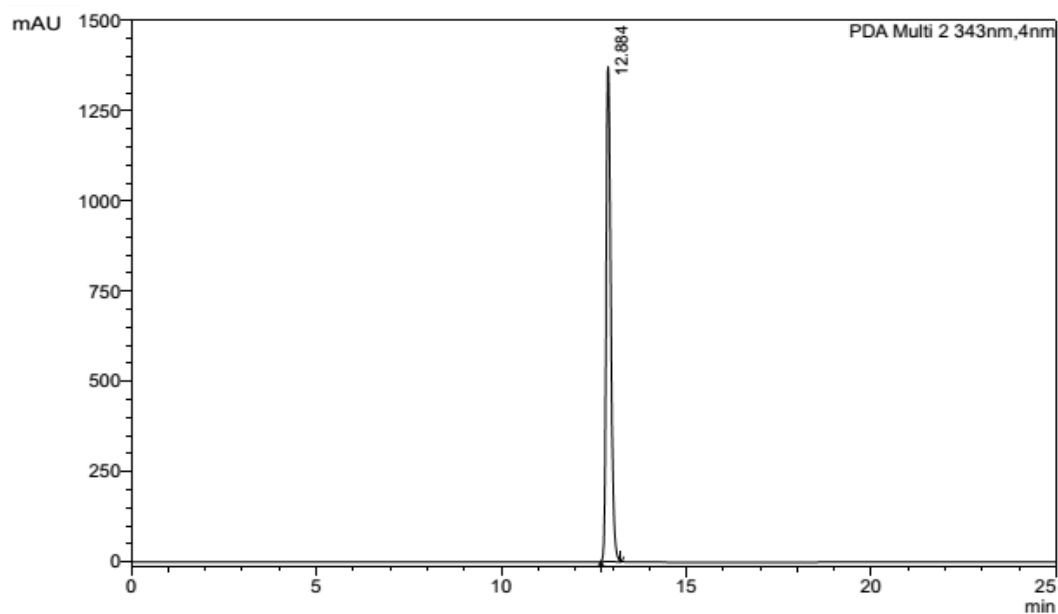
Peptide/ peptidomimetics	HPLC Gradient	Flow rate (ml/min)	Retention time (Rt)	Purity (%)
A $\beta$ 14-23	0-98 % MeCN (0.1% TFA) in H <sub>2</sub> O (0.1% TFA) for 25 min	8	10.1 min	>99
A $\beta$ 14-23Py	0-98 % MeCN (0.1% TFA) in H <sub>2</sub> O (0.1% TFA) for 25 min	8	12.8 min	>99
Akd <sup>NMC</sup>	0-98 % MeCN (0.1% TFA) in H <sub>2</sub> O (0.1% TFA) for 25 min	8	10.2 min	>99
Akd <sup>NMCPy</sup>	0-98 % MeCN (0.1% TFA) in H <sub>2</sub> O (0.1% TFA) for 25 min	8	13.0 min	>99

HPLC Chromatogram and HRMS data of A $\beta$ 14-23

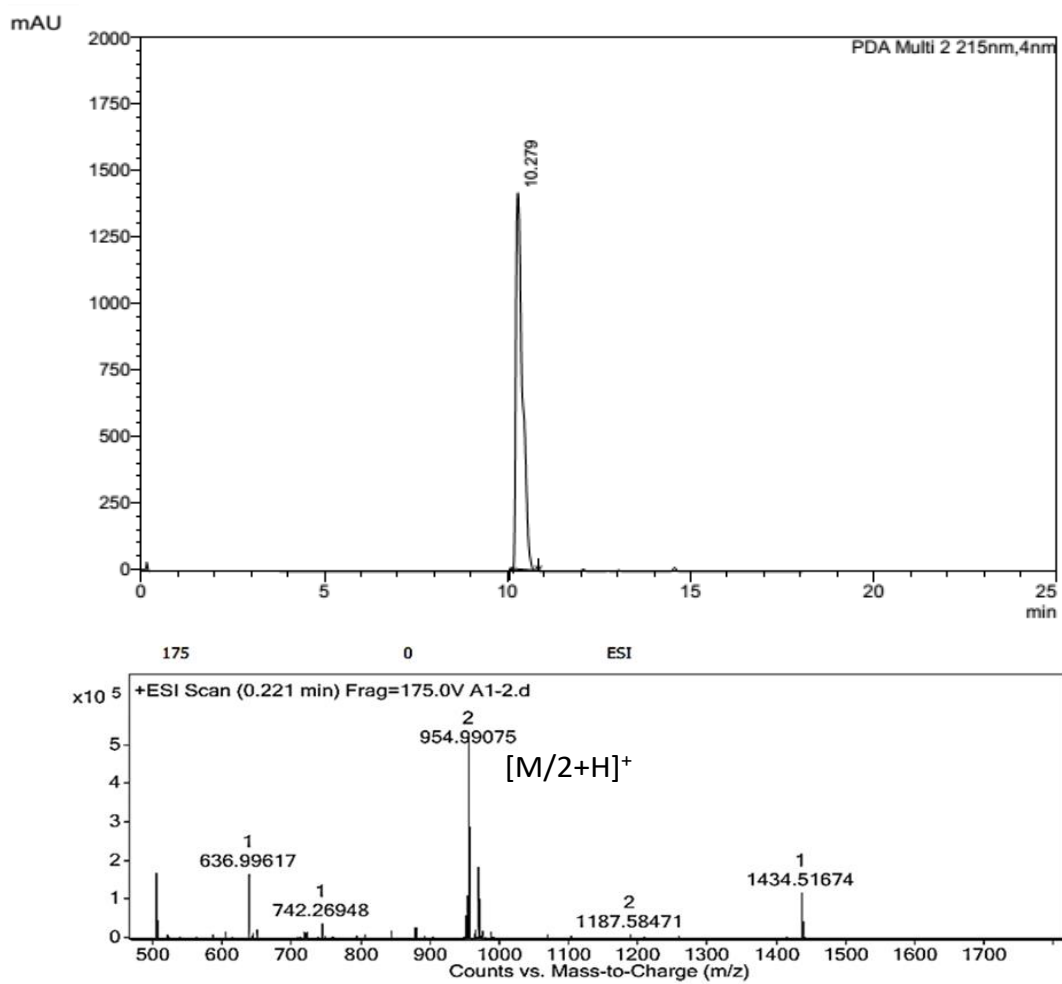




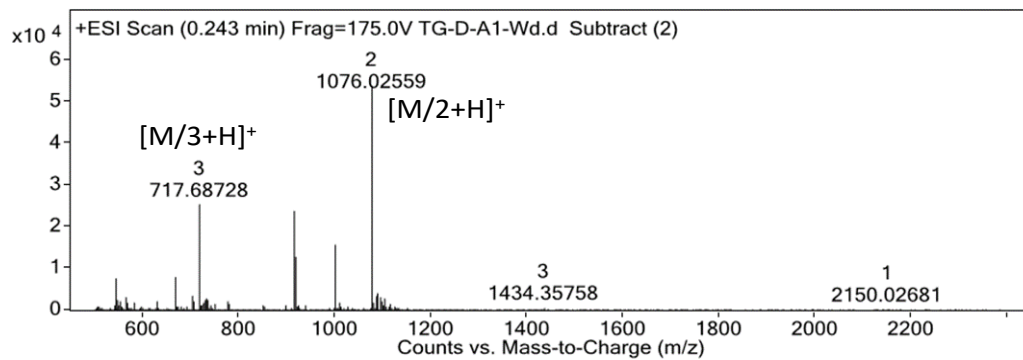
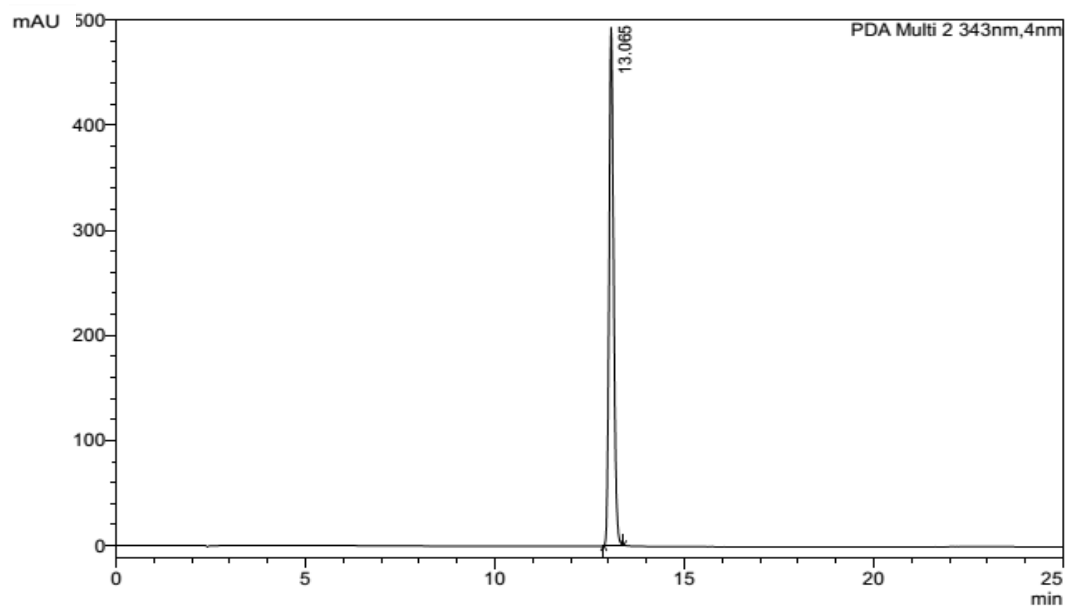
HPLC Chromatogram and HRMS data of A $\beta$ 14-23Py



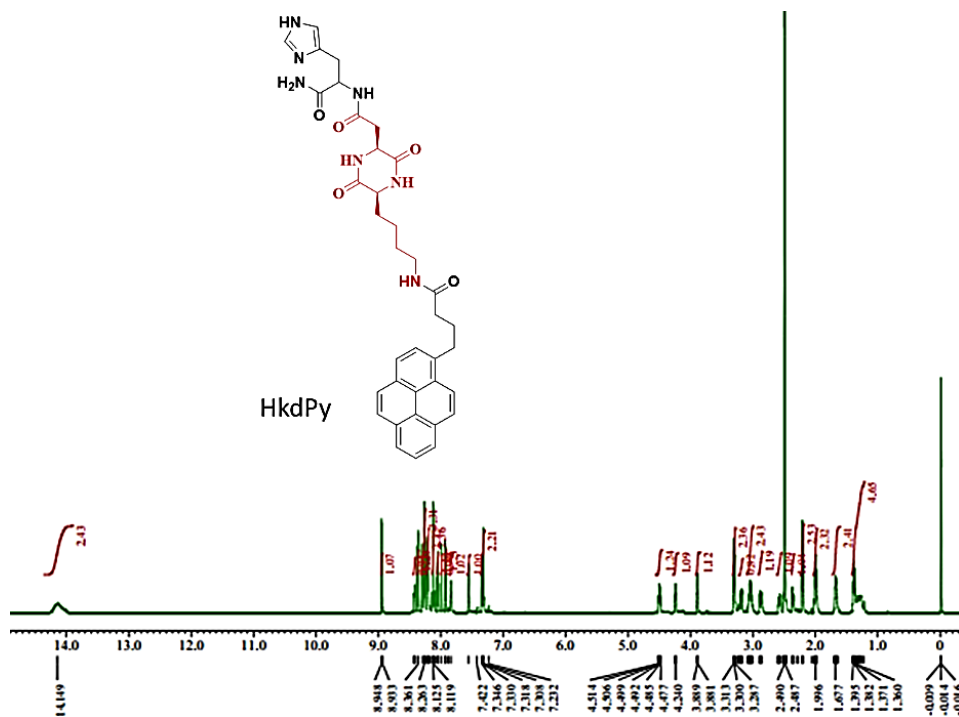
HPLC Chromatogram and HRMS data of Akd<sup>NMC</sup>



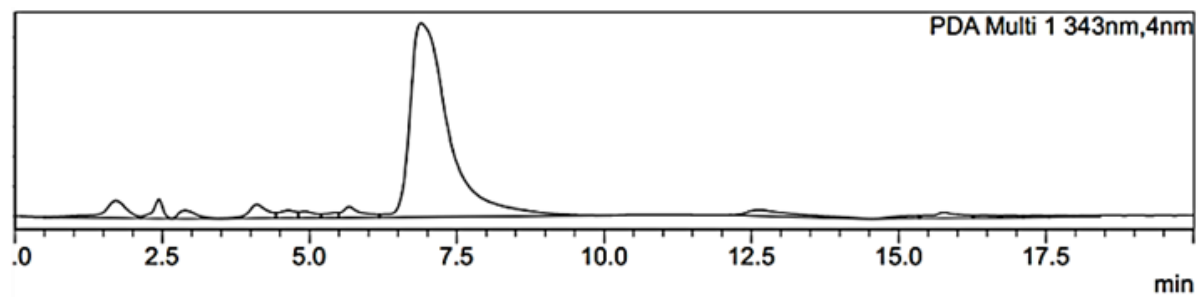
HPLC Chromatogram and HRMS data of Akd<sup>NMC</sup>Py



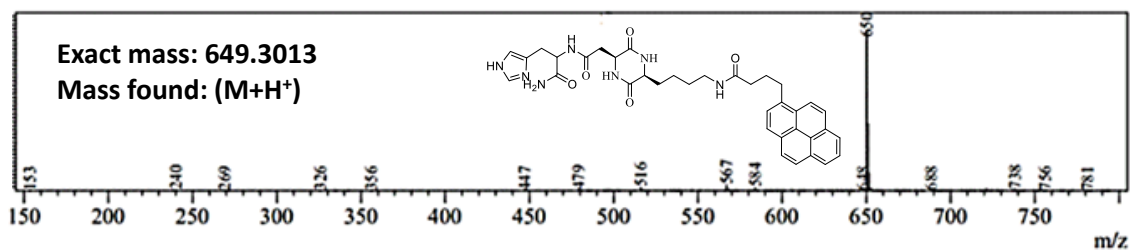
$^1\text{H}$  NMR and LCMS of HkdPy



LC



MS



## Statistical analysis of Figure 15C

Nonlin fit		A
		Data Set-A
		Y
1	Michaelis-Menten	
2	Best-fit values	
3	VMAX	6.024e-008
4	KM	0.4988
5	Std. Error	
6	VMAX	3.728e-009
7	KM	0.09788
8	95% Confidence Intervals	
9	VMAX	5.193e-008 to 6.854e-008
10	KM	0.2807 to 0.7168
11	Goodness of Fit	
12	Degrees of Freedom	10
13	R <sup>2</sup>	0.9804
14	Absolute Sum of Squares	7.311e-017
15	Sy.x	2.704e-009
16	Constraints	
17	KM	KM > 0.0
18	Number of points	
19	Analyzed	12

### 3.5 References

- [1] Avinash, M.; Govindaraju, T. Architectonics: design of molecular architecture for functional applications. *Acc. Chem. Res.* **2018**, *51*, 414-26.
- [2] Moorthy, H.; Datta, L. P.; Govindaraju, T. Molecular architectonics-guided design of biomaterials *Chem. Asian J* **2021**, *16*, 423-42.
- [3] Ariga, K.; Nishikawa, M.; Mori, T.; Takeya, J., Shrestha, L. K.; Hill, J. P. *Sci. Technol. Adv. Mater.* **2019**, *20*, 51-95.
- [4] Roy, B.; Govindaraju, T. Amino acids and peptides as functional components in arylenediimide-based molecular architectonics *Bull Chem Soc Jpn* **2019**, *92*, 1883-901.
- [5] Levin, A.; Hakala, T. A.; Schnaider, L.; Bernardes, G. J.; Gazit, E.; Knowles, T. P.; Biomimetic peptide self-assembly for functional materials *Nat. Rev. Chem.* **2020**, *4*, 615-34.
- [6] Ariga, K. L.; Shrestha, K.; *APL Mater.*, **2019**, *7*, 120903-12.
- [7] Hamley, I.W.; Peptide fibrillization *Angew. Chem. Int. Ed.* **2007**, *46*, 8128-47.
- [8] Knowles, T. P.; Buehler, M. J.; Nanomechanics of functional and pathological amyloid materials *Nat. Nanotechnol.* **2011**, *6*, 469-79.
- [9] Lengyel, Z.; Rufo, C. M.; Moroz, Y. S.; Makhlynets, O. V.; Korendovych, I. V.; Copper-containing catalytic amyloids promote phosphoester hydrolysis and tandem reactions *ACS Catal.* **2018**, *8*, 59-62.
- [10] Rufo, C. M.; Moroz, Y. S.; Moroz, O. V.; Stöhr, J.; Smith, T. A.; Hu, X.; et al. Short peptides self-assemble to produce catalytic amyloids *Nat. Chem.* **2014**, *6*, 303-9.
- [11] Roy, B.; Pal, S.; Govindaraju T. Intrinsic role of molecular architectonics in enhancing the catalytic activity of lead in glucose hydrolysis *ACS Appl. Mater. Interfaces* **2020**, *12*, 14057-63.
- [12] Díaz-Caballero, M.; Nuez-Martínez, S.; Peccati, M.; Rodríguez- L. F.; Santiago, M. Sodupe, et al. pH-responsive self-assembly of amyloid fibrils for dual hydrolase-oxidase reactions *ACS Catal.* **2020**, *11*, 595-607.
- [13] Balachandra, C.; Padhi, D.; Govindaraju, T. Cyclic Dipeptide: A privileged molecular scaffold to derive structural diversity and functional utility *ChemMedChem* **2021**, *16*, 1-31
- [14] Manchineella, S.; Govindaraju, T. Molecular self-assembly of cyclic dipeptide derivatives and their applications *ChemPlusChem* **2017**, *82*, 88-106.

- [15] Gazit, E.; Chen, Y.; Yang, Y.; Orr A. A.; Makam, P.; Redko, B. et al. Self-assembled peptide nano-superstructure towards enzyme mimicking hydrolysis *Angew. Chem. Int. Ed.* **2021**, *60*,17164-69
- [16] Gonzalez, P.; Vileno, B.; Bossak, K.; Khoury, E. L.; Hellwig, Y.; Bal, P. et al. Cu (II) binding to the peptide Ala-His-His, a chimera of the canonical Cu (II)-binding motifs Xxx-His and Xxx-Zzz-His *Inorg. Chem.* **2017**, *56*, 14870-79.
- [17] Madhu, C.; Voshavar, C.; Rajasekhar, K.; Govindaraju, T. Cyclic dipeptide based cell-penetrating peptidomimetics for effective DNA delivery *Org. Biomol. Chem.* **2017**, *15*, 3170-74.
- [18] Solomon, E. I. et al. Copper active sites in Biology *Chem. Rev.* **2014**, *114*, 7, 3659–3853.
- [19] Avinash, M.; Govindaraju, T. Two-dimensional Nanoarchitectonics: organic and hybrid materials *Nanoscale* **2012**, *4*, 6102-17.
- [20] Insua, I.; Montenegro, J. 1D to 2D Self Assembly of Cyclic Peptides *J. Am. Chem. Soc.* **2019**, *142*, 300-7.
- [21] Trott, O.; Olson, A. J. AutoDock Vina: improving the speed and accuracy of docking with a new scoring function, efficient optimization, and multithreading *J. Comput. Chem.* **2010**, *31*, 455-61.
- [22] Mondal, T.; Mandal, B. Total degradation of extracellular amyloids by miniature artificial proteases *Chem. Commun.* **2020**, *56*, 2348-51.
- [23] Giri, N.; James, S. L. A metal complex that imitates a micelle *Chem. Commun.* **2011**, *47*, 245-47.
- [24] Reddy, S. M. M.; Raßlenberg, E.; Sloan-Dennison, S.; Hesketh, S.; Silberbush, T.; Tuttle, O. T. et al. Elucidation of the structure of supramolecular polymorphs in peptide nanofibres using Raman spectroscopy *Adv. Mater.* **2020**, *32*, 2003511.
- [25] Makhlynets, O. V. Gosavi, P. M. Korendovych, I. V. Short Self-Assembling Peptides Are Able to Bind to Copper and Activate Oxygen *Angew. Chem. Int. Ed.* **2016**, *55*, 9017-20.
- [26] Filice, M. Palomo, J. M. Cascade Reactions catalyzed by bionanostructures *ACS Catal.* **2014**, *4*, 1588-98.
- [27] Friedmann, M. P. Torbeev, V. Zelenay, V. Sobol, A. Greenwald, Riek, J. R. Towards Prebiotic Catalytic Amyloids Using High Throughput Screening *PLoS One* **2015**, *10*, e0143948.

- [28] Du, Z. Yu, D. Du, Scott, X. P. Ren, Qu, J. X. Self-triggered click reaction in an Alzheimer's disease model: in situ bifunctional drug synthesis catalyzed by neurotoxic copper accumulated in amyloid- $\beta$  plaques *Chem. Sci.* **2019**, *10*, 10343-50.
- [29] Madhu, C.; Voshavar, C.; Rajasekhar, K.; Govindaraju, T. Cyclic dipeptide based cell-penetrating peptidomimetics for Effective DNA Delivery. *Org. Biomol. Chem.* **2017**, *15*, 3170–3174.
- [30] Konar, M.; Ghosh, D.; Samanta, S.; Govindaraju, T. Combating amyloid-induced cellular toxicity and stiffness by designer peptidomimetics *RSC Chem. Biol.*, **2022**, DOI: 10.1039/d1cb00235j
- [31] Piovesan, D.; Minervini, G.; Tosatto, S. C. The RING 2.0 web server for high quality residue interaction networks *Nucleic Acids Res.* **2016**, *44*, W367-W74.
- [32] Lengyel, Z. C.; Rufo, M.; Moroz, Y. S.; Makhlynets, O. V.; Korendovych, I. V. Copper-containing catalytic amyloids promote phosphoester hydrolysis and tandem reactions *ACS Catal.* **2018**, *8*, 59-62.



## **Chapter 4**

### **Dihydrophthalazinediones Accelerate Amyloid $\beta$ Peptide Aggregation to Nontoxic Species**



AD is a most common neurodegenerative disorder affecting more than 45 million people worldwide, which is expected to reach >135 million by 2050.<sup>1,2</sup> The pathophysiology of AD involve aberrant accumulation of amyloid plaques in the brain which cause multifaceted toxicity characterized by oxidative stress, synaptic dysfunction, neuroinflammation and mitochondrial damage leading to neuronal loss.<sup>3-9</sup> The toxic A $\beta$  plaques are predominantly formed by A $\beta$ 42 peptides which in turn are produced by proteolytic cleavage of amyloid precursor protein (APP), a transmembrane protein mostly expressed in the neuronal cells.<sup>1,10</sup> The soluble fragments of APP (A $\beta$  monomers) undergo self-aggregation from insoluble A $\beta$  plaques in the AD brain. The formation of this insoluble plaque is a complex multistep process that requires the organization of various short-lived and long-lived, on- and off-pathway aggregation species, whose chemical and biological actions are mostly unexplored<sup>11</sup>. Under AD conditions, A $\beta$  monomers transform into small  $\beta$ -sheet-rich oligomers and protofibrils that are on-pathway to the build-up of more ordered amyloid fibrils.<sup>12,13</sup> Besides, A $\beta$  monomers can form globular non- $\beta$ -sheet oligomers, which are eventually taking part in A $\beta$  self-aggregation by transforming themselves into  $\beta$ -sheet-rich species, this process is effectively modulated by well-designed A $\beta$  aggregation targeting small molecules.<sup>14,15</sup>

Dedicated efforts have been undertaken by researchers in developing small molecules, peptides, peptidomimetics, and antibodies to modulate the toxic amyloid aggregation process, by interfering with the self-aggregation process of A $\beta$  peptides.<sup>7, 16-25</sup> Notwithstanding, there are no clinically approved drugs for AD, which is attributed to limited or poor understanding of various underlying mechanisms of aggregation and ineffective designs of compounds to modulate the aggregation process.<sup>26</sup> The design of small molecules to modulate A $\beta$  aggregation is particularly interesting as the molecular interactions are considered at the early onset of the process and anticipated to help

in understanding the aggregation-based disease pathogenesis.<sup>22</sup> Osmolytes such as trimethylamine N-oxide and glycerol are shown to modulate (accelerate) the toxic A $\beta$  aggregation, which leads to the formation of nontoxic fibrillar structures<sup>27,28</sup>. In otherward, designer small molecules can effectively reduce the multifaceted A $\beta$  toxicity similar to A $\beta$  aggregation inhibitors by accelerating the nontoxic aggregation pathways. Some of our recent works involved the development of multifunctional small molecules and peptidomimetics to inhibit the toxic A $\beta$  aggregation pathways. In particular, peptoids and hybrid multifunctional modulators (HMMs) are reported as A $\beta$  aggregation inhibitors which established the fact that judiciously designed small molecules are the potential tools to ameliorate the toxic amyloid aggregation cascades by preventing the aggregation or dissolving the pre-formed aggregation species or influencing structural changes in the aggregation pathways.<sup>7, 16-19</sup> The current work deals with the acceleration of A $\beta$  aggregation to form nontoxic species by employing the hydrophobic and halogen interactions.

#### 4.1 Design and synthesis

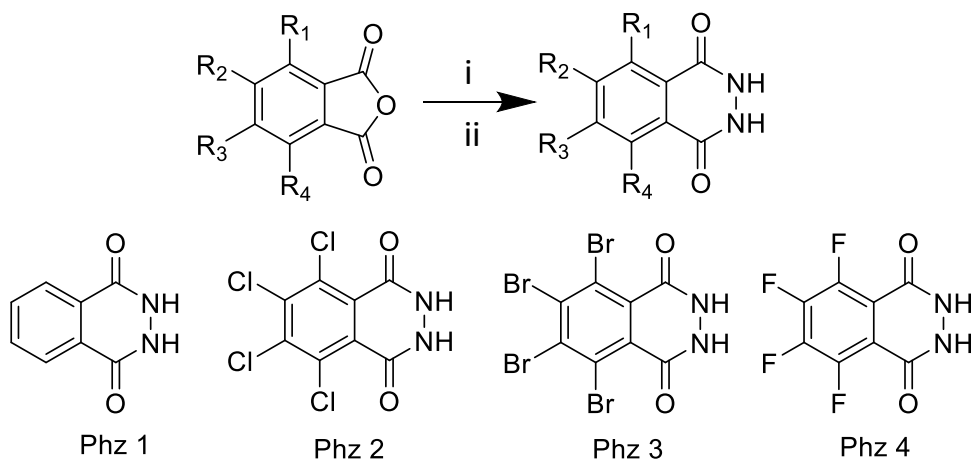
As discussed (*vide supra*), small molecule-based modulation of A $\beta$ 42 aggregation is essentially associated with two contrasting mechanism of actions, i) disrupt or stop the A $\beta$  self-aggregation, or ii) accelerate the aggregation towards the formation of nontoxic species. In this context, we designed and synthesized a set of 2,3-dihydrophthalazine-1,4-dione based small molecules (Phz 1-4) with different halogen substituents to modulate the A $\beta$  amyloidogenesis (Scheme 1). The detailed studies show that the fluorinated dihydrophthalazinedione derivative effectively modulate the aggregation towards nontoxic pathway. In literature, fluorinated compounds have been reported to modulate A $\beta$ 42 aggregation and contribute significantly in the PET imaging studies of A $\beta$  plaques.<sup>29-35</sup> Similarly, modulation of aggregation is reported when A $\beta$  peptide interacts with poly (tetrafluoroethylene) surfaces or fluorinated nanoparticles.<sup>36,37</sup> Among all the halogenated

surfaces, fluorinated surface showed better modulation efficiency which suggests that fluorine play an important role in the modulation of A $\beta$  aggregation process.<sup>37</sup> Strikingly, fluorinated derivative (Phz 4) accelerates the rate of A $\beta$  aggregation when compared to other halogenated (chloro and bromo) derivatives (Phz 2 and Phz 3, respectively) and non-halogenated derivative (Phz 1). The detailed biochemical and biophysical studies have revealed that Phz 4 possibly interact and interfere with amyloid self-aggregation of A $\beta$ 42 peptide<sup>38</sup> and accelerated the aggregation towards the formation of species that are non-cytotoxic to neuronal cells.

## **4.2 Results and discussion**

### **4.2.1 Synthesis of dihydrophthalazinedione derivatives**

2,3-Dihydrophthalazine-1,4-dione and its derivatives have potential pharmacological and biological implications.<sup>39</sup> The dihydrophthalazinediones are particularly interesting molecular scaffolds to design perspective AD therapeutic agents. In this article, we report design and syntheses of dihydrophthalazinedione (Phz 1) and tetra-halogen containing dihydrophthalazinedione derivatives (Phz 2, Phz 3 and Phz 4) to assess the role of halogen substitutions towards the modulation of A $\beta$ 42 aggregation (Scheme 1). The phthalic anhydride or and tetra-halogen substituted phthalic anhydrides (fluoro, chloro and bromo) were added to the glacial acetic acid solution and refluxed for 1 h under nitrogen atmosphere. Subsequently, hydrazine hydrate (N<sub>2</sub>H<sub>4</sub> H<sub>2</sub>O) was added to each of the reaction mixtures and refluxed for 1 h to obtain 2,3-dihydrophthalazine-1,4-dione derivatives (Phz 1-4) in good yield. All the compounds were thoroughly characterized by nuclear magnetic resonance (NMR) spectroscopy and high-resolution mass spectrometry (HRMS) analysis.



**Scheme 1.** Synthesis of 2,3-dihyphthalazine-1,4-dione derivatives (Phz 1-4). Reagents: i) AcOH, 120 °C, 1 h, reflux and ii) N<sub>2</sub>H<sub>4</sub>.H<sub>2</sub>O, 120 °C, 1 h, reflux.

#### 4.2.2 Inhibition of amyloid $\beta$ aggregation: thioflavin T assay

Initially, the aggregation propensity of A $\beta$ 42 was assessed in presence of dihyphthalazinedione derivatives (Phz 1-4) in thioflavin-T (ThT) fluorescence assay.<sup>7,16,40,41</sup> We examined the fibrillation of A $\beta$ 42 at a concentration of 10  $\mu$ M in phosphate buffer saline (PBS, 20 mM, pH=7.4) at 37 °C, in the absence and presence of Phz 1-4 (50  $\mu$ M). The data in Figure 1A show that ThT fluorescence ( $\lambda_{\text{ex}}=482$  nm,  $\lambda_{\text{em}}=482$  nm) was enhanced by about four-fold in presence of Phz 4, while Phz 1-3 showed an insignificant reduction in ThT fluorescence emission. The self-aggregation of Phz 4 was independently assessed in the presence and absence of ThT to rule out the self-induced fluorescence enhancement. We recorded ThT (10  $\mu$ M) emission spectra ( $\lambda_{\text{ex}}=442$ ) in presence of two different concentrations of Phz 4 (50 and 100  $\mu$ M) which did not show any interference of Phz 4 with ThT emission characteristics. These results showed that Phz 4 individually or with ThT is not capable of forming any higher-order aggregation to exhibit enhanced fluorescence (Figure 1B-C).

Next, we assessed the effect of Phz 4 on the aggregation kinetics of A $\beta$ 42 in the presence of pre-formed fibrils (Figure 1C). For this experiment, the pre-formed A $\beta$ 42 (20  $\mu$ M) aggregates were

incubated in PBS (control) and with two different concentrations of Phz 4 (100 and 200  $\mu\text{M}$ ). As expected, the ThT fluorescence gradually increased with time for A $\beta$ 42 aggregates in PBS. While the rate of fluorescence enhancement for A $\beta$ 42 in presence of Phz 4 was significantly higher which dependent on the concentration of Phz 4 and time (Figure 1C). This study reiterates that Phz 4 interferes with A $\beta$ 42 fibrillations and further accelerates A $\beta$ 42 aggregation process to form possibly reordered aggregation species. Generally, hydrophobic and hydrogen bonding interactions are among the two major driving forces that control protein aggregation.<sup>16,17,42,43</sup> There are three definite regions within the A $\beta$ 42 sequence that involved in its aggregation process, i) the central hydrophobic cluster corresponding to the A $\beta$ 17–21 region, ii) the A $\beta$ 23–28 region and the hydrophobic C-terminus.<sup>43</sup> The probable mode of interaction between Phz 4 and A $\beta$ 42 is speculated to involve fluorine interaction with the hydrophobic regions of the peptide sequence. The hydrophobic, hydrogen bonding, and fluorine interactions between A $\beta$ 42 aggregates and Phz 4 are speculated to contribute towards reorganization and acceleration of A $\beta$  assembly to form distinct aggregation species (vide infra) which show enhanced ThT fluorescence.

#### **4.2.3 Dot blot assay**

To further validate the acceleration of A $\beta$ 42 aggregation by Phz 4 in ThT fluorescence assay, dot blot analysis was performed. In a set of independent experiments A $\beta$ 42 monomer (10  $\mu\text{M}$ ) was incubated with Phz 1-4 (50  $\mu\text{M}$ ) independently for 48 h at 37 °C in PBS (pH= 7.4). The samples were spotted on a nitrocellulose membrane and treated with A $\beta$ 42 aggregate-specific antibody (OC) to determine the extent of aggregation. The blot intensity determined by the histogram analysis was found to be in the order Phz 4  $\approx$  Phz 2 > Phz 1 > Phz 3, which is in agreement with the data from ThT fluorescence assay (vide supra) and confirmed that

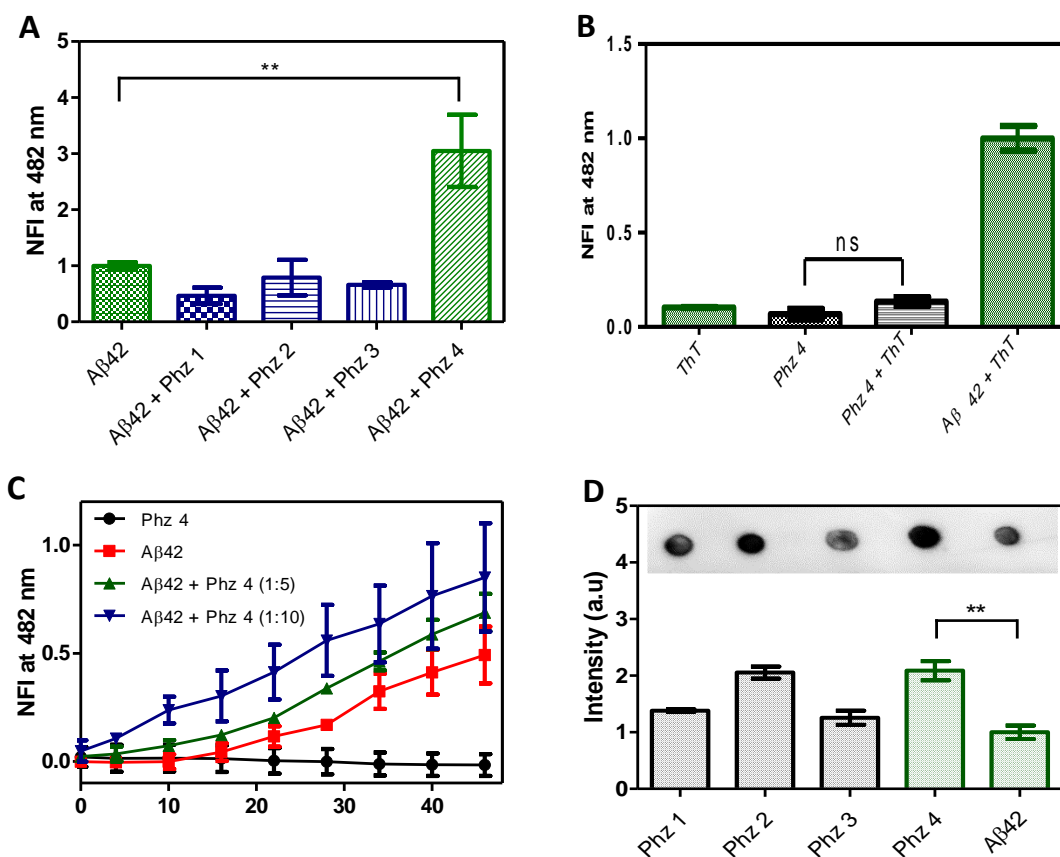


**Figure 1.** (A) The modulation of Aβ42 aggregation studied by thioflavin (ThT) assay, Aβ42 (10 μM) was incubated alone and independently with Phz 1-4 in 1: 5 stoichiometry and their influence on aggregation is quantified by measuring ThT fluorescence intensity, which is represented as normalized fluorescence intensity (NFI) at 482 nm for a given time point (48 h). (B) The self-aggregation of Phz 4 (25 μM) was monitored through ThT fluorescence assay. (C) Kinetic profiles of Aβ42 peptides (20 μM) in the absence and presence of Phz 4 (1: 5, 1: 10 molar ratios of Aβ42 to Phz 4). (D) Dot blot analysis of Aβ42 (10 μM) fibrils using amyloid fibrils specific primary antibody, OC (1: 3000) in the absence and presence of Phz 1-4 (50 μM). Each experiment was repeated thrice (n = 3); error bars represent the standard deviation (SD) One-way ANOVA analysis followed by Tukey's multiple comparison post-test was performed (p= 0.0014).

Phz 4 is a potent modulator of amyloid aggregation by accelerating the rate of the aggregation process (Figure 1D). On the other hand, a negligible effect was observed with Phz 1 and bromine-containing analogue (Phz 3). Although chlorine-containing analogue (Phz 2) showed modulation efficiency as good as Phz4 in dot blot assay, a marginal or low modulation effect was observed in ThT fluorescence assay (Figure 1A). Therefore, ThT fluorescence assay and dot blot analysis together revealed that Phz 4 is an effective and potent accelerator of Aβ42 aggregation compared



to other analogues Phz 1-3, which supports our design strategy and encouraged us to evaluate the cytotoxicity of Phz 4 induced amyloid aggregation species in cells.

#### 4.2.4 TEM analysis

The effect of Phz 4 treatment on the A $\beta$ 42 aggregation was investigated through transmission electron microscopy (TEM) analysis. A $\beta$ 42 monomers were incubated for 48 h at 37 °C in the presence and absence of Phz 4 and fibril formation was subsequently visualized under TEM (Figure 2). The soluble fraction of untreated aggregation reactions after 48 h incubation showed A $\beta$ 42 fibrils with a diameter of 10–15 nm (Figure 2A).

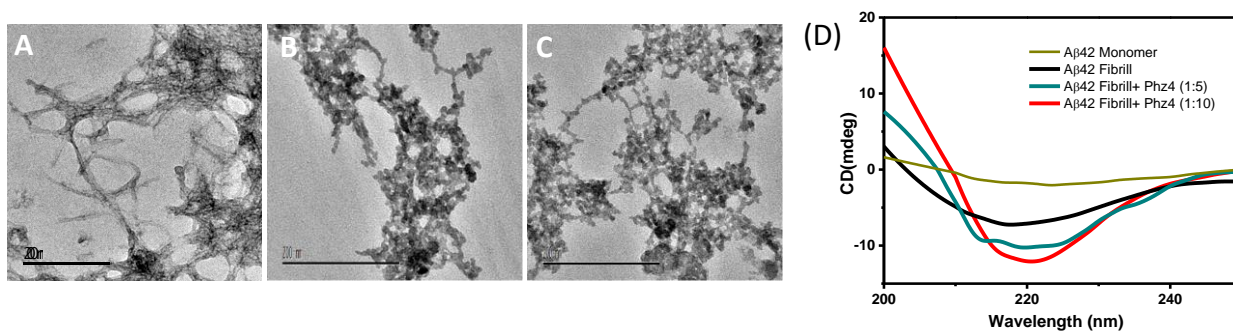


**Figure 2.** TEM images of A $\beta$ 42 aggregates in the absence (A) and in the presence of Phz 4 after 48 (B) and 72 h (C) of incubation. Scale bar: 200 nm. (D) CD study for A $\beta$ 42 monomer and A $\beta$ 42 fibril with increasing concentration of Phz4 (1:5, 1:10).

In contrast, Phz 4 treated A $\beta$ 42 samples for 48 h revealed large lumps of segregated structures which suggest the transformation of A $\beta$  peptide into larger reorganized and random aggregates upon treatment with Phz 4 (Figure 2B). Interestingly, further incubation of Phz 4 treated A $\beta$ 42 samples (72 h) displayed a higher amount of aggregates compared to 48 h incubated sample (Figure 2C). These results confirmed that Phz 4 accelerated A $\beta$ 42 aggregation in a distinct pathway (formation of more  $\beta$ -sheet rich species, Figure 2D) which is in good agreement with ThT fluorescence and dot blot assay data (Figure 1A and D).

### 4.2.5 Phz induced neuronal cell rescue assay

Next, we evaluated the toxicity of Phz 4 treated A $\beta$ 42 aggregates in the cellular milieu to assess its therapeutic potential to ameliorate the A $\beta$ 42 toxicity. The cytotoxicity of all compounds, Phz 1-4 was investigated in 3-(4,5-dimethylthiazol-2-yl)2,5-diphenyltetrazolium bromide (MTT) assay with PC12 cells. The cells were treated with compounds Phz 1-4 at three different concentrations (25, 50 and 100  $\mu$ M) and incubated for 24 h in cell growth media. Followed by the incubation, the experimental cells were further treated with MTT (15  $\mu$ L, 5 mg/mL) and further incubated for 3 h at 37  $^{\circ}$ C. Finally, the media was exchanged with DMSO and MeOH (1:1) mixture to assess the cytotoxicity through absorbance (570 nm) measurement. MTT assay data showed that compounds Phz 1-4 are biocompatible and nontoxic to cells at concentrations as high as 100  $\mu$ M (Figure 3A).

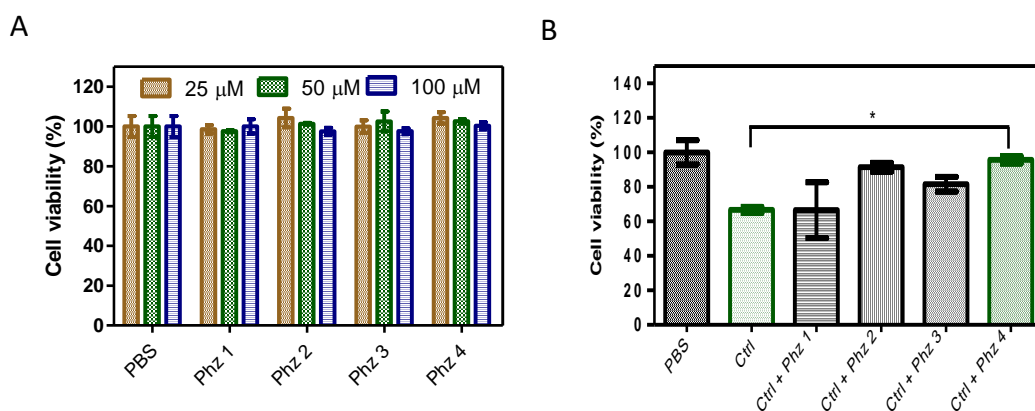


**Figure 3.** (A) Cell viability of PC12 cells treated with Phz 1-4 separately at three different concentrations (25, 50 and 100  $\mu$ M). (B) Cell viability (PC12 cells) after incubation (24 h) with A $\beta$ 42 fibrils (ctrl; 5  $\mu$ M) and A $\beta$ 42 (5  $\mu$ M) fibrils with Phz (1-4). Each experiment was repeated thrice (n = 3); error bars represent the standard deviation (SD). One-way ANOVA analysis followed by Tukey's multiple comparison post test were performed (p= 0.0293).

To simulate AD-like conditions, PC12 cells were treated with A $\beta$ 42 fibrillar aggregates (5  $\mu$ M) which showed 30% reduction in viability (70% viable cells) compared to untreated cells (control,

100% viability). Interestingly, the toxicity of A $\beta$ 42 fibrillar aggregates to PC12 cells was effectively modulated by Phz 4 (25  $\mu$ M) which rescue the cells and enhanced the cell viability to 95%. On the other hand, compounds Phz 1-3 showed 65, 92 and 80% cell viability, respectively, when compared to the control (100%) (Figure 3B). The viability data and rescue of PC12 cells from A $\beta$ 42 toxicity is in good agreement with the corresponding order of their acceleration efficacy towards A $\beta$ 42 aggregation observed in the ThT fluorescence assay, dot blot analysis and TEM data. The A $\beta$  oligomers and fibrils are known to interact with cell membranes causing cellular toxicity and neuronal death.<sup>1,16,19,44</sup> In this context, Phz 4 and Phz 2 interact with A $\beta$ 42 and drive its aggregation to nontoxic species through distinct aggregation pathways (globular intermediates) and protect cells from membrane toxicity and apoptosis. Previous work from our laboratory has shown that toxicity monitored by the cytotoxicity assay and ROS production correlates directly with the extent of the interaction of the oligomers and fibrils with cell membranes<sup>16,18</sup> and the current work showed markedly reduced toxicity of A $\beta$ 42 in the presence of Phz 4, which drives the aggregation of A $\beta$ 42 to form nontoxic species.

### **4.3 Conclusion**

We synthesized dihydrophthalazinedione derivatives (Phz 1-4) and studied their modulation efficiency against A $\beta$ 42 aggregation to ameliorate A $\beta$ 42 toxicity. The detailed studies from ThT fluorescence assay, dot blot and TEM analysis demonstrated that Phz 4 is a potent accelerator to drive the A $\beta$ 42 aggregation to nontoxic species compared to Phz 1-3. In addition to possible hydrophobic and hydrogen bonding interactions, fluorine interactions of Phz 4 with A $\beta$ 42 peptide induce distinct aggregation through conformational intermediates (globular intermediates) to form nontoxic species as revealed by the cell viability and protection of PC12 cells from A $\beta$  toxicity (Figure 4). Overall, the excellent cell viability and neuronal rescue from amyloid toxicity by Phz

4 demonstrated an alternative route to target the amyloid aggregation process (accelerating the A $\beta$  aggregation to nontoxic species) employing fluorinated compounds. Furthermore, there is a scope to enhance the modulation efficiency of Phz 4 through additional chemical modifications to develop effective therapeutic agents to tackle the multifaceted A $\beta$  toxicity of AD.

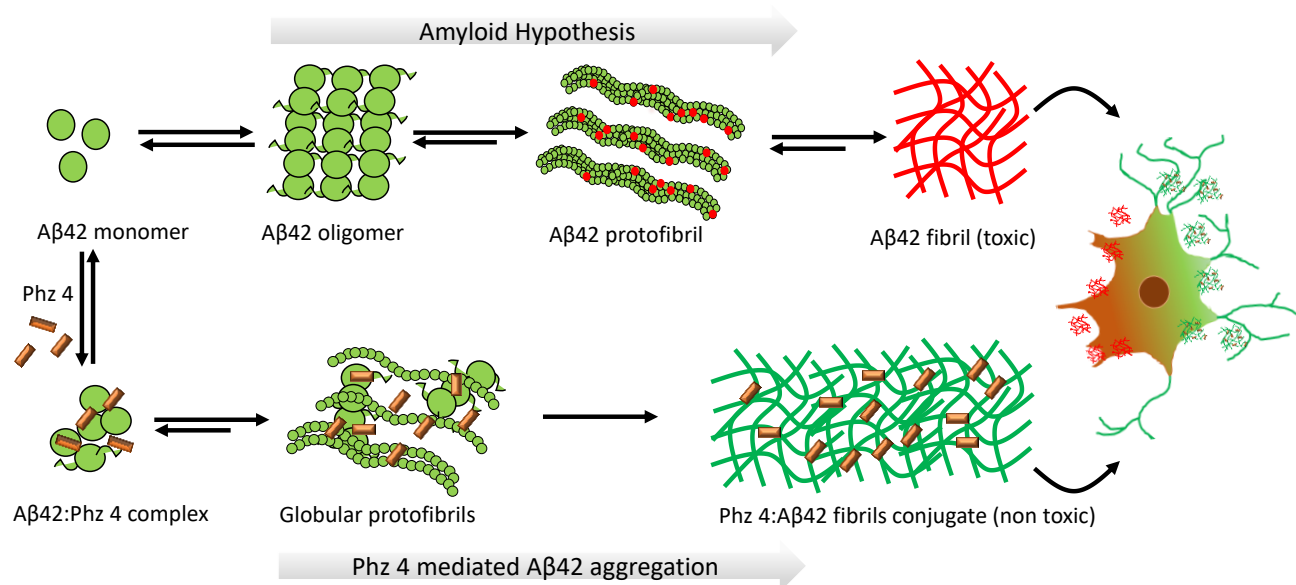


**Figure 4.** Schematic illustration of A $\beta$ 42 aggregation in the absence and presence of Phz 4 to form toxic and nontoxic aggregation species, respectively.

## 4.4 Materials and methods

### 4.4.1 Syntheses of dihydrophthalazinedione derivatives

The phthalic anhydride derivatives in AcOH were refluxed at 120 °C. After 1 h, the reaction mixture was cooled to 25 °C and hydrazine monohydrate was added dropwise into the reaction flask followed by refluxing the reaction mixture at 120 °C for 30 min (Scheme 1). The product was filtered and washed with petroleum ether (3 x 10 mL) and dried in a vacuum. The overall reaction is a two-step process, involving hydrolysis of anhydride derivative and condensation

reaction between the acid and hydrazine hydrate to give the desired product in good yield. All dihydrophthalazinedione derivatives were prepared by above-mentioned procedure.

#### 4.4.2 A $\beta$ 42 monomer and fibrils

A $\beta$ 42 (PP69-0.25MG, Merck) peptide was dissolved in 1, 1, 1, 3, 3, 3-hexa-fluoro-2-propanol (HFIP, Spectrochem). After sonication for 45 min at room temperature, HFIP was first removed by nitrogen gas flow and stored under vacuum. The concentration of A $\beta$ 42 peptide was determined by UV–vis spectrometry (Agilent Technologies, Cary 5000 UV-vis-NIR spectrophotometer) using a molar extinction coefficient of  $1450 \text{ cm}^{-1} \text{ M}^{-1}$  at 276 nm. A $\beta$ 42 peptide sample was dissolved in PBS (20 mM, pH= 7.4) containing 2% DMSO to obtain a final concentration of 100  $\mu\text{M}$  (monomer).<sup>18</sup> The A $\beta$ 42 fibrils were prepared by incubating A $\beta$ 42 monomer for 48 h in PBS (20 mM, pH = 7.4). ThT fluorescence and CD measurements were carried out to confirm the formation of A $\beta$ 42 fibrils.

#### 4.4.3 Thioflavin T (ThT) fluorescence assay

All the dihydrophthalazinedione derivatives were dissolved in DMSO. Phz 1-4 were added separately to the freshly prepared A $\beta$ 42 (10  $\mu\text{M}$ ) sample in PBS buffer (20 mM, pH 7.4) and kept at 37 °C. For kinetic studies, A $\beta$ 42 (20  $\mu\text{M}$ ) sample was pre-incubated for 24 h at 37 °C. The ThT solution was filtered using a 0.2 mm syringe filter before adding to the A $\beta$  samples. The ThT bound to fibrils exhibits excitation maximum at 442 nm and emission at 482 nm.<sup>16,19</sup> ThT (5–10  $\mu\text{M}$ ) was added and fluorescence was recorded at 482 nm after 48 h incubation using SpectraMax i3x microplate reader (Molecular Devices). The data were plotted and analyzed by GraphPad Prism 5 software.

#### **4.4.4 Dot blot analysis**

All compounds (Phz 1-4, 50  $\mu$ M) were independently added to a freshly prepared A $\beta$ 42 (10  $\mu$ M) sample in PBS (20 mM, pH 7.4) and incubated at 37 °C for 48 h. Then the incubated samples were spotted on PVDF membranes (Biorad). The nonspecific sites were blocked using skim milk for 1 h at room temperature and the membranes were incubated overnight with A $\beta$ 42 fibrils specific primary antibody, OC (1: 1000, Merck Millipore) at 4 °C. After incubation, the membranes were washed with PBS (3  $\times$  5 min) and further incubated with the secondary antibody (1:10000) conjugated with horseradish peroxidase (HRP) for 2 h at room temperature.<sup>19</sup> Finally, the membranes were washed with PBS (3  $\times$  5 min) and incubated with enhanced chemiluminescence (ECL) reagent for 2 min and the chemiluminescence was recorded in Gel Doc (Gel Doc XR + System Biorad). The blot intensity of all the samples was quantified and analyzed by histogram analysis in ImageJ software.

#### **4.4.5 Transmission electron microscopy (TEM)**

The A $\beta$ 42 peptide (100  $\mu$ M) was incubated at 37 °C with each of the dihydrophthalazinedione derivatives (2 mM) in a PBS buffer (20 mM, pH= 7.4) for 48 h. The incubated samples were placed on a copper grid carbon support film (400 mesh, 3 mm) for 20 min and negative staining was performed with uranyl acetate (2%). Further, excess uranyl acetate and salts were washed with deionized water (Milli-Q). The grids were visualized using a JEOL (JEM3010) TEM instrument operating at 300 kV accelerating voltage.

#### **4.4.6 Cell viability assay**

To assess the effect of A $\beta$ 42 in the absence and presence of dihydrophthalazinedione derivatives on PC12 cells, MTT (3-(4, 5-dimethylthiazol-2-yl)-2, 5-diphenyltetrazolium bromide) assay was

performed. At first PC12 cells were seeded in a 96-well plate at a density of 12,000 cells/well in RPMI (Roswell Park Memorial Institute) medium (Gibco, Invitrogen) with fetal bovine serum (FBS, 10%), horse serum (HS, 5%), and pen-strep (1%) at 37 °C in an atmosphere of 5% CO<sub>2</sub>. The media was replaced with low serum media (RPMI, 2% serum) and exposed for 24 h to Aβ42 fibrils (5 μM) and pre-incubated Aβ42 fibrils with Phz 1-4 (25 μM). Then 15 μL of MTT solution (5 mg/mL) was added to each well and incubated for 3 h. The media was discarded and 100 μL of 1:1 (DMSO: methanol) solution was added and the reduced form of MTT was measured by recording absorption at 570 nm (significance was determined by one way ANOVA from GraphPad prism).<sup>16</sup>

#### 4.4.7 Characterization of dihydrophthalazinedione derivatives

**2,3-Dihydrophthalazine-1,4-dione (Phz1).** White solid (Yield 63 %), <sup>1</sup>H-NMR (400 MHz, DMSO-d<sub>6</sub>): δppm 7.88 (dd, J = 6 Hz, 2H), 8.06 (t, J = 5.2 Hz, 2H), 11.52 (s, 2H); <sup>13</sup>C NMR (100 MHz, DMSO-d<sub>6</sub>): 167.9, 154.5, 132.5, 127.1, 125.0 HRMS (ESI): Molecular weight (MW): Calcd. 162.0429 for C<sub>8</sub>H<sub>6</sub>N<sub>2</sub>O<sub>2</sub>, found 163.0503 [M+H]<sup>+</sup>.

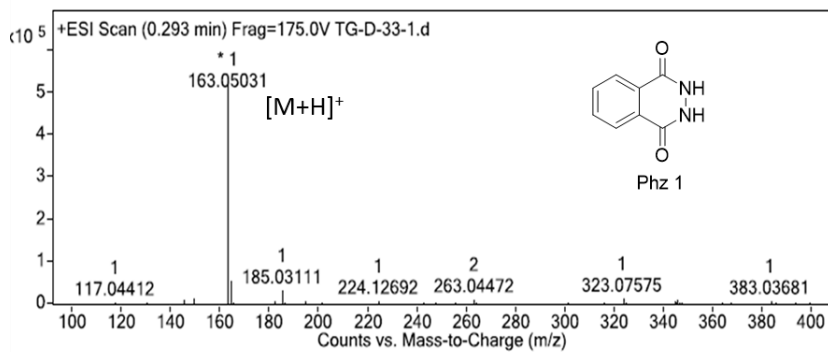
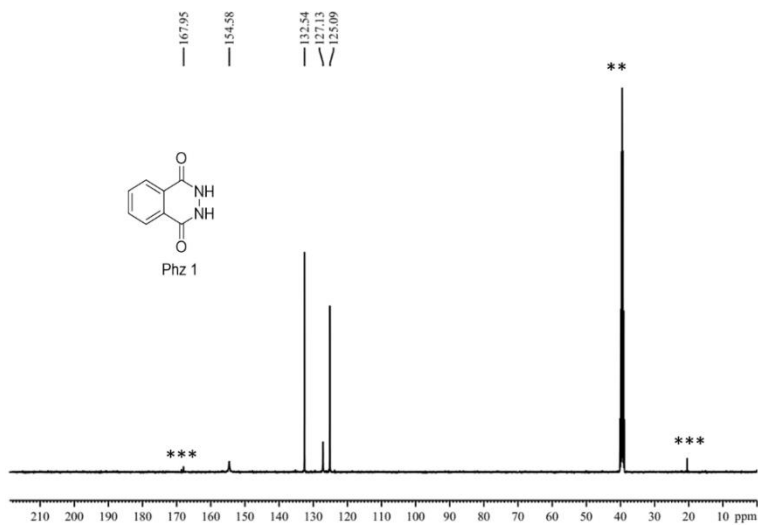
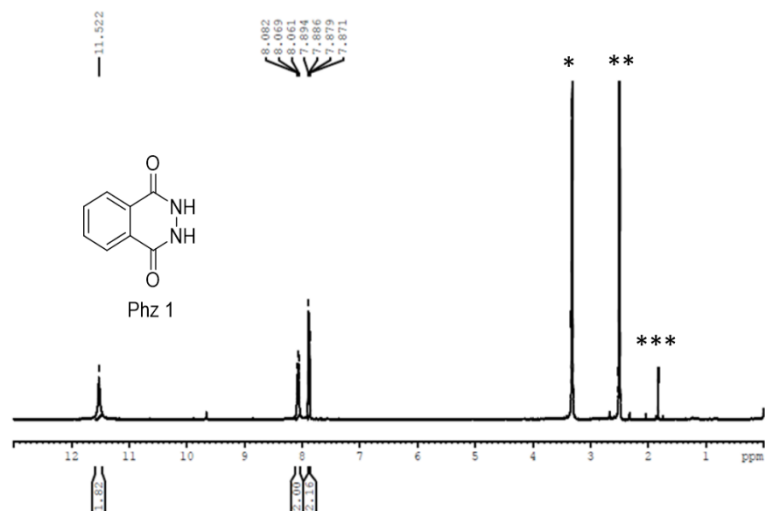
**5,6,7,8-Tetrachloro-2,3-dihydrophthalazine-1,4-dione (Phz 2).** White solid (Yield 83 %); <sup>1</sup>H-NMR (400 MHz, DMSO-d<sub>6</sub>): δppm 10.80 (s, 2H); <sup>13</sup>C NMR (100 MHz, DMSO-d<sub>6</sub>): 168.5, 160.8, 139.1, 128.8, 126.1; HRMS (ESI): MW: Calcd. 297.887 for C<sub>8</sub>H<sub>2</sub>Cl<sub>4</sub>N<sub>2</sub>O<sub>2</sub>, found 298.8930 [M+H]<sup>+</sup>, 299.8961 [M+2H]<sup>+</sup>, 300.8930 [M+3H]<sup>+</sup>.

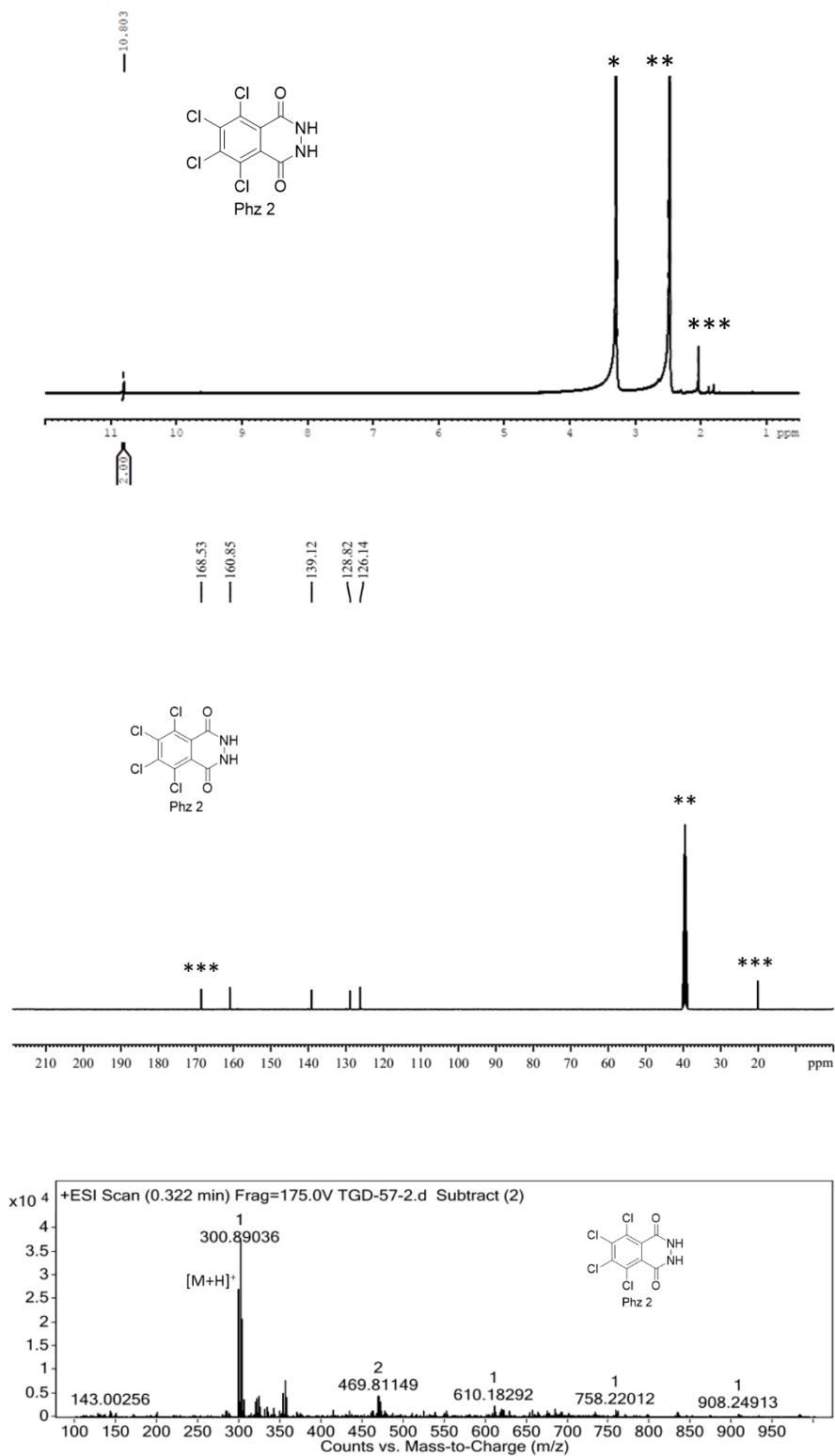
**5,6,7,8-Tetrabromo-2,3-dihydrophthalazine-1,4-dione (Phz 3).** Light yellow solid (Yield 90 %), <sup>1</sup>H-NMR (400 MHz, DMSO-d<sub>6</sub>): δppm 10.78 (s, 2H), <sup>13</sup>C NMR (100 MHz, DMSO-d<sub>6</sub>) 168.2, 161.2, 137.3, 128.9, 121.2; HRMS (ESI): MW: Calcd. 473.685 for C<sub>8</sub>H<sub>2</sub>Br<sub>4</sub>N<sub>2</sub>O<sub>2</sub> found 474.6899 [M+H]<sup>+</sup>, 476.478.6886 [M+2H]<sup>+</sup>, 478.6857 [M+3H]<sup>+</sup>.

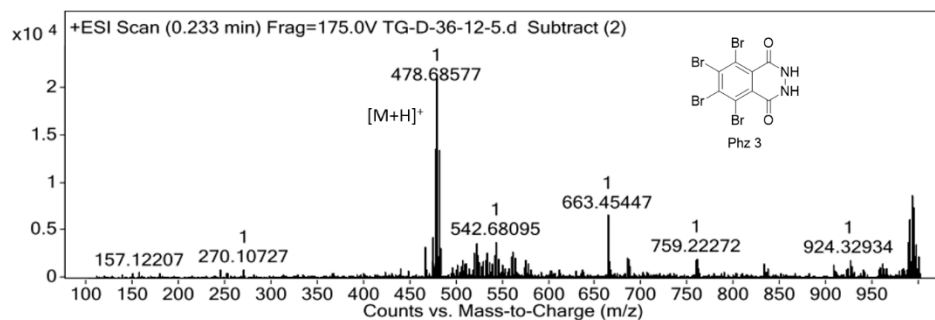
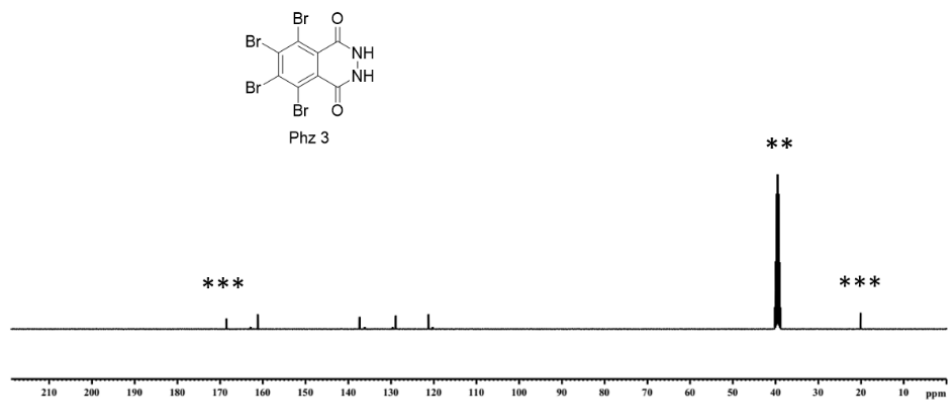
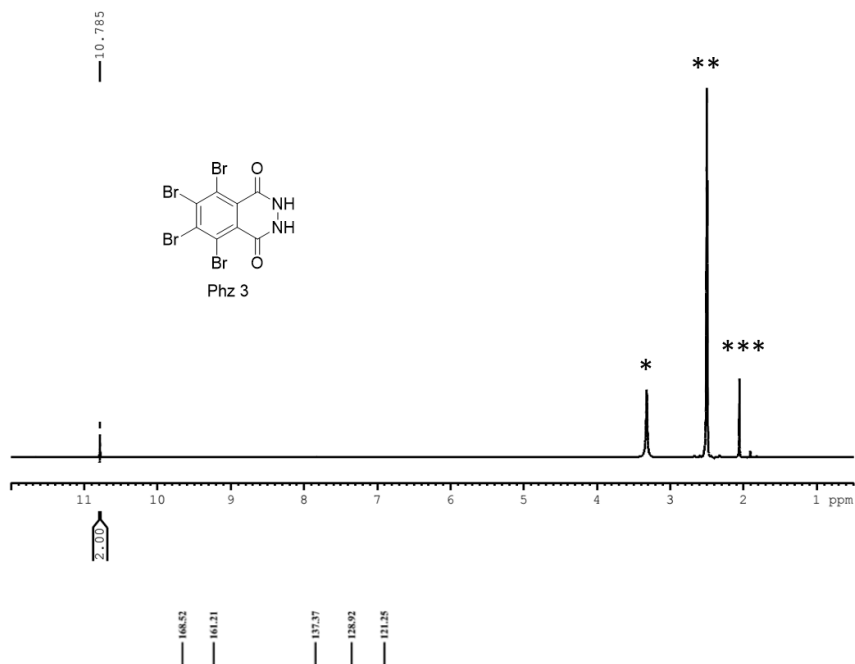
**5,6,7,8-Tetrafluoro-2,3-dihydrophthalazine-1,4-dione (Phz 4).** White solid (Yield 70 %), <sup>1</sup>H-NMR (400 MHz, DMSO-d<sub>6</sub>) δppm 9.66 (s, 2H); <sup>13</sup>C NMR (100 MHz, DMSO-d<sub>6</sub>) δppm 173.9, 169.0, 167.9, 143.6, 141.1; <sup>19</sup>F NMR(400 MHz, DMSO-d<sub>6</sub>): δppm -137.4, -140.1, -147.8, -150.0; HRMS (ESI) MW: Calcd. 234.0052 for C<sub>8</sub>H<sub>2</sub>F<sub>4</sub>N<sub>2</sub>O<sub>2</sub> found 235.0153 [M+H]<sup>+</sup>.

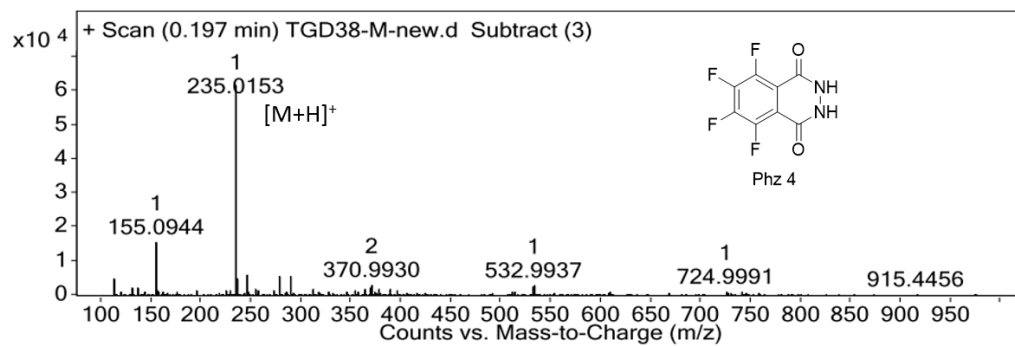
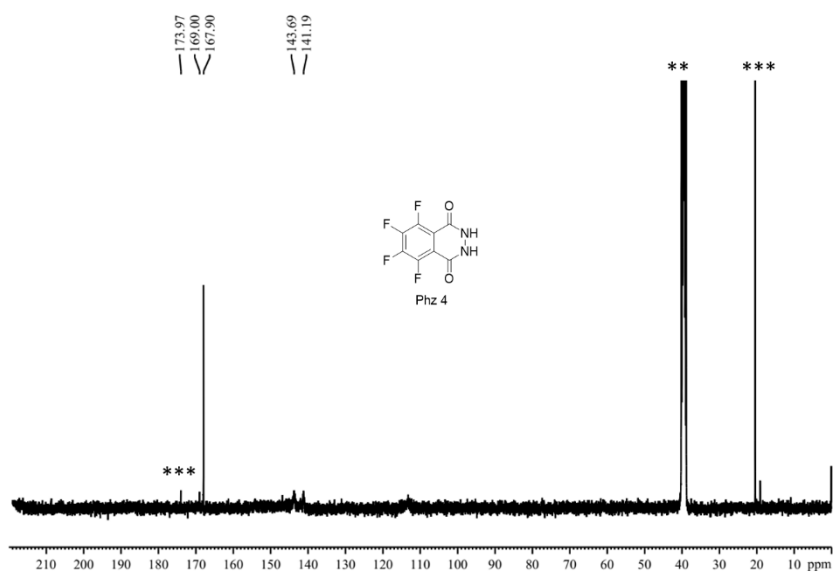
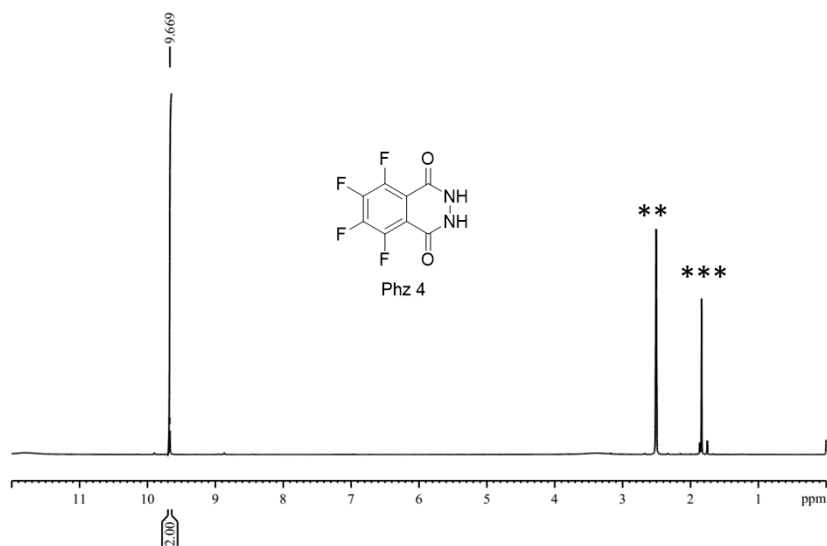


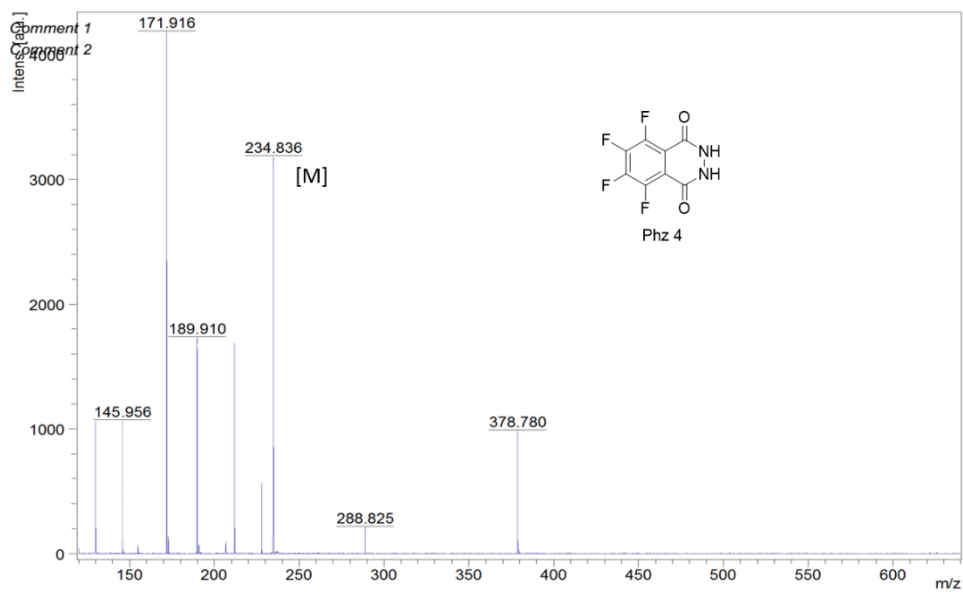
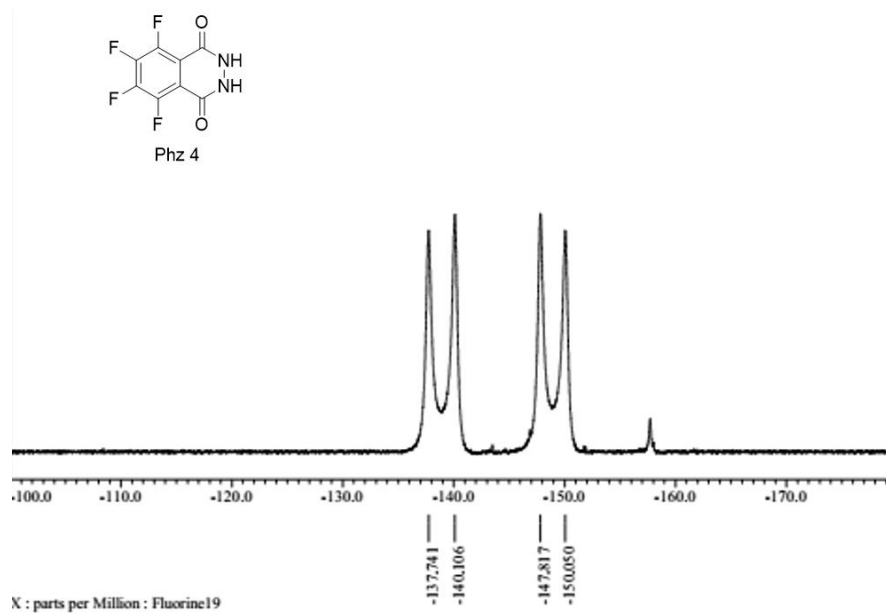
## Characterization data of compounds Phz 1-4

NMR ( $^1\text{H}$ ,  $^{13}\text{C}$ ) and HRMS data of Phz 1

NMR ( $^1\text{H}$ ,  $^{13}\text{C}$ ) and HRMS data of Phz 2

NMR ( $^1\text{H}$ ,  $^{13}\text{C}$ ) and HRMS data of Phz 3

NMR ( $^1\text{H}$ ,  $^{13}\text{C}$ ,  $^{19}\text{F}$ ), HRMS, MALDI data of Phz 4

**Note**

\* H<sub>2</sub>O (in DMSO-d<sub>6</sub>)

\*\* DMSO-d<sub>6</sub>

\*\*\* CH<sub>3</sub>COOH

## Statistical analysis of Figure 1A

1way ANOVA						
1	Table Analyzed	Data 4				
2						
3	One-way analysis of variance					
4	P value	0.0014				
5	P value summary	**				
6	Are means signif. different? (P < 0.05)	Yes				
7	Number of groups	5				
8	F	10.32				
9	R squared	0.8050				
10						
11	ANOVA Table	SS	df	MS		
12	Treatment (between columns)	13.38	4	3.344		
13	Residual (within columns)	3.240	10	0.3240		
14	Total	16.62	14			
15						
16	Tukey's Multiple Comparison Test	Mean Diff.	q	Significant? P < 0.05?	Summary	95% CI of diff
17	Aβ42 vs Aβ42 + Phz 1	0.5354	1.629	No	ns	-0.9942 to 2.065
18	Aβ42 vs Aβ42 + Phz 2	0.2106	0.6408	No	ns	-1.319 to 1.740
19	Aβ42 vs Aβ42 + Phz 3	0.3392	1.032	No	ns	-1.190 to 1.869
20	Aβ42 vs Aβ42 + Phz 4	-2.049	6.235	Yes	**	-3.579 to -0.5195
21	Aβ42 + Phz 1 vs Aβ42 + Phz 2	-0.3248	0.9882	No	ns	-1.854 to 1.205
22	Aβ42 + Phz 1 vs Aβ42 + Phz 3	-0.1962	0.5970	No	ns	-1.726 to 1.333
23	Aβ42 + Phz 1 vs Aβ42 + Phz 4	-2.585	7.864	Yes	**	-4.114 to -1.055
24	Aβ42 + Phz 2 vs Aβ42 + Phz 3	0.1286	0.3912	No	ns	-1.401 to 1.658
25	Aβ42 + Phz 2 vs Aβ42 + Phz 4	-2.260	6.876	Yes	**	-3.789 to -0.7301
26	Aβ42 + Phz 3 vs Aβ42 + Phz 4	-2.388	7.267	Yes	**	-3.918 to -0.8587

## Statistical analysis of Figure 1B

1way ANOVA						
1	Table Analyzed	Data 3				
2						
3	One-way analysis of variance					
4	P value	P<0.0001				
5	P value summary	***				
6	Are means signif. different? (P < 0.05)	Yes				
7	Number of groups	4				
8	F	145.7				
9	R squared	0.9820				
10						
11	ANOVA Table	SS	df	MS		
12	Treatment (between columns)	1.821	3	0.6071		
13	Residual (within columns)	0.03333	8	0.004166		
14	Total	1.855	11			
15						
16	Tukey's Multiple Comparison Test	Mean Diff.	q	Significant? P < 0.05?	Summary	95% CI of diff
17	ThT vs Phz 4	0.03544	0.9510	No	ns	-0.1333 to 0.2042
18	ThT vs Phz 4 + ThT	-0.03123	0.8380	No	ns	-0.2000 to 0.1375
19	ThT vs Aβ42 + ThT	-0.8967	24.06	Yes	***	-1.065 to -0.7279
20	Phz 4 vs Phz 4 + ThT	-0.06667	1.789	No	ns	-0.2354 to 0.1021
21	Phz 4 vs Aβ42 + ThT	-0.9321	25.01	Yes	***	-1.101 to -0.7633
22	Phz 4 + ThT vs Aβ42 + ThT	-0.8654	23.22	Yes	***	-1.034 to -0.6967

Statistical analysis of Figure 1D

1way ANOVA						
1	Table Analyzed	Data 2				
2						
3	One-way analysis of variance					
4	P value	0.0002				
5	P value summary	***				
6	Are means signif. different? (P < 0.05)	Yes				
7	Number of groups	5				
8	F	17.22				
9	R squared	0.8732				
10						
11	ANOVA Table	SS	df	MS		
12	Treatment (between columns)	2.883	4	0.7208		
13	Residual (within columns)	0.4186	10	0.04186		
14	Total	3.302	14			
15						
16	Tukey's Multiple Comparison Test	Mean Diff.	q	Significant? P < 0.05?	Summary	95% CI of diff
17	Phz 1 vs Phz 2	-0.6716	5.686	Yes	*	-1.221 to -0.1219
18	Phz 1 vs Phz 3	0.1256	1.064	No	ns	-0.4241 to 0.6754
19	Phz 1 vs Phz 4	-0.7061	5.978	Yes	*	-1.256 to -0.1564
20	Phz 1 vs Aβ42	0.3830	3.242	No	ns	-0.1668 to 0.9327
21	Phz 2 vs Phz 3	0.7973	6.750	Yes	**	0.2475 to 1.347
22	Phz 2 vs Phz 4	-0.03445	0.2917	No	ns	-0.5842 to 0.5153
23	Phz 2 vs Aβ42	1.055	8.928	Yes	***	0.5048 to 1.604
24	Phz 3 vs Phz 4	-0.8317	7.041	Yes	**	-1.381 to -0.2820
25	Phz 3 vs Aβ42	0.2573	2.178	No	ns	-0.2924 to 0.8071
26	Phz 4 vs Aβ42	1.089	9.220	Yes	***	0.5393 to 1.639

Statistical analysis of Figure 3B

1way ANOVA						
1	Table Analyzed	Data 2				
2						
3	One-way analysis of variance					
4	P value	0.0293				
5	P value summary	*				
6	Are means signif. different? (P < 0.05)	Yes				
7	Number of groups	6				
8	F	3.703				
9	R squared	0.6068				
10						
11	ANOVA Table	SS	df	MS		
12	Treatment (between columns)	3177	5	635.4		
13	Residual (within columns)	2099	12	171.6		
14	Total	5236	17			
15						
16	Tukey's Multiple Comparison Test	Mean Diff.	q	Significant? P < 0.05?	Summary	95% CI of diff
17	PBS vs Ctrl	33.35	4.410	No	ns	-2.576 to 69.29
18	PBS vs Ctrl + Phz 1	33.48	4.427	No	ns	-2.450 to 69.41
19	PBS vs Ctrl + Phz 2	8.587	1.135	No	ns	-27.34 to 44.52
20	PBS vs Ctrl + Phz 3	18.43	2.437	No	ns	-17.50 to 54.36
21	PBS vs Ctrl + Phz 4	4.332	0.5728	No	ns	-31.60 to 40.26
22	Ctrl vs Ctrl + Phz 1	0.1268	0.01674	No	ns	-35.80 to 36.06
23	Ctrl vs Ctrl + Phz 2	-24.77	3.275	No	ns	-60.70 to 11.16
24	Ctrl vs Ctrl + Phz 3	-14.92	1.973	No	ns	-50.86 to 21.01
25	Ctrl vs Ctrl + Phz 4	-29.02	3.838	No	ns	-64.95 to 8.908
26	Ctrl + Phz 1 vs Ctrl + Phz 2	-24.89	3.292	No	ns	-60.83 to 11.04
27	Ctrl + Phz 1 vs Ctrl + Phz 3	-15.05	1.990	No	ns	-50.98 to 20.88
28	Ctrl + Phz 1 vs Ctrl + Phz 4	-29.15	3.854	No	ns	-65.06 to 6.762
29	Ctrl + Phz 2 vs Ctrl + Phz 3	9.844	1.302	No	ns	-26.09 to 45.77
30	Ctrl + Phz 2 vs Ctrl + Phz 4	-4.255	0.5626	No	ns	-40.19 to 31.68
31	Ctrl + Phz 3 vs Ctrl + Phz 4	-14.10	1.884	No	ns	-50.03 to 21.83

---

---

## 4.5 References

- (1) Rajasekhar, K.; Chakrabarti, M.; Govindaraju, T. Function and toxicity of amyloid beta and recent therapeutic interventions targeting amyloid-beta in Alzheimer's disease. *Chem. Commun.* **2015**, *51*, 13434-13450.
- (2) Alzheimer's, A. 2015 Alzheimer's disease facts and figures. *Alzheimer's & dementia: the journal of the Alzheimer's Association* **2015**, *11*, 332.
- (3) Selkoe, D. J.; Hardy, J. The amyloid hypothesis of Alzheimer's disease at 25 years. *EMBO Mol. Med.* **2016**, *8*, 595-608.
- (4) Knowles, T. P.; Vendruscolo, M.; Dobson, C. M. The amyloid state and its association with protein misfolding diseases. *Nat. Rev. Mol. Cell Biol.* **2014**, *15*, 384-396.
- (5) De Strooper, B.; Karran, E. The cellular phase of Alzheimer's disease. *Cell* **2016**, *164*, 603-615.
- (6) Chiti, F.; Dobson, C. M. Protein misfolding, amyloid formation, and human disease: a summary of progress over the last decade. *Annu. Rev. Biochem.* **2017**, *86*, 27-68.
- (7) Rajasekhar, K.; Suresh, S.; Manjithaya, R.; Govindaraju, T. Rationally designed peptidomimetic modulators of A $\beta$  toxicity in Alzheimer's disease. *Sci. Rep.* **2015**, *5*, 8139.
- (8) Rajasekhar, K.; Govindaraju, T. Current progress, challenges and future prospects of diagnostic and therapeutic interventions in Alzheimer's disease. *RSC Adv.* **2018**, *8*, 23780-23804.
- (9) Soto, C.; Sigurdsson, E. M.; Morelli, L.; Kumar, R. A.; Castaño, E. M.; Frangione, B.  $\beta$ -sheet breaker peptides inhibit fibrillogenesis in a rat brain model of amyloidosis: implications for Alzheimer's therapy. *Nat. Med.* **1998**, *4*, 822.
- (10) Walsh, D. M.; Selkoe, D. J. A $\beta$  oligomers—a decade of discovery. *J. Neurochem.* **2007**, *101*, 1172-1184.
- (11) Stefani, M.; Dobson, C. M. Protein aggregation and aggregate toxicity: new insights into protein folding, misfolding diseases and biological evolution. *J. Mol. Med.* **2003**, *81*, 678-699.
- (12) Chimon, S.; Shaibat, M. A.; Jones, C. R.; Calero, D. C.; Aizezi, B.; Ishii, Y. Evidence of fibril-like  $\beta$ -sheet structures in a neurotoxic amyloid intermediate of Alzheimer's  $\beta$ -amyloid. *Nat. Struct. Mol. Biol.* **2007**, *14*, 1157.
- (13) Mastrangelo, I. A.; Ahmed, M.; Sato, T.; Liu, W.; Wang, C.; Hough, P.; Smith, S. O. High-resolution atomic force microscopy of soluble A $\beta$ 42 oligomers. *J. Mol. Biol.* **2006**, *358*, 106-119.



- (14) Rajasekhar, K.; Madhu, C.; Govindaraju, T. Natural tripeptide-based inhibitor of multifaceted amyloid  $\beta$  toxicity. *ACS Chem. Neurosci.* **2016**, *7*, 1300-1310.
- (15) Ramesh, M.; Makam, P.; Voshavar, C.; Khare, H.; Rajasekhar, K.; Ramakumar, S.; Govindaraju, T.: L-Dopa and dopamine conjugated naphthalene diimide modulate amyloid  $\beta$  toxicity. *Org. Biomol. Chem.* **2018**, *16*, 7682-7692.
- (16) Samanta, S.; Rajasekhar, K.; Babagond, V.; Govindaraju, T. Small molecule inhibits metal-dependent and-independent multifaceted toxicity of Alzheimer's disease. *ACS Chem. Neurosci.* **2019**, *10*, 3611-3621.
- (17) Rajasekhar, K.; Mehta, K.; Govindaraju, T. Hybrid multifunctional modulators inhibit multifaceted A $\beta$  toxicity and prevent mitochondrial damage. *ACS Chem. Neurosci.* **2018**, *9*, 1432-1440.
- (18) Herbst, M.; Wanker, E. E. Therapeutic approaches to polyglutamine diseases: combating protein misfolding and aggregation. *Curr. Pharm. Des.* **2006**, *12*, 2543-2555.
- (19) Habchi, J.; Arosio, P.; Perni, M.; Costa, A. R.; Yagi-Utsumi, M.; Joshi, P.; Chia, S.; Cohen, S. I.; Müller, M. B.; Linse, S. An anticancer drug suppresses the primary nucleation reaction that initiates the production of the toxic A $\beta$ 42 aggregates linked with Alzheimer's disease. *Sci. Adv.* **2016**, *2*, e1501244.
- (20) Habchi, J.; Chia, S.; Limbocker, R.; Mannini, B.; Ahn, M.; Perni, M.; Hansson, O.; Arosio, P.; Kumita, J. R.; Challa, P. K. Systematic development of small molecules to inhibit specific microscopic steps of A $\beta$ 42 aggregation in Alzheimer's disease. *PNAS* **2017**, *114*, E200-E208.
- (21) Bieschke, J.; Russ, J.; Friedrich, R. P.; Ehrnhoefer, D. E.; Wobst, H.; Neugebauer, K.; Wanker, E. E. EGCG remodels mature  $\alpha$ -synuclein and amyloid- $\beta$  fibrils and reduces cellular toxicity. *PNAS* **2010**, *107*, 7710-7715.
- (22) Ladiwala, A. R. A.; Dordick, J. S.; Tessier, P. M. Aromatic small molecules remodel toxic soluble oligomers of amyloid  $\beta$  through three independent pathways. *J. Biol. Chem.* **2011**, *286*, 3209-3218.
- (23) Ehrnhoefer, D. E.; Bieschke, J.; Boeddrich, A.; Herbst, M.; Masino, L.; Lurz, R.; Engemann, S.; Pastore, A.; Wanker, E. E. EGCG redirects amyloidogenic polypeptides into unstructured, off-pathway oligomers. *Nat. Struct. Mol. Biol.* **2008**, *15*, 558.
- (24) Cummings, J. L.; Morstorf, T.; Zhong, K. Alzheimer's disease drug-development pipeline: few candidates, frequent failures. *Alzheimers Res.* **2014**, *6*, 37.

- (25) Yang, D.-S.; Yip, C. M.; Huang, T. J.; Chakrabartty, A.; Fraser, P. E. Manipulating the amyloid- $\beta$  aggregation pathway with chemical chaperones. *J. Biol. Chem.* **1999**, *274*, 32970-32974.
- (26) Limbocker, R.; Chia, S.; Ruggeri, F. S.; Perni, M.; Cascella, R.; Heller, G. T.; Meisl, G.; Mannini, B.; Habchi, J.; Michaels, T. C. T.; Challa, P. K.; Ahn, M.; Casford, S. T.; Fernando, N.; Xu, C. K.; Kloss, N. D.; Cohen, S. I. A.; Kumita, J. R.; Cecchi, C.; Zasloff, M.; Linse, S.; Knowles, T. P. J.; Chiti, F.; Vendruscolo, M.; Dobson, C. M. Trodusquemine enhances A $\beta$ 42 aggregation but suppresses its toxicity by displacing oligomers from cell membranes. *Nat. Commun.* **2019**, *10*, 225.
- (27) Shoup, T.; Normandin, M.; Takahashi, K.; Griciuc, A.; Dhaynaut, M.; Quinti, L.; Moon, S.-H.; Guehl, N.; Brugarolas, P.; Tanzi, R. E. Fluorinated cromolyn derivatives for potential Alzheimer's disease treatment. *J. Nucl. Med.* **2019**, *60*, 114-114.
- (28) Cheng, Y.; Ono, M.; Kimura, H.; Kagawa, S.; Nishii, R.; Kawashima, H.; Saji, H. Fluorinated benzofuran derivatives for PET imaging of  $\beta$ -amyloid plaques in Alzheimer's disease brains. *ACS Med. Chem. Lett.* **2010**, *1*, 321-325.
- (29) Ono, M.; Kawashima, H.; Nonaka, A.; Kawai, T.; Haratake, M.; Mori, H.; Kung, M.-P.; Kung, H. F.; Saji, H.; Nakayama, M. Novel benzofuran derivatives for PET imaging of  $\beta$ -amyloid plaques in Alzheimer's disease brains. *J. Med. Chem.* **2006**, *49*, 2725-2730.
- (30) Ono, M.; Cheng, Y.; Kimura, H.; Cui, M.; Kagawa, S.; Nishii, R.; Saji, H. Novel <sup>18</sup>F-labeled benzofuran derivatives with improved properties for positron emission tomography (PET) imaging of  $\beta$ -amyloid plaques in Alzheimer's brains. *J. Med. Chem.* **2011**, *54*, 2971-2979.
- (31) Loureiro, J. A.; Crespo, R.; Börner, H.; Martins, P. M.; Rocha, F. A.; Coelho, M.; Pereira, M. C.; Rocha, S. Fluorinated beta-sheet breaker peptides. *J. Mater. Chem. B* **2014**, *2*, 2259-2264.
- (32) Rajasekhar, K.; Narayanaswamy, N.; Murugan, N. A.; Viccaro, K.; Lee, H.-G.; Shah, K.; Govindaraju, T. A  $\beta$  plaque-selective NIR fluorescence probe to differentiate Alzheimer's disease from tauopathies. *Biosens. Bioelectron.* **2017**, *98*, 54-61.
- (33) Rajasekhar, K.; Narayanaswamy, N.; Murugan, N. A.; Kuang, G.; Ågren, H.; Govindaraju, T. A high affinity red fluorescence and colorimetric probe for amyloid  $\beta$  aggregates. *Sci. Rep.* **2016**, *6*, 23668.
- (34) Giacomelli, C. E.; Norde, W. Conformational changes of the amyloid  $\beta$ -peptide (1-40) adsorbed on solid surfaces. *Macromol. Biosci.* **2005**, *5*, 401-407.

- (35) Rocha, S.; Thünemann, A. F.; do Carmo Pereira, M.; Coelho, M.; Möhwald, H.; Brezesinski, G. Influence of fluorinated and hydrogenated nanoparticles on the structure and fibrillogenesis of amyloid beta-peptide. *Biophys. Chem.* **2008**, *137*, 35-42.
- (36) Kim, W.; Hecht, M. H. Generic hydrophobic residues are sufficient to promote aggregation of the Alzheimer's A $\beta$ 42 peptide. *PNAS* **2006**, *103*, 15824-15829.
- (37) Jalili-Baleh, L.; Nadri, H.; Moradi, A.; Bukhari, S. N. A.; Shakibaie, M.; Jafari, M.; Golshani, M.; Moghadam, F. H.; Firoozpour, L.; Asadipour, A. New racemic annulated pyrazolo [1, 2-b] phthalazines as tacrine-like AChE inhibitors with potential use in Alzheimer's disease. *Eur. J. Med. Chem.* **2017**, *139*, 280-289.
- (38) Levine III, H. Thioflavine T interaction with synthetic Alzheimer's disease  $\beta$ -amyloid peptides: Detection of amyloid aggregation in solution. *Protein Sci.* **1993**, *2*, 404-410.
- (39) Hellstrand, E.; Boland, B.; Walsh, D. M.; Linse, S. Amyloid  $\beta$ -protein aggregation produces highly reproducible kinetic data and occurs by a two-phase process. *ACS Chem. Neurosci.* **2009**, *1*, 13-18.
- (40) Petkova, A. T.; Ishii, Y.; Balbach, J. J.; Antzutkin, O. N.; Leapman, R. D.; Delaglio, F.; Tycko, R. A structural model for Alzheimer's  $\beta$ -amyloid fibrils based on experimental constraints from solid state NMR. *PNAS* **2002**, *99*, 16742-16747.
- (41) Pike, C. J.; Walencewicz-Wasserman, A. J.; Kosmoski, J.; Cribbs, D. H.; Glabe, C. G.; Cotman, C. W. Structure-activity analyzes of  $\beta$ -amyloid peptides: contributions of the  $\beta$ 25–35 region to aggregation and neurotoxicity. *J. Neurochem.* **1995**, *64*, 253-265.
- (42) Sen, S.; Konar, S.; Pathak, A.; Dasgupta, S.; DasGupta, S. Effect of Functionalized Magnetic MnFe<sub>2</sub>O<sub>4</sub> nanoparticles on fibrillation of human serum albumin. *J. Phys. Chem. B* **2014**, *118*, 11667–11676.
- (43) Shughrue, P.; Acton, P.; Breese, R.; Zhao, W. Q.; Chen Dodson, E.; Hepler, R.; Wolfe, A.; Matthews, M.; Heidecker, G.; Joyce, J. Anti-ADDL antibodies differentially block oligomer binding to hippocampal neurons. *Neurobiol. Aging* **2010**, *31*, 189-202.



## Chapter 5

**Tryptophan Rich Peptide Selectively Recognize and Modulates *i*-motif  
Structural Dynamics of HIF-1 $\alpha$  DNA**



Besides the well-known double-helical structure, DNA adopt several noncanonical conformations under physiological conditions, such as G-quadruplex (G4) and intercalated motif (*i*-motif) structure.<sup>1,2</sup> Of the two structures, G4 DNA formed by the guanine (G)-rich region of genome has been extensively studied. In contrast, knowledge on the structural or biological role of *i*-motif DNA is poorly understood. The *i*-motif is formed by the stack of intercalating hemi-protonated cytosine-cytosine<sup>+</sup> (C:C<sup>+</sup>) stabilized in slightly acidic conditions (pH 4.6 to 5.2). Due to the widespread distribution of C-rich regions in the human genome, various biophysical techniques have been used to characterize in vitro *i*-motifs derived from the promoter regions of telomeres, centromeres, and proto-oncogenes.<sup>3,4</sup> The biophysical analyzes show the formation of both intramolecular and intermolecular *i*-motif structures. The overall stability of the *i*-motif structure depends on the number of cytosines in the sequence and the length and composition of the loop. In vitro stability of *i*-motif's highly dependent on chemical and physical environmental factors such as acidic pH, low ionic strength, molecular stiffness, and low temperature. These conditions are not normally available in the cellular environment to stabilize the *i*-motif structure. However, recent studies have shown that the *i*-motif is stable and can exist in the nucleus of living cells.<sup>5</sup> This suggests that *i*-motif may have role to play in gene regulation and is thought to be involved in several cancer-related pathophysiological processes. In this regard, ligands that preferentially target or induce *i*-motif formation in the genomic DNA in cellular environment may be useful in targeting cancer. Such ligands also provide detailed insight into the possible effects of *i*-motif structure on physiological processes (Figure 1).<sup>6-8</sup> Therefore, simple and rapid high-throughput screening methods can be used to identify *i*-motif-inducible or binding ligands at physiological pH. Despite the debate over the biological importance, researchers have developed several applications including pH sensors, delivery systems, ATP sensors, switchable nanostructures, and

memory devices based *i*-motif structures with stimuli responsive property.<sup>9</sup> Recently, *i*-motif-based molecular DNA switches have been used in live cells for real-time monitoring of intracellular pH and pH-triggered drug administration.<sup>10,11</sup>

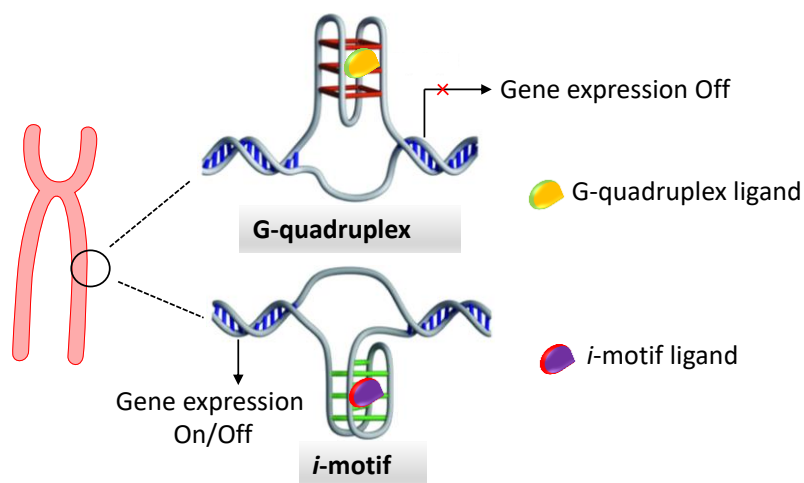


**Figure 1.** Preferential targeting of GQs and *i*-motifs by small molecules or peptides.

The discovery of specific *i*-motif binding small molecules or peptides lags behind the well-documented examples of G4 binders.<sup>12,13</sup> TMPyP4, bisacridine (BisA), and phenanthroline derivatives have been investigated as *i*-motif binding ligands.<sup>14,15</sup> Some of them have stabilizing effect, without selectivity over other DNA structures. Similarly, several molecules containing metals (terbium and ruthenium) have been investigated as potential *i*-motif binders, which are found to lack selectivity and destabilize *i*-motif structures.<sup>16,17</sup> The first reported *i*-motif selective probe is the carboxyl-modified single-walled carbon nanotubes (C-SWNTs).<sup>18</sup> In vitro and in vivo investigations by Quet *et al.* revealed C-SWNTs inhibition of telomerase activity and interfere with telomere functions, leading to senescence and apoptosis in cancer cells. Hurley *et al.* identified a ligand IMC-48 by screening a library of 1990 compounds, which binds and stabilizes the *i*-motif structure created by the C-rich sequence of BCL2 gene promoter. Several small-



molecule ligands, such as the type 2 topoisomerase inhibitor mitoxantrone, the para-isomer of the peptidomimetic ligand PBP1, and thiazole orange have been studied to expand the *i*-motif-specific ligands library. Shu *et al.* recently showed that an acridone-based molecule could bind to and stabilize c-MYC promoter *i*-motif while minimizing the binding to G4 and duplex DNA. This resulted in c-MYC transcription and expression being downregulated, causing tumor cell death.<sup>13,19,20</sup>

### 5.1 Design and synthesis

It has been reported that oligopeptides containing aromatic amino acids are capable of forming stacked complexes with DNA.<sup>21</sup> A tripeptide Lysine-Tryptophan-Lysine (Lys-Trp-Lys) has been shown to form complexation with single-stranded polynucleotides and double-stranded DNA through stacking interactions. Fluorescence studies of the binding of peptides containing Lys and Trp residues with nucleic acids revealed two types of complex formation. One of them involves a direct interaction of the Trp-indole ring with nucleobases, which leads to fluorescence quenching. The <sup>1</sup>H NMR and CD data showed that the fluorescence quenching is due to stacking of Trp-indole ring with nucleobases. Another type of complexation is the electrostatic interaction between lysine (cationic) and DNA backbone (anionic). Several peptide-based ligands have been reported to exhibit preferential binding to G4 DNA.<sup>22,23</sup>

Herein, we demonstrate that Trp (W)-Lys (K) rich decapeptide W<sub>5</sub>K<sub>5</sub> recognizes the *i*-motif DNA over duplex DNA compared to Phe (F)-Lys (K) decapeptide, F<sub>5</sub>K<sub>5</sub> (Figure 2). W<sub>5</sub>K<sub>5</sub> specifically binds *i*-motif formed by the gene sequence present in Hypoxia-Inducible Factor (HIF) family of transcription factors (TFs) (Figure 3).<sup>24</sup> William G. Kaelin Jr., Sir Peter J. Ratcliffe, and Gregg L. Semenza were honored with the 2019 Nobel prize in physiology or medicine for their work on deciphering the hypoxia mechanism. The binding interaction of W<sub>5</sub>K<sub>5</sub> was studied by various

biophysical techniques. TFs in the HIF family (HIF1A, EPAS1, and HIF3A) regulate the cellular response to hypoxia, which are linked to development of a variety of disorders, including cancer, diabetes, and erythrocytosis.

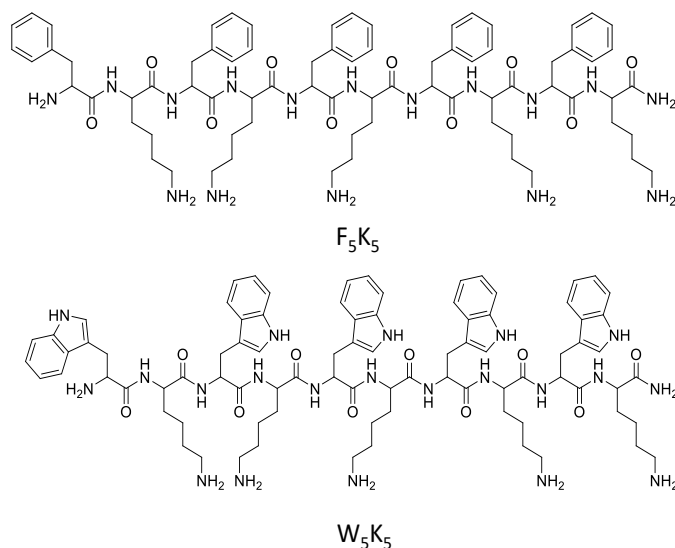


**Figure 2.** Chemical structures of decapeptides  $F_5K_5$  and  $W_5K_5$ .

A comprehensive map of links between the HIF family of genes and diverse omics categories is yet to be developed. Heterodimeric HIF TFs contain  $\alpha$  and  $\beta$  subunits. The  $O_2$ -sensitive component ( $\alpha$ -subunit) of HIF heterodimer acts as a master regulator of numerous genes implicated in the hypoxia pathway. The  $\beta$  subunit of HIF heterodimer (HIF1B, HIF-1 $\beta$ ) with official gene aryl hydrocarbon nuclear translocator (ARNT) is constitutively expressed.<sup>25</sup>

Encouraged by the preliminary results, we employed CD spectroscopy and polyacrylamide gel electrophoresis (PAGE) to study the effect of  $W_5K_5$  on the folding and structural conformation of *i*-motif DNA. Experiments were performed using an unlabeled *i*-motif forming sequence (HIF-1 $\alpha$ , 5'-d[CGCGTCCCGCCCCCTCTCCCCTCCCCGCGC]-3'). The dual-labelled human HIF *i*-motif forming sequence (HIF-1 $\alpha$  5'-FAM d[CGCGTCCCGCCCCCTCTCCCCTCCCCGCGC]-3') was used to perform DNA melting analysis, which offers the measure of peptide-induced alteration of

folded conformation. Förster resonance energy transfer (FRET) based assays were carried out in sodium cacodylate buffer (10 mM, 5 mM NaCl) at pH 4.6 and 7.4.

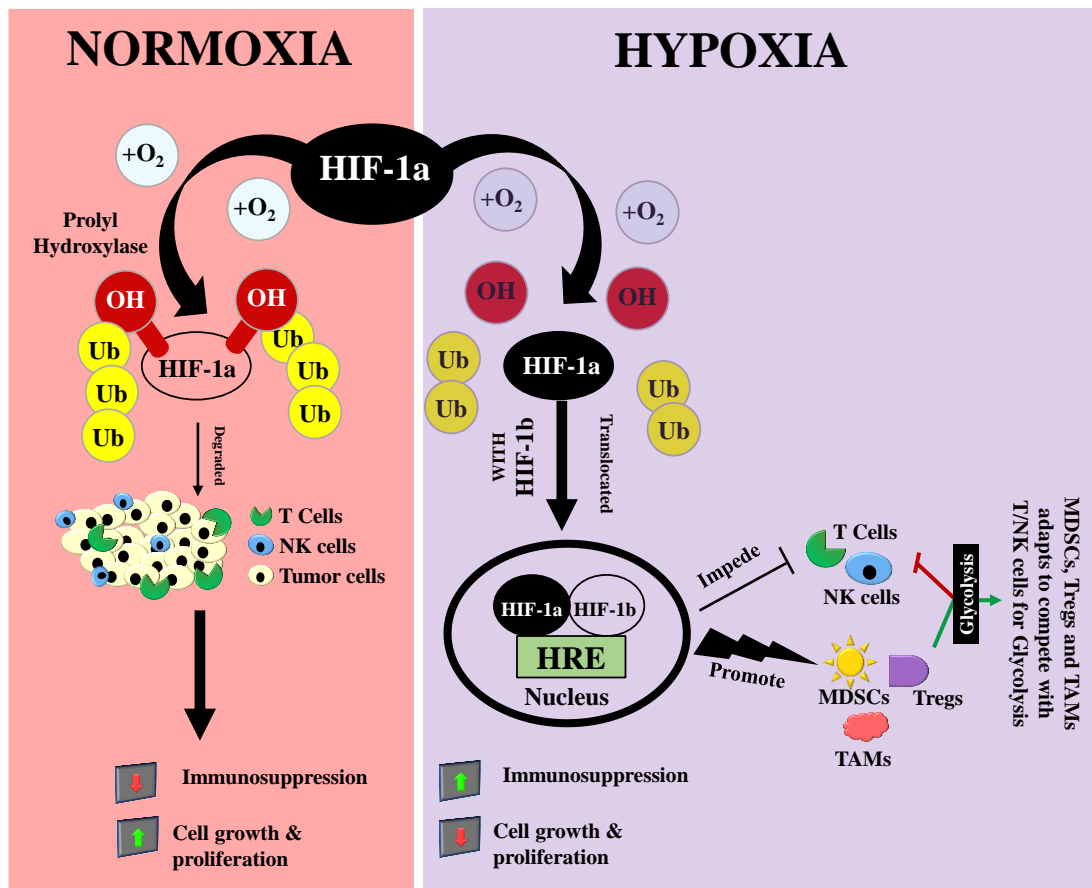


**Figure 3.** The hypoxic tumor microenvironment. HIF-1 $\alpha$  is generated under normal conditions and abundant oxygen, through the action of prolyl hydroxylase, aids in its extensive degradation with no negative consequences. Immune cells such as NK and T cells can effectively remove fast proliferating tumor cells. When the oxygen source is insufficient, as in tumor hypoxia, HIF-1 $\alpha$  degradation is suppressed, resulting in HIF-1 $\alpha$  translocation to the nucleus and a cascade of events including HIF-1 $\alpha$  and HIF-1 $\beta$  heterodimers binding to hypoxia-responsive elements (HREs) on DNA. The consequences of these processes ultimately influence hypoxia-responsive outcomes such as the incidence of pro-tumor immunosuppressant myeloid-derived suppressor cells (MDSCs), regulatory T cells (Tregs), and tumor-associated macrophages (TAMs). These immunosuppressive entities adapt to oxygen-depleted environments by competing for glycolysis with T/NK cells, lowering the T/NK cell functional efficacy. The cumulative effect of these events leads to changes in cell metabolism, increased angiogenesis, tumor development, and medication resistance. The figure is reproduced with permission from ref 25. Copyright 2020 Springer Nature.

## 5.2 Results and discussions

### 5.2.1 Trp fluorescence-based screening assay

We studied the binding interaction of W<sub>5</sub>K<sub>5</sub> and F<sub>5</sub>K<sub>5</sub> with GQs and *i*-motif of various promoter genes (DNA) sequences with distinct topologies (parallel, mixed, and anti-parallel) and duplex DNAs by monitoring the intrinsic fluorescence response of Trp ( $\lambda_{em}= 353$  nm) and Phe ( $\lambda_{em}= 285$  nm) residues (Figure 5A, B). As shown in Figure 4C and Figure 5A, W<sub>5</sub>K<sub>5</sub> (2  $\mu$ M) exhibited significant and specific fluorescence quenching in the presence of HIF-1 $\alpha$  (1  $\mu$ M) sequence compared to other *i*-motif, GQ, and duplex DNA topology sequences. To further validate the specific binding interaction, we performed CD and PAGE experiments.

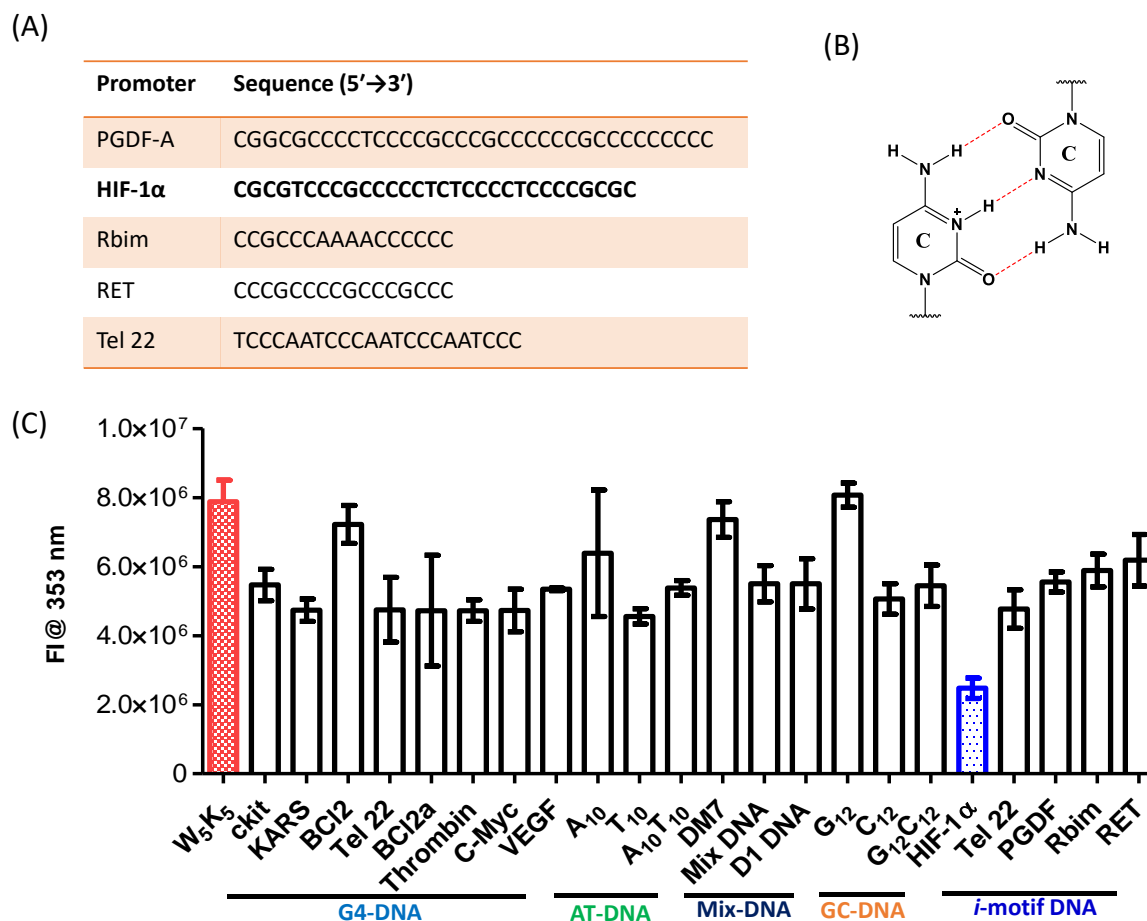


**Figure 4.** (A) The table enlist the *i*-motif forming oligonucleotide sequences located in the promoters of oncogenes (PGDF-A, HIF-1 $\alpha$ , RBIM, RET) and telomere (TEL22). (B) A hemi-protonated cytosine–cytosine (CH<sup>+</sup>-C) base pair, which intercalate to form the *i*-motif structure. (C) Normalized fluorescence

intensity (NFI) of W<sub>5</sub>K<sub>5</sub> in the presence of parallel or antiparallel GQ, *i*-motif and AT/GC- rich duplex DNAs.

### 5.2.2 CD study

CD spectroscopy is a sensitive technique to investigate ligand binding or ligand-induced conformational changes of nucleic acids. In tris-HCl aqueous buffer (10 mM, pH 4.6), HIF-1 $\alpha$  DNA adopt parallel *i*-motif structure which shows Cotton effects at 257 nm (negative) and 289 nm (positive). With increasing conc. of W<sub>5</sub>K<sub>5</sub>, the CD spectra reflected the unfolding of the *i*-motif to random coil conformation of DNA. These changes indicate that W<sub>5</sub>K<sub>5</sub> binding perturbs the conformation of HIF-1 $\alpha$  (Figure 5C). Under similar experimental conditions, F<sub>5</sub>K<sub>5</sub> was not found to induce such structural perturbation to *i*-motif conformation (Figure 5D).

### 5.2.3 Electrophoretic gel mobility shift assay (EMSA)

EMSA was performed to study the interaction of peptides with *i*-motif DNA at different pH conditions. The assay was carried out by incubating 1  $\mu$ M of DNA (HIF-1 $\alpha$ ) independently with W<sub>5</sub>K<sub>5</sub> and F<sub>5</sub>K<sub>5</sub> peptides in 1: 2 ratios at different pH conditions (pH 2, 4.6, 7.4, 12.6) for 4 h at 4 °C. The DNA binding ability of peptides was assessed by the appearance of a new band in the electrophoretic migration. As shown in Figure 5E, addition of W<sub>5</sub>K<sub>5</sub> to HIF-1 $\alpha$ , particularly in pH 4.6, led to the appearance of a new higher-order gel band in electrophoretic migration of *i*-motif DNA (lane 4) compared to unbound DNA (lane 3). On the other hand, no significant change (appearance of the new band) in the electrophoretic migration of *i*-motif DNA band was observed in the presence of F<sub>5</sub>K<sub>5</sub> at different pH conditions (Figure 5F). Thus, appearance of a new band in the EMSA indicates effective and strong binding affinity of W<sub>5</sub>K<sub>5</sub> with *i*-motif HIF-1 $\alpha$  DNA.

### 5.2.4 FRET melting assay

We performed FRET-based DNA melting assay to assess ligand-induced alterations in melting temperature of different DNA structures, which in turn anticipated to reveal peptide-DNA-interacting abilities (Figure 6). The FRET-based melting experiments showed that W<sub>5</sub>K<sub>5</sub> has a destabilization effect ( $\Delta T_m = 5.5$  °C at 1:4 ratio) on *i*-motif forming sequences HIF-1 $\alpha$ . Such destabilization effect was not observed for F<sub>5</sub>K<sub>5</sub> ( $\Delta T_m = 0.1$  °C) under similar conditions (Figure 7A, B).

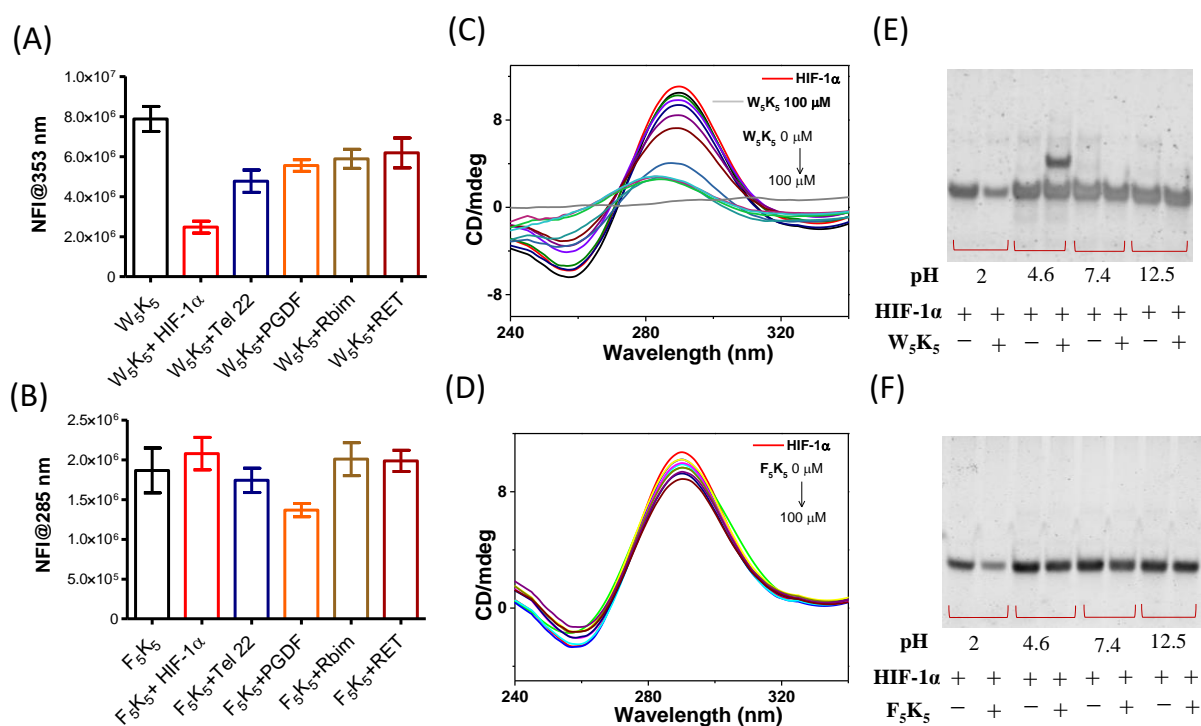


**Figure 5.** (A, B) Normalized fluorescence intensity (NFI) of W<sub>5</sub>K<sub>5</sub> and F<sub>5</sub>K<sub>5</sub> in the presence of parallel/antiparallel *i*-motif DNAs. (C, D) CD titration of 0–100  $\mu$ M W<sub>5</sub>K<sub>5</sub>/F<sub>5</sub>K<sub>5</sub> into HIF-1 $\alpha$  (2  $\mu$ M) DNA in Tris-HCl buffer (pH 4.6). (E, F) HIF-1 $\alpha$  *i*-motif DNA (1.5  $\mu$ M) is incubated in the absence or presence of peptides at 5.5  $\mu$ M at different pH conditions (2, 4.6, 7.4, 12.5). The upper (E) and lower (F) gel images are corresponding to EMSA of *i*-motif DNA (HIF-1 $\alpha$ ) in the presence of W<sub>5</sub>K<sub>5</sub> and F<sub>5</sub>K<sub>5</sub>, respectively.

### 5.2.5 Peptide-induced intramolecular folding and unfolding dynamics of HIF-1 $\alpha$

We used an *i*-motif forming HIF-1 $\alpha$  DNA sequence with 5' and 3'-ends are conjugated with a donor

(Fluorescein amidite: FAM) and acceptor (Tetramethylrhodamine: TAMRA) fluorophores, respectively, which serve as FRET reporters. C-rich random coil conformation (5' FAM-CGCGTCCCGCCCCCTCTCCCCTCCCCGCGC-TAMRA) transforms to *i*-motif under acidic conditions (pH 4.6). The FAM and TAMRA dyes were chosen as donor and acceptor pair because of their high fluorescence quantum yield and excellent FRET efficiency. Under normal physiological conditions (pH > 7), HIF-1 $\alpha$  sequence exists in the random coil structure, which is termed as an unfolded conformation. Under acidic conditions, cytosine nucleobases undergo protonation at the N1 position (CH<sup>+</sup>) to drive unfolded conformation to *i*-motif or folded

HIF-1 $\alpha$ : FAM-CGCGTCCCGCCCCCTCTCCCCTCCCCGCGC-TAMRA

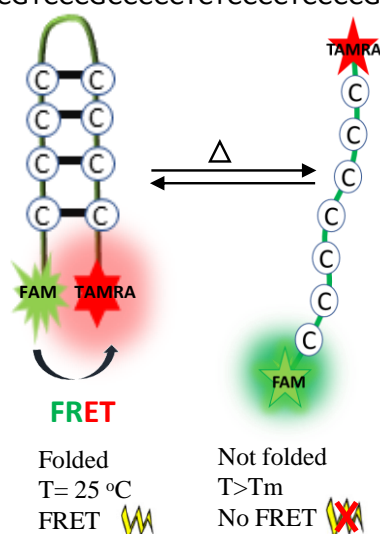


**Figure 6.** Schematic representation of FRET modulation during *i*-motif structure denaturation. At T= 25 °C, the folded structure leads to quenching of the donor (FAM) fluorescence by the quencher (TAMRA). Temperature-induced unfolding of the *i*-motif leads to decrease in FRET efficiency and a concomitant increase in FAM fluorescence emission.

Conformation (Figure 4B). In the folded conformation, the predisposed proximity of FAM (donor,  $\lambda_{em}= 520$  nm) and TAMRA (acceptor,  $\lambda_{ex}= 520$  nm) dyes is appropriately placed for efficient FRET. Further, the fluorescence spectra of FAM-HIF-1 $\alpha$ -TAMRA (100 nM), with increasing concentration of peptide was recorded. Upon increasing conc. of W<sub>5</sub>K<sub>5</sub>, the fluorescence spectra

showed a gradual decrease in emission at 580 nm (TAMRA, acceptor emission) and the corresponding increase at 485 nm (FAM, donor emission) suggesting decrease in the FRET between FAM and TAMRA, which is attributed to peptide induced perturbation in *i*-motif conformation (Figure 8A, 9A). Under similar experimental conditions, F<sub>5</sub>K<sub>5</sub> did not affect the *i*-motif conformation, indicating the absence of any interaction (Figure 8B, 9B).

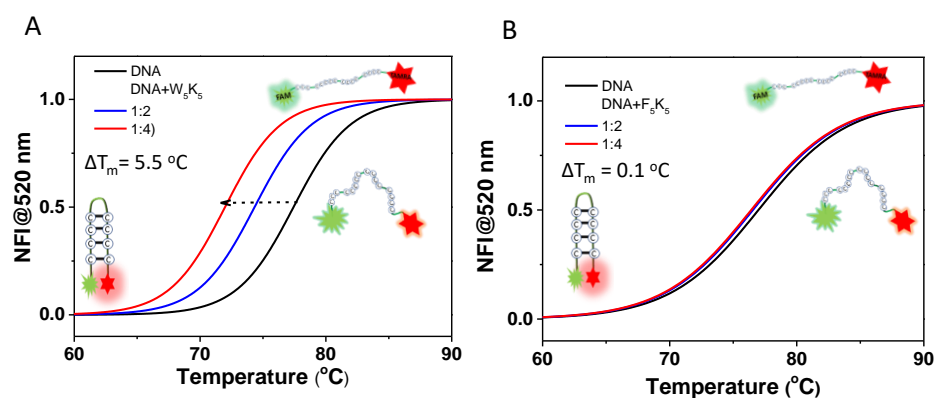


**Figure 7.** FRET melting curves for HIF-1 $\alpha$  with (A) W<sub>5</sub>K<sub>5</sub> (1:2, 1:4) (B) F<sub>5</sub>K<sub>5</sub> (1:2, 1:4)

### 5.2.6 Time correlated single photon counting (TCSPC) measurement

TCSPC experiment was carried out to gain insight into the interaction between peptides and FAM-HIF-1 $\alpha$ -TAMRA. The experiment was performed by keeping the DNA concentration fixed at 100 nM and peptide concentration was varied from 1:2 to 1:6 (DNA: peptide) ratio. The experimental data revealed that the decay pattern of DNA is di-exponential, and the average lifetime ( $\tau_{avg}$ ) is 2.5 ns. Further addition of W<sub>5</sub>K<sub>5</sub> up to 600 nM,  $\tau_{avg}$  value increased gradually from 2.5 to 3.03 ns (Figure 9C). This increase in  $\tau_{avg}$  is attributed to the change in the micro-environment of FAM fluorophore of FAM-HIF-1 $\alpha$ -TAMRA upon interaction with W<sub>5</sub>K<sub>5</sub>.



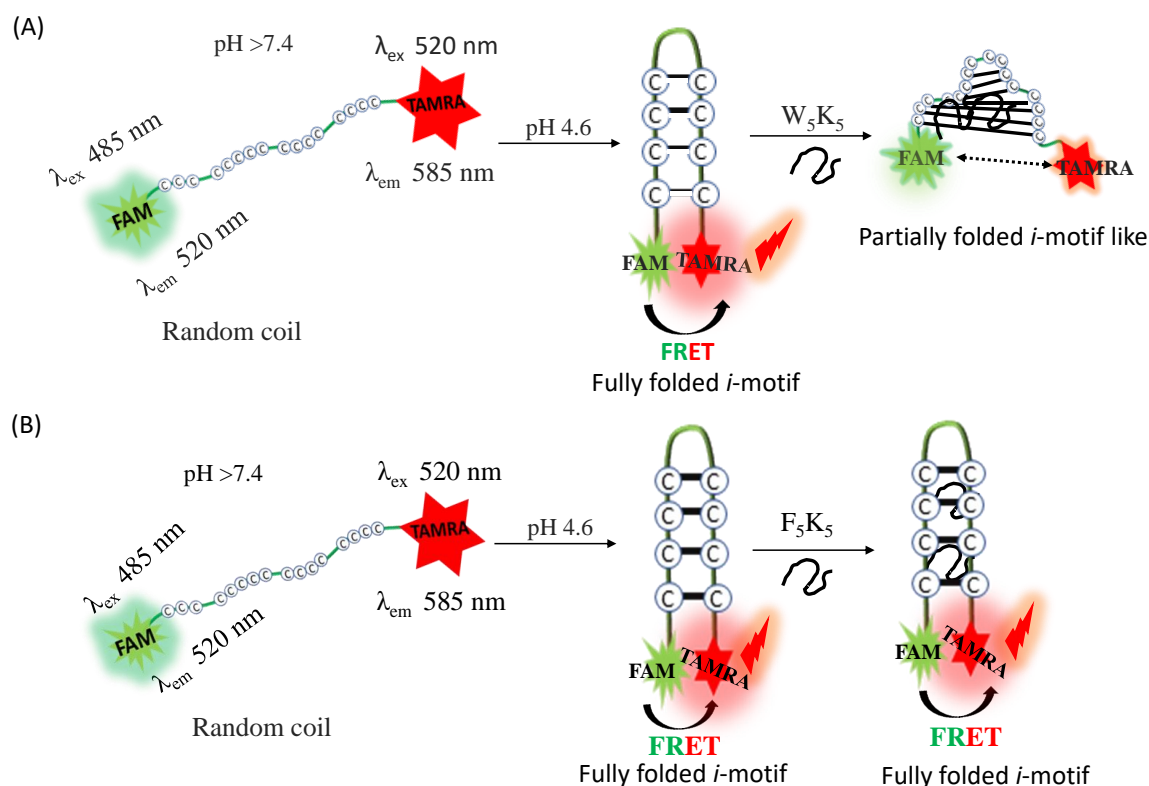


**Figure 8.** Monitoring of HIF-1 $\alpha$  structural dynamics by FRET measurements. At higher pH, DNA remains as unfolded conformation, which increases the distance between the FAM (D) and TAMRA (A) and causes a significant increase in FAM fluorescence. In folded (*i*-motif structure) conformation at lower pH, the D/A pair are in proximity results efficient FRET.  $W_5K_5$  bind and perturb the *i*-motif conformation, while  $F_5K_5$  did not such effect under similar conditions.

### 5.3 Conclusion

We have designed, synthesized, and validated decapeptide ( $W_5K_5$ ) with alternative tryptophan and lysine amino acids selectively recognize and modulate the *i*-motif structure of HIF-1 $\alpha$  DNA over other DNA conformations. The mode of interaction between  $W_5K_5$  and *i*-motif DNA was studied using different photophysical techniques. We are working on understanding the detailed insights on the mechanism of binding interaction of  $W_5K_5$  with HIF-1 $\alpha$  *i*-motif by molecular docking study. We are also studying the  $W_5K_5$  and DNA interaction *in cellulo* conditions and its implications. Our

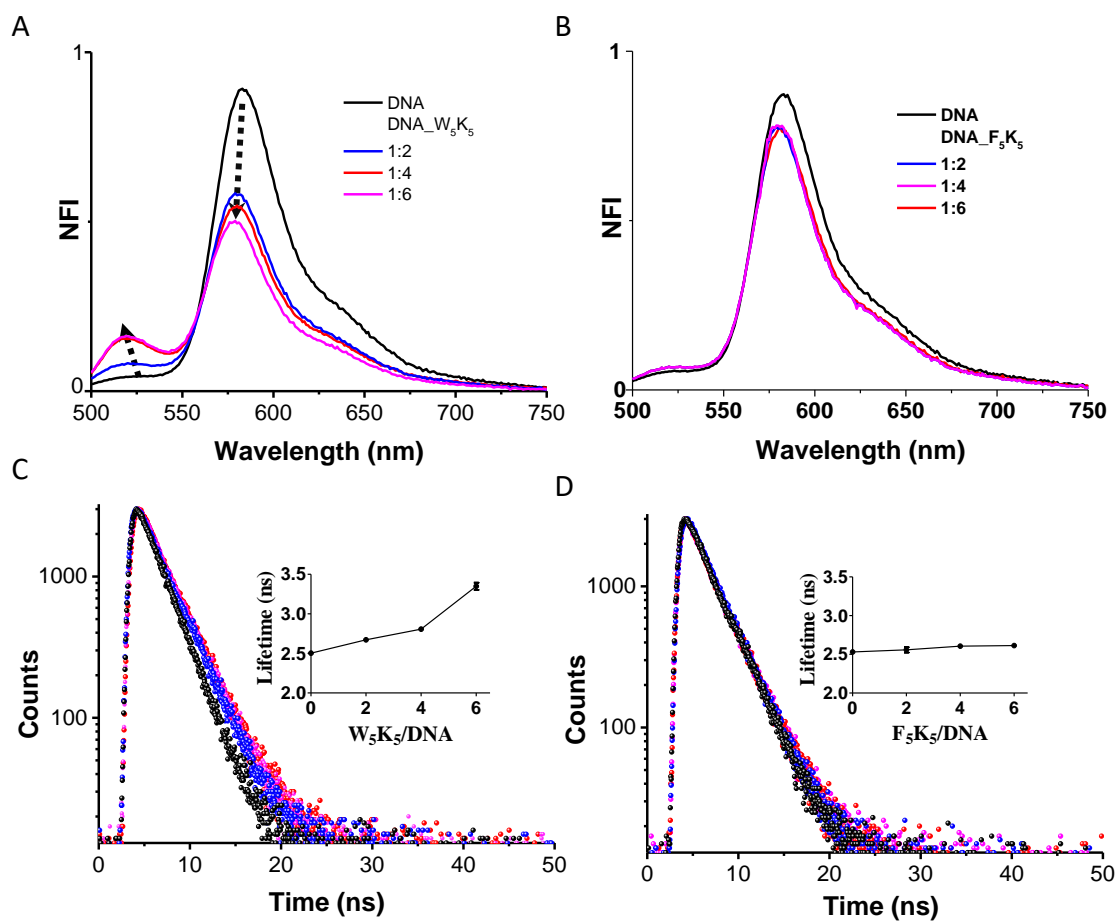


**Figure 9.** Normalized fluorescence intensity (NFI) and fluorescence lifetime of FAM and TAMRA labeled *i*-motif DNA (FAM-HIF-1 $\alpha$ -TAMRA) (100 nM) in the absence and presence of W<sub>5</sub>K<sub>5</sub> (A, C) and F<sub>5</sub>K<sub>5</sub> (B, D).

findings could pave the way for the rational design of peptide-based molecular tools to study *i*-motifs, and their structural and functional dynamics.

## 5.4 Experimental methods

### 5.4.1 Synthesis of W<sub>5</sub>K<sub>5</sub>/F<sub>5</sub>K<sub>5</sub>

Fmoc protected Rink amide resin was used to synthesize W<sub>5</sub>K<sub>5</sub> and F<sub>5</sub>K<sub>5</sub> peptides. Fluorenylmethoxycarbonyl (Fmoc)-protected amino acid (2.5 eq.), 2-(1H-benzotriazol-1-yl)-1,1,3,3-tetramethyluronium (HBTU, 2.5 eq.), and N, N-Diisopropylethylamine (DIPEA, 4 eq.) were used for the couplings. Standard Fmoc-protected amino acids were coupled for 1 h, followed by four 45 s washes with dimethylformamide (DMF). The resin-bound peptide was washed with dichloromethane (DCM) at room temperature for 45 s. The Fmoc deprotection was performed in DMF with 20% piperidine, followed by washing. A cleavage cocktail (4 mL) containing 95 percent TFA (Trifluoroacetic acid), 2.5 percent H<sub>2</sub>O, and 2.5 percent TIPS (triisopropylsilane) was used for the final cleavage. The cleavage cocktail was evaporated using a stream of nitrogen after the resin was vortex mixed for 3 h at room temperature. The peptide was precipitated from solution using ice cold diethyl ether, centrifuged at 6000 rpm for 25 min, and washed three times with ice cold ether. Finally, the crude peptides were lyophilized after being dissolved in H<sub>2</sub>O/acetonitrile (MeCN). The obtained crude peptides were purified by reverse-phase HPLC on a C18 column (19 × 250 mm) with a purity of >98%. The molecular masses of the products were confirmed by high resolution (electrospray ionization) mass spectrometry HRMS (ESI-MS) analysis.

### 5.4.2 DNA sequences used in the study

Several DNA sequences including G4 forming sequences (BCL2, VEGF, KRAS, C-Myc, BCL2a, TEL 22, Thrombin), *i*-motif forming sequences (HIF-1 $\alpha$ , RET, C-kit, TEL 22, PGDF) and duplex forming sequences (G<sub>12</sub>C<sub>12</sub>, A<sub>10</sub>T<sub>10</sub>, A<sub>12</sub>T<sub>12</sub>, DM<sub>7</sub>, mix DNA 5'-GCGCAAATTTAAATTTAAATTTGCGC-3'), were used in the study. Further, HIF-1 $\alpha$  sequence

with FRET pair, fluorescein (FAM, donor) and tetramethyl rhodamine (TAMRA, acceptor) at the 5' and 3' ends, respectively, were employed. This FRET pair has been widely used in the literature due to their high fluorescence quantum yield (0.2) and high energy transfer from FAM to TAMRA.<sup>26</sup>

#### **5.4.3 DNA sample preparation**

The 5' FAM-labeled oligonucleotide sequences were purchased as dry powder from Integrated DNA Technologies (IDT). The oligonucleotides were resuspended in water to obtain a stock solution of concentration of 100  $\mu$ M. The samples were then diluted to a concentration of 100 nM in sodium cacodylate buffer (10 mM, pH 4.6). The samples were then heated to 95 °C for 10 min before being allowed to cool slowly at room temperature overnight. The samples were stored in a dark environment to protect the fluorophore labels from the light exposure.

#### **5.4.4 GEL electrophoresis**

PAGE was performed in 1 $\times$  TBE buffer solution (90 mM tris-boric acid and 2 mM EDTA) using 15% polyacrylamide gel containing 100 mM KCl. Oligonucleotides (1  $\mu$ M) were loaded on the gel, and the electrophoresis experiment was performed at 90 V for 1 h at 4 °C. After electrophoresis, the gel was stained using 1 $\times$  SYBR Gold, under constant agitation for 15 min, then lightly rinsed with water and visualized using Chemidoc MP imaging system (Biorad).

#### **5.4.5 CD measurement**

CD spectra were recorded on a JASCO J-805 circular dichroism spectrophotometer using a 10 mm path length quartz cuvette. CD experiments were carried out at 298 K with a response time of 2 s, 1 nm pitch, and 0.5 nm bandwidth over a wavelength range of 240-340 nm. The recorded spectra are a smoothed average of three scans that have been zero-corrected at 340 nm. The buffer absorbance was subtracted from the spectra that were recorded. All samples were prepared in a

total volume of 210  $\mu\text{L}$  containing 2.5  $\mu\text{M}$  oligonucleotide in 10 mM Na cacodylate buffer (pH 4.6) for *i*-motif-forming sequences.

#### 5.4.6 Fluorescence measurement

Fluorescence lifetime and emission data were measured ( $\lambda_{\text{ex}} = 485 \text{ nm}$ ) on Edinburgh Instruments FLS 1000 spectrophotometer equipped with a micro flash lamp ( $\mu\text{F}$ ) set-up. A 485 nm nano-LED with a pulse repetition rate of 1 MHz was used as the light source. The instrument response function (IRF) was collected using a scatterer (Ludox AS40 colloidal silica). From the measured decay traces, the data were fitted with a multi-exponential decay, and  $\chi^2$  was less than 1.1.

#### 5.4.7 FRET melting assay

Assessment of the ligand-induced change in melting temperature of DNA was performed using a FRET melting assay. The oligonucleotides were labeled with the donor fluorophore FAM and acceptor fluorophore TAMRA. Solid DNA samples were initially dissolved as a stock solution in purified water (100  $\mu\text{M}$ ); further dilutions were carried out in the respective sodium cacodylate buffer: 0.2  $\mu\text{M}$  DNA in 10 mM sodium cacodylate at pH 4.6 (HIF-1 $\alpha$ : 5' FAM-CGCGTCCCGCCCCCTCTCCCCTCCCCGCGC-TAMRA). Strip-tubes (4titude, Biotechnology company in Wotton, England) were prepared with DNA solution and added W<sub>5</sub>K<sub>5</sub> and F<sub>5</sub>K<sub>5</sub> (1:2, 1:4, and 1:6 ratio). Control samples for each run were prepared with the same quantity of water with the DNA in buffer. Fluorescence melting points were measured in a QuantStudio RT-PCR machine (Thermo Fisher Scientific), using a total volume of 20  $\mu\text{L}$ . Samples were held at 25  $^{\circ}\text{C}$  for 5 min then ramped to 95  $^{\circ}\text{C}$  at increments of 1  $^{\circ}\text{C}$ , holding the temperature at each step for 1 min. Measurements were made with excitation at 480 nm and detection at 520 nm. DNA melting points were determined using the first derivative of the melting curve. The final analysis of the data was carried out using Origin 9.0 software.

### 5.4.8 FRET theory

The rate of energy transfer from a donor to an acceptor,  $k_T(r)$ , is given by Förster's theory

$$k_T(r) = \frac{1}{\tau_D} \left(\frac{R_0}{r}\right)^6 \dots\dots\dots (1)$$

where  $\tau$  is the donor's decay time in the absence of the quencher,  $R_0$  is the Förster distance, and  $r$  is the distance between the donor and the acceptor. When  $r$  equals  $R_0$ , the energy transfer rate is equal to the donor's decay rate ( $1/\tau_D$ ), and the transfer efficiency is 50% (calculated from equation 1).

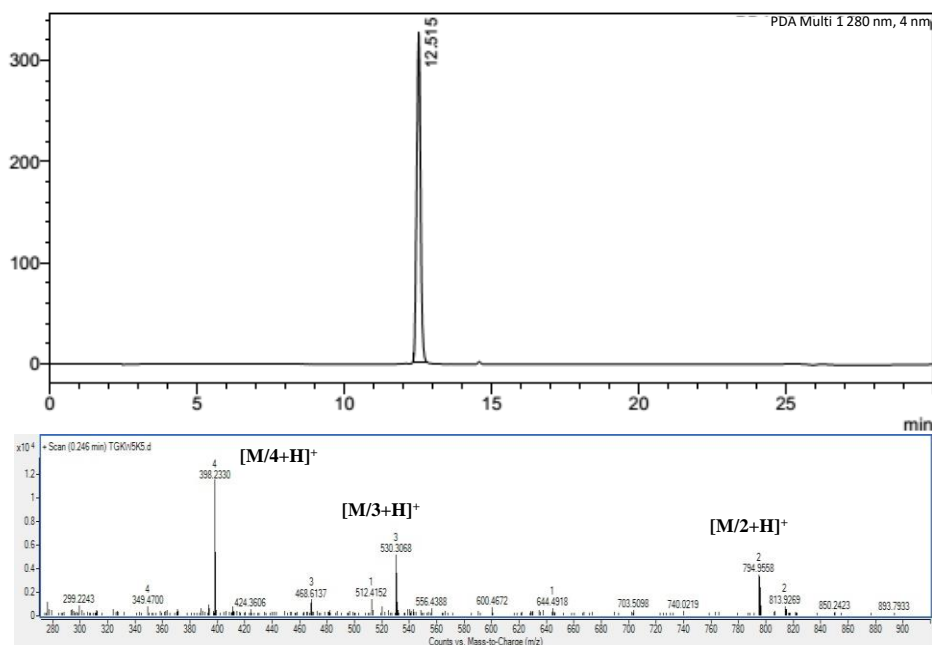
HRMS analysis data of W<sub>5</sub>K<sub>5</sub> and F<sub>5</sub>K<sub>5</sub>

Peptide	Sequence	Purity (%)	Exact (calculated) mass	Observed mass (HRMS)
W <sub>5</sub> K <sub>5</sub>	WKWKWKWKWK	98.9	1587.8979	794.9558 [M/2+H] <sup>+</sup>
				530.3068 [M/3+H] <sup>+</sup>
				398.2330 [M/4+H] <sup>+</sup>
F <sub>5</sub> K <sub>5</sub>	FKFKFKFKFKF	98.6	1392.8434	697.4275 [M/2+H] <sup>+</sup>
				465.2878 [M/3+H] <sup>+</sup>
				349.2182 [M/4+H] <sup>+</sup>

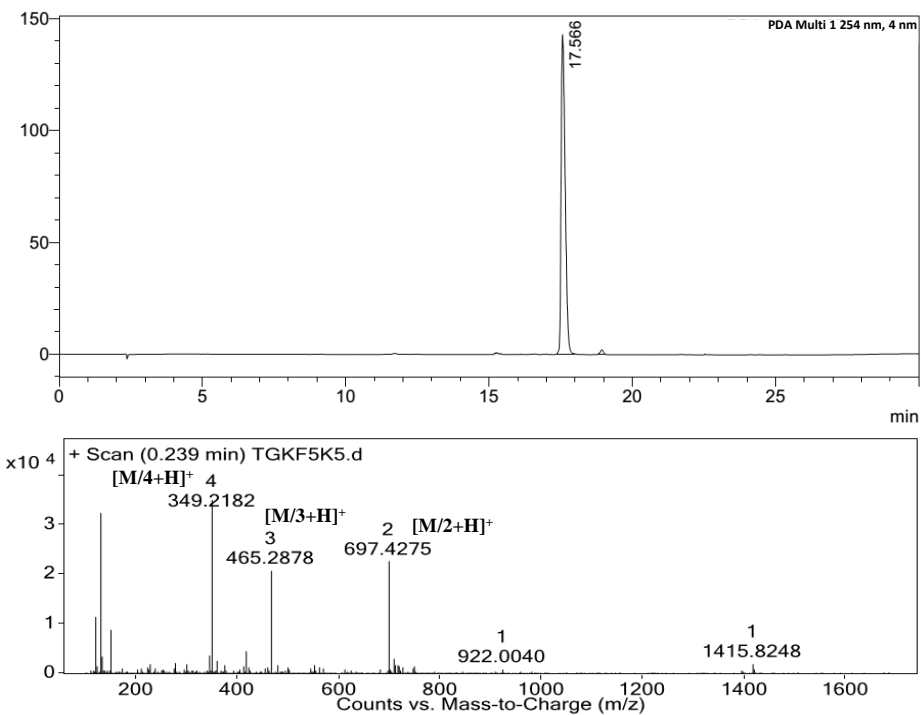
HPLC analysis of W<sub>5</sub>K<sub>5</sub> and F<sub>5</sub>K<sub>5</sub>

Peptide	Gradient	Flow rate (mL/min)	Retention time (t <sub>r</sub> )	Purity (%)
W <sub>5</sub> K <sub>5</sub>	0-98 % MeCN (0.1% TFA) in H <sub>2</sub> O (0.1% TFA) for 30 min	8	12.5 min	99.6
F <sub>5</sub> K <sub>5</sub>	0-98 % MeCN (0.1% TFA) in H <sub>2</sub> O (0.1% TFA) for 30 min	8	17.5 min	98.6

## HPLC chromatogram and HRMS data

W<sub>5</sub>K<sub>5</sub> mAUF<sub>5</sub>K<sub>5</sub>

mAU





## 5.5 References

- (1) Parkinson, G. N.; Lee, M. P.; Neidle, S. Crystal structure of parallel quadruplexes from human telomeric DNA. *Nature* **2002**, *417*, 876-880.
- (2) Suseela, Y.; Narayanaswamy, N.; Pratihari, S.; Govindaraju, T. Far-red fluorescent probes for canonical and non-canonical nucleic acid structures: current progress and future implications. *Chem. Soc. Rev.* **2018**, *47*, 1098-1131.
- (3) Phan, A. T.; Guéron, M.; Leroy, J.-L. The solution structure and internal motions of a fragment of the cytidine-rich strand of the human telomere. *J. Mol. Biol.* **2000**, *299*, 123-144.
- (4) Huppert, J. L.; Balasubramanian, S. Prevalence of quadruplexes in the human genome. *Nucleic Acids Res.* **2005**, *33*, 2908-2916.
- (5) Zeraati, M.; Langley, D. B.; Schofield, P.; Moye, A. L.; Rouet, R.; Hughes, W. E.; Bryan, T. M.; Dinger, M. E.; Christ, D. I-motif DNA structures are formed in the nuclei of human cells. *Nat. chem.* **2018**, *10*, 631-637.
- (6) Kendrick, S.; Kang, H.-J.; Alam, M. P.; Madathil, M. M.; Agrawal, P.; Gokhale, V.; Yang, D.; Hecht, S. M.; Hurley, L. H. The dynamic character of the BCL2 promoter i-motif provides a mechanism for modulation of gene expression by compounds that bind selectively to the alternative DNA hairpin structure. *J. Am. Chem. Soc.* **2014**, *136*, 4161-4171.
- (7) Brown, R. V.; Wang, T.; Chappeta, V. R.; Wu, G.; Onel, B.; Chawla, R.; Quijada, H.; Camp, S. M.; Chiang, E. T.; Lassiter, Q. R. The consequences of overlapping G-Quadruplexes and i-Motifs in the platelet-derived growth factor receptor  $\beta$  core promoter nuclelease hypersensitive element can explain the unexpected effects of mutations and provide opportunities for selective targeting of both structures by small molecules to downregulate gene expression. *J. Am. Chem. Soc.* **2017**, *139*, 7456-7475.
- (8) Tikhomirov, A. S.; Abdelhamid, M. A.; Nadysev, G. Y.; Zatonksy, G. V.; Bykov, E. E.; Chueh, P. J.; Waller, Z. A.; Shchekotikhin, A. E. Water-soluble heliomycin derivatives to target i-motif DNA. *J. Nat. Prod.* **2021**, *84*, 1617-1625.
- (9) Mattath, M. N.; Ghosh, D.; Pratihari, S.; Shi, S.; Govindaraju, T. Nucleic Acid Architectonics for pH-Responsive DNA Systems and Devices. *ACS Omega* **2022**. DOI org/10.1021/acsomega.1c06464
- (10) Modi, S.; Swetha, M.; Goswami, D.; Gupta, G. D.; Mayor, S.; Krishnan, Y. A DNA nanomachine that maps spatial and temporal pH changes inside living cells. *Nat. Nanotechnol.* **2009**, *4*, 325-330.
- (11) Narayanaswamy, N.; Nair, R. R.; Suseela, Y.; Saini, D. K.; Govindaraju, T. A molecular beacon-based DNA switch for reversible pH sensing in vesicles and live cells. *Chem. Commun.* **2016**, *52*, 8741-8744.

- (12) Suseela, Y. V.; Satha, P.; Murugan, N. A.; Govindaraju, T. Recognition of G-quadruplex topology through hybrid binding with implications in cancer theranostics. *Theranostics* **2020**, *10*, 10394.
- (13) Debnath, M.; Ghosh, S.; Chauhan, A.; Paul, R.; Bhattacharyya, K.; Dash, J. Preferential targeting of i-motifs and G-quadruplexes by small molecules. *Chem. Sci.* **2017**, *8*, 7448-7456.
- (14) Martino, L.; Pagano, B.; Fotticchia, I.; Neidle, S.; Giancola, C. Shedding light on the interaction between TMPyP4 and human telomeric quadruplexes. *J. Phys. Chem. B* **2009**, *113*, 14779-14786.
- (15) Alberti, P.; Ren, J.; Teulade-Fichou, M. P.; Guittat, L.; Riou, J.-F.; Chaires, J. B.; Hélène, C.; Vigneron, J.-P.; Lehn, J.-M.; Mergny, J.-L. Interaction of an acridine dimer with DNA quadruplex structures. *J. Biomol. Struct. Dyn* **2001**, *19*, 505-513.
- (16) Xu, H.; Zhang, H.; Qu, X. Interactions of the human telomeric DNA with terbium–amino acid complexes. *J. Inorg. Biochem.* **2006**, *100*, 1646-1652.
- (17) Shi, S.; Geng, X.; Zhao, J.; Yao, T.; Wang, C.; Yang, D.; Zheng, L.; Ji, L. Interaction of [Ru (bpy) 2 (dppz)] 2+ with human telomeric DNA: Preferential binding to G-quadruplexes over i-motif. *Biochimie* **2010**, *92*, 370-377.
- (18) Chen, Y.; Qu, K.; Zhao, C.; Wu, L.; Ren, J.; Wang, J.; Qu, X. Insights into the biomedical effects of carboxylated single-wall carbon nanotubes on telomerase and telomeres. *Nat. Commun.* **2012**, *3*, 1-13.
- (19) Wright, E. P.; Day, H. A.; Ibrahim, A. M.; Kumar, J.; Boswell, L. J.; Huguin, C.; Stevenson, C. E.; Pors, K.; Waller, Z. A. Mitoxantrone and analogues bind and stabilize i-motif forming DNA sequences. *Sci. Rep.* **2016**, *6*, 1-7.
- (20) Sheng, Q.; Neaverson, J. C.; Mahmoud, T.; Stevenson, C. E.; Matthews, S. E.; Waller, Z. A. Identification of new DNA i-motif binding ligands through a fluorescent intercalator displacement assay. *Org. Biomol. Chem.* **2017**, *15*, 5669-5673.
- (21) Toulmé, J.-J.; Charlier, M.; Hélène, C. Specific recognition of single-stranded regions in ultraviolet-irradiated and heat-denatured DNA by tryptophan-containing peptides. *PNAS* **1974**, *71*, 3185-3188.
- (22) Minard, A.; Morgan, D.; Raguseo, F.; Di Porzio, A.; Liano, D.; Jamieson, A. G.; Di Antonio, M. A short peptide that preferentially binds c-MYC G-quadruplex DNA. *Chem. Commun.* **2020**, *56*, 8940-8943.
- (23) Sengupta, P.; Banerjee, N.; Roychowdhury, T.; Dutta, A.; Chattopadhyay, S.; Chatterjee, S. Site-specific amino acid substitution in dodecameric peptides determines the stability and unfolding of c-MYC quadruplex promoting apoptosis in cancer cells. *Nucleic Acids Res.* **2018**, *46*, 9932-9950.
- (24) Semenza, G. L. Hypoxia-inducible factors in physiology and medicine. *Cell* **2012**, *148*, 399-408.

- (25) Bhattacharya, S.; Calar, K.; de la Puente, P. Mimicking tumor hypoxia and tumor-immune interactions employing three-dimensional in vitro models. *J. Exp. Clin. Cancer Res.* **2020**, *39*, 1-16.
- (26) Renčiuk, D.; Zhou, J.; Beaurepaire, L.; Guédin, A.; Bourdoncle, A.; Mergny, J.-L. A FRET-based screening assay for nucleic acid ligands. *Methods* **2012**, *57*, 122-128.



---

---

## List of Publications

### Publications included in PhD thesis

- **Konar, M.\*; Ghosh, D.\*;** Samanta, S.; Govindaraju, T. Combating the amyloid-induced cellular toxicity and stiffness by designer peptidomimetics. *RSC Chem. Biol.* **2022**, *3*, 220-226. (\* Co-first author).
- **Ghosh, D.;** Konar, M.; Mandal, T.; Govindaraju, T. Differential copper-guided architectures of amyloid  $\beta$  peptidomimetics modulate oxidation states and catalysis. *Nanoscale Adv.*, **2022**, doi.org/10.1039/D2NA00161F
- **Ghosh, D.;** Pratihar, S.; Govindaraju, T. Tryptophan rich peptide selectively recognize and modulates *i*-motif structural dynamics of HIF-1 $\alpha$  DNA (Under preparation).
- **Ghosh, D.;** Samanta, S; Govindaraju, T. Dihydrophthalazinediones accelerate amyloid  $\beta$  peptide aggregation to nontoxic species. *Bull. Mater. Sci.* **2020**, *43*, 309.

### Miscellaneous publication

- Roy, B.; **Ghosh, D.;** Govindaraju, T. Molecular-architectonics-guided dynamic assembly to generate fluorescent organic nanoclusters with implications for optical imaging. *ACS Appl. Nano Mater.* **2021**, *4*, 2, 979–984.
- Ganguly, S.; **Ghosh, D.;** Narayanaswamy, N.; Govindaraju, T.; Basu, G. Dual DNA binding mode of a turn-on red fluorescent probe thiazole coumarin. *PLoS One* 2020, *15*, 0239145.
- Ganguly, S.; Murugan, N. A.; **Ghosh, D.;** Narayanaswamy, N.; Govindaraju, T.; Basu, G. DNA Minor groove-induced cis – trans isomerization of a near-infrared fluorescent probe. *Biochemistry* **2021**, *60*, 26, 2084–2097.
- Kavitha, B. S.; Sridevi, S.; Makam, P.; **Ghosh, D.;** Govindaraju, T. Asokana, S.; Sood, A. K. Highly sensitive and rapid detection of mercury in water using functionalized etched fiber bragg grating sensors. *Sensors. Sens. Actuators, B* **2021**, *333*, 129550.

---

---

### **Review**

- **Ghosh, D.;** Datta, L. P.; Govindaraju, T. Molecular architectonics of DNA for functional nanoarchitectures. *Beilstein J. Nanotechnol.* **2020**, *11* (1), 124-140.
- Mattath, M. N.; **Ghosh, D.;** Pratihari, S.; Shi, S.; Govindaraju, T. Nucleic acid architectonics for pH-responsive DNA systems and devices. *ACS Omega* **2022**, DOI: 10.1021/acsomega.1c06464

### **Book Chapter**

- Roy, B.; **Ghosh, D.;** Govindaraju, T. Functional molecule-templated DNA nanoarchitectures, in: *Templated DNA Nanotechnology: Functional DNA Nanoarchitectonics*, Govindaraju, T., (Ed.); Jenny Stanford Publishing: New York City, NY, U.S.A., 2019; pp 69–106.
- Datta, L. P.; **Ghosh, D.;** Govindaraju, T. Functional molecule-templated DNA molecular architectonics, in: *Molecular Architectonics and Nanoarchitectonics*, Govindaraju, T., Ariga, K., (Eds.); Springer Nature Series of Nanostructure Science and Technology; Springer Nature: Singapore, 2021, pp 281-305.

---

---

## About the Author



The author, **Mr. Debasis Ghosh**, was born in Barkola, West Bengal. After his initial schooling at Barkola Vivekanand High School, he received his BSc (Hons.) in Chemistry from Midnapore College, West Bengal, India in 2013, and MSc in Chemistry from the Indian Institute of Technology Guwahati in 2015. Currently, he is pursuing a Ph.D. under the supervision of Prof. T. Govindaraju, at JNCASR. His research interests include design and synthesis of peptides, modulation of protein aggregation, understanding the structural aspects of peptidomimetics by utilizing various biophysical approaches, and design and function of materials nanoarchitectonics.